THE UNIVERSITY *of* EDINBURGH

Modelling of FRP-concrete interfacial bond behaviour

by

Feng-chen An

A dissertation submitted in partial fulfilment
for the degree of
Doctor of Philosophy

in the

Institute for Infrastructure and Environment
School of Engineering
UNIVERSITY OF EDINBURGH

2015

Declaration

This thesis entitled "Modelling of FRP-concrete interfacial bond behaviour" is submitted to the College of Science and Engineering, The University of Edinburgh, for the degree of Doctor of Philosophy.

The research work presented in this thesis has been completed solely by Feng-Chen An, under the supervision of Prof. Jian-Fei Chen and Dr. Pankaj Pankaj. I confirm that:

- Where I have consulted the published work of others, this is always clearly attributed. Where I have quoted from the work of others, the source is given.
- I have acknowledge all main sources of help.

Signed: _____

Date: _____

ABSTRACT

Externally bonding of fibre-reinforced polymer (FRP) strips or sheets has become a popular strengthening method for reinforced concrete structures over the last two decades. For most such strengthened concrete beams and slabs, the failure is at or near the FRP-concrete interface due to FRP debonding. The objective of this thesis is to develop a deeper understanding of the debonding behaviour of the FRP-concrete interface through mesoscale finite element simulation. Central to the investigation is the use of the concrete damaged plasticity (CDP) model for modelling the concrete. The FRP is treated as an elastic material.

The numerical simulation is focused on the single shear test of FRP-concrete bonded joints. This problem is known to be highly nonlinear and has many difficulties in achieving a converged solution using the standard static loading procedures. A dynamic loading procedure is applied in this research and various parameters such as time step, loading rate etc. are investigated. In particular, the effect of the damping ratio is investigated in depth and an appropriate selection is recommended for solving such problems.

It has been identified that the concrete damage model can have a significant effect on the numerical predictions in the present problem. Various concrete empirical damage models are assessed using cyclic test data and simulation of the single shear test of the FRP-concrete bonded joint and it is proposed that the Birtel and Mark's (2006) model is the most appropriate one for use in the present problem.

Subsequently, the effects of other aspects of the concrete behaviour on the FRP-concrete bond behaviour are investigated. These include the tensile fracture energy, compression strain energy and different concrete compression stress-strain models. These leads to the conclusion that the CEBFIP1990 model is the most appropriate one for the problem.

An important issue for recognition is that the actual behaviour of the FRP-concrete bonded joints is three dimensional (3D), but most numerical simulations have treated the problem as two dimensional (2D) which has a number of imitations. True 3D simulation is however very expensive computationally and impractical. This study proposes a simple procedure for modelling the joint in 2D with the 3D behaviour properly considered. Numerical results show that the proposed method can successfully overcome the limitations of the traditional 2D simulation method.

The above established FE model is then applied to simulate a large number of test specimens. The bond stress-slip relationship is extracted from the mesoscale FE simulation results. An alternative model is proposed based on these results which is shown to be advantageous compared with existing models. This new model provides the basis for further investigation of debonding failures in FRP strengthened concrete structures in the future.

Acknowledgements

The undertaking of this thesis project has not only given me a great opportunity to improve my knowledge, but also to grow and enhance my personality, which makes me know how to solve problems even in life and not only in the research.

I would like to take this opportunity to thank my previous principal supervisor Prof. Jian-Fei Chen for accepting me as one of his PhD student five years ago, for his enlightening guidance, rigorous training, and continuous support throughout the course of my PhD study even after he left for another university. Moreover, I also want to thank my current principal supervisor Dr. Pankaj Pankaj, for his spending time and patience to understand my thesis project and further giving me valuable suggestions for my research.

Besides, I also don't dare to forget the continuous fatherlike support from Professor Shuangyin Cao during my PhD study; he was my supervisor during my master study in China.

At this point I would also like to thank my friends and colleagues in my institute making many darks days brighter. Specifically, many thanks need to go to Ofonime Harry, JP Morrissey and Chris Ness for their language support, Chuanchuan Hou and Ali MacLeod for their encouragement and push, Pratap Kasina, Rongxin Zhou, Xiaobo Cheng, and Utibe Umoh for their concern in my thesis writing period. I would also like to thank those friends who have graduated but gave me great support during my early days in Edinburgh. These friends include: Yi Tao, Yin Wang, Xiaoqin Li, Shiqing Li, Noel Conlisk, Nick Brown and Lei Chen.

I'm also very grateful for the studentship provided to me by China Scholarship Council and The University of Edinburgh for making this project possible.

A special thanks also needs to be made to the School's IT department for all their assistance, particularly at times when my account was not working.

And last, but not least, my parents and girlfriend who were always willing to listen and offered me tremendous support throughout my study. Without their unconditional support and endless love, none of this would have been possible.

Don't waste life in doubts and fears

-Ralph Waldo Emerson

TABLE OF CONTENTS

LIST OF FIGURES

LIST OF TABLES

Chapter 1
Introduction

1.1 Background

Generally speaking, a normally designed reinforced concrete structure is expected to serve a lifespan of 50 to 100 years (EN 1992-1-1 2004). An increasing number of structures are in need of repair or retrofitting, due to design or construction defects; structural degradation caused by environmental factors such as earthquakes, hurricanes, impact, explosions and fire; service life extension from limited initial design life; increased load demand due to functional shifts of buildings; or revision of the relevant structural design code, which in turn causes the existing structure to fail to meet standard safety requirements. Demolishing all these structures and reconstructing new infrastructure are not sustainable, let alone economical feasibility. As such, the most feasible alternative for deteriorated structures is to strengthen or rehabilitate them. In view of that point, the global market for strengthening work has grown considerably. According to the 2009 Report Card of the American Society of Civil Engineers, the total expense to strengthen and repair existing infrastructures in the US is up to USD 1.1 trillion from 2009 to 2014 (Delmon and Delmon 2012).

Traditionally, engineers strengthened deteriorated concrete structures by externally post-tensioning, section enlargement, concrete replacement or by adding more supports under flexural elements. Addition of pre-stressed reinforced bars requires minimal time for repair. However, there are many serious issues associated with this approach, such as poor ductility under seismic and impact loads, no resistance to fire due to exposure to air and tendency towards corrosion due to exposure to air. As a consequence it requires long-term maintenance and periodic checks.

By contrast, the methods of section enlargement and concrete replacement have overcome the shortcomings of pre-stressed reinforced bars, but they both need a period to cure the concrete, which may have financial implications in many cases.

Addition of supports under beams to shorten beam span, thereby increasing ultimate load of the strengthened beam is another approach for retrofitting and repair. This approach might be limited due to the availability of space or affect utilization of space beneath the strengthened beam.

To meet the requirements and needs of strengthening buildings, the technique of externally bonding steel plates onto soffits of flexural elements has been employed to improve the flexural capacity and ductility. The research work into the performance of members strengthened through externally bonding steel plates was pioneered simultaneously in South Africa and France in the 1960s (Fleming and King 1967; L'Hermite and Bresson 1967; Lerchenthal 1967). The increased use of this technique led to the development of specifications or advice associated with this method of strengthening (e.g. UK Department of Transport Advice Note (1994)). However, there are still many disadvantages to this method which can be summarised as follows:

- Steel corrosion when exposed to the environment, which affects the lifespan of the strengthening structures.
- Difficulty of handling plates while bonding due to their heavy weight.
- Similarly, support to the bonding plate during curing period is necessary, which may in turn affect its implementation due to the availability of space.
- Steel plate can corrode, leading to a deterioration of the bond between steel and concrete (ACI Committee 440 2002).
- Intolerance to uneven bonding surfaces, which may cause peeling of the plate (Swamy and Mukhopadhyaya 1995).

Due to these disadvantages, researchers have developed and employed Fibre Reinforced Polymers (FRP), as an alternative to steel plate for strengthening or retrofitting deteriorated structures.

FRP systems are available in a variety of forms, including wet layup (i.e. FRP sheet) and pre-cured systems (i.e. FRP plate). They are formed by embedding continuous fibres in a resin matrix that binds the fibres together.

Compared to steel plates, the prominent features of FRP composites include resistance to corrosion caused by various environmental factors, tailorability, resistance to fatigue or cyclic loads, low creep, ease for construction, and high strength-to-weight ratio, which is normally more than 10 times as high as that of mild steel with a corresponding weight of only 20% (ACI Committee 440 2002; Darby et al. 2004; Hollaway and Leeming 1999).

1.2 Use of FRP for strengthening and retrofitting

Experimental work using FRP materials for retrofitting concrete structures was reported as early as 1978 in Germany (Wolf and Miessler 1989). Research in Switzerland led to the first application of externally bonded FRP systems to reinforced concrete bridges for flexural strengthening (Meier 1987; Rostasy 1987). Subsequently, in the 1980s, the development and research into the use of these materials in structural strengthening appeared in many countries. The research activities led to its application in several projects involving a wide range of environmental problems.

Use of FRP for strengthening is not without problems. A number of experiments and engineering works, have shown that FRP strengthened beams can fail due to various possible mechanisms, which are determined by concrete strength, rebar provision and properties of FRP composites (Au and Büyüköztürk 2006). Identified failure modes are summed up as follows:

1. Concrete crushing before reinforced bar yielding
2. Steel yielding followed by concrete crushing
3. Steel yielding followed by FRP rupture
4. Shear failure
5. Concrete cover delamination
6. Debonding in the vicinity of FRP bond interface

Failure modes 1, 2 and 4 are issues in conventional reinforced concrete applications with established design specifications. Failure mode 3 is a flexural failure, similar to failure mode 2. In view of these considerations, failure modes 1, 2, 3 and 4 are

excluded from this study. The last two are debonding failure mode, which are usually premature and of brittle nature.

Debonding at FRP-concrete bonded interface is a phenomenon observed in FRP strengthened beams induced by the cracks in the deteriorated beam and nonconformity between FRP and concrete material in terms of elastic modulus. Generally, for an FRP strengthened beams, interfacial debonding is a very brittle phenomenon and occurs with very little or no visible warnings at a much lower ultimate load compared to its design load. Consequently it is not the desired failure mode for designers (Hearing 2000).

For FRP-concrete bonded interface there are three materials and two interfaces involved, thus there are five possibilities of failure locations in theory. However, there are only three failure locations observed in experiments, namely damage in FRP body (i.e. called FRP delamination), damage at FRP-adhesive interface (i.e. called FRP-concrete decohesion) and debonding in the body of concrete (Buyukozturk et al. 2002; Kaiser 1989; Ritchie et al. 1991; Saadatmanesh and Ehsani 1990; Sharif et al. 1994).

Amongst these three failure locations, the first two are attributed to the use of poor quality of FRP or its poor application. These can be avoided with good quality of FRP material and good surface preparation (Gdoutos et al. 2000). In contrast, solution to prevention of debonding in the body of concrete is not readily available. In view of this, the present study only focuses on the debonding happening in the concrete body around FRP-concrete bonded interface.

From the fracture mechanics viewpoint, debonding at FRP-concrete bonded interface can be categorised as: debonding under Mode I, debonding under Mode II and debonding under Mixed Mode (Bazant and Planas 1997), as shown in Figure 1.1.

Figure 1.1 Different debonding fracture modes for FRP-concrete bonded interface, such as (a) Mode I, (b) Mode II and (c) Mixed mode

Pure Mode I debonding failure mode, as seen in Figure 1.1 (a), is unlikely to occur in FRP strengthened beams. Even so, a quasi-Mode I debonding failure mode is still observed at the end of FRP (Figure 1.2) due to high stress concentration of peel stress and shear stress at discontinuity, where shear cracks are likely to develop under the load (Au 2005). Usually, this type of failure in strengthened RC beams with FRP is prevented by various types of anchors like L-shaped stirrups, anchor bolts, U-stirrups and full stirrups, which have been shown to be effective to prevent such a failure from occurring (Garden and Hollaway 1998; Gunes 2004; Khalifa and Nanni 2000; Khalifa et al. 1998; Sharif et al. 1994; Smith and Teng 2001).

The Mode II debonding failure mode typically occurs at a flexural crack away from the ends of the strengthening FRP plate (Figure 1.2). Debonding is induced by the relative displacement while the flexural crack widens. This failure mode often occurs when strengthened beams are reinforced with the end anchors. The addition of these anchors forces the weakest point to move to the midspan of the strengthened beam, where the mechanical conditions are more challenging to tackle as there have been many shear and flexural cracks prior to bonding (Hearing 2000; Mohamed Ali et al. 2001a; b).

Mixed mode debonding failure mode as shown in Figure 1.1 (c) is approximately what amounts to the flexure-shear crack as shown in Figure 1.2. In general, flexure-shear crack debonding is a coupled behaviour of crack widening and differential vertical movement of the crack mouth.

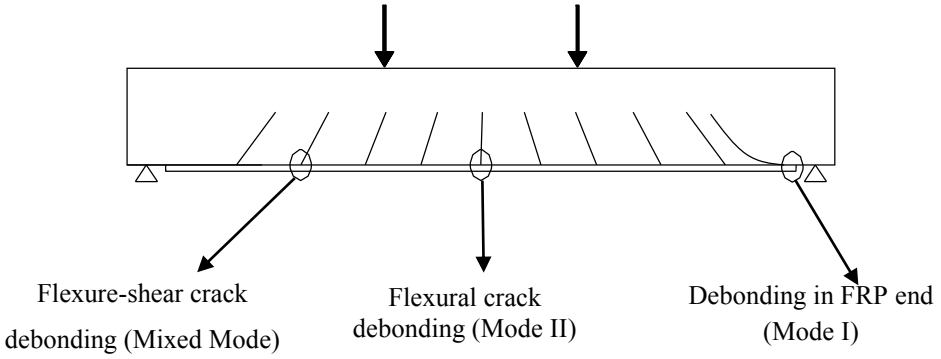

Figure 1.2 Possible debonding failures of FRP strengthened beam

As discussed above, understanding the debonding mechanism at FRP-concrete interface via simulations or experiments on FRP strengthened beams is complicated. In view of this, different simplified experimental setups have been designed to examine the debonding mechanism at the FRP-concrete interface (Chen and Teng 2001; Chen et al. 2001; Yao et al. 2005). According to the differences in mechanical behaviour, they are classified as follows:

- Single shear pulling test (Figure 1.3 (a)), in which FRP composite is bonded on one surface of concrete, and a reinforced bar is embedded into concrete body and used to pull the specimen.
- Double shear pulling test (Figure 1.3 (b)), in which two FRP composites are bonded on opposing sides of two concrete blocks. Reinforcement bars embedded in the two blocks are used to apply the loading.
- Single shear pushing test (Figure 1.3 (c)), in which FRP composite is bonded on the surface of concrete, and the specimen is actually loaded from FRP while it is constrained at the front side,
- Double shear pushing test (Figure 1.3 (d)), in which two FRP composites are bonded on opposing sides of two concrete blocks. A loading machine is placed between them to push them apart.
- Beam test (see Figure 1.3 (e)), in which one FRP composite is bonded on one side of two concrete blocks to connect them together, and on the opposing side,

is connected by joint, so that they form a combined beam, which could be loaded under a four-point load.

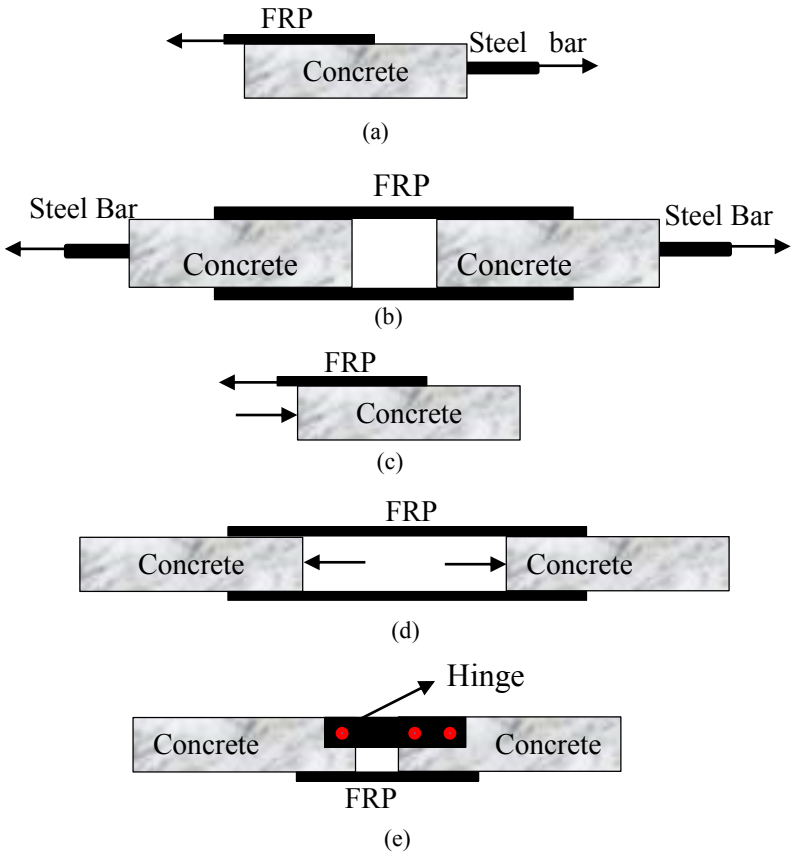

Figure 1.3 Different schemes for bond strength tests

The first four groups could be classified into two categories, viz double and single shear tests. When comparing the results from the experiments with different set-ups, double-shear tests are found to fail at a lower level of ultimate load in comparison to single shear tests. This is because the existence of inevitable asymmetry, which arises from the heterogeneity of the concrete, surface imperfections or loading eccentricity, results in the failure being initiated on one side of the specimen (Miller and Nanni 1999). Single shear pulling test is only proposed from the standpoint of concept and is very difficult to conduct in physical tests because the specimen will rotate when it is loaded. For all these reasons, amongst the four setups, the single shear push test set-up is considered the most reliable configuration for FRP-concrete debonding

investigation, and will be employed to test the performance of the proposed simulation approach in this thesis.

Real applications resemble the beam test more closely than the shear tests, but include the effects of moment variation and shear force in the concrete block. As a consequence they are not ideal for developing a preliminary understanding of FRP-concrete bonded interfacial debonding.

In view of this, single shear pushing test (Figure 1.3 (c)) is employed to investigate the mechanical behaviour of FRP-concrete bonded interface in the remaining part of this thesis. Eventually, with reference to Specimen B2-150-00 in Pan and Leung (2007), beam test is only used as a supplement to further test the reasonability of the proposed model in this thesis.

1.3 Research objective and approach

A number of experiments (Yao et al. 2005) and simulations (Lu et al. 2005b) with regard to FRP-concrete bonded interface have been conducted since its application in the field of civil engineering. Even so, the failure mechanism of FRP-concrete bonded interface is still a mystery and affects optimising design of cost-effective strengthening of deteriorated structures.

Central to this investigation is modelling of FRP-concrete bonded interface with appropriate constitutive models and the relevant parameters for analyses. Specifically, they need to include: (1) appropriate analysis techniques and if dynamic approaches are used then investigation into the effect of the mass and stiffness proportional damping ratios in simulations, thereby proposing an appropriate approach to determine the value for stiffness proportional damping; (2) an appropriate damage model for subsequent simulations through a series of comparisons between the corresponding cyclic testing data and different mathematical models; (3) the effect of concrete compression strain energy and concrete tensile fracture energy; (4) an appropriate concrete compression stress-strain model obtained from a series of comparisons

between testing data and different mathematical models; and (5) proposals of simple formula-based approaches to describe the width effect of FRP-concrete bonded interface in 2D model.

1.4 Thesis organization

This thesis consists of nine subsequent chapters.

Chapter 2 briefly discusses strengthening of reinforced concrete beams using FRP. This is followed by a literature review on debonding, including observations in practice and lab experiments; simulations through computational models; and analytical approaches.

Chapter 3 introduces general modelling information about simulations of FRP-concrete bonded interface, with reference to Specimen III-1 from Yao et al. (2005) (i.e. it is also a single shear pushing test, as shown in Figure 1.3 (c)). Specifically, it includes constitutive modelling of FRP and concrete, FE meshing approach of the FRP-concrete bonded interface, and loading scheme employed in simulation.

Chapter 4 examines the dynamic numerical approaches for the solution of the debonding problem. In particular, it investigates the effects of stiffness and mass proportional Rayleigh damping ratios on the mechanical behaviour in different cases.

Chapter 5 reviews various concrete empirical damage models, which are compared respectively with the corresponding cyclic testing data to evaluate their performance in predicting loading/unloading paths. The effect of these damage models in simulation of FRP-concrete bonded interface is investigated through element tests and simulation of FRP-concrete bonded interface, with reference to Specimen III-1 from Yao et al. (2005).

Chapter 6 uses different values of tensile fracture energy and compression hardening strain energy of concrete, each of which is considered by shape-changing and constant

shape approaches, on their effects on the mechanical behaviour in simulations of FRP-concrete bonded interface.

Chapter 7 reviews various concrete compression stress-strain models existing in the literature, which are used to compare the compression stress-strain curves from experiments of short and plain concrete cylinders with a wide range of concrete strength. The effect of these concrete compression stress-strain models is then investigated through the simulation of FRP-concrete bonded interface. The effect of different cut-off thresholds in Young's (1960) and CEBFIP (1990) compression stress-strain model are investigated respectively and a recommendation is provided for cut-off thresholds.

Chapter 8 first examines the strain distribution across the FRP section for tests conducted by Yao et al. (2005). This is followed by a proposal of a formula, describing quantitatively the effect of FRP-concrete width ratio on the ultimate load of FRP-concrete bonded interface in 2D models. Subsequently, based on 2D mesoscale model, this proposed formula is used to simulate experiments of Yao et al. (2005), Mazzotti et al. (2009), Ali-ahmad et al. (2006) and Pan et. al. (2007) to test its reasonability in predicting the mechanical behaviour at the FRP-concrete bonded interface.

Chapter 9 first reviews different bond-slip models existing in current literature. This is followed by a discussion on different methods to obtain the bond stress and slip for bond-slip models. Subsequently, FE studies using the developed mesoscale model of Chapter 8 are conducted to investigate effects of different parameters in bond-slip model, such as interfacial fracture energy, maximum shear stress and slip at maximum shear stress. On basis of the above parameter analyses, a new bond slip relationship is proposed to describe the interfacial behaviour of FRP-concrete bonded interface. Eventually, the proposed model is used to simulate the specimens from Yao et al. (2005), Mazzotti et al. (2009) and Ali-ahmad et al. (2006) to test its suitability in predicting the mechanical behaviour at the FRP-concrete bonded interface.

Chapter 10 summarises the whole thesis, thereby drawing conclusions from the work. Areas of further research are proposed and some recommendations are made for

possible improvement in the understanding of FRP-concrete interfacial debonding behaviour.

Chapter 2
Literature review

2.1 Introduction

As mentioned before, lifecycle of an FRP retrofitted flexural RC system hinges upon the quality and stability of the bond to a large extent. This chapter reviews the existing knowledge related to FRP-concrete bonded interface system from the perspective of experiments, theory and simulations. Attention is mainly focused on research of pull-out tests, since in subsequent chapters of this thesis we mainly use it for analysis.

2.2 FRP strengthened Reinforced concrete beams

As discussed in Chapter 1, externally bonding FRP on soffits of flexural structural components has become a popular strengthening method. In the following paragraphs the background to FRP and relevant strengthening techniques are reviewed.

2.2.1 FRP composites

In FRP composites, fibres are embedded in a resin matrix. Mechanical properties of FRP composites for structural applications, in most cases, are determined by fibre reinforcements. The resin matrix helps the fibres work as a composite; besides, it may protect the fibres from corrosion, fire and other environmental effects. In view of that, the fibres and resin matrix are discussed respectively in the following.

2.2.1.1 Fibres

In construction industry, there are mainly three types of fibres available, namely carbon, glass and aramid.

Carbon fibre is most notably used to reinforce composite materials, particularly the class of materials known as carbon fibre or graphite reinforced polymers. Carbon fibre,

alternatively graphite fibre, carbon graphite or CF, is a material consisting of fibres about 5–10 μm in diameter and composed mostly of carbon atoms. To produce carbon fibre, the carbon atoms are bonded together in crystals that are more or less aligned parallel to the long axis of the fibre as the crystal alignment gives the fibre high strength-to-volume ratio. Several thousand carbon fibres are bundled together to form a tow, which may be used by itself or woven into a fabric. Each carbon filament is produced from a precursor polymer such as polyacrylonitrile (PAN), rayon, petroleum, or coal pitch. The fabrication of all kinds of fibres involves a spinning process. Tensile strength of PAN-based fibres has always been higher than the pitch-base fibres. Thus, most carbon fibres used today are Pan-based. The typical strength of carbon fibres is 4.1-5.2 GPa, which is about 20 times that of structural steel. In general, carbon fibres are more brittle than glass fibres are. The stiffness of CFRP normally is equal to or higher than that of steel, ranging from 120 GPa to more than 800 GPa (Peters, 1998; Kelly, 1989; Chung, 1994; Weeton et al., 1987; Au, 2005).

Glass fibre is a kind of inorganic fibres, which are made of calcium alumina borosilicate formulations and does not support combustion. Glass fibres are categorised as: E-glass and S-glass. In general, E-glass fibre, whose name is abbreviated from Electrical glass fibre, has excellent electrical insulation characteristics while, S-glass fibre, whose name is abbreviated from Structural glass fibre, has better performance in terms of strength. The typical tensile strength and stiffness of E-glass fibres are 2.8 GPa and 104 GPa respectively. In comparison, S-glass fibres have higher strength due to their alumina content. In comparison to carbon fibre, glass can undergo more elongation before it breaks (Au 2005; Kelly 1989; Peters 1998; Weeton et al. 1987).

Aramid fibres are a class of heat-resistant and strong synthetic organic fibres. They are fibres in which the chain molecules are highly oriented along the fibre axis, so the strength of the chemical bond can be exploited. Compared to inorganic fibres like carbon or glass, aramid fibres are superior for fire resistance because the fibres themselves do not readily conduct heat into the matrix. The typical decomposition temperature is around 450℃. Another advantage of the material is that they have high

fracture energy thus excellent resistance to impact. However, one major disadvantage is that they buckle easily under compression forces. The typical tensile strength and stiffness are 2.8 GPa and 104 GPa respectively (Au 2005; Kelly 1989; Peters 1998; Shook 1986).

2.2.1.2 Resin Matrix

Broadly resin matrix is categorised into two types, namely thermoplastics and thermosets. Thermoplastic resins can return to their original liquid state on heating and under pressure while thermoset resin cannot once they have been cured. The thermosets also have other excellent mechanical properties, such as limited shrinkage upon curing and good viscosity during processing temperature (Eckold 1994). Given these advantages, thermoset resins are dominant in structural applications. For the thermoset resins, there are still two types that are most commonly used in structural applications, namely epoxy and polyester resins (Au, 2005).

Epoxy resin is a strong performance resin, providing excellent adhesion to a wide variety of fibres due to its inherent polar nature. After curing, the material has a low level of shrinkage and there is no bubble-like void formation produced. However, its ductility is reported to be relatively low, and the epoxy has a tendency to absorb moisture both in the cured and uncured periods, which can affect its long-term performance (Au, 2005).

Polyester resin has generally excellent mechanical properties and very good environmental durability. Compared to epoxy resin, polyester resin is less costly, but it does not provide adequate adhesion to carbon and aramid fibres. Owing to the adhesion problem, polyester resin usually goes with glass fibres, and less commonly with carbon and aramid fibres. In addition, shrinkage due to curing is also relatively large in the long term (Au, 2005).

The aforementioned information about the resin matrix is only for the factory manufactured FRP composites often called FRP plates (e.g. Mazzotti et al. (2009). On the other hand, FRP strips (i.e. sometimes called FRP sheets) are impregnated in-situ

with epoxy resin through wet, hand lay-up method before being applied to the already prepared soffits of the beams. In general, both FRP strips and FRP plates are called FRP in the remainder of this thesis for brevity.

2.2.1.3 Structural adhesives

The structural adhesives are used to bond the aforementioned composites to would-be bonding surface of the deteriorated structures. These adhesives need not be but often are not the same as those used as resin materials in FRP composite products, although they belong to the same class. Like resin matrix, the structural adhesives are also classified as thermoplastic and thermoset.

As mentioned earlier, thermoplastic is softened by heating and re-hardens upon cooling without undergoing any chemical transformation under high temperature or pressure. Owing to this deficiency, thermoset is the dominant choice for the structural adhesives. Within thermoset, epoxy adhesives are the most widely known and used due to their superior versatility of tailoring properties. Usually, they are obtained by adding different additives (i.e. various hardeners, fillers and toughenners) into the epoxy base, which is the basic material and exactly the same as that used in resin matrix for composites (Au 2005).

Epoxy hardener is an additive to improve mechanical properties after the epoxy is cured. In general, it is categorised into three main groups, namely aliphatic polyamines, cycloaliphatic amines and aromatic amines. Amongst these hardeners, aliphatic polyamines are one of the most commonly used in room temperature curing of epoxy adhesive systems. The hardened adhesives are rigid and resistant to chemicals, solvents and moisture. The other two types of hardeners are only used for special purposes; cycloaliphatic amines are employed to deal with low temperature and humidity while aromatic amines are adopted to improve heat and chemical resistance (Au 2005).

Sand or silica are often added as fillers to reduce costs, fill gaps on concrete surfaces, reduce creep, reduce exothermal reaction, inhibit corrosion, act as fire retardants, and

most interestingly, improve troweling ability for overhead and vertical applications without dripping (Au 2005). Nonetheless, they are not recommended to be used in locations with high moisture and chemical ingress (Comyn 1981).

Toughener, an agent made of rubber, is used as an extra energy absorption agent of unmodified epoxy. It also improves resistance to peel fracture. Typically, the toughener that is most commonly used is carboxyl-terminated butadiene acrylonitrile (CTBN).

2.2.2 Construction procedure

Before strengthening, the would-be bonding surface of concrete beam is required to be prepared to remove the weak surface layer of the concrete and the loosing debris in cracks, thereby exposing the concrete aggregate to improve the bond with FRP (Teng et al. 2002). When surface preparation is done, structural adhesive, is used to fill the cracks and the cavities that are left by the already removed debris or emerge during surface preparation. Subsequently, the FRP is externally bonded to the soffits of concrete beams.

In Mazzotti et al. (2009), different techniques for surface preparation, namely sand blasting and grinding, have been adopted to investigate its effect on debonding strength. In sand blasting, concrete surfaces are sand blasted to remove the layer of mortar over the aggregates, thereby obtaining a very rough concrete surface. In the grinding approach, surfaces of concrete are grinded with a stone wheel to remove the top layer of mortar, just until the aggregates become visible. The concrete surface is very smooth due to the very small dimension of the marble power glued to the wheel. Research has shown that the ultimate loads in the cases with sand blasting are higher than those with grinding (Mazzotti et al., 2009). In addition, in the cases where concrete surface is prepared through sand blasted, the characteristic inclined cracks on the concrete surface are observed, and a significantly thicker and rough layer of concrete is attached to FRP. On the other hand, in the cases with concrete surface grinded, only a very thin layer of concrete is attached to FRP and in some portions there is no concrete at all.

The former one is preferable from the standpoint of enhancing the ultimate load of the interface.

2.3 Observed failure modes at FRP-concrete bonded interface

As summarised in Yao et al. (2005), there are mainly three different kinds of failure modes at FRP-concrete bonded interface, namely debonding in concrete, debonding at the adhesive-concrete interface and concrete prism failure (abbreviated as CPF failure mode).

2.3.1 Debonding in concrete

Debonding in concrete, as shown in Figure 2.1, is a kind of damage that that occurs in concrete at a small distance from the adhesive-concrete interface, thus FRP is debonded with a layer of concrete, which varies between 1 and 5 mm in its thickness. Usually, for specimens which fail by debonding in concrete, the failure process starts with visible concrete cracking near the loaded end of the concrete prism. The surface cracks observed on the sides of the FRP strip have been reported to be about 45° to the longitudinal axis of the FRP (Yao et al., 2005). As the load increases, visible cracking in the concrete initiates at the loaded end, and then propagates towards the far end of FRP (Yao et al., 2005). Eventually, FRP is completely debonded from concrete prism. Research has shown that the duration of this debonding process depends on the bonded length of FRP. Specimen III-1 from Yao et al. (2005) (discussed later) will be taken as the reference case for debonding failure mode in this study.

Figure 2.1 Debonding failure mode at FRP-concrete interface from Yao et al. (2005)

2.3.2 Debonding at the adhesive-concrete interface

In this failure mode damage occurs mostly along the adhesive-concrete interface. The damaging process is quite similar to that of debonding in concrete. The only difference between these two failure modes is that much little concrete is attached to the FRP as it debonds (Yao et al., 2005). As stated by Yao et al. (2005), this damage mode is attributed to poor surface preparation. Thus, this type of failure mode can be avoided if an appropriate preparation is undertaken. It for this reason this failure mode is excluded in this thesis.

2.3.3 Concrete prism failure

This failure mode is called CPF failure mode in the remaining part of this thesis and represents damage that occurs in concrete while keeping intact FRP-concrete bonded interface. This failure mode is initiated by a crack in the concrete prism near the far end of the FRP. Once the crack appears, it propagates almost immediately towards the upper end of the support block till the specimen fails (see Figure 2.2) (Yao et al., 2005). This failure mode is reported to only occur when the FRP-concrete width ratio is beyond a value of 0.8 (Yao et al., 2005). Specimens III-5 and Specimen III-6 (Yao et

al., 2005) will be taken as the reference cases for CPF failure mode in the studies of this thesis.

Figure 2.2 CPF (i.e. failure in concrete prism) failure mode at FRP-concrete bonded interface from Yao et al. (2005)

In this thesis, only debonding in concrete (i.e. called debonding failure mode for brevity) and concrete prism failure (i.e. called CPF failure mode) are considered.

2.4 Experimental studies on FRP-concrete debonding

As discussed in Chapter 1, amongst various set-ups for experimental evaluation of debonding, single shear pushing test (i.e. also called pull-out test) is the most suitable type to investigate the debonding behaviour at FRP-concrete bonded interface (Chen et al. 2001), whereas combined beam test may be used as a supplement to the pull-out test.

In view of that, three pull-out tests, namely Yao et al.'s (2005) test, Mazzotti et al.'s (2009) test and Ali-ahmad et al.'s (2006) test, are discussed here. This is followed by an introduction of Pan and Leung's (2007) test, as a typical example of beam test.

2.4.1 Yao et al.'s (2005) test

Yao et al. (2005) used a concrete prism bonded with FRP (Figure 2.3) and fitted into a steel setup with its far end fixed using a positioning frame as shown in Figure 2.4. In

this setup, the loading position could be adjusted vertically as per the needs of the offset in the experiment to ensure that the specimen was loaded with a prescribed offset, δ. Specifically, Specimens II-1 and II-4 had a loading offset δ=4 mm (equivalent to an initial loading angle of 1.7°), whereas specimen II-3 and II-6 had a loading offset δ=-4 mm. All other specimens had no loading offset. In addition, different support blocks were employed to achieve the desired support height h_b on the prism, as shown in Figure 2.3. The free support height of the concrete prism h_c was varied from 5 mm to 120 mm.

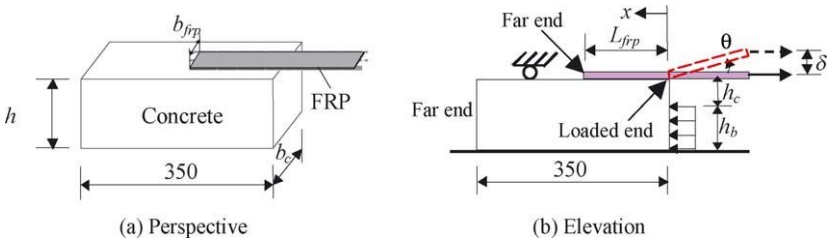

Figure 2.3 Test specimens extracted from Yao et al. (2005)

In design of these specimens a wide range of factors, which may affect the ultimate load of FRP-concrete bonded interface, were considered. These include the bond length of FRP strips L_{FRP} (varied from 75 mm to 240 mm), the FRP-concrete width ratio b_{FRP}/b_c (varied from 25/150 to 1.0), and concrete strength (varied from 18.9 MPa to 27.1 MPa).

Two kinds of concrete prisms were used to attain the desired FRP-concrete width ratio. Half of the specimens in Series III and V used 100×150×350 mm concrete prisms, whereas all the other specimens used 150×150×350 mm concrete prisms.

GFRP was used in Specimen III-7 and III-8 while CFRP was used in all others. The nominal thickness for the CFRP and GFRP were 0.165 mm and 1.27 mm, respectively. The elastic moduli for the CFRP and GFRP were 256 GPa and 22.5 GPa, respectively.

In Yao et al. (2005), loading was applied through a hydraulic jack (Figure 2.4) at an increment of about 5% of the ultimate load predicted by Chen and Teng's (2001) bond

strength model (discussed later in this chapter). Strain gauges were used to measure strains in FRP and displacements at various positions.

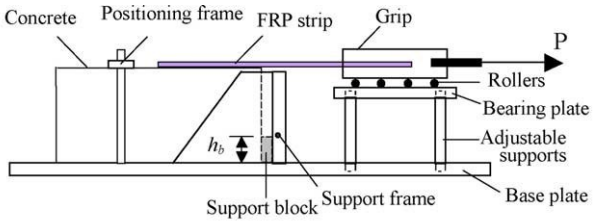

(a) Elevation

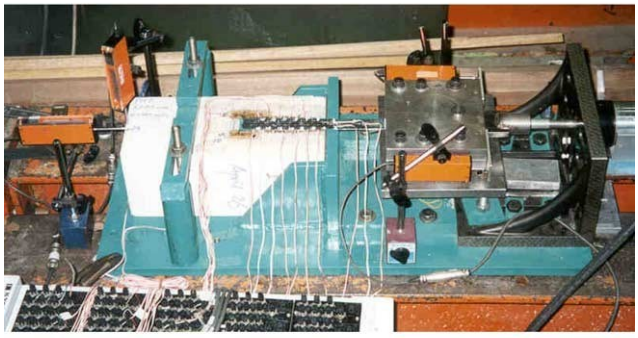

(b) Photograph

Figure 2.4 Test rig extracted from Yao et al. (2005)

Yao et al. (2005) showed that the single shear pushing test was reliable and robust as a standard bond test. They found that the free support height did have some effect on the bond strength. In terms of bond length, their results supported the concept of an effective length in Chen and Teng's (2001) model, beyond which the bond strength almost remained unchanged. It was also found that both positive and negative loading angles reduced the bond strength significantly, an effect that becomes less significant when the bonded length becomes large. The effect of FRP-concrete width ratio almost conforms to the predictions of Chen and Teng's (2001) model, except when the width ratio is larger than 0.8. In summary, the test results obtained in Yao et al. (2005) were in close agreement with the predictions of Chen and Teng's (2001) model.

2.4.2 Mazzotti et al.'s (2009) test

A similar pull-out test was also conducted by Mazzotti et al. (2009). Like Yao et al.'s (2005) test, a concrete prism bonded with FRP was fitted into a steel rig in this test, with free end of FRP clamped with a steel apparatus and the other end of FRP loaded with displacement control, as shown in Figure 2.5. A 60 mm high reaction element was placed at the front side of the concrete prism so as to restrain its movement in horizontal direction. The purpose of clamping the free end of FRP was to prevent the uplift of the specimen while loading and to prevent steep drop when FRP was completely debonded from concrete prism, thereby obtaining a stable debonding process in tests.

The dimensions of concrete prism in this test were 150 (width) × 200 (depth) × 600 (length) mm. The compressive strength 52.7 MPa and tensile strength 3.81 MPa were obtained respectively on the standard cylinder with a size of 15 × 30 cm (φ × h) at an age of 20 months. Apart from that, the elastic modulus was E_{cm}=30700 MPa and Poisson's ratio ν = 0.227.

Both CFRP sheets and plates were used. For Specimens P5 and P8, CFRP sheets were used with thickness t_f of 0.13 mm and width b_f of 80 mm. For Specimens P1, P6 and P9, CFRP plates were used with thickness t_f of 1.2 mm and width b_f of 80 mm.

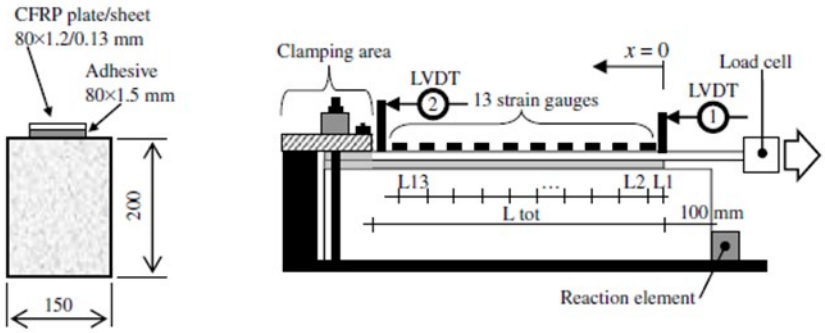

(a) (b)

Figure 2.5 Experimental setup: (a) specimen transverse section; (b) side view with instrument position and clamping system for both concrete specimen and CFRP plate extracted from Mazzotti et al. (2009)

The bonded length of FRP starts at 100 mm from the front side of the specimen, as shown in Figure 2.5 and the original unbonded length of FRP was 500 mm. However, the presence of the steel clamping system makes the FRP-concrete interface subject to debonding test reduce to 350 mm.

Different techniques for surface preparation were used by Mazzotti et al. (2009), which were been discussed in Section 2.2.1.3.

Mazzotti et al. (2009) obtained strain distributions along FRP and load-displacement curves for these specimens. They also developed a bond-slip model through axial strain measurements of strain gauges in physical tests, and then used it to simulate the tests. Through the comparisons between test and simulation results, they found that the loading stiffness in simulation is much lower than that obtained in physical test, a phenomenon that indicates that the stiffness of the derived bond-slip model is not quite right although its interfacial fracture energy (estimated through applied force corresponding to debonding) is proposed correctly. Moreover, it is seen that the experimental setup is effective in stabilising debonding behaviour. It is also found that interfacial fracture energy of mode II fracture mode is higher when FRP sheets are bonded to concrete with respect to FRP plates. In addition, the interfacial fracture

energy and ultimate load are also affected by the manner of surface preparation. Specifically, the ultimate load from the specimen which is sand blasted is 15-20% higher than that prepared using grinding.

2.4.3 Ali-ahmad et al.'s (2006) test

A similar test was conducted by Ali-ahmad et al. (2006) with the 28-day concrete compressive strength 38 MPa. Similar to Yao et al.'s (2005) test, a concrete prism bonded with an FRP strip was fitted into a steel rig, as shown in Figure 2.6. A positioning frame was placed at the far end of the prism to prevent it from moving while loading. The test was performed under displacement control with the loading rate 0.00065 mm/s at an age of 97 days of concrete.

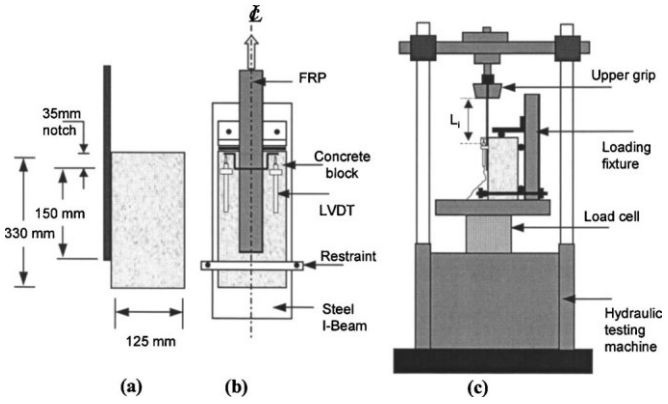

Figure 2.6 Specimen geometry and loading arrangement: (a) specimen dimensions; (b) loading fixture; and (c) test setup (extracted from Ali-ahmad et al. (2006))

Specifically, the dimensions of concrete prism are 125 (width) × 125 (depth) × 330 (length) mm. CFRP sheets were used with thickness t_f = 0.167 mm, width b_f = 46 mm and length l_f = 150 mm. A series of measures were taken on concrete surface before bonding, as discussed in Section 2.2.1.3, to ensure that the FRP was perfectly bonded to concrete prism. A 35 mm notch was introduced at the front side of the FRP-concrete interface, as shown in Figure 2.6 (a) to avoid a possible hedge failure in the concrete body.

Ali-ahmad et al. (2006) obtained ultimate loads, strain distributions along FRP at different loading levels, and load-displacement curves for these specimens. They developed a bond-slip model through axial strain measurement in physical tests, but did not verify it through simulations. In the postpeak part of the load response, it was found that there is a constant stress transfer length between the concrete and the FRP sheets, a length that was found to be approximately equal to 90 mm. Additionally, the fracture energy, which is required to create a unit surface area of the interfacial crack, was found to be constant and independent of the location of the crack along the interface.

2.4.4 Pan and Leung's (2007) test

Pan and Leung's (2007) test was designed with the concept of combined beam test, as shown in Figure 2.7. Specifically, it assembles a concrete block and a metal block as a combined beam through FRP strips and steel bar. The loading angle of FRP strips at the bottom of the beam is adjusted vertically across 0 mm, 4 mm and 8 mm. With a prescribed offset distance, this combined beam is loaded by four-point bending with loading span of 600 mm and supporting span of 1800 mm. The test is performed under displacement control with loading rate 0.1 mm/min.

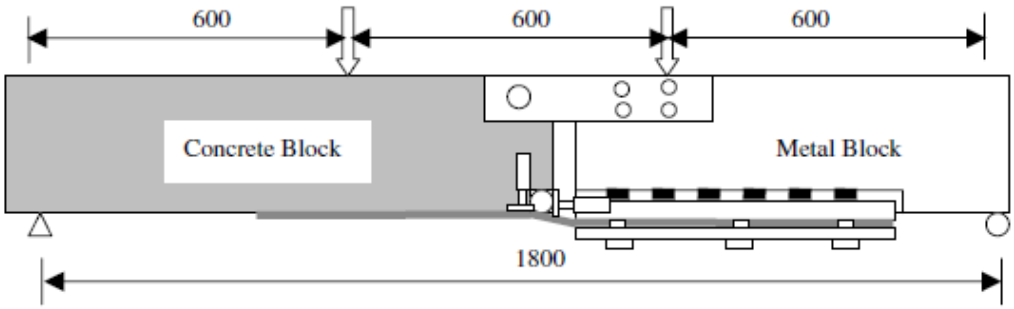

Figure 2.7 Setup of Pan and Leung's (2007) test

The dimensions of the concrete block were 200 (width) × 220 (depth) × 1100 (length) mm and the metal block was about the same size. The compressive strength of concrete was 40.5 MPa. All the concrete blocks were reinforced internally with two 10-mm

diameter high yield bars (i.e. its yielding strength is at 335 MPa) as tensile reinforcements and two 8-mm diameter high yield bars as compressive reinforcements.

Carbon fibre reinforced polymer (CFRP) of 50 mm width and 0.22 mm thickness was employed with elastic modulus of 235 GPa. The FRP bonded length was varied between 150 mm and 450 mm.

Pan and Leung (2007) obtained ultimate loads for these specimens from these physical tests. In general, it was found that the ultimate load decreases with the increase of offset distance in a combined beam test. It was also found that the ultimate load increases with FRP stiffness.

2.5 FRP-concrete bond strength models

A great number of bond strength models have been proposed for specimens of concrete prisms bonded with FRP or steel plate. According to their theoretical background, these model can be classified into three categories: elastic bond strength models, fracture mechanics based models, and empirical models.

In the models reviewed below, P_{u} is the bond strength of FRP-concrete interface (i.e. the maximum force in FRP); b_{p} and b_{c} are the widths of FRP and concrete prism respectively; E_{p} and E_{c} are the elastic moduli of FRP and concrete; L_{p} and t_{p} is the length and thickness of FRP; L_{e} is the effective length of FRP; and f_{ctm} is the concrete surface tensile strength.

2.5.1 Elastic bond strength models

On the basis of the test results, elastic bond strength models were proposed by assuming FRP-concrete bonded interface in elastic stage (Bizindavyi and Neale, 1999; Taljsten, 1997). For loads less than the initial cracking load, the analytical results were seen to be in good agreement with the experimental data (Bizindavyi and Neale, 1999; Taljsten, 1997). The specimens with very short FRP length are the examples of such a

case. That is because in physical tests, there are very few cracks generated at this level and FRP-concrete interface almost stays in the elastic regime. However, once at high loading level, the prediction of the strain variations in the FRP strips fails to conform to that evaluated in tests. Given these issues, the elastic model is not applicable to the evaluation of strain distributions after FRP debonding initiation. In spite of this, the strength models have made a great contribution and provided theoretical support to the proposal of empirical models.

2.5.2 Empirical models

The empirical models, which are only proposed experimental test data without any theoretical support, are presented here.

1. Hiroyuki and Wu's (1997) model

Based on a set of double shear tests on FRP strengthened RC members, an empirical formula between shear stress τ_u (MPa) and the bond length L (cm) is proposed by Hiroyuki and Wu (1997) and given as

$$\tau_{\mathrm{u}} = 5.88 L_{\mathrm{p}}^{-0.669} \tag{2.1}$$

Accordingly, the bond strength P_u is given as

$$P_{\mathrm{u}} = \tau_{\mathrm{u}} b_{\mathrm{p}} L_{\mathrm{p}} \tag{2.2}$$

where, L_{p} is the FRP length.

In this model, the bond length L_{p} was used to predict the bond strength at FRP-concrete bonded interface. In fact, the bond strength is affected by the FRP stiffness and concrete strength (Chen and Teng 2001). On the contrary, it is not affected by the bond length L_{p} for specimens with long enough FRP, but by the effective length (Chen and Teng 2001). That is because the ultimate load at the interface is only resisted by one part of FRP (i.e. the effective length) when it is long enough.

2. Tanaka's (1996) model

Similarly, with the same form of bond strength interface P_u as that in Hiroyuki and Wu's (1997) model, Tanaka (1996) proposed another model of bond stress τ_u, which is given as

$$\tau_u = 6.13 - \ln L_p \tag{2.3}$$

Similar to Hiroyuki and Wu's (1997) model, this model also failed to consider the effect of the FRP stiffness, concrete strength and effective length of FRP on the bond strength.

3. Maeda et al.'s (1997) model

In addition, a more robust model (Maeda et al. 1997) is proposed with the concept of effective bond length L_e, which is given as

$$L_e = e^{6.13-0.580\ln E_p t_p} \tag{2.4}$$

Note that E_p is in gigapascals and t_p is in millimeters in the above equation.

The bond shear stress τ_u is given as

$$\tau_u = 110.2 \times 10^{-6} E_p t_p \tag{2.5}$$

In view of that, the bond strength of interface P_u is given as

$$P_u = \tau_u b_p L_e. \tag{2.6}$$

In comparison to the previous two models, this model has been improved to some degree, because the stiffness ($E_p t_p$) of FRP and effective length of FRP had been considered, although the effect of concrete strength was also excluded.

2.5.3 Fracture mechanics models

Another branch of the bond strength models are obtained based on fracture mechanics and presented here. In the models reviewed below, L_p is the FRP bond length, E_p is the elastic modulus of FRP, t_p is the thickness of FRP.

1. Holzenkampfer's (1994) model

Holzenkampfer (1994) first proposed a formula to predict the bond strength between steel plate and concrete substrate, from the standpoint of nonlinear fracture mechanics (NLFM). It is given by

$$P_u = c_1 k_b b_p \sqrt{E_p t_p f_{ctm}} \tag{2.7}$$

with

$$k_b = 1.06 \sqrt{\frac{2 - b_p/b_c}{1 + b_p/400}} \tag{2.8}$$

where, the parameter c_1 can be obtained through calibration with the corresponding bond test result.

This model has been regarded as a milestone in the development of theoretical research of FRP-concrete bonded interface behaviour, especially in fracture mechanics models, and a great number of similar models have been proposed based on it. The main issue of this model is that it failed to consider the effect of effective length of FRP.

2. Blaschko et al.'s (1996) model

Blaschko et al.'s (1996) model is obtained from Holzenkampfer's (1994) model to describe the bond strength between steel and concrete, which is given as

$$P_{\mathrm{u}} = \begin{cases} 0.78 b_{\mathrm{p}} \sqrt{2 G_{\mathrm{f}} E_{\mathrm{p}} t_{\mathrm{p}}} & \text{if } L \geq L_{\mathrm{e}} \\ 0.78 b_{\mathrm{p}} \sqrt{2 G_{\mathrm{f}} E_{\mathrm{p}} t_{\mathrm{p}}} \dfrac{L}{L_{\mathrm{e}}} \left(2 - \dfrac{L}{L_{\mathrm{e}}}\right) & \text{if } L < L_{\mathrm{e}} \end{cases} \tag{2.9}$$

with effective bond length L_e and fracture energy G_{f} given as

$$L_{\mathrm{e}} = \sqrt{\frac{E_{\mathrm{p}} t_{\mathrm{p}}}{4 f_{\mathrm{ctm}}}} \tag{2.10}$$

$$G_{\mathrm{f}} = c_{\mathrm{f}} k_{\mathrm{p}}^2 f_{\mathrm{ctm}} \tag{2.11}$$

where, $c_{\mathrm{f}}$is a constant determined from a linear regression analysis through the results from double shear tests; k_{p} is the geometrical factor related to the width of the bonded plate and concrete members and given as

$$k_{\mathrm{p}} = \sqrt{1.125 \frac{2 - b_{\mathrm{p}}/b_{\mathrm{c}}}{1 + b_{\mathrm{p}}/400}} \tag{2.12}$$

This model provided a good framework to consider the effect of various parameters of FRP-concrete bonded interface, although the accuracy of its predicted result is not that successful.

3. Neubauer and Rostasy's (1997) model

Neubauer and Rostasy's (1997) model is also obtained from Holzenkampfer's (1994) model to describe the bond strength between steel and concrete by assigning a triangular shape to the bond-slip relationship. It is given as

$$P_{\mathrm{u}} = \begin{cases} 0.64 k_{\mathrm{p}} b_{\mathrm{p}} \sqrt{E_{\mathrm{p}} t_{\mathrm{p}} f_{\mathrm{ctm}}} & \text{if } L \geq L_{\mathrm{e}} \\ 0.64 k_{\mathrm{p}} b_{\mathrm{p}} \sqrt{2 G_{\mathrm{f}} E_{\mathrm{p}} t_{\mathrm{p}}} \dfrac{L}{L_{\mathrm{e}}} \left(2 - \dfrac{L}{L_{\mathrm{e}}}\right) & \text{if } L < L_{\mathrm{e}} \end{cases} \tag{2.13}$$

with the effective bond length L_e given as

$$L_e = \sqrt{\frac{E_p t_p}{4 f_{ctm}}} \tag{2.14}$$

and the fracture energy G_f given as

$$G_f = c_f f_{ctm} \tag{2.15}$$

In this model, the width of concrete prism is not considered on the bond strength.

4. Taljsten's (1994) model

Once again based on Holzenkampfer (1994), Taljsten's (1994) model predicts the bond strength between steel and concrete using nonlinear fracture mechanics. It is given as

$$P_u = \sqrt{\frac{2 E_p t_p f_{ctm}}{1 + \alpha_T} b_p} \tag{2.16}$$

where, $\alpha_T = \frac{E_p t_p}{E_c t_c}$

In this model, the concept of effective length of FRP has been excluded, so it could not accurately predict the load of the specimens with FRP shorter than effective length.

5. Yuan and Wu's (1999) model

Based on the model in Taljsten (1994), a modified form was obtained to predict the bond strength at FRP-concrete bonded interface (Yuan and Wu, 1999). In this model the form is exactly the same as that in Taljsten's (1994) model, except that α_T is changed to

$$\alpha_T = \frac{b_p E_p t_p}{b_c E_c t_c} \tag{2.17}$$

Similar to Taljsten's (1994) model, the concept of effective length of FRP was not considered, so it could not predict the load of the specimens with FRP shorter than effective length.

6. Wu et al.'s (2001) model

Wu et al. (2001) developed a model to predict the bond strength of FRP-concrete bonded interface, which is given as

$$P_{\mathrm{u}} = \frac{\tau_{\mathrm{f}} b_{\mathrm{p}}}{\lambda_2} \frac{\delta_{\mathrm{f}}}{\delta_{\mathrm{f}} - \delta_1} \sin(\lambda_2 a) \tag{2.18}$$

where, parameter *a* is obtained by solving the equation:

$$\tanh[\lambda_1 (L-1)] = \frac{\lambda_1}{\lambda_2} \tan(\lambda_2 a) \tag{2.19}$$

where, τ_{f} is the maximum shear stress (i.e. also called bond stress) in the bond-slip model at FRP-concrete bonded interface and δ_1 is the slip corresponding to the maximum shear stress; δ_f is the maximum slip; and λ_1 and $\lambda_2$are defined as

$$\lambda_1^2 = \frac{\tau_{\mathrm{f}}}{\delta_1 E_{\mathrm{p}} t_{\mathrm{p}}} (1 + \alpha_{\mathrm{Y}}) \tag{2.20}$$

and

$$\lambda_2^2 = \frac{\tau_{\mathrm{f}}}{(\delta_{\mathrm{f}} - \delta_1) E_{\mathrm{p}} t_{\mathrm{p}}} (1 + \alpha_{\mathrm{Y}}) \tag{2.21}$$

In this solution, the relationship between P_{u} and L is an implicit function and is dependent on the coefficients in bond-slip models, which are not easy to obtain in test (Dai et al. 2005). In Wu et al. (2001), the effective bond length is defined when the load reaches 97% of load capacity if L is infinite. This is given as

$$L_{\mathrm{e}} = a_0 + \frac{1}{2\lambda_1}\ln\frac{\lambda_1 + \lambda_2\tan(\lambda_2 a_0)}{\lambda_1 - \lambda_2\tan(\lambda_2 a_0)} \tag{2.22}$$

with

$$a_0 = \frac{1}{\lambda_2}\sin^{-1}\left(0.97\sqrt{\frac{\delta_{\mathrm{f}} - \delta_{\mathrm{t}}}{\delta_{\mathrm{f}}}}\right) \tag{2.23}$$

There two issues in this model: firstly, this model is so complicated that it is very difficult to use to predict the bond strength of FRP-concrete bonded interface, because it highly relies on shape of the bond-slip model of the interface; secondly, the effect of the width of concrete prism was not considered on the bond strength.

7. Chen and Teng's (2001) model

Also inspired by Holzenkampfer's (1994) model, another model was developed to predict the bond strength of FRP-concrete interface by Chen and Teng (2001). In this model the bond strength is given by

$$P_{\mathrm{u}} = 0.427\beta_{\mathrm{p}}\beta_{\mathrm{L}}\sqrt{f_{\mathrm{c}}'}b_{\mathrm{p}}L_{\mathrm{e}} \tag{2.24}$$

with the width ratio effect at FRP-concrete bond interface given as

$$\beta_{\mathrm{p}} = \sqrt{\frac{2 - b_{\mathrm{p}}/b_{\mathrm{c}}}{1 + b_{\mathrm{p}}/b_{\mathrm{c}}}} \tag{2.25}$$

and effective length L_e given as

$$L_{\mathrm{e}} = \sqrt{\frac{E_{\mathrm{p}}t_{\mathrm{p}}}{\sqrt{f_{\mathrm{c}}'}}} \tag{2.26}$$

and with

$$\beta_{\mathrm{L}} = \begin{cases} 1 & \text{if } L \geq L_{\mathrm{e}} \\ \sin\dfrac{\pi L}{2L_{\mathrm{e}}} & \text{if } L < L_{\mathrm{e}} \end{cases} \tag{2.27}$$

Based on the a large number of experimental results, some modifications were conducted on the parameters, such as FRP-concrete width ratio, effective length in Blaschko et al.'s (1996) model, so that this model has the best performance in predicting ultimate bond strength and effective length for FRP-concrete bonded interface varied with different parameters (Kalfat and Al-Mahaidi 2014).

2.6 Numerical simulation of debonding

There have been a number of studies that have used simulations to understand the behaviour of the FRP-concrete interface. According to their modelling methods, generally they are classified into four categories: interface approach, discrete crack approach, smeared crack approach, and a combination of discrete and smeared crack approaches, which will be detailed as follows.

2.6.1 Interface approach

This is the simplest approach to simulate the debonding behaviour at FRP-concrete bonded interface (Lu et al. 2005a). In this approach the material properties of concrete and FRP parts are set as linear elastic and debonding is simulated via an interfacial layer modelled using springs or cohesive elements, whose mechanical behaviour is defined through bond-slip models. A number of bond-slip models have been proposed (Dai and Ueda 2003; Dai et al. 2005; Lu et al. 2005a; Monti et al. 2003; Nakaba et al. 2001; Savioa et al. 2003a).

This method is very cost-effective in terms of computational time, since the nonlinear mechanical behaviour restricted to a limited number of interfacial elements, while the other elements are set as linear elastic.

Bond-slip approach is considered in this thesis (Chapter 9) and it is shown that these models severely deviate from that from corresponding test results.

2.6.2 Discrete crack approach

Discrete crack approach usually works with cohesive elements or other interface elements, which are set to zero thickness and used to connect concrete elements. It is the incorporation of cohesive elements that allows a crack to grow along element boundaries in simulations when the nodal force at the crack tip exceeds a tensile strength criterion (Figure 2.8).

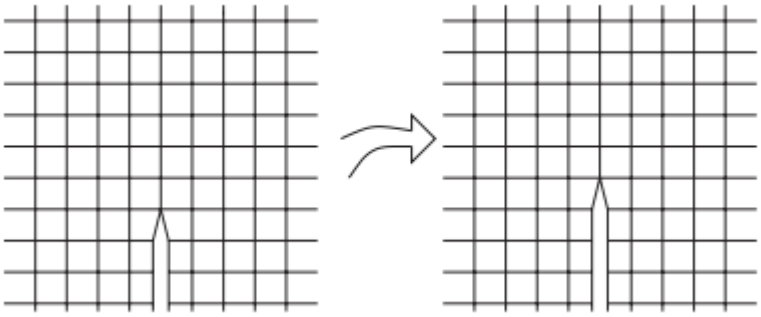

Figure 2.8 Discrete crack modelling

The discrete element was first applied in simulations of FRP-concrete interface, when Yang et al. (2003) used it to model interfacial debonding behaviour. However, initiation of cracking in Yang et al. (2003) is regarded as complete separation of elements due to the use of linear elastic fracture mechanics (LEFM), which means that any post-cracking traction at the fracture surface is not considered in their study.

In Niu and Wu (2005), strengthened RC beams with FRP are simulated through predefined the flexural cracks using vertically-oriented and evenly-distributed interfacial elements, whose constitutive law is defined using concrete properties. Further FRP is connected to concrete beams through interfacial elements whose constitutive law is defined based on assumed bond-slip model with unspecified interfacial fracture energy. They found that crack spacing has a significant effect, but

their positions were defined beforehand by the analyst through cohesive elements. The interfacial fracture energy was also found to have decisive effect on the ultimate load capacity. This FE model thus is clearly not a predictive model although the results seems reasonable compared to test results in terms of load versus displacement curves, which are valuable for understanding debonding mechanism at FRP-concrete bonded interface to some extent.

The discrete crack approach in FE simulations has a number of disadvantages. They include: (1) cracks cannot occur in the middle of an element and can only arise at element boundaries, so the crack positions in simulations highly rely on the mesh (2) computation difficulty is experienced, when mesh bias and automatic remeshing are used to solve the issues of inaccurate cracking positions in simulations. Specifically, the computation difficulty is that the computation needs to stop for remeshing before restarting (Ingraffea and Saouma 1985). (3) continuous change in topology increases the computation cost.

2.6.3 Smeared crack approach

The smeared crack approach represents cracking by changing the constitutive behaviour in the cracking region.

In this approach, damage in concrete is modelled by reducing the elastic modulus of concrete once after crack initiation; the damage is expressed in terms of a scalar degradation variable *d* as

$$E = (1 - d)E_0 \tag{2.28}$$

Further stiffness degradation can be used in conjunction with strain-softening plasticity wherein the load carrying capacity of concrete reduces after a peak stress level has been achieved (Figure 2.10). As a consequence of strain softening in a layer of elements, said to be experiencing strain localisation, it is likely that other elements may undergo elastic unloading.

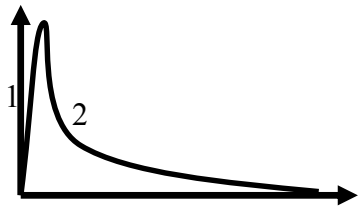

Figure 2.9 Typical curve for constitutive model

It has been shown that strain softening is not a material property but a structural property (Bažant and Oh 1983; Bazant and Planas 1997) and requires nonlocal continuum (Bažant 1986) and gradient models (Bažant 1984) for mesh objective solution. Amongst these, crack band model is the most widely used mathematical tool to approach the localisation problem and make the solution objective.

Specifically, in the crack band model, stress-strain model is changed with the element size so as to make fracture energy independent of element size. This is done by adjusting the softening branch of stress-strain curve (i.e. Path 2 in Figure 2.9).

Compared to the discrete crack approach, the smeared crack approach can be more conveniently applied in FRP-concrete interface debonding simulations as it does not assume any assume any predefined crack location and easily permits evolution of several cracks. It has been applied in such simulations in three different ways.

The first one is to model RC beams strengthened with FRP by assuming perfect bond between FRP and concrete (Arduini et al. (1997); Fanning and Kelly (2000); Niteraka and Neale (1999); Rahimi and Hutchinson (2001)). These FE models generally failed to predict the debonding failure mode although the trend of overall load-displacement curves generally matched well with that of the test results (Chen 2010).

The second approach is to model RC beams strengthened with FRP by discarding the assumption of perfect bond between FRP and concrete (Lu et al. 2007; Neale et al. 2006; Niu and Karbhari 2008; Nour et al. 2007a; Pham and Almahaidi 2007; Pham and Al-Mahaidi 2005; Pham et al. 2006; Wong and Vecchio 2003). These studies used the bond-slip model proposed by Lu et al. (2005a) to connect FRP and concrete. In

comparison to the first approach, these simulations are reported to provide improved results (Chen 2010).

The third approach is to model pull-out tests with mesoscale model (i.e. with element size of 0.5 to 1 mm) and assuming perfect bond between FRP and concrete (Chen and Tao 2011; Lu et al. 2005b; Tao and Chen 2015), based on the consideration that FRP is debonded from concrete prism and the fine mesh at the interface is able to capture the debonding response.

2.6.4 Combination of discrete and smeared approaches

In order to take advantage of the merits of both discrete and smeared crack models, a combination has been used to simulate FRP-concrete interfacial debonding behaviour (Kishi et al., 2005; Pham et al., 2006; Camata et al., 2007). In this approach the discrete model is employed to simulate geometrical discontinuities, such as the development of dominant cracks, slipping of axial rebars and debonding at FRP-concrete bonded interface. On the other hand, smeared crack model is used to model minor cracks by assigning its material properties to concrete element to capture such minor cracks where the discrete cracks are not predefined.

2.7 Key issues in simulations with mesoscale models

As discussed in Section 2.6, FRP-concrete bonded interface (i.e. single shear pushing test) has been simulated with a 2D mesoscale model (i.e. with a fine mesh), with good agreements in terms of ultimate loads in some special cases (Chen and Tao 2011; Lu et al. 2005b; Tao and Chen 2015). Even so, there still remain many issues that need to be addressed as listed below.

Issue 1: Approach to post-process width effect of FRP-concrete bonded interface

In this approach, the widths of both concrete and FRP parts in simulations are set to a value of unity. The simulation results are post-processed with the width ratio factor in the bond strength formula, proposed by Chen and Teng (2001), to reflect the difference

induced by different FRP-concrete width ratios. These simulation results include the load versus slip at FRP-concrete bonded interface, axial strain of FRP strips at different loading stages. One evident issue is that there is only one failure mode in simulations even with different FRP-concrete width ratios (e.g. when simulating the specimens in Series III from Yao et al. (2005)), because the width effect is only considered in the postprocessing of the results. In fact, the failure mode at FRP-concrete bonded interface varies with FRP-concrete width ratio in physical tests as discussed in Section 2.3.

Issue 2: In physical test specimen fails in CPF (Concrete Prism Failure) mode, whereas in simulation it fails in debonding mode

In this issue, Specimen III-6 from Yao et al. (2005) is taken as the reference case. In this specimen, both FRP strips and concrete block are 150 mm wide. In physical test, the specimen failed by CPF mode due to its large width ratio, as shown in Figure 2.2. By contrast, in the simulation with this approach, it appears as debonding mode, as shown in Figure 2.10. Further the studies conducted by Lu et al. (2005) and Chen and Tao (2011) reduced the model size to reduce computational effort. In this the height of the free support was shortened arbitrarily from 120 mm in the physical test (see Figure 2.2) to 30 mm and the specimen height reduces from 150mm to 45mm. These arbitrary changes resulted in incorrect prediction of the failure mode.

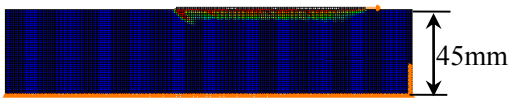

Figure 2.10 Failure mode of pull-out test in the simulation with this approach

Issue 3: In physical test specimen fails as deboning mode, whereas in simulation fails by CPF mode

In this issue, Specimen II-2 in Yao et al. (2005) is taken as the reference case. Specifically, it is fabricated with 25mm wide FRP strips and 150mm wide concrete prism, but with 120 mm high free support while testing. In physical tests it failed in

debonding mode, as shown in Figure 2.1. However, it appears as CPF mode in the corresponding simulation with this approach, as shown in Figure 2.11, when full-scale model is employed.

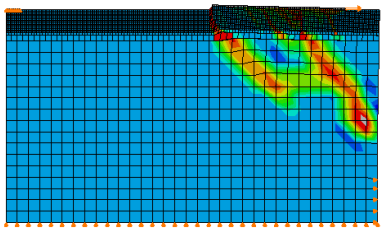

Figure 2.11 Failure mode of pull-out test in the simulation with this approach

Issue 4: In physical test combined beam fails as deboning mode, whereas in simulation fails as CPF mode

In simulations of combined beam tests, the influence of the FRP-concrete width ratio at bonded interface is more evident and significant but more difficult to simulate than in pull-out tests.

Specimen B2-150-00 in Pan and Leung (2007) is taken as the reference case to further explain this issue. In its physical test the failure mode is observed as debonding mode (Pan and Leung 2007), as shown in Figure 2.12; whereas in its corresponding simulation with this approach (i.e. the out-of-plane thicknesses of both the concrete and steel blocks set to a value of 1 mm in the combined beam test), it is found that the model is damaged in the concrete body beyond the end of FRP strips (i.e. similar to CPF mode), as shown in Figure 2.13, rather than at FRP-concrete bonded interface.

(a)

(b)

Figure 2.12 (a) The damaged surface of the concrete block (b) the debonded FRP plate with a thin layer of concrete on the surface from Pan and Leung (2007)

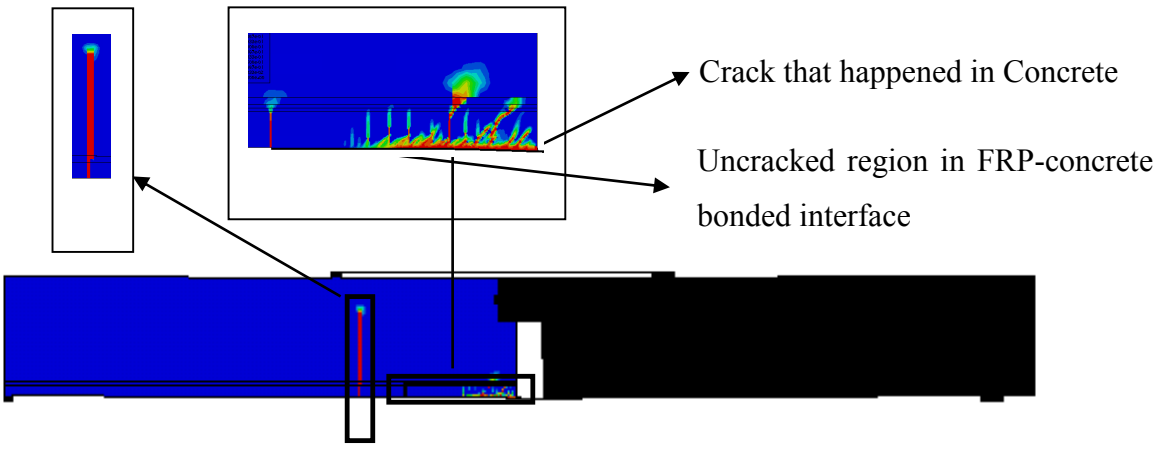

Figure 2.13 Failure mode of beam test in the simulation with this approach

In summary, the approach is definitely not applicable for simulations of FRP-concrete bonded interface, and a new approach is needed indeed.

2.8 Conclusions

This Chapter has discussed the materials involved in FRP-concrete bonded interface, namely FRP, resin matrix and structural adhesive, and surface preparation techniques. Subsequently, two different failure modes observed at FRP-concrete bonded interface were introduced; these will be used as the reference cases for parameter analyses in this thesis. This is followed by the collections and detailed introductions of some typical experimental studies, which will be used to validate the reasonability of the proposed models.

The chapter then discussed different theoretical models for predicting bond strength of FRP-concrete bonded interface. It is found that a model proposed by Chen and Teng (2001) has the best performance in predicting ultimate bond strength and effective length for FRP-concrete bonded interface varied with different parameters, such concrete strength, FRP-concrete width ratio and FRP length (Kalfat and Al-Mahaidi 2014).

It is followed by a review of different numerical simulation methods, ranging from interface model approach to discrete crack approach to smeared crack approach to a combination of discrete and smeared crack approaches. At last the issues in simulations of FRP-concrete bonded interface using mesoscale approaches are considered.

Based on the review and discussions presented in this chapter, the following conclusion can be drawn:

- There are two different failure modes at FRP-concrete bonded interface, viz debonding and CPF failure modes, and will be used as the reference cases in parameter analyses of this thesis;

- A large number of experimental studies have investigated debonding behaviour and these can be used to validate modelling approaches (e.g. Ali-ahmad et al. (2006); Mazzotti et al. (2009); Pan and Leung (2007); Yao et sal. (2005));
- Chen and Teng's (2001) bond strength model appears to be best one in predicting the ultimate load at FRP-concrete interface (Kalfat and Al-Mahaidi 2014);
- Simulations of FRP-concrete interface with smeared crack approach, especially for crack band approach, preferable compared to discrete crack approach due to its relative ease of implementation;
- Bond-slip model is needed because it plays a very important role in simulation of strengthened beams with FRP (as stated in Section 2.6.1).

Chapter 3
FE Modelling of FRP-concrete debonding behaviour

3.1 Introduction

As discussed in Chapter 2, there are a number of challenges associated with modelling of the FRP-concrete interfacial debonding behaviour.

This chapter discusses the key features associated with the simulation of debonding behaviour. These features include material constitutive modelling, geometrical modelling, boundary conditions and loading in simulations. The focus is to come up with models and parameters that will be employed in the rest of the thesis.

The geometry and the boundary conditions are discussed with particular reference to the experiment conducted by Yao et al. (2005) discussed in the last chapter. Mesh convergence studies are conducted and implicit dynamic approach is employed.

Various loading approaches are considered to identify one which is most suitable for this study.

3.2 Constitutive models for simulations

3.2.1 Modelling of FRP

The FRP, as a kind of unidirectional material, has a high stiffness in the longitudinal direction (i.e. parallel to the pull direction), but have a very small stiffness in the other two directions. In view of this, a set of formulae is adopted to obtain the values of the elastic moduli and Poisson's ratios of the FRP (Vinson 1999), on the basis of volume fractions and properties of constituent materials as

$$P = \frac{P_{\mathrm{f}} V_{\mathrm{f}} + \eta P_{\mathrm{m}} V_{\mathrm{m}}}{V_{\mathrm{f}} + \eta V_{\mathrm{m}}} \tag{3.1}$$

where, the elastic constants P, P_f, and P_m relate to FRP, fibre and matrix respectively. V_f and V_m are the volume fractions of the fibres and the matrix in the FRP composite, respectively. P, P_f, and P_m relate to a range of elastic properties and the term η depends on elastic constants evaluated as shown in Table 3.1.

Table 3.1 Determination of composite properties from fibre and matrix properties

Elastic Constant	P	P_f	P_m	η
E_{11} (MPa)	E_{11}	E_{11f}	E_m	1
ν_{12}	ν_{12}	ν_{12f}	ν_m	1
G_{12} (MPa)	$1/G_{12}$	$1/G_{12f}$	$1/G_m$	η_6
G_{23} (MPa)	$1/G_{23}$	$1/G_{23f}$	$1/G_m$	η_4
K_T	$1/K_T$	$1/K_f$	$1/K_m$	η_k

The expressions for E_{11} and ν_{12} are called Rule of Mixture. In Table 3.1, the terms K and η are given as

$$K_f = \frac{E_f}{2(1-\upsilon_f)}, K_m = \frac{E_m}{2(1-\upsilon_m)} \tag{3.2}$$

$$\eta_6 = \frac{1+G_m/G_{12f}}{2}, \eta_4 = \frac{3-4\upsilon_m+G_m/G_{23f}}{4\,(1-\upsilon_m)}, \eta_k = \frac{1+G_m/K_f}{2\,(1-\upsilon_m)} \tag{3.3}$$

The shear modulus of matrix material, G_m, if isotropic, is given as

$$G_m = \frac{E_m}{2(1+\nu_m)} \tag{3.4}$$

The transverse moduli of the composite, E_{22}=E_{33}, are given as

$$E_{22} = E_{33} = \frac{4K_T G_{23}}{K_T + mG_{23}}, \text{ MPa} \tag{3.5}$$

where

$$m = 1 + \frac{4K_T \upsilon_{12}^2}{E_{11}} \tag{3.6}$$

The equations above have been written in general for composites reinforced with anisotropic fibres such as some graphite, aramid fibres, glass fibres and carbon fibres. If the fibres are isotropic, the fibre properties E_f, G_f and υ_f relate as:

$$G_f = \frac{E_f}{2(1+\upsilon_f)} \tag{3.7}$$

Chiao et al. (1980) notes that for most polymeric matrix structural composites, $G_m/G_f < 0.05$. If that is the case, then the η parameters are approximately given as

$$\eta_6 \approx 0.5;\ \eta_4 = \frac{3-4\upsilon_m}{4(1-\upsilon_m)};\ \eta_K = \frac{1}{2(1-\upsilon_m)} \tag{3.8}$$

Finally, noting that $\upsilon_m = 0.35$ for most epoxies, then η_4 =0.62 and η_k =0.77.

In addition, Poisson's ratio v_{23}, can be written as

$$\upsilon_{23} = \upsilon_{12}V_f + \upsilon_m(1-V_f)\left[\frac{1+\upsilon_m-\upsilon_{12}\left(\frac{E_m}{E_{11}}\right)}{1-\upsilon_m^2+\upsilon_m\upsilon_{12}\left(\frac{E_m}{E_{11}}\right)}\right] \tag{3.9}$$

where, v_{12f} is Poisson's ratio of the fibre composite and v_m is Poisson's ratio of epoxy, see Table 3.1.

Assuming total thickness of FRP is equal to 1 mm, typical properties for Yao et al.'s, (2005) test discussed in Chapter 2 are given in Table 3.2.

Table 3.2 Typical properties of FRP for Yao et al.'s (2005) test

	E_{11} (MPa)	E_{22}=E_{33} (MPa)	G_{12} (MPa)	G_{23} (MPa)	υ_{12}	υ_{23}
CFRP	43068	1315	531	503	0.34	0.45

For 2D simulations conducted in this study, only E_{11} and ν_{12} are employed by assuming FRP as linear elastic, as only the longitudinal behaviour of the FRP is of interest here. Similar suggestions are found in Lu et al (2005) and Tao and Chen (2014).

3.2.2 Modelling of concrete

A wide range of criteria (Coulomb 1776; Drucker and Prager 1952; Evert Hoek 1980; Leon 1935; Menetrey and Willam 1995; von Mises 1913; Mohr 1990; Ottosen 1997) are available to model mechanical behaviour of concrete in FEM. One criterion that is able to reproduce key characteristics of concrete, namely its asymmetric strength in tension and compression, its pressure sensitivity associated with yielding and stiffness degradation associated with damage, is concrete damaged plasticity available in ABAQUS. This constitutive model is discussed in the following and used in the rest of the thesis.

Yield Criterion

The yield function, incorporated in concrete damaged plasticity model in ABAQUS (2011), originally proposed by Lubliner et al. (1989) and modified by Lee and Fenves (1998), is used to account for the evolution of concrete strength in various complex stress states. The yield function is given as

$$F\left(\bar{\sigma}, \tilde{\varepsilon}^{\mathrm{pl}}\right) = \frac{1}{1-\alpha}\left(\bar{q} - 3\alpha\bar{p} + \beta\left(\tilde{\varepsilon}^{\mathrm{pl}}\right)\langle\hat{\bar{\sigma}}_{\max}\rangle - \gamma\langle-\hat{\bar{\sigma}}_{\max}\rangle\right) - \bar{\sigma}_{\mathrm{c}}\left(\tilde{\varepsilon}_{\mathrm{c}}^{\mathrm{pl}}\right) \leq 0 \tag{3.10}$$

with

$$\alpha = \frac{\sigma_{\mathrm{b0}} - \sigma_{\mathrm{c0}}}{2\sigma_{\mathrm{b0}} - \sigma_{\mathrm{c0}}} \tag{3.11}$$

where, σ_{c0} is initial axial compressive yielding stress, and σ_{b0} is initial equibiaxial compressive yielding stress (usually, $\sigma_{\mathrm{b0}} = 1.16\sigma_{\mathrm{c0}}$). The parameter β is given by

$$\beta\left(\tilde{\varepsilon}^{\mathrm{pl}}\right) = \frac{\bar{\sigma}_{\mathrm{c}}(\tilde{\varepsilon}_{\mathrm{c}}^{\mathrm{pl}})}{\bar{\sigma}_{\mathrm{t}}(\tilde{\varepsilon}_{\mathrm{t}}^{\mathrm{pl}})}(1-\alpha) - (1+\alpha) \tag{3.12}$$

where, $\bar{\sigma}_{\mathrm{t}}$ and $\bar{\sigma}_{\mathrm{c}}$ are the effective tensile and compressive cohesion stresses, respectively and the parameter γ is given by

$$\gamma = \frac{3(1-K_{\mathrm{c}})}{2K_{\mathrm{c}} - 1} \tag{3.13}$$

where, K_c is the ratio of the second stress invariant on the tensile meridian to that of the compressive meridian. The parameter γ in Eq. (3.11) only gets involved when $\hat{\bar{\sigma}}_{max}$ is less than zero.

The effective hydrostatic pressure $\bar{p}$ is given by

$$\bar{p} = -\frac{1}{3}\bar{\boldsymbol{\sigma}} : \mathbf{I} \tag{3.14}$$

The Mises equivalent effective stress $\bar{q}$ is given by

$$\bar{q} = \sqrt{\frac{3}{2}\bar{\mathbf{S}} : \bar{\mathbf{S}}} \tag{3.15}$$

where, $\bar{\mathbf{S}}$ is the deviatotric part of the effective stress tensor $\bar{\boldsymbol{\sigma}}$ and given by

$$\bar{\mathrm{S}} = \bar{p}\mathrm{I} + \bar{\sigma} \tag{3.16}$$

The yield function in plane stress for various biaxial loading conditions is plotted in Figure 3.1.

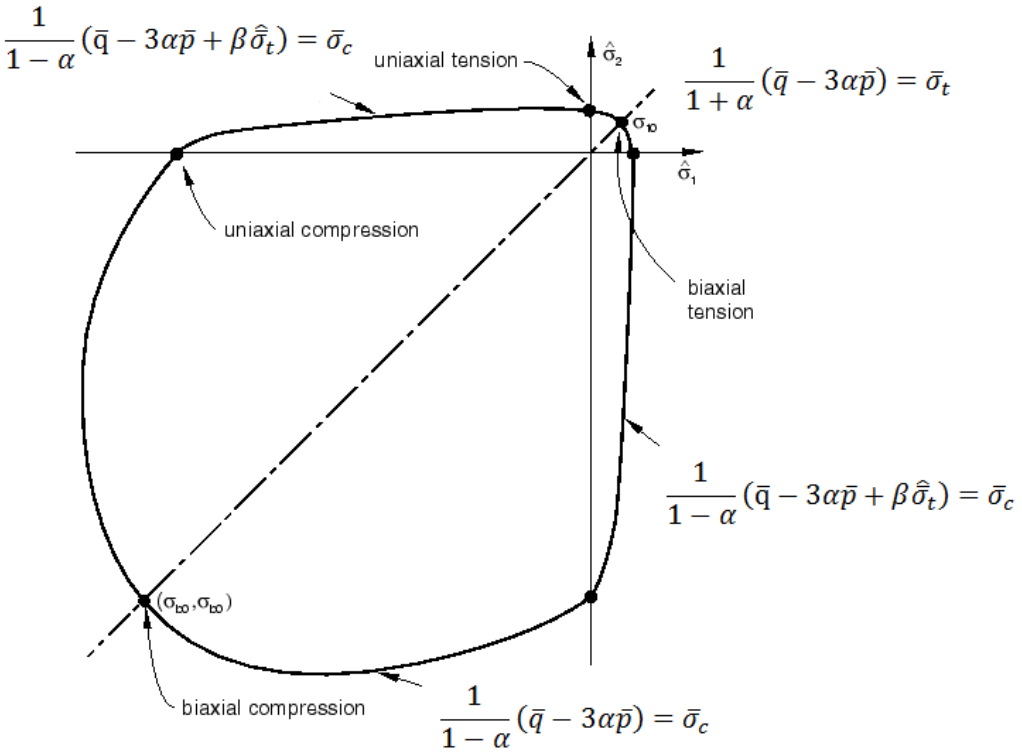

Figure 3.1 Yield surface in plane stress in different quadrants adapted from ABAQUS (2011)

As discussed in this section, the yield function is established in the space of effective stress $\bar{\sigma}$, which is connected with Cauchy stress σ by the damage factor d_x through the equation $\overline{\sigma} = \sigma/(1-d_x)$. Further, the criterion requires definitions of the evolution of compression and tension stresses with increasing plastic strain.

Concrete in compression

As discussed above, the model requires definition of variation of uniaxial compressive stress with plastic strain. To define the stress-strain curve in uniaxial compression, the relationship proposed by CEB-FIP (1993) is adopted for a large part of this thesis (other relationships are also investigated in Chapter 7). In this, uniaxial stress σ is related to strain ε through

$$\sigma = \left[\frac{\frac{E_0}{E_s}\frac{\varepsilon}{\varepsilon_0} - \left(\frac{\varepsilon}{\varepsilon_0}\right)^2}{1+\left(\frac{E_0}{E_s}-2\right)\frac{\varepsilon}{\varepsilon_0}}\right] f_c', \text{MPa} \quad \text{for } \varepsilon < \varepsilon_{c,lim} \tag{3.17}$$

where,

f_c' is the concrete strength (MPa) obtained from cylinder specimen and also appears as a peak value in the compression stress versus strain relationship,

$E_0 = 4730\sqrt{f_c'}$ (MPa) is the initial tangent modulus of concrete,

$E_s = f_c'/\varepsilon_0$ (MPa) is the secant modulus from the origin to the peak compression stress f_c',

ε_0 is the compression strain corresponding to the peak compression stress f_c' and given as $\varepsilon_0(‰) = 0.7{f_c'}^{0.31} < 2.8$.

For strains $\varepsilon > \varepsilon_{c,lim}$, the descending branch of the compression stress-strain relationship may be described as follows:

$$\sigma = \left[\left(\frac{1}{\varepsilon_{c,lim}/\varepsilon_0}\xi - \frac{2}{(\varepsilon_{c,lim}/\varepsilon_0)^2}\right)\left(\frac{\varepsilon}{\varepsilon_0}\right)^2 + \left(\frac{4}{\varepsilon_{c,lim}/\varepsilon_0} - \xi\right)\frac{\varepsilon}{\varepsilon_0}\right]^{-1} \sigma_{c0}, \text{MPa} \tag{3.18}$$

with

$$\xi = \frac{4\left(\frac{\varepsilon_{c,lim}}{\varepsilon_0}\right)^2\left(\frac{E_0}{E_s}-2\right) + 2\frac{\varepsilon_{c,lim}}{\varepsilon_0} - \frac{E_0}{E_s}}{\left[\frac{\varepsilon_{c,lim}}{\varepsilon_0}\left(\frac{E_0}{E_s}-2\right)+1\right]^2} \tag{3.19}$$

The strain $\varepsilon_{c,lim}$ at $\sigma_{c,lim} = 0.5f_{cm}$ is given as

$$\frac{\varepsilon_{c,lim}}{\varepsilon_0} = \frac{1}{2}\left(\frac{1}{2}\frac{E_0}{E_s}+1\right) + \left[\frac{1}{4}\left(\frac{1}{2}\frac{E_0}{E_s}+1\right)^2 - \frac{1}{2}\right]^{1/2} \tag{3.20}$$

It is important to note that according to existing studies (Bazant and Planas 1997; Li 2012; Wang 1996), size dependence is not evident in compressive behaviour of concrete.

For Specimen III-1 in Yao et al. (2005) used extensively in this thesis, the concrete strength $f_c' = 27.1$ was used. The uniaxial compression stress-strain curve employed is shown in Figure 3.2. From this, the corresponding stress versus plastic strain curve in compression was derived by deducting the elastic strain

corresponding to the undamaged material ε_{0c}^{el} (i.e. $\varepsilon_{0c}^{el} = \sigma_c/E_0$) from the total strain, as shown in Figure 3.3.

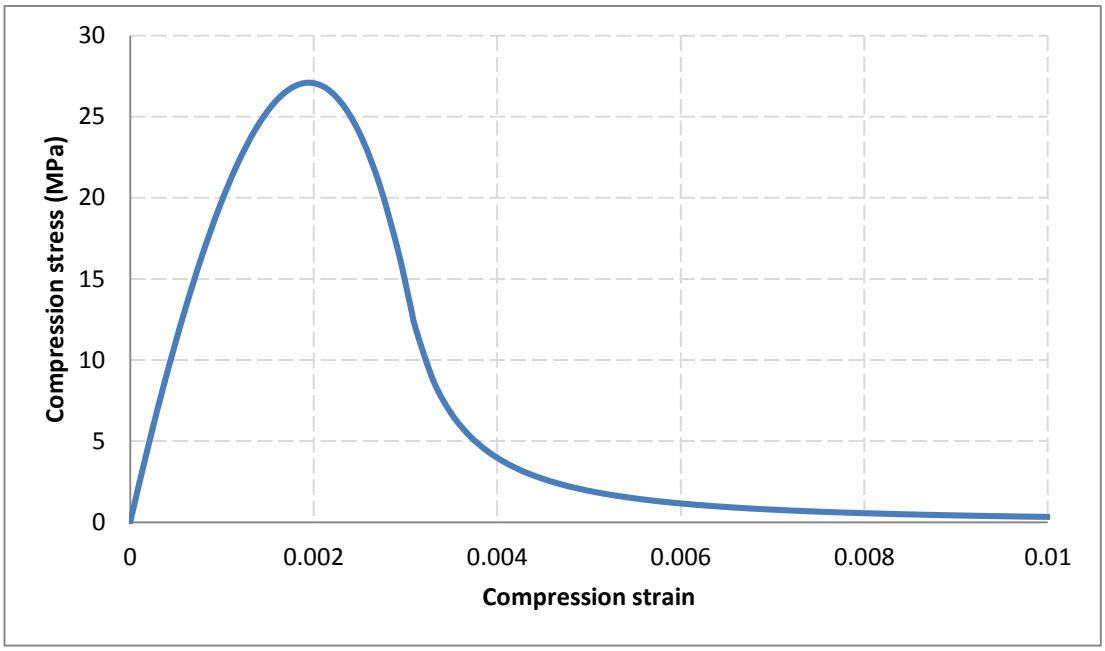

Figure 3.2 Uniaxial compressive stress-strain curve for concrete used in Specimen III-1 in Yao et al. (2005)

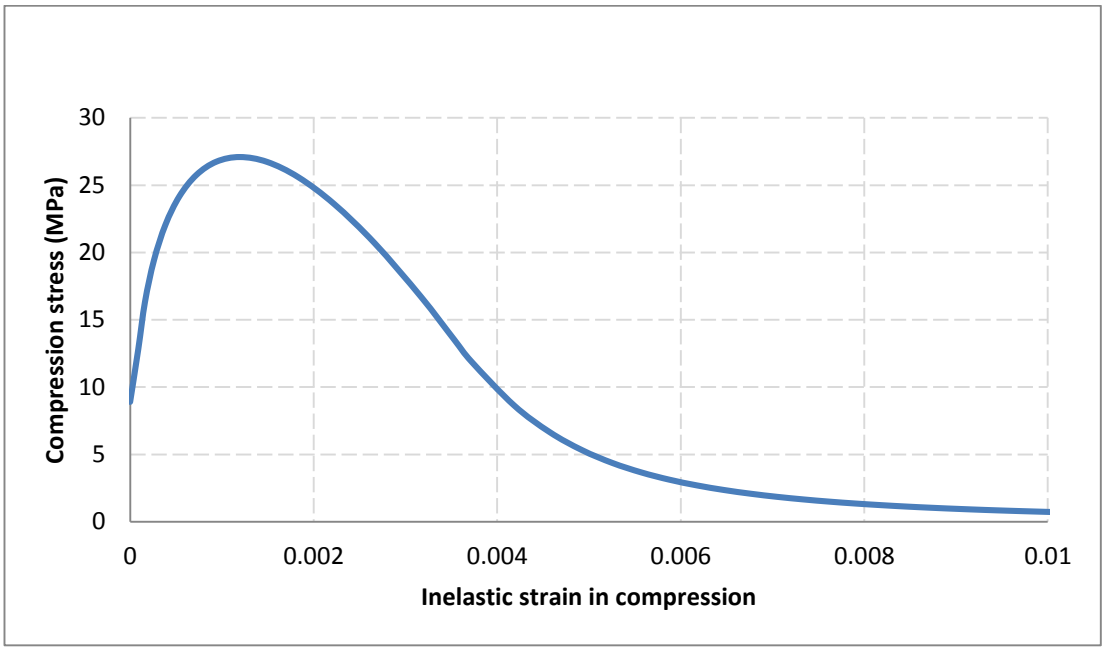

Figure 3.3 Uniaxial compressive stress-inelastic strain curve for concrete used in Specimen III-1 in Yao et al. (2005)

Concrete in tension

The CDP model also requires definition of variation of uniaxial tension stress, σ_t, with cracking displacement, ω_t. To define the stress-cracking displacement curve in uniaxial tension, the relationship proposed by Hordijk (1991) was used

$$\frac{\sigma_t}{f_t} = \left\{\left[1 + \left(c_1 \frac{\omega_t}{\omega_{cr}}\right)^3\right] e^{\left(-c_2 \frac{\omega_t}{\omega_{cr}}\right)} - \frac{\omega_t}{\omega_{cr}} (1 + c_1^3) e^{(-c_2)}\right\} \quad (3.21)$$

with

$$\omega_{cr} = 5.14 \frac{G_F}{f_t}, \text{ mm} \quad (3.22)$$

where

ω_{cr} (mm) is the critical crack opening displacement of concrete, beyond which the tension stress is assumed to be zero,

f_t (MPa) is the concrete tension strength under uniaxial loading,

G_F (N/mm) is the tensile fracture energy of concrete under opening mode,

c_1=3.0 and c_2=6.93 are constants determined from relevant tensile tests of concrete.

As such, unless available from the experimental data, f_t and G_F may be estimated by (CEBFIP 1993)

$$f_t = 1.4 \left(\frac{f_c' - 8}{10}\right)^{\frac{2}{3}}, \text{MPa} \tag{3.23}$$

$$G_F = (0.0469\, d_a^2 - 0.5\, d_a + 26) \left(\frac{f_c'}{10}\right)^{0.7}, \text{N/mm} \tag{3.24}$$

where, d_a is the maximum aggregate size in concrete. In the current study, it was assumed to be 20 mm, if not provided in the relevant experimental report.

Often in tension, stress-strain curves are used rather than tension stress-cracking displacement curve. In simulations, these are known to cause element size sensitivity (Bazant, 1976); Bazant and Cedolin, 1979).

To obtain an objective result in simulations, crack band theory (see Bazant (1976); Bazant and Cedolin (1979)) is employed to convert the model in Eq. (3.21) into tension stress-cracking strain relationship for different element sizes. Thus, tensile fracture energy G_F is converted as

$$G_F = \int \sigma \, d\omega_t = h \int \sigma \, d\varepsilon_t, \text{N/mm} \tag{3.25}$$

where, h is the characteristic length of square element with four integration points (i.e. CPS4 in ABAQUS) and is set to a value $\sqrt{2}e$ (i.e. e is the side length of the square element), as recommended in Rots (1988).

For specimen III-1 in Yao et al. (2005) adopted in this thesis, the uniaxial tension stress-cracking displacement curve employed, based on Eq. (3.21), is shown in Figure 3.4.

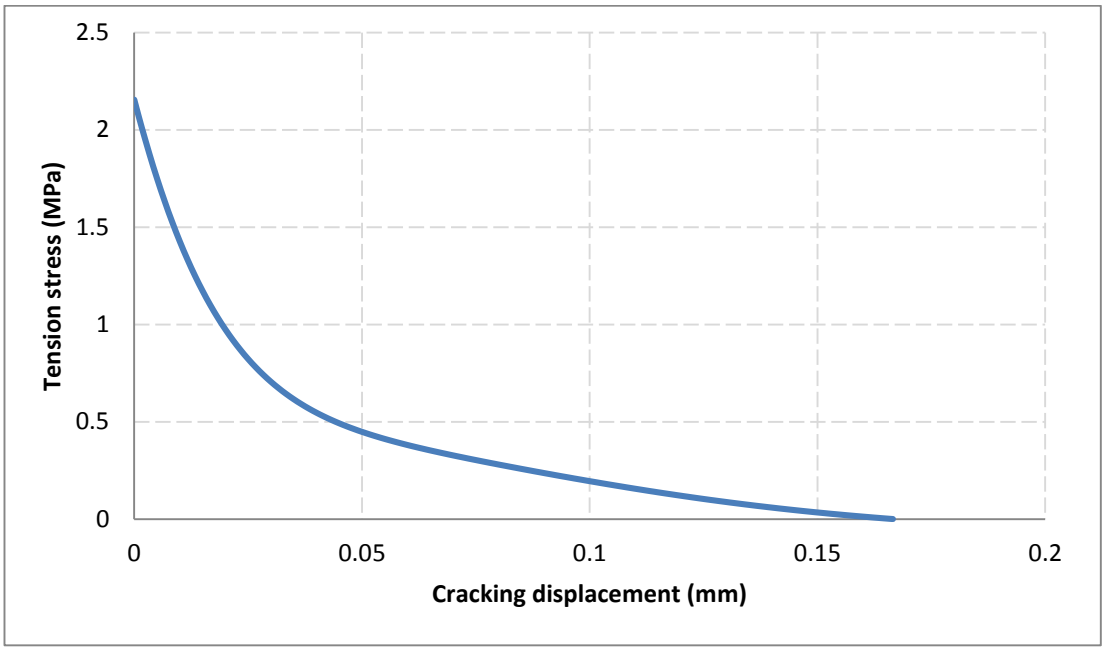

Figure 3.4 The relationship of tension stress versus cracking displacement adopted for concrete used in Specimen III-1 in Yao et al. (2005)

Damage model for concrete

Concrete damaged plasticity model also permits inclusion of a damage factor, which varies with inelastic deformation (i.e. inelastic strain in compression or cracking strain in tension). In Chapter 5, the effect of different damage definitions is examined in detail. However, for most of the thesis, the model proposed by Birtel and Mark (2006) is used. In this, a single scalar variable d_x is related to inelastic deformation ε_x^{in} through

$$d_x = \frac{(1-b_x)\varepsilon_x^{in}}{(1-b_x)\varepsilon_x^{in} + b_x\sigma_x/E_0}; \qquad 0 \le d \le 1 \tag{3.26}$$

where, ε_x^{in} is inelastic strain;σ_x is the uniaxial stress; the subscript x can become c for compression, or t for tension. A value b_x=0.7 fits well with experimental data of cyclic tests in both comparison and tension cases as detailed in Chapter 5. In general, the single scalar variable d_x, as an increasing function with plastic strain, takes values ranging from zero, for the undamaged material, to unity, for the fully damaged material.

In the plastic-damage model, the damage factor d_x is used to degrade the elastic stiffness of concrete through

$$E = (1 - d_x)E_0, \text{ MPa } \ 0 \leq d_x \leq 1 \tag{3.27}$$

For Specimen III-1 in Yao et al. (2005) analysed in this thesis, the variation of damage with inelastic strain based on Eq.(3.21) is shown in Figure 3.5. The corresponding elastic reductions induced by the damage factor in compression and tension are shown in Figure 3.6.

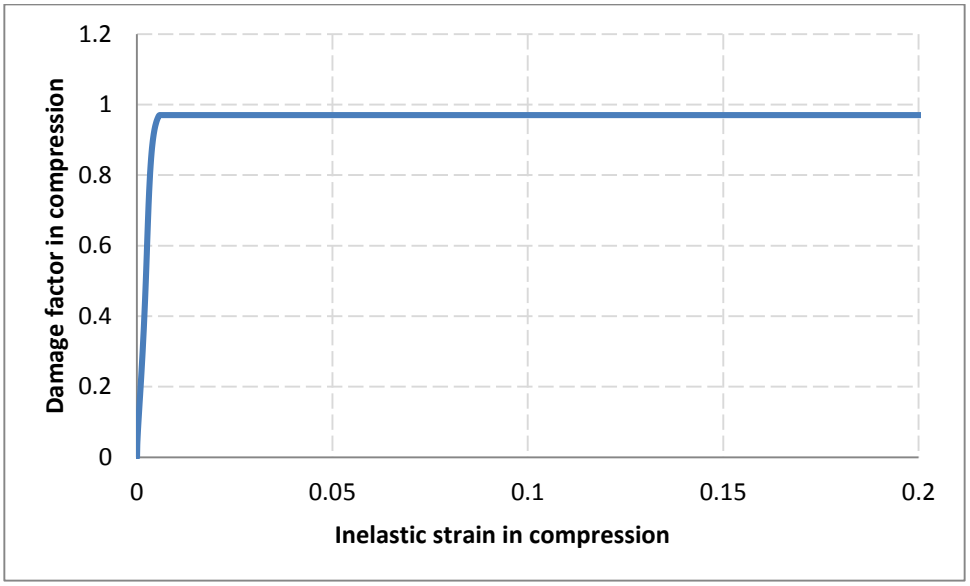

(a)

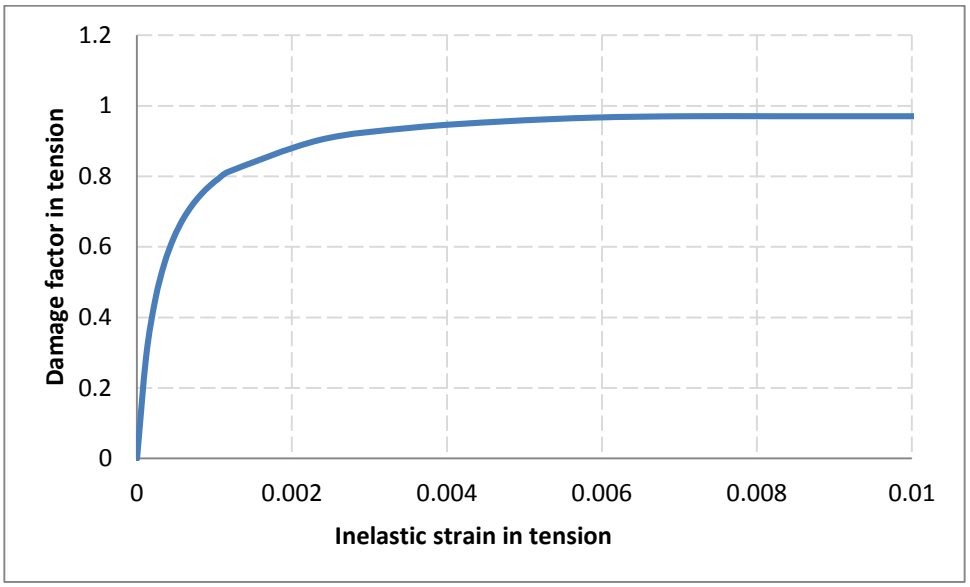

(b)

Figure 3.5 Variation of damage with inelastic strain in (a) compression and (b) tension

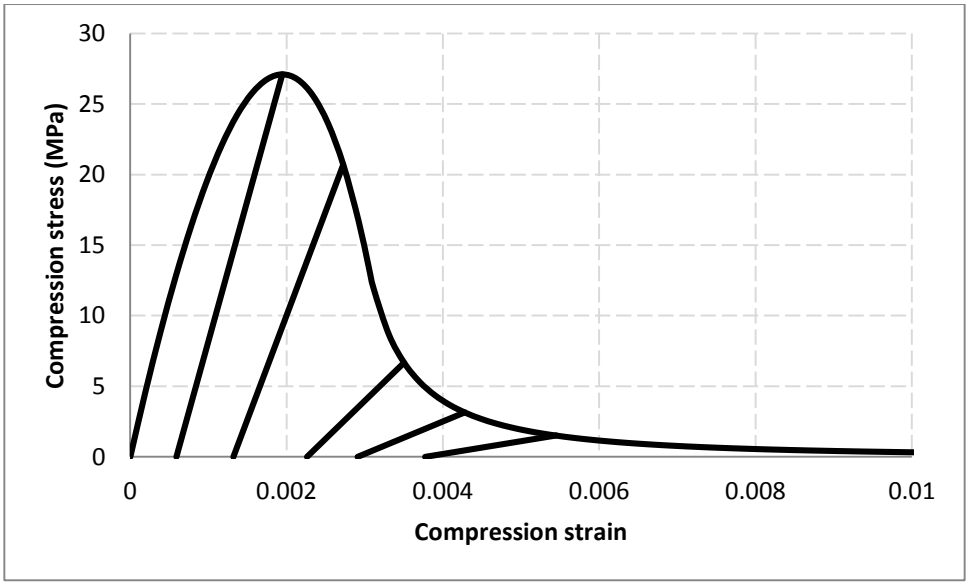

(a)

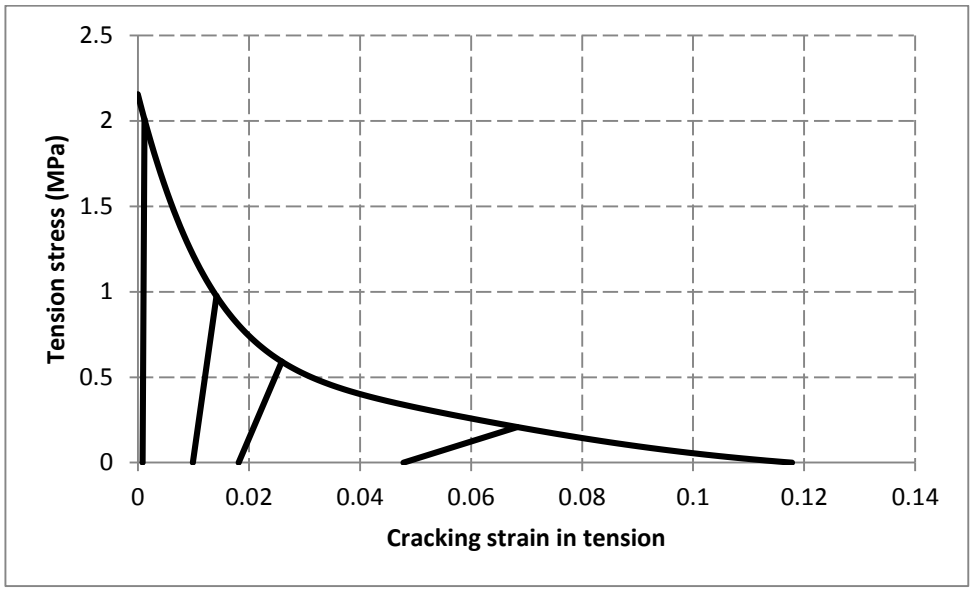

(b)

Figure 3.6 Elastic reductions in both (a) compression and (b) tension cases

3.3 FE mesh and boundary conditions

In simulations of FRP-concrete bonded interface, a 4-node plane stress element (CPS4) with four integration points is employed to establish the geometrical model for both FRP and concrete parts. FRP part is directly connected to concrete part by each sharing nodes, with the presence of adhesive ignored in the geometrical modelling. That is because in physical tests FRP is usually observed to be torn from concrete prism along with a thin layer of concrete (i.e. 2–5 mm) unless adhesive layer is rather weak (Chen and Teng 2001).

In geometrical modelling of the FRP part, the thickness of FRP t_f is assumed to be 1 mm with side length of (square) element 1 mm. The width of FRP part is set as per real width of FRP in physical tests. In the cases with physical thickness of FRP beyond 1 mm, its thickness in geometrical modelling is still taken as 1 mm for convenience while the elastic modulus of FRP is adjusted by keeping constant the value of FRP

stiffness $E_f t_f$ in the longitudinal direction. For Specimen III-1 in Yao et al. (2005), the width of FRP is 25 mm and the width of concrete prism is 150 mm.

For geometrical modelling of the concrete part, the width of concrete part is set as per the real width of concrete prism in the physical test. In this thesis, a full-scale geometrical modelling is required in simulations of FRP-concrete bonded interface so as to reflect the mechanical differences arising from different free support heights; such a phenomenon has been verified in physical tests in Yao et al. (2005) but has long been ignored in previous simulation studies (Lu et al. 2005b; Tao and Chen 2015). In such a full-scale geometrical modelling, the number of nodes needs to be minimised for the sake of computational efficiency; on the other hand, fine meshes are required in the zone adjacent to FRP for the sake of computational accuracy.

In view of that, to balance the computational accuracy with efficiency, an FE mesh scheme is proposed. It divides the concrete part into different zones: A1, A2, A4, A8 and B8, as shown in Figure 3.7, and will be employed in subsequent simulations of FRP-concrete bonded interface in this thesis. Correspondingly, the side length of element size is 1 mm in A1 zone, 2 mm in A2 zone, 4 mm in A4 zone, and 8mm in A8 and B8 zones. The dimensions for these zones are specified as follows: A1 is set as 136 × 24 mm, B8 is set as 228 ×24 mm, A2 is set as 364 × 2mm, A4 is set as 364 ×4 mm, and A8 is set as 364 ×120 mm (see Figure 3.7). The elements in the same zone are connected with each other through sharing nodes, while the neighbouring elements in the different zones are connected to each other with the tie command in ABAQUS (2011).

With reference to Specimen III-1 in Yao et al. (2005), the boundary conditions in simulations of FRP-concrete bonded interface are shown in Figure 3.8. Specifically, the model is restrained vertically along the bottom (i.e. to simulate the restraints from the ground in physical tests) and on the steel plate at the top left (see Figure 3.8) to prevent it from uplifting while loading. Apart from that, the model was also restrained horizontally at the lower part of front side to simulate the reaction element in physical

tests. Besides, a displacement load is applied onto the right end of FRP part, as shown in Figure 3.8.

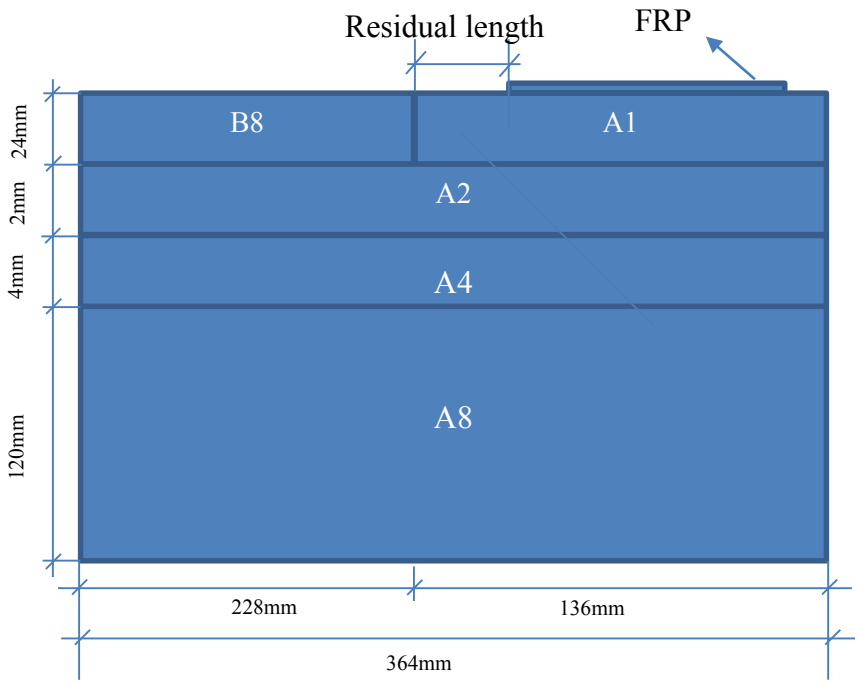

Figure 3.7 Diagrammatic sketch of FE mesh in simulations of FRP-concrete bonded interface with reference to Specimen III-1 from Yao et al. (2005)

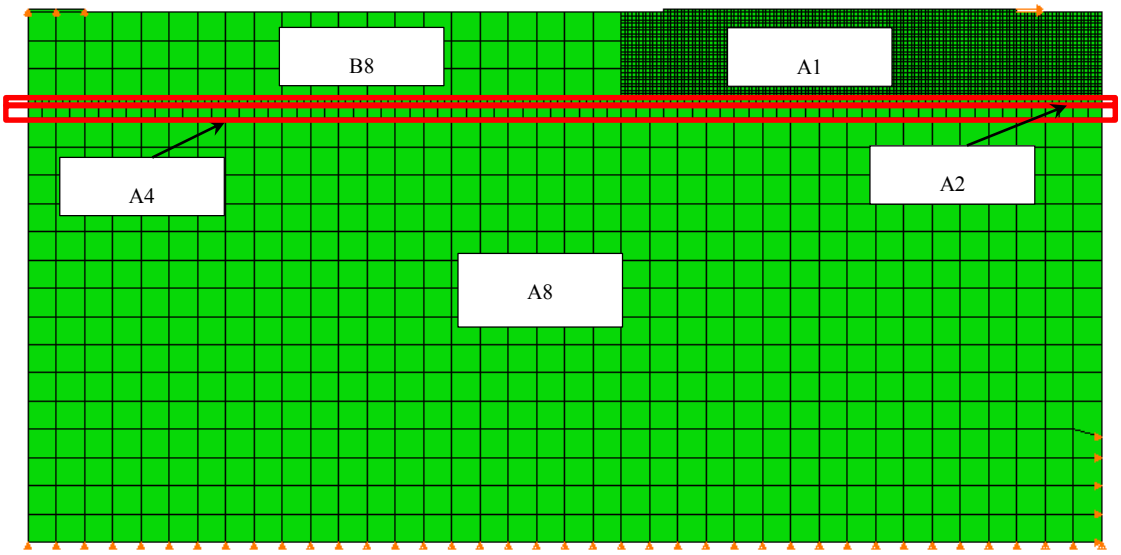

Figure 3.8 FE mesh and boundary conditions in simulations of FRP-concrete bonded interface with reference to Specimen III-1 from Yao et al. (2005)

3.4 Loading approach

As discussed in Chapter 2, the debonding failure, namely concrete delamination, which usually only occurs in concrete body in physical tests, is the most observed failure mode for FRP-concrete bonded interface, which is comprised of FRP and concrete parts (Teng et al. 2003). As discussed in Section 3.2, in simulations of FRP-concrete bonded interface linear elastic property is used in FRP part, whereas concrete damaged plasticity model is used in concrete part. In view of that, the success of simulations of FRP-concrete interfacial simulations is determined by the convergence in the computation of concrete part to a great degree.

However, it is well recognised that numerical simulation of cracking using static approach are fraught with the problem of convergence (de Borst 1986, 1987; Crisfield 1981, 1986; Rots 1988). Because of this, very few FE studies on FRP-concrete bonded interface have succeeded in simulating the full debonding process (e.g. Kishi et al., 2005; Niu and Karbhari, 2008). Approaches used to overcome this problem, included modified Newton-Raphson approach (Clarke and Hancock 1990) and the arc-length approach (Crisfield 1991) but severe convergence issues still persisted in the late stage

of loading probably due to severe nonlinearities caused by concrete cracking or crushing.

To overcome the aforementioned convergence issues in simulations associated with concrete or other concrete-like brittle materials, a quasi-static approach (i.e. called implicit dynamic approach in ABAQUS (2011)) has been suggested as an alternative numerical solution method to obtain essential static solutions (Chen et al. 2009; Chen 2010). In view of this, a series of suggested schemes and parameters by Chen et al. (2009) and Chen (2010) are considered for the implicit dynamic approach in the following section before being adopted in the subsequent simulations of FRP-concrete bonded interface in this thesis.

Chen et al. (2009) and Chen (2010) identified three key parameters for successful implementation with dynamic approach: loading scheme, loading time and time increment size. The analysis they conducted was with respect to a beam, but is equivalently applicable to the problems considered in this study.

3.4.1 Loading scheme

Chen et al. (2009) and Chen (2010), considered three displacement controlled loading schemes: step load (Figure 3.9 (a)), ramp load (Figure 3.9 (b)) and smooth load (Figure 3.9 (c)). In their investigation, the loading time t_0 is set to a value of $10T_1$, where T_1 is the period of the fundamental vibration mode of Beam D. The load-deflection curves at the mid-span of the beam being investigated by the authors are shown in Figure 3.10. They found that both smooth and ramp loading schemes result in a similar response close to the test data; whereas the step loading scheme leads to a significantly different response. In this study, ramp loading scheme is employed in simulations of FRP-concrete bonded interface in this thesis.

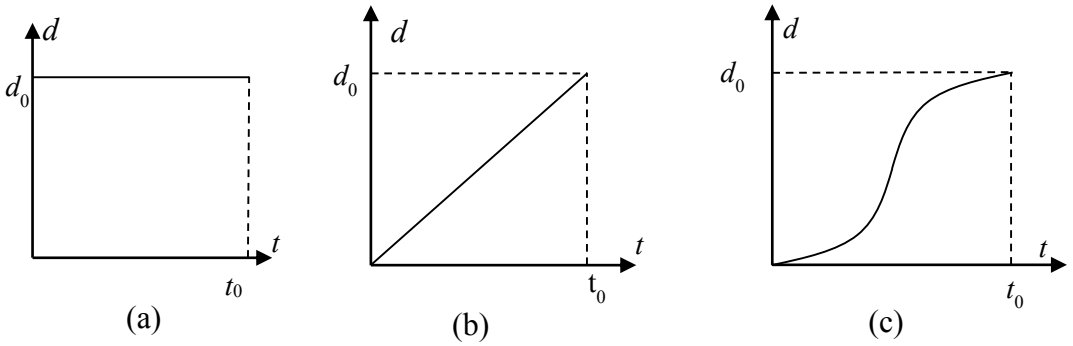

Figure 3.9 Different displacement-controlled loading schemes (extracted from Chen (2010)), namely (a) step, (b) ramp and (c) smooth loading schemes

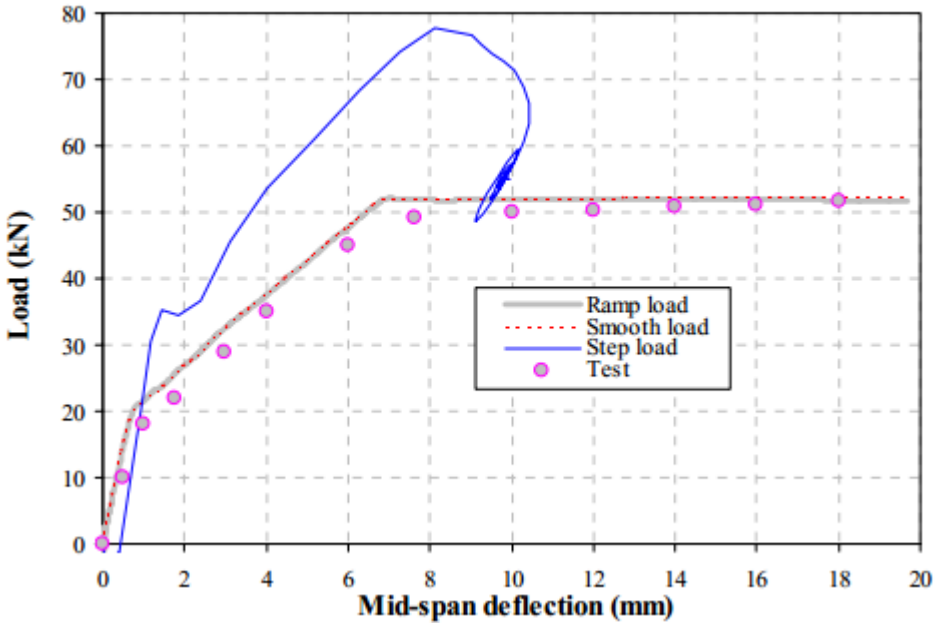

Figure 3.10 Response of beam under different loading schemes (extracted from Chen (2010))

3.4.2 Loading time t_0

In simulations with ramp loading scheme, the loading time t_0 is an important factor to obtain reliable results as it relates to the loading speed. Theoretically, the loading time t_0 should be set as long as possible so as to obtain an essentially static solution and

avoid any disturbance arising from dynamic load in such simulations. However, larger time results in increased cost of computation.

Chen et al. (2009) and Chen (2010), with reference to the beam they analysed, considered different values of loading time t_0 to evaluate their effects on the ultimate load (Figure 3.11). Figure 3.11 shows that there is little difference in the results beyond loading time $t_0 = 50T_1$. However, the authors recommended loading time $t_0 = 100T_1$. To examine the effect of loading time, Specimen III-1 in Yao et al. (2005) was analysed. The geometrical modelling and material properties assignments were as discussed in sections 3.2 and 3.3.

The peak load values with loading time of $50T_1$, $100T_1$, $1000T_1$ and $2000T_1$ were considered, with increment size Δt set to $0.01T_1$. The results are shown in Figure 3.12. It can be seen that as found in Chen et al. (2009) and Chen (2010), the peak load reduces with the increase of loading time. The ultimate load reduces when the loading time is increased from $50T_1$ to $200T_1$ by approximately 3%. However, this reduction is only 0.4% when the loading time is further increased from $100T_1$ to $1000T_1$. In this study, therefore, a loading time $100T_1$ was adopted.

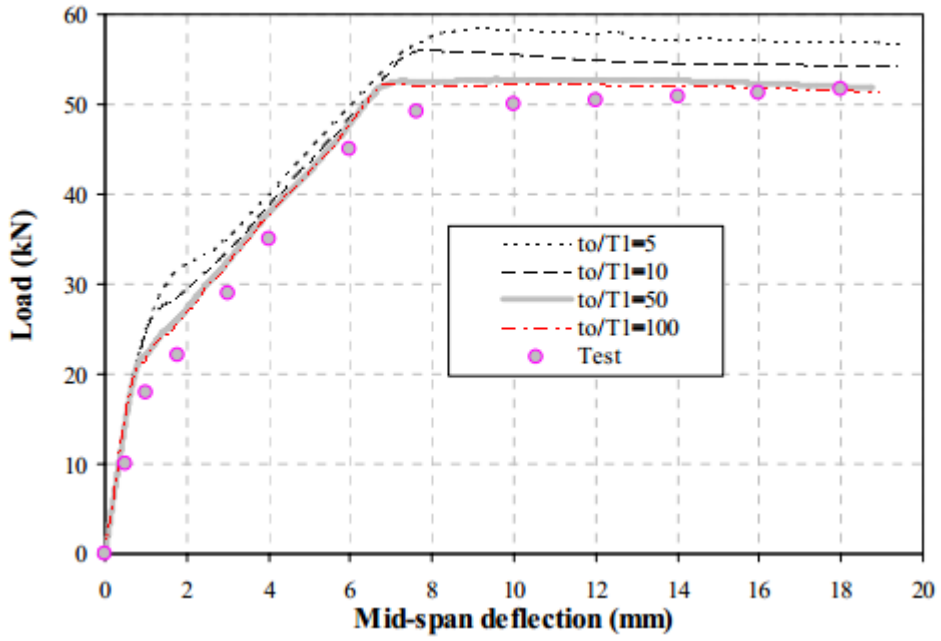

Figure 3.11 Effect of loading time on the predicted load-displacement curve (extracted from Chen (2010))

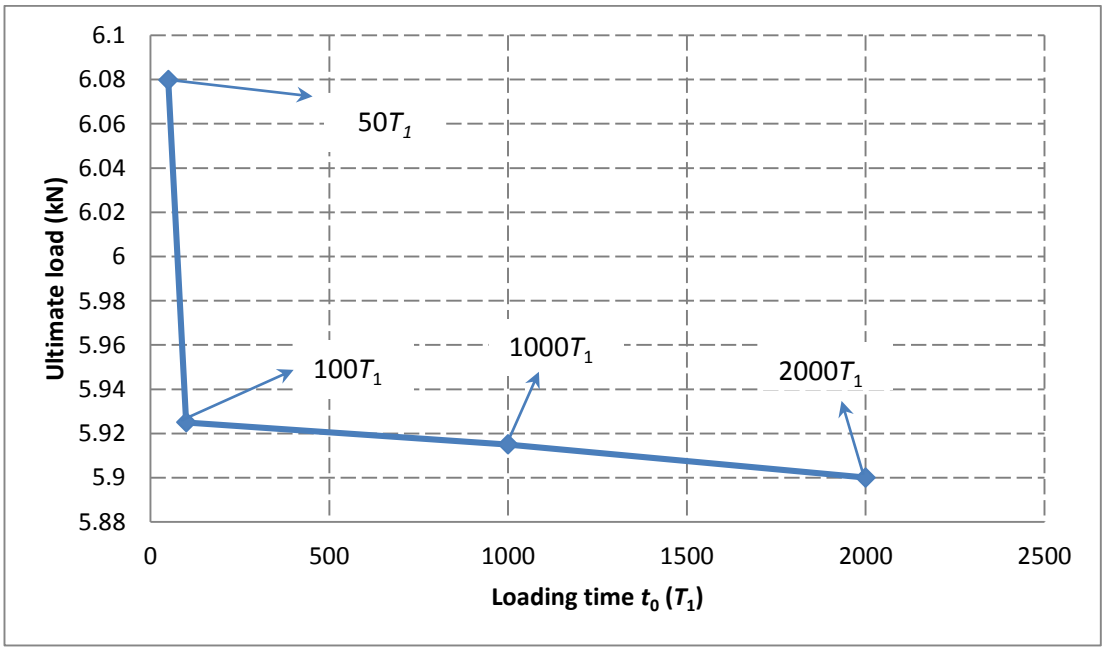

Figure 3.12 Variation of ultimate load with loading time t_0 in simulations of FRP-concrete bonded interface

3.4.3 Increment size Δt

Stability and accuracy of implicit time scheme are affected by the choice of time increment size Δt. In this study, $\Delta t = T_1/100$ was employed based on the previous studies by Chen and Virgin (2006), Chen (2010) and Chen et al. (2009).

Existing studies (e.g. Chen and Virgin, 2006) show that nonlinear analysis could reach a satisfactory result, when increment size (Δt) is smaller than $T_1/20$. Moreover, in Chen et al. (2009) and Chen (2010), the increment size (Δt) is recommended as $T_1/100$, which will be used in subsequent simulations of FRP-concrete bonded interface in this thesis.

3.4.4 Rayleigh damping

Rayleigh damping was used to regularise and improve convergence behaviour.

In simulations of Specimen III-1 from Yao et al. (2005), stiffness proportional Rayleigh damping coefficient β was used ($\mathrm{C} = \beta \mathrm{K}$) with $\beta = 3\times10^{-8}$ resulting in a damping ratio of 3×10^{-4} corresponding to lowest frequency of vibration.

More details about Rayleigh damping will be discussed in Chapter 4.

3.5 Determination of element size and dimensions for A1 zone

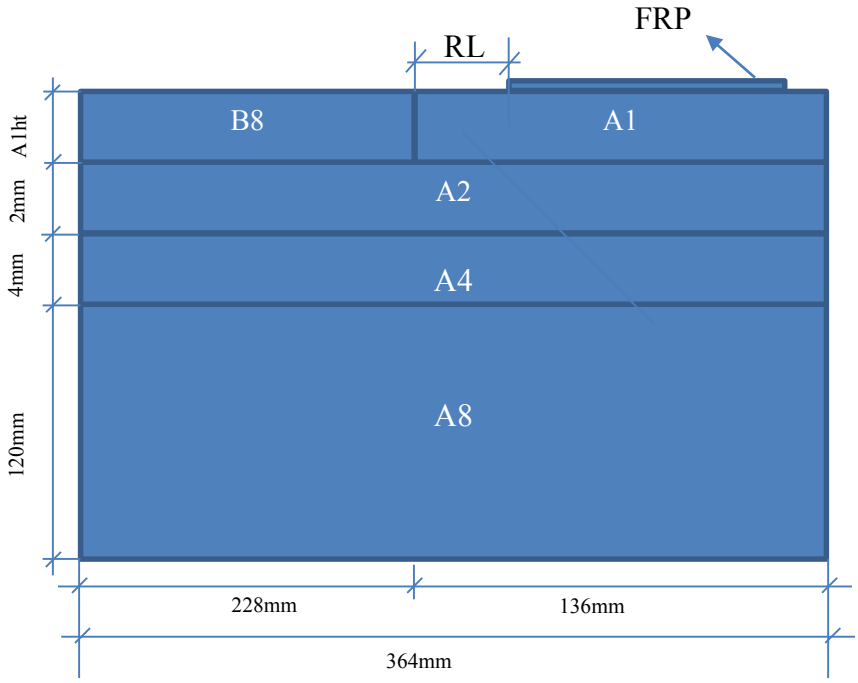

Figure 3.13 Diagrammatic sketch of FE mesh in simulations of FRP-concrete bonded interface with reference to Specimen III-1 from Yao et al. (2005)

As discussed in Section 3.3, the concrete part in simulations has been divided into different zones, which are meshed with different element sizes. Amongst them, A1 zone is considerably important as it plays a pivotal role in the stress transferring process at FRP-concrete bonded interface. Specifically, as discussed earlier, a number of experiments have shown that a thin layer of concrete gets torn away at the interface during the debonding process (Chen and Teng 2001). To determine the element size and dimensions for A1 zone, a number of variations are considered; different element sizes employed in A1 zone and the height (A1ht) and residual length (RL) of the zone are varied (Figure 3.13). The simulations of these variations are discussed in the following sections.

3.5.1 Effect of element size in A1 zone

Four different element sizes in A1 zone were considered: 0.5 mm, 1 mm, 2 mm and 4 mm. In all these cases A1 zone was taken as 24×136 mm. The load-displacement curves for each of these cases with different element sizes are shown in Figure 3.14. It can be seen that the load in all cases remains roughly at the same level. Larger element sizes, however, result in a more evident jagged response arising from intermittent release of stress due to the cracking of concrete at the interface. Decrease of element size reduces the jagged nature of the response. Element size of 1 mm was deemed to be acceptable and used in the subsequent simulations.

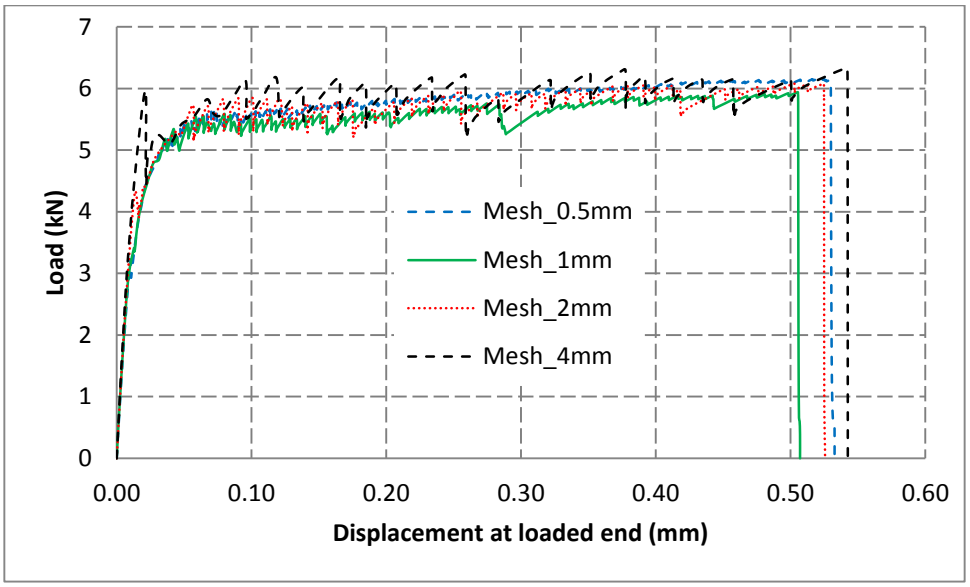

Figure 3.14 Load-displacement curves with different element sizes in A1 zone

3.5.2 Effect of variation in the dimensions of A1 zone

The dimensions of A1 zone were changed to examine their effect on the load-displacement behaviour. In the first set of simulations, the height, A1ht, was varied from 8 mm to 40 mm at an interval of 8 mm. For these simulations, the residual length remained as 24 mm. The resulting load-displacement curves are shown in Figure 3.15. Very little difference is observed amongst these cases. Thus, it is reasonable to set the height of A1 zone to a value of 24 mm, as stated in Section 3.3, for subsequent

simulations of FRP-concrete bonded interface. Although in these simulations, even a small height of A1 zone gives a satisfactory result, subsequent simulations of wider FRP, discussed in Chapter 8, indicated that A1ht is equal to 24 mm was satisfactory for most simulations. This was adopted for subsequent work.

Next, the effect of the length of A1 zone was investigated by changing the residual length, RL, of A1 zone. Dimension RL = 4, 12, 20, 28, 36 mm was considered. The resulting load-displacement curves are shown in Figure 3.16. It is found that there is very little difference amongst the cases. A value of 12 mm was adopted for the residual length for subsequent simulations of FRP-concrete bonded interface.

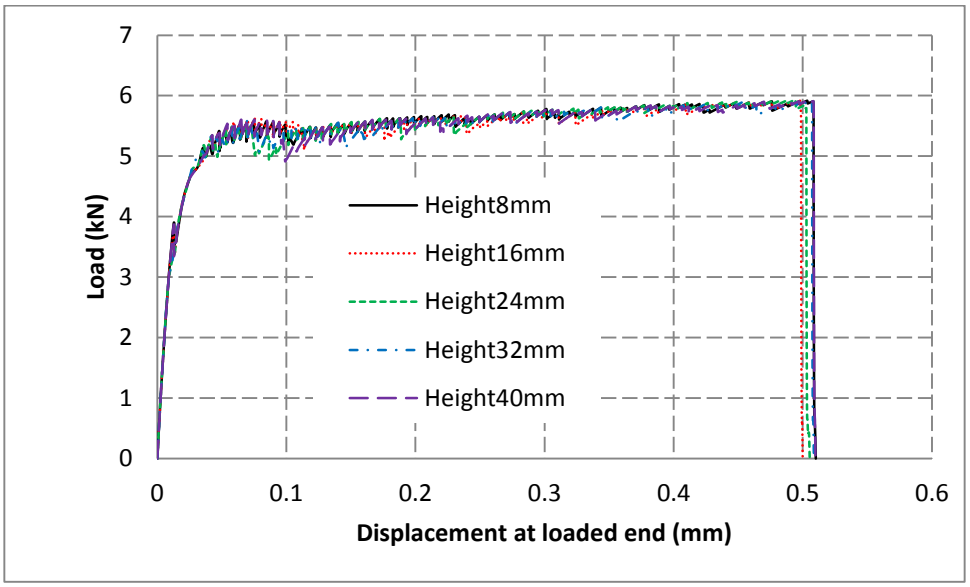

Figure 3.15 Effect of height of A1 zone on mechanical behaviour of FRP-concrete bonded interface

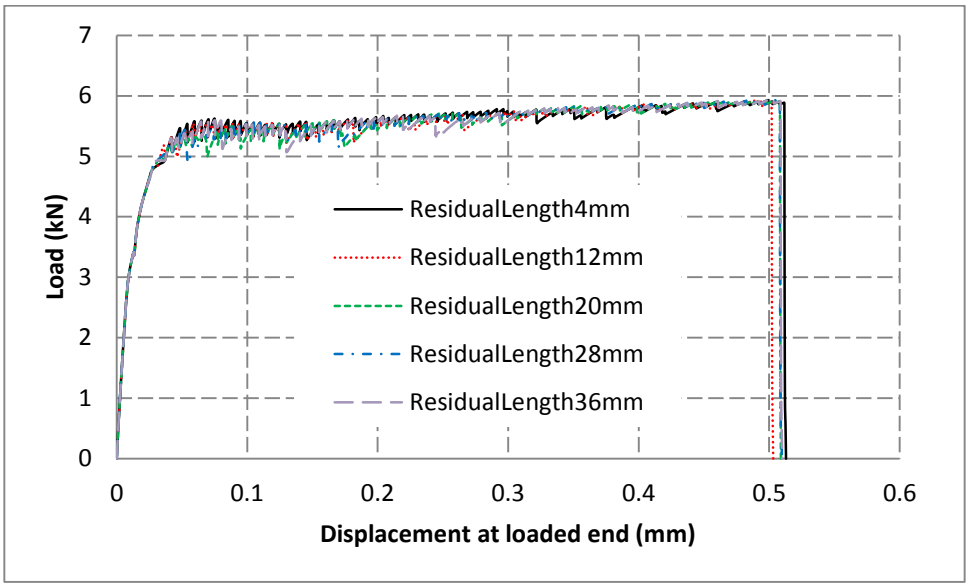

Figure 3.16 Effect of residual length of A1 zone on mechanical behaviour of FRP-concrete bonded interface

3.6 Conclusions

In this chapter, the key features essential for modelling debonding at the FRP-concrete bonded interface are introduced comprehensively. Specifically, the FRP part was regarded as elastic isotropic material, whilst concrete part is modelled with concrete damaged plasticity model, in which the compression stress-strain relationship, tension stress-strain relationship, damage factor versus inelastic strain relationship under tension and compression, and characteristic length were defined in detail. Based on computational accuracy and efficiency, the FE mesh scheme, as shown in Figure 3.7, was proposed to divide concrete part into different zones, in which different element sizes are used.

Together with a simple suggested value of Rayleigh damping ratio by this study (i.e. will be discussed in detail in Chapter 4), the suggestions about various key parameters for implicit dynamic loading approach, including loading schemes, loading time t_0 and increment size Δt, were introduced in detail from Chen et al. (2009) and Chen (2010),

and further verified with different loading times t_0, with reference to Specimen III-1 in Yao et al. (2005).

Once again, Specimen III-1 in Yao et al. (2005) is also taken as the reference case to investigate the effects of element size in A1 zone and the dimensions of A1 zone on the simulation results, respectively. Specifically, the effect of element size in A1 zone (i.e. also called mesh convergence study) were investigated with different (square) element sizes in A1 zone (i.e. 0.5 mm, 1 mm, 2 mm and 4 mm in side length of element), while keeping the rest zones unchanged. Through comparisons of the simulation results, it is found that it is acceptable to employ 1 mm sized element to mesh A1 zone of concrete part in subsequent FRP-concrete bonded interfacial simulations in this thesis. Besides, effects of dimensions of A1 zone were investigated through different heights and lengths of A1 zone. It is found that it is reasonable to set the height of A1 zone as 24 mm and set residual length as 12 mm for subsequent simulations of FRP-concrete bonded interface.

Chapter 4
Dynamic simulation of quasi-static problems: effect of Rayleigh damping

4.1 Introduction

Material softening in plain concrete, such as cracking and crushing, often leads to an unstable behaviour in simulations and makes such simulations very difficult to converge if static approaches are used in FEA. As discussed in Chapter 2, the FRP-concrete bonded interface is usually composed of FRP and a plain concrete prism without internal reinforcing bars. The success of the simulation of FRP-concrete bonded interface highly depends on the convergence of computations.

To overcome this convergence issue in simulations associated with concrete, an implicit dynamic approach is used in this thesis. In such simulations, it is essential to introduce a damping system to consume dynamic energies generated by dynamic loads in quasi-static problems. Amongst various damping systems in simulations, Rayleigh damping (Rayleigh 1877) is the most widely used to model dissipative forces in complex engineering structures and various dynamic problems.

There are still many uncertainties existing in usage of Rayleigh damping in analysis of structures, especially in strengthened structures with FRP, although a great number of studies have been performed. Specifically, in Alipour and Fareian (2008) a single degree of freedom (SDOF) frame is used to investigate the effect of Rayleigh damping; the use of the reference case directly undermined the reliability of its conclusion and application in simulations with a large scale of elements. Even in some literatures (e.g. Charney (2005)) a multi degree of freedom (MDOF) model was considered but only traditional structural components were focused, whose fundamental frequency are quite low. They even suggested that the stiffness proportional damping could be excluded in simulations. Obviously, these conclusions are not applicable to the simulations of FRP-concrete bonded interface.

The effect of Rayleigh damping in FRP strengthened beams is investigated in Chen et al. (2015). Specifically, it is found that HHT-α (Hilber et al. 1977), an implicit dynamic approach, is capable of automatically damping out the higher frequency response due to the presence of its inherent numerical damping and there is no need to define an additional damping for the stiffness proportional damping. However, this conclusion is drawn from the research on beams strengthened with FRP, whose response may be dominated by lower frequency vibrations and may be different from that of FRP-concrete bonded interface.

In order to achieve a deep insight into the effect of Rayleigh damping in simulations with implicit dynamic approaches, different values of mass and stiffness proportional damping ratios are first employed respectively in element tests under Mode I and Mode II fracture modes in this chapter. Subsequently, different values of mass and stiffness proportional damping ratios are also employed respectively in simulations of FRP-concrete bonded interface with both debonding and CPF failure modes to further investigate their effects on the mechanical behaviour.

4.2 Effect of Rayleigh damping in element tests under different fracture modes

4.2.1 Background

The Rayleigh damping (Rayleigh 1877) is defined by a damping matrix formed as a linear combination of the mass and stiffness matrices and given as

$$C = \alpha M + \beta K \tag{4.1}$$

where, α is the mass proportional damping coefficient, M is the mass matrix, β is the stiffness proportional damping coefficient, and K is the stiffness matrix. For a given mode i, the critical damping ratio ξ_i in Rayleigh damping is expressed in terms of damping coefficients α and β as:

$$\xi_i = \frac{\alpha}{2\omega_i} + \frac{\beta\omega_i}{2} \tag{4.2}$$

where, ω_i is the circular frequency of mode i. In this section, the damping ratio, obtained through coefficient α alone, is called mass proportional Rayleigh damping ratio ξ_α. Similarly, the damping ratio, obtained through coefficient β alone, is called stiffness proportional Rayleigh damping ratio ξ_β.

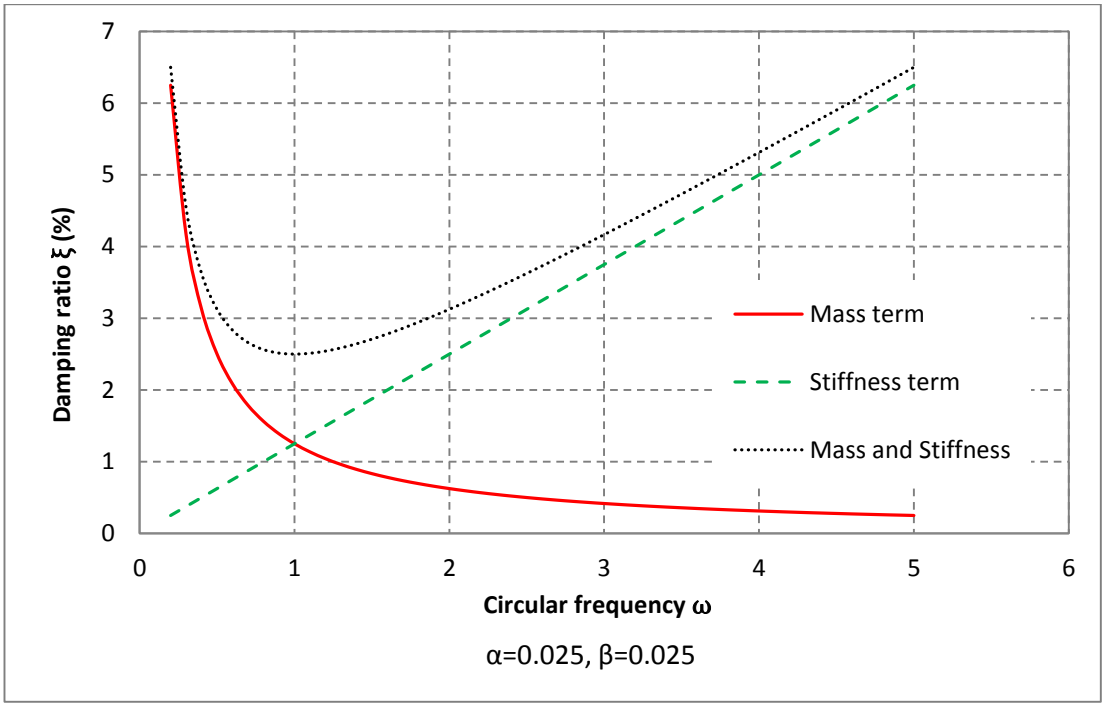

Figure 4.1 Variation of damping ratio with circular frequency

In general, the mass proportional damping coefficient α damps the lower frequencies, whereas the stiffness proportional damping coefficient β damps the higher frequencies, as shown in Figure 4.1 (ABAQUS 2011). However, this conclusion is too abstract to apply in simulations. In view of that, an element bar with 310 elements under two different loading (i.e. Mode I and Mode II fracture modes see Bazant and Planas (1997)) modes, is used to demonstrate this qualitative conclusion.

4.2.2 Element tests under Mode I fracture mode

In this subsection, different values of mass and stiffness proportional damping coefficients are used separately to investigate their effects on simulation results, with reference to an element bar with uniaxial loads (i.e. the loads under Mode I fracture mode), as shown in Figure 4.2. The dimension of the element bar is 310 × 100 mm and side length of element is 10 mm. The strength of concrete is set at 23 MPa in the whole element bar except the middle layer (in the red frame in Figure 4.2), in which it is set at 90% of that in the rest. The purpose of that is to make sure that the crack occurs in the middle layer (see Figure 4.2). The same material properties are used as in Chapter 3 except for Rayleigh damping ratio setting. The boundary conditions in the model are set as shown in Figure 4.2, to make sure the model is under uniaxial tension loads.

In this study, the damping ratio varies across 0, 0.05%, 5% and 50%. The values of mass and stiffness proportional damping coefficients are calculated from their corresponding damping ratios through Eq. (4.2) with the fundamental circular frequency of the element bar 2959 rad/s, which is obtained through frequency analysis in ABAQUS (2011). The relevant results are shown in Table 4.1.

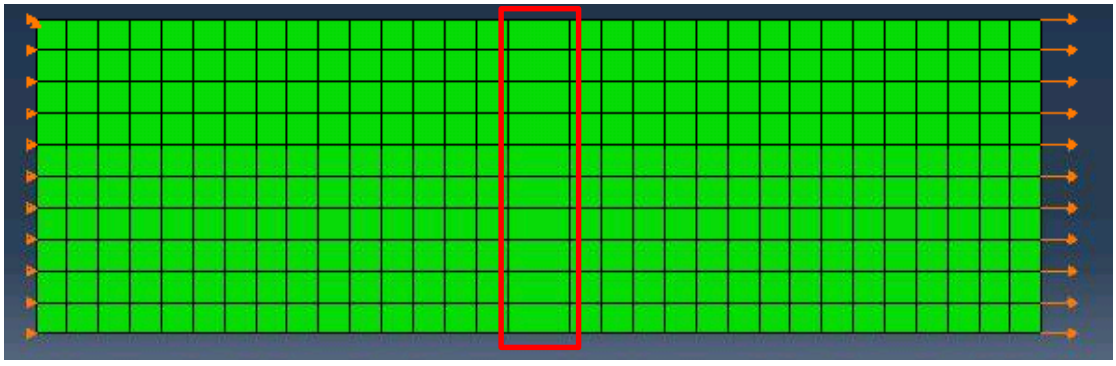

Figure 4.2 The boundary conditions of specimen under Mode I fracture mode (deformed shape)

Different values of mass proportional damping coefficient α in Table 4.1 are first employed alone to assign Rayleigh damping ratio ξ in the element test, thereby investigating its effect on the results. The stress-displacement curves from the relevant

results are shown in Figure 4.3 and variation of peak stress under Mode I with mass proportional damping ratio ζ_α is plotted in Figure 4.4. It is found that the stress-displacement curve from the case with zero damping (i.e. which will also be used in the investigation with stiffness proportional damping ratio ζ_β) is exactly the same as that in other cases. Through such comparisons, it seems that there is no need to define damping ratio for improvement of convergence in this simulation, due to the presence of numerical damping in HHT-α method (HILBER et al., 1977; ABAQUS, 2011; Chen et al., 2015). Plus, it is also found that mass proportional damping coefficient α seems to have no effect on the results in this simulation.

Table 4.1 Values of mass and stiffness proportional damping coefficients for different damping ratios

Damping ratio ξ	Mass proportional damping coefficient α	Stiffness proportional damping coefficient β
0.00%	0	0
0.05%	0.471	3.38×10^{-7}
5.00%	47.1	3.38×10^{-5}
50.00%	471	3.38×10^{-4}

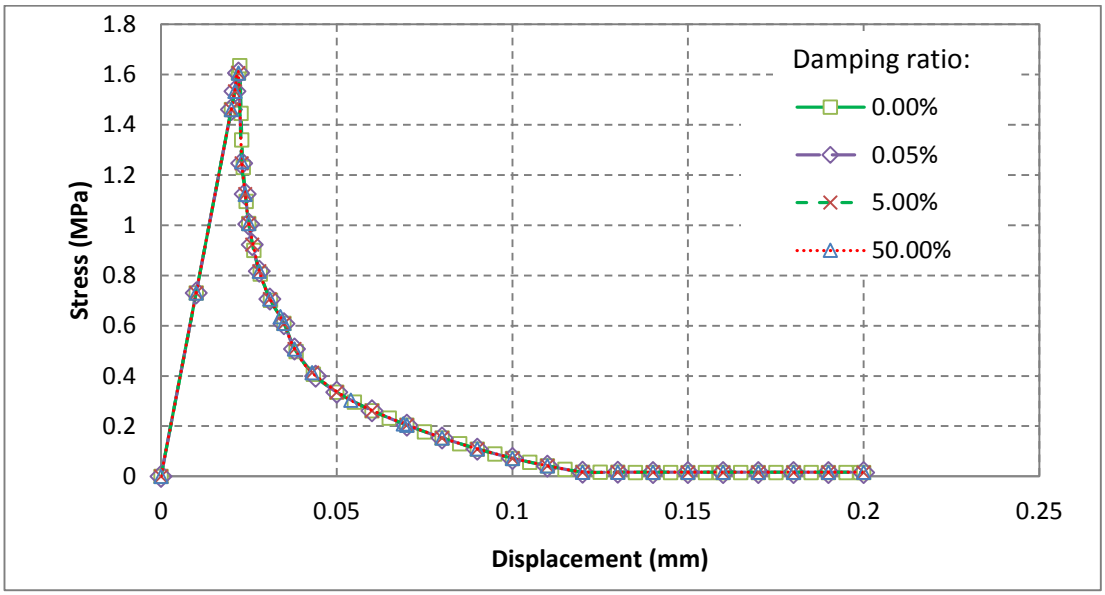

Figure 4.3 Effect of mass proportional damping ratio ξ_α on Mode I cracking

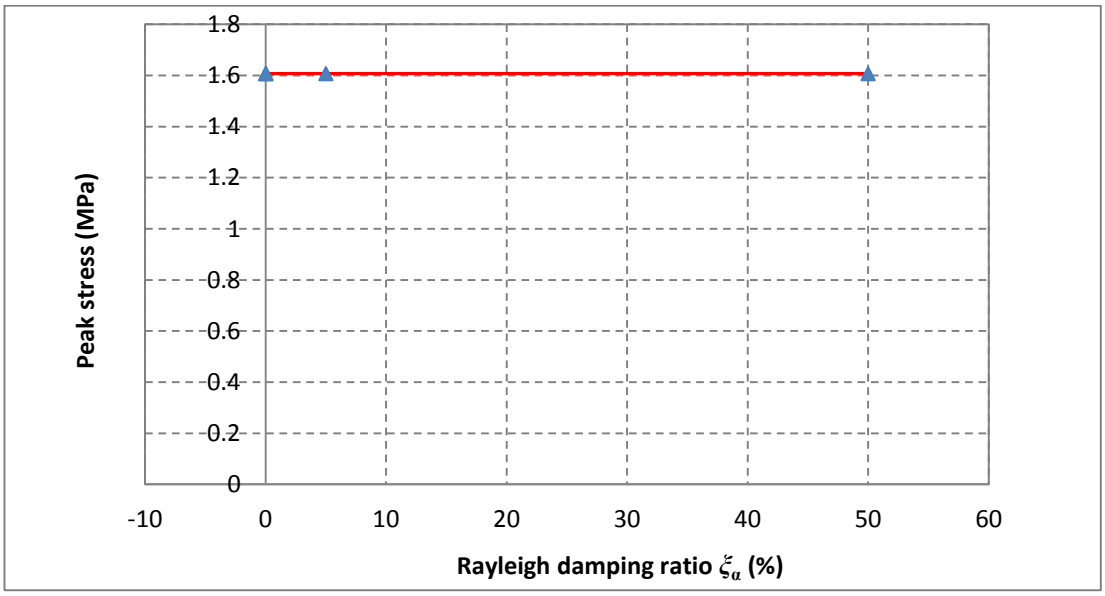

Figure 4.4 Variation of peak stress with mass proportional damping ratio ξ_α under Mode I fracture mode

Different values of stiffness proportional damping coefficient β in Table 4.1 are also employed alone to assign Rayleigh damping ratio ξ in the element test, thereby investigating its effect on the results. The stress-displacement curves from the relevant results are shown in Figure 4.5 and variation of peak stress under Mode I fracture mode

with stiffness proportional damping ratio ξ_β is plotted in Figure 4.6. It is found that the stress-displacement curves from the case with zero damping (i.e. which has also been used as the reference case in the investigation with mass proportional damping ratio ξ_α) is almost the same as that with damping ratio ξ_α of 0.05%, a phenomenon which indicates that the result from the case with damping ratios ξ_α of 0.05% should be trusted. On the other hand, the loads in the cases with damping ratios ξ_α of 5% and 50% are found to increase with the value of damping ratio, as shown in Figure 4.6. Through this comparison, it is found that for stiffness proportional damping ratio ξ_β the range between 0.00% and 0.05% is a suitable interval in this simulation, in which a satisfactory result could be achieved in simulations and beyond which the simulation results may not be true. In fact, this is a special case, in which the oscillations are not very serious and could be removed by the numerical damping in implicit dynamic approaches even when damping ratio is set to 0.00%. On the other hand, in most cases, especially in Mode II fracture mode, it is impossible to set the lower limit of such an interval to 0.00%.

Furthermore, the presence of numerical damping in implicit dynamic approaches has been verified by Chen et al. (2015) with Figure 4.7.

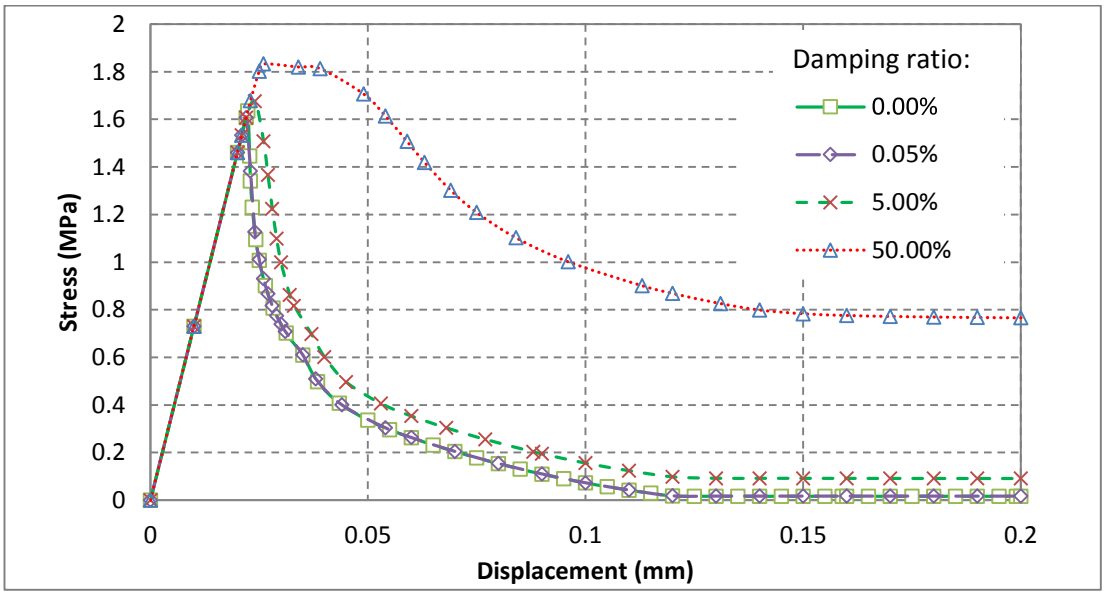

Figure 4.5 Effect of stiffness proportional damping ratio ξ_β on Mode I cracking

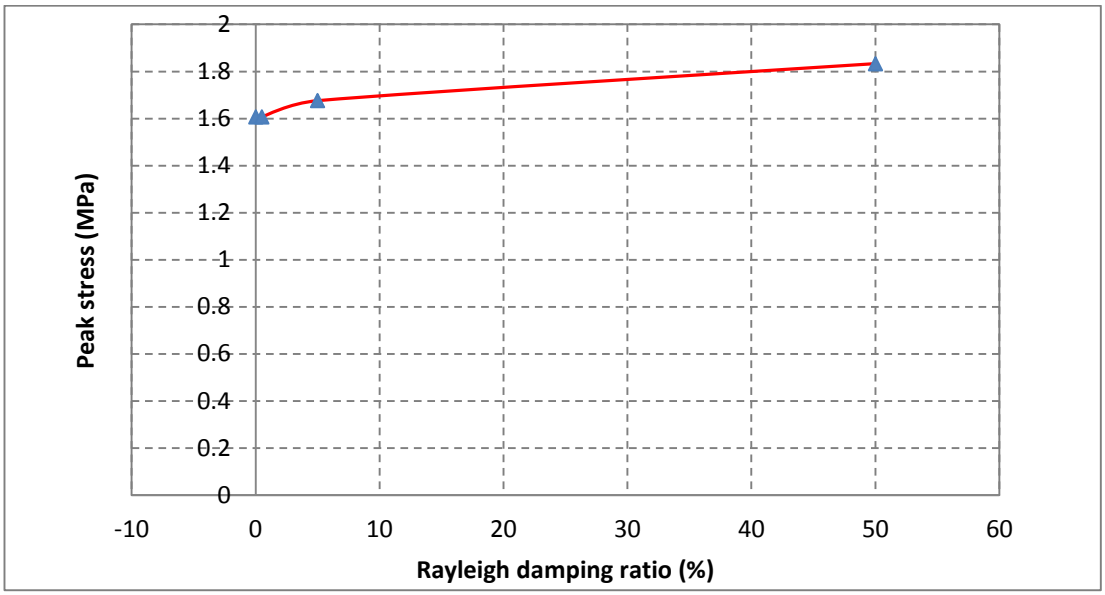

Figure 4.6 Variation of peak stress with stiffness proportional damping ratio ξ_β for Mode I cracking

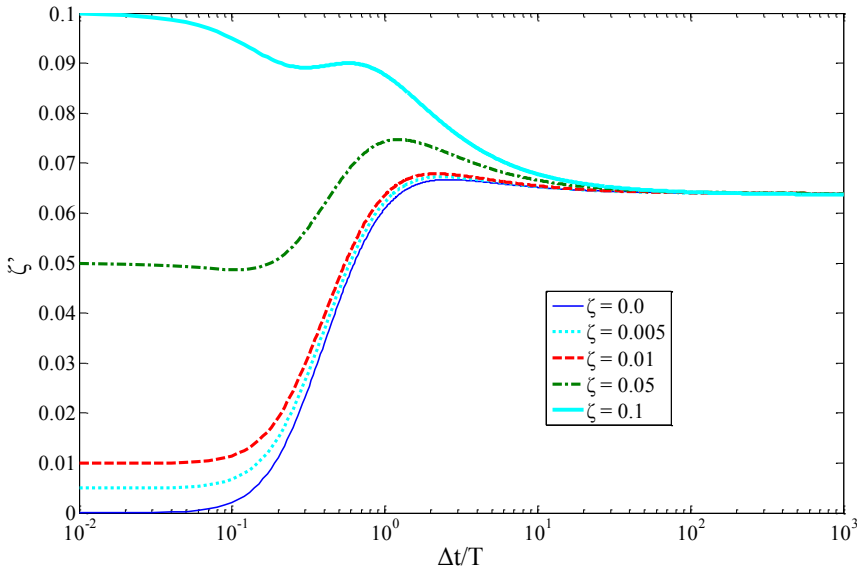

Figure 4.7 Algorithmic damping ratio ζ versus Δt/T for the HHT-α method from Chen et al. (2015)

In summary, in the element test under Mode I fracture mode, mass proportional Rayleigh damping ratio ξ_α has no negative effect on the ultimate result, whereas the

stiffness proportional damping coefficient ξ_β have its own safe interval, only within which a satisfactory result could be achieved in simulations.

4.2.3 Element tests under Mode II fracture mode

In this section, the same element bar as that in section 4.2.2 (i.e. the same dimensions and material properties, except for damping ratio) is employed but with a pure shear load (i.e. the loads under Mode II fracture mode) instead. Specifically, the element bar is constrained in the first direction at the two ends, while the top right side is pushed vertically with bottom left side constrained, as shown in Figure 4.8. Similarly, different values of mass and stiffness proportional damping coefficients are employed to investigate their effects on the ultimate load in the element test. They are calculated through Eq. (4.2) with the fundamental circular frequency of 8375 rad/s from their corresponding damping ratios ξ, which are shown in Table 4.2.

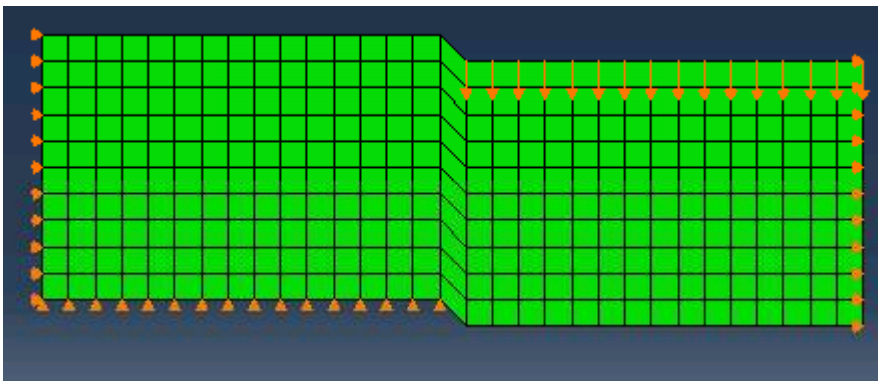

Figure 4.8 The boundary conditions of specimen under Mode II fracture mode (deformed shape)

Table 4.2 Values of mass and stiffness proportional damping coefficients and their corresponding damping ratios ξ

Damping ratio ξ	Mass proportional damping coefficient α	Stiffness proportional damping coefficient β
0.00%	0	0

0.05%	0.471	3.38×10^{-7}
0.50%	4.71	3.38×10^{-7}
5.00%	47.1	3.38×10^{-5}
50.00%	471	3.38×10^{-4}

Different values of mass proportional damping coefficient α in Table 4.2 are also employed alone to assign Rayleigh damping ratio ξ in the element test to investigate its effect on the results. The stress-displacement curves from the relevant results are shown in Figure 4.9 and variation of peak stress with mass proportional damping ratio ξ_α under Mode II fracture mode is plotted in Figure 4.10. It is found that stress-displacement curves are almost the same (including the peak stress and stiffness), except that oscillations are generated in all the cases when the stress in the element bar is dropping to zero. The failure of oscillation removal indicates that mass proportional damping ratio ξ_α is really not able to damp high frequency vibrations, as implied in Figure 4.1. Even so, the simulation in this case is still converged because of the presence of the inherent numerical damping in HHT-α method (HILBER et al., 1977; ABAQUS, 2011; Chen et al., 2015).

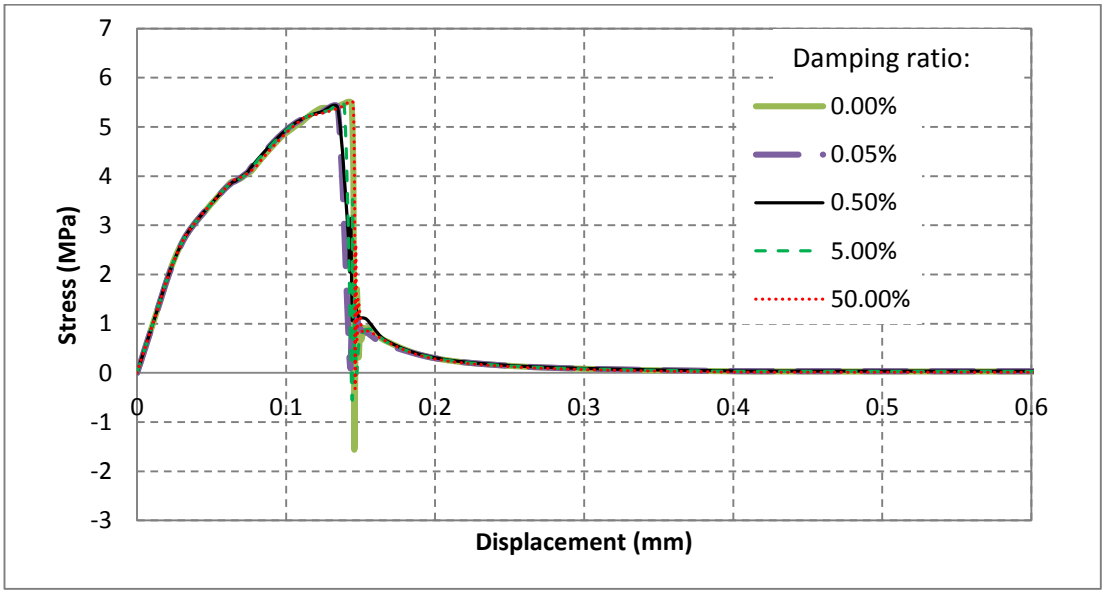

Figure 4.9 Effect of mass proportional damping ratio ξ_α on Mode II cracking

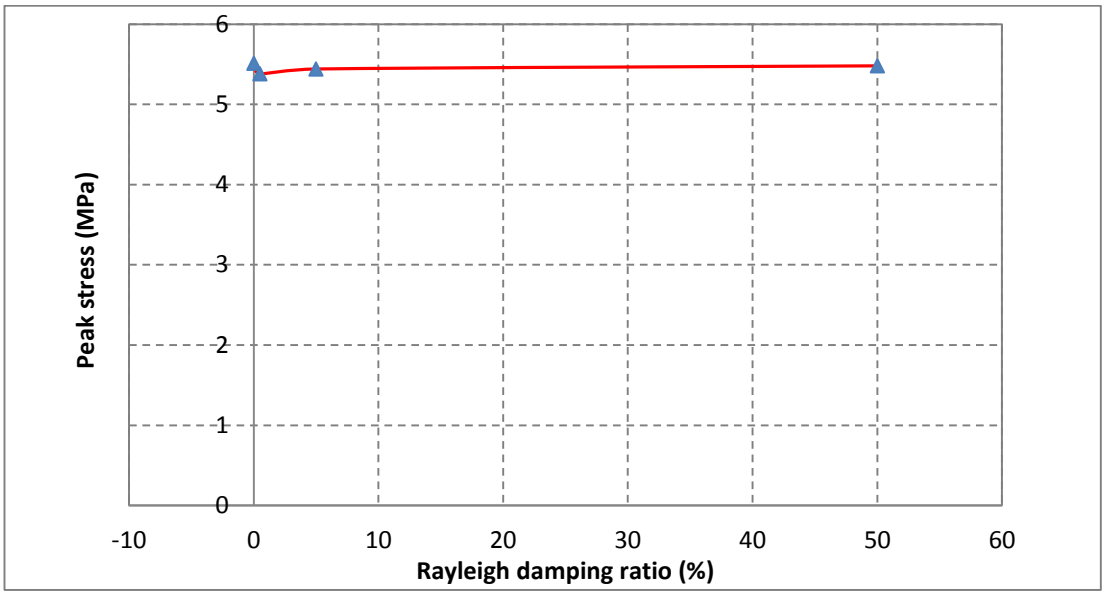

Figure 4.10 Variation of peak stress with mass proportional damping ratio ξ_α under Mode II fracture mode

Different values of stiffness proportional damping coefficient β in Table 4.2 are also employed alone to investigate its effect on the results in the element test under pure shear loads (i.e. Mode II loads). The stress-displacement curves from the results are shown in Figure 4.11 and variation of peak stress with stiffness proportional damping ratio ξ_β under Mode II is plotted in Figure 4.12. It is found that the stress-displacement curve from the case without any damping ratio (i.e. which has also been used as the reference case in the investigation with mass damping ratio) is almost the same as that from the cases with damping ratio ξ_β lower than 5%. Amongst these cases the only difference lies in the position where the stress in the element bar is steeply dropping to zero. For the cases with damping ratio ξ_β of 0.00% and 0.05%, oscillations are observed whereas in the case with damping ratio ξ_β=0.50%, 5% and 50% no oscillation is observed. Amongst these three cases, there is no difference between the cases with damping ratio ξ_β of 0.50% and 5%, whereas the ultimate load increases with the value of damping ratio ξ_β between the cases with damping ratio ξ_β of 5% and 50%, as shown in Figure 4.12. Through the aforementioned analyses, it is found that a suitable interval for stiffness proportional Rayleigh damping ratio ξ_β is in the range between 0.50% and

5%, within which oscillations could be removed properly without sacrificing any accuracy.

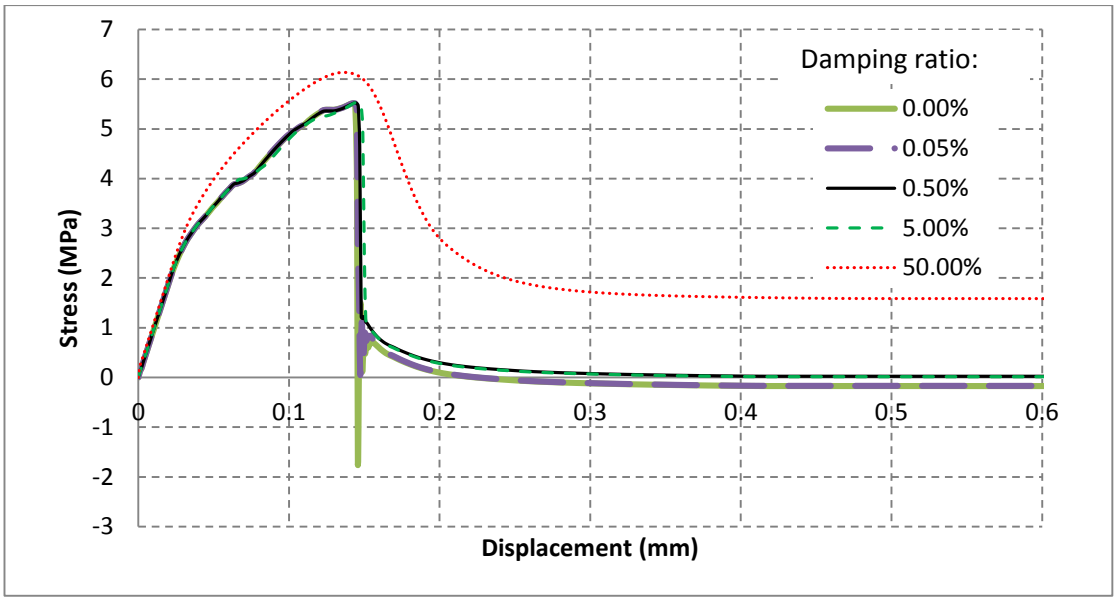

Figure 4.11 Effect of stiffness proportional damping ratio ξ_β on Mode II cracking

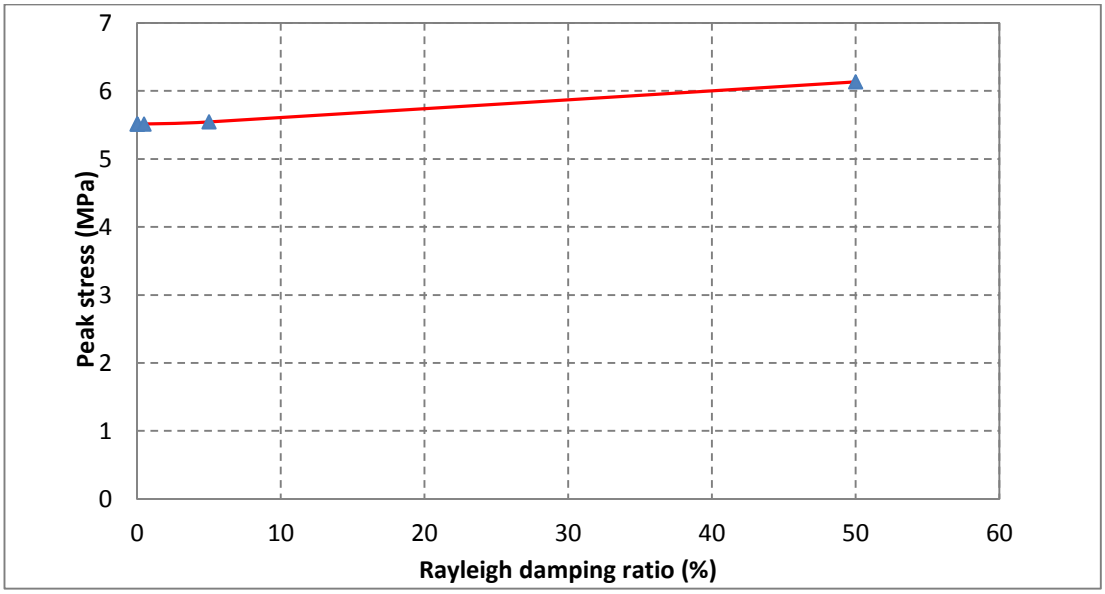

Figure 4.12 Variation of peak stress with stiffness proportional damping ratio ξ_β under Mode II fracture mode

In summary, through the investigation in this subsection, it is found that setting of stiffness proportional damping ratio ξ_β is essential to regularise unstable behaviour (i.e. oscillations in load-displacement curves) for simulations loaded under Mode II fracture mode using dynamic approaches, although it is a little bit complicated and labouring to find out a safe interval, as mentioned earlier.

4.3 Effect of Rayleigh damping in simulations of FRP-concrete bonded interface

In simulations of FRP-concrete bonded interface, the dynamic effect could be categorised into two kinds: a) oscillations generated before the element is completely softened; b) the jagged shapes in the load-displacement curves arising from concrete cracking. The former one is the one that has been discussed in Section 4.2 and does not exist in physical test; by contrast, the latter one is the one that could also be observed in physical test. In view of that, in a reasonable simulation of FRP-concrete bonded interface, the former one is required to be removed while the latter one to be retained.

In this section, investigation of the effect of Rayleigh damping ratio ξ includes two parts, namely mass and stiffness proportional damping ratio. In each part, different values damping ratio ξ are employed to investigate their effects on the mechanical behaviour of FRP-concrete bonded interface with reference to Specimen III-1 from Yao et al. (2005), as an example of debonding failure mode, and Specimen III-6 from Yao et al. (2005), as an example of CPF failure mode. In the simulations of the reference cases, the geometrical modelling and the assignment of material properties are the same as in Chapter 3. The only variation is Rayleigh damping ratio used.

4.3.1 Effect of mass proportional damping

The effect of mass proportional damping ratio ξ_α is investigated in two ways, namely FRP-concrete bonded interface with debonding and CPF failure modes.

1. Debonding failure mode

With reference to Specimen III-1 from Yao et al. (2005), different values of mass proportional damping ratio ξ_α are used to investigate its effect on the mechanical behaviour in simulations. The value of mass proportional damping ratio ξ_α varies from 0.0005% to 50% at a multiple of 10.

With the fundamental frequency of 9978 rad/s in this reference case, through Eq. (4.2) the values of mass proportional coefficient α are calculated from the desired values of damping ratio ξ_α, as shown in Table 4.3. Subsequently, these values are used alone to assign Rayleigh damping ratio ξ in the simulations of this reference case.

The load-displacement curves extracted from these simulation results are shown in Figure 4.13. As shown in the damage scale in Figure 4.15, the red colour stands for completely damaged state (i.e. cracks in physical tests) while blue colour does for undamaged state in concrete. This damage scale is applicable to damage contours in the whole thesis. Thus, it is found that FRP is not completely debonded as shown in Figure 4.14 due to convergence issues, although the ultimate load in these cases (i.e. around 5.62 kN) is found to be close to that from the test data (5.94kN), with an error of 5%.

Through this investigation, it is also found that mass proportional damping ratio ξ_α is not able to eliminate negative effects induced by dynamic loads in simulations of FRP-concrete bonded interface, although in the early loading stage the simulation is still converged due to the presence of the inherent damping system in HHT-α method (HILBER et al., 1977; ABAQUS, 2011; Chen et al., 2015).

Table 4.3 The values of mass proportional damping coefficient α and its corresponding damping ratio ξ_α for Specimen III-1

Mass proportional damping coefficient ξ_α	0.0005%	0.005%	0.05%	0.5%	5%	50%

Mass proportional damping coefficient α	0.0998	0.998	9.98	99.8	998	9980

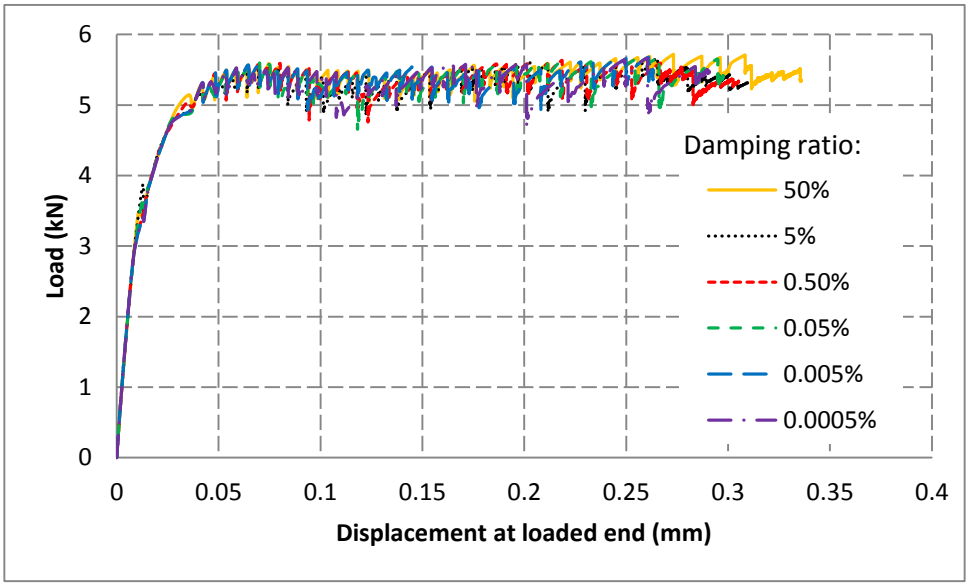

Figure 4.13 Effect of mass proportional damping ratio ξ_α on debonding failure mode of FRP-concrete bonded interface

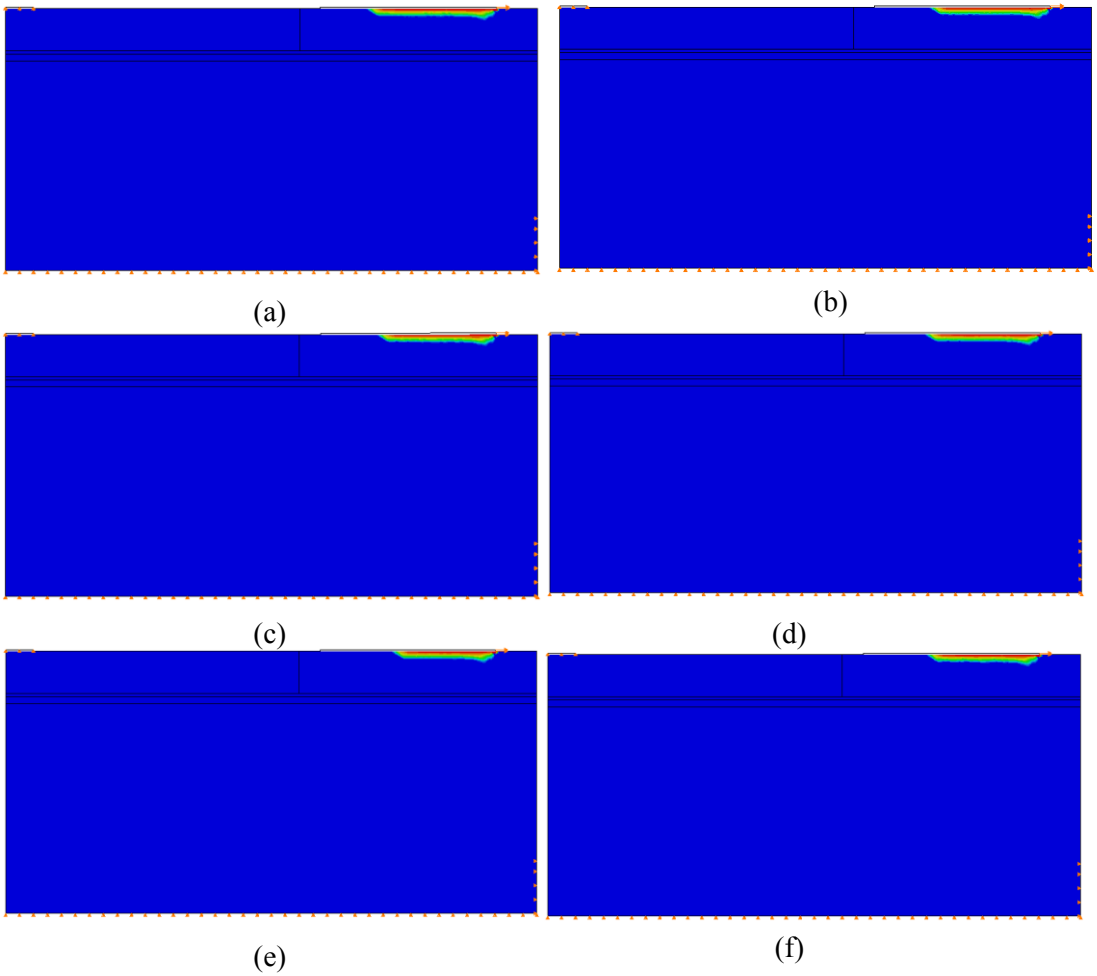

Figure 4.14 Damage contours of Specimen III-1 with mass proportional damping ratio ξ_α set to a value of (a) 50%, (b) 5%, (c) 0.5%, (d) 0.05%, (e) 0.005%, and (f) 0.0005%

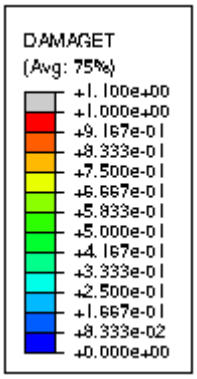

Figure 4.15 Damage scale in simulations of FRP-concrete bonded interface

2. CPF failure mode

With reference to Specimen III-6 from Yao et al. (2005), different values of mass proportional damping ratio ξ_α are used alone to investigate its effect on the mechanical behaviour in simulations of FRP-concrete bonded interface. The value of mass proportional damping ratio ξ_α varies from 0.0005% to 50% at a multiple of 10.

With the fundamental frequency of 9973 rad/s in this reference case, the values of mass proportional coefficient α are obtained from the desired values of damping ratio ξ_α through Eq. (4.2), as shown in Table 4.4. Subsequently, these values are used to assign Rayleigh damping ratio ξ in the simulations of this reference case. The load-displacement curves from these simulation results are shown in Figure 4.16. It is also found that in the later loading stage there are very evident oscillations in load-displacement curves from these simulation results, no matter how much mass proportional damping ratio ξ_α is used in these simulations. Even so, in the early loading stage the simulation is still converged due to the presence of the inherent damping system in HHT-α method (HILBER et al., 1977; ABAQUS, 2011; Chen et al., 2015). In addition, the damage failure mode is observed very vague due to failure of oscillation removals, as shown in Figure 4.17. Through this investigation, it is also found that mass proportional damping ratio ξ_α is not able to eliminate negative effects induced by dynamic loads in simulations of FRP-concrete bonded interface with CPF failure mode.

Table 4.4 The values of mass proportional damping coefficient α and its corresponding damping ratio ξ_α for Specimen III-6

Mass proportional damping ratio ξ_α	0.0005%	0.005%	0.05%	0.5%	5%	50%
Mass proportional damping coefficient α	0.0997	0.997	9.97	99.7	997	9970

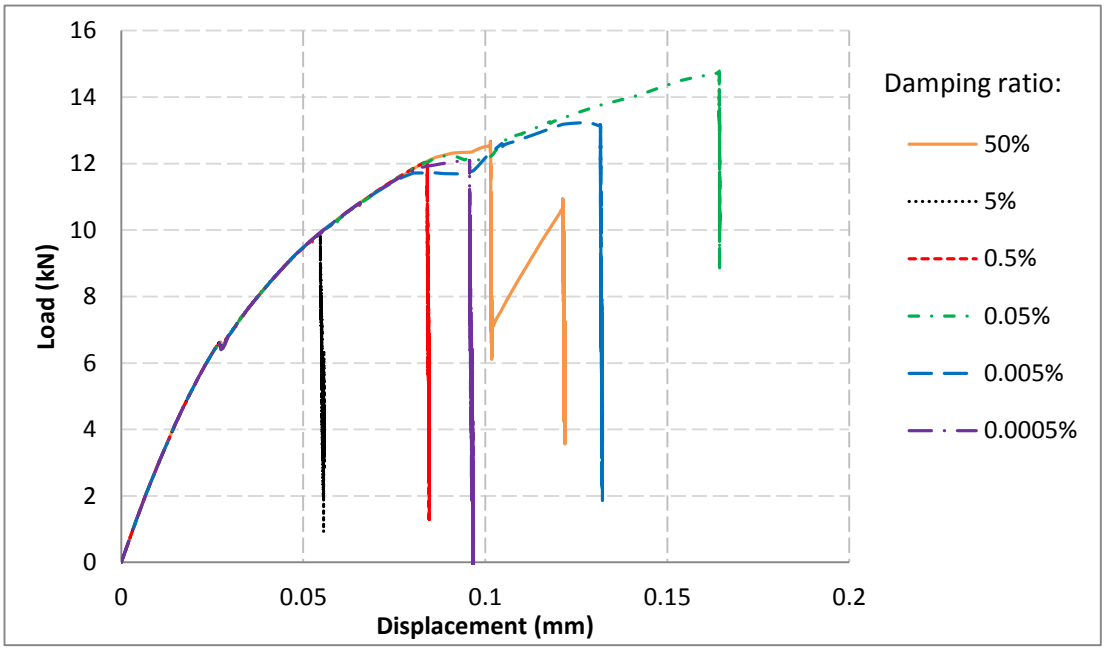

Figure 4.16 Effect of mass proportional damping ratio ξ_α in the simulation of Specimen III-6 from Yao et al. (2005)

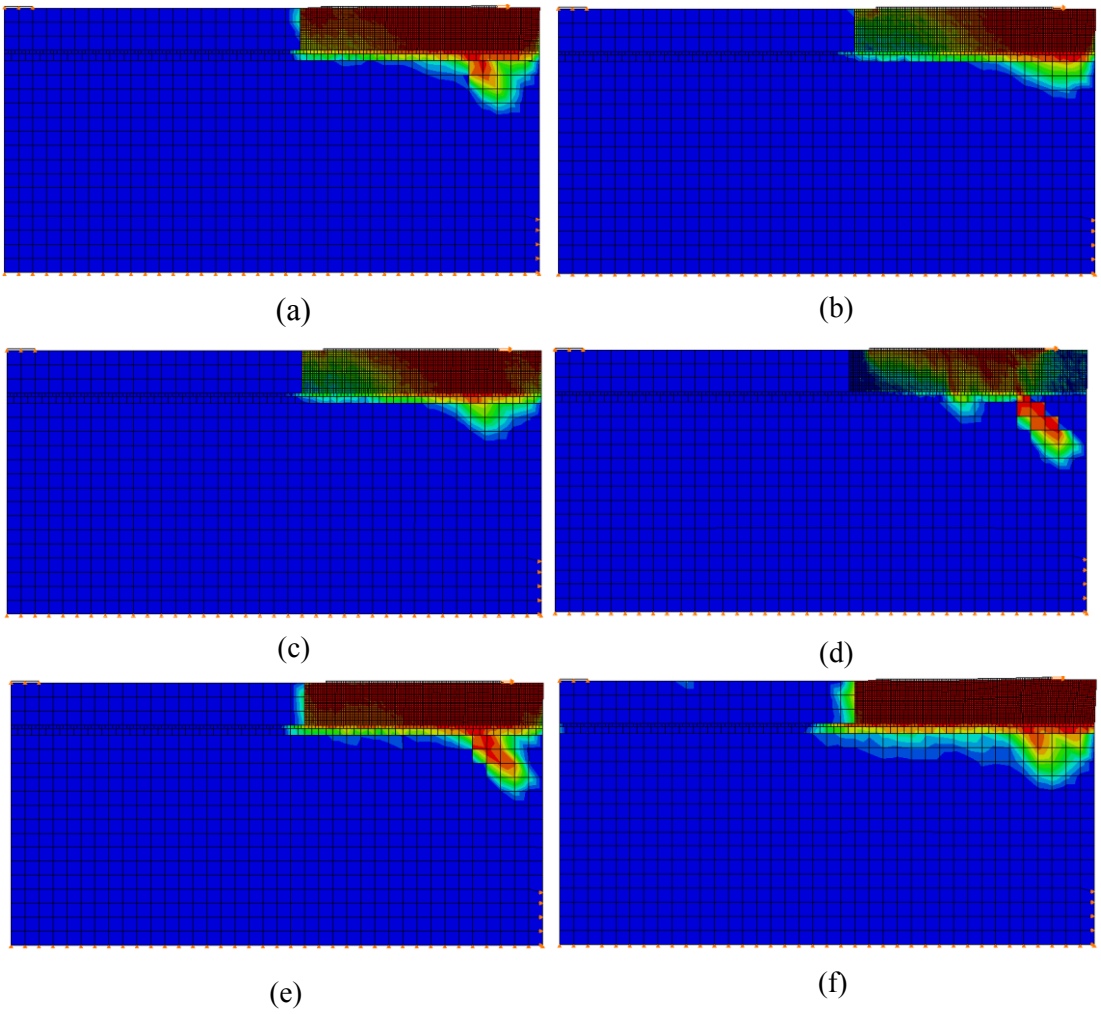

Figure 4.17 Damage contours of Specimen III-6 with mass proportional Rayleigh damping ratio ξ_α set to a value of (a) 50%, (b) 5%, (c) 0.5%, (d) 0.05%, (e) 0.005%, and (f) 0.0005%

4.3.2 Effect of stiffness proportional damping

The effect of stiffness proportional damping ratio ξ_β is investigated in two ways, namely FRP-concrete bonded interface with debonding and CPF failure mode.

1. Debonding failure mode

With reference to Specimen III-1 from Yao et al. (2005), different values of stiffness proportional damping ratio ξ_β are used to investigate its effect on the mechanical

behaviour in simulations. The value of stiffness proportional damping ratio ξ_β varies from 0.0005% to 50% at a multiple of 10.

With the fundamental frequency of 9978 rad/s in this reference case, through Eq. (4.2) the values of stiffness proportional coefficient β are calculated from the desired values of damping ratio ξ_β, as shown in Table 4.5. Subsequently, these values are used to assign Rayleigh damping ratio ξ in the simulations of this reference case.

The load-displacement curves from these simulation results are shown in Figure 4.18, and their damage contours are shown in Figure 4.19. It is found that there is very little or no differences in terms of load-displacement curves between the cases with different values of damping ratio ξ_β in the range of 0.005% to 0.5%. However, the ultimate load in the other cases with damping ratio ξ_β in range between 5% and 50% is shown significantly higher than that in the other cases; furthermore, the jagged shapes, which indicate that FRP debonding behaviour, have completely disappeared. On the other hand, the difficulty of convergence is also experienced when stiffness proportional damping ratio ξ_β is set lower than a value of 0.0005%, a phenomenon that is similar to that in the cases with mass proportional damping ratio ξ_α set alone in the Section 4.3.1. Even so, in the early loading stage the simulation is still getting converged due to the presence of the inherent damping system in HHT-α method (HILBER et al., 1977; ABAQUS, 2011; Chen et al., 2015). Therefore, the FRP is partially debonded from concrete, as shown in Figure 4.19 (f). Of course, in the other cases (see Figure 5.19 (a), (b), (c), (d) and (e)) it is found that the FRP is debonded from concrete prism, a damage contour that conforms to that observed in physical tests.

In addition, the ultimate load (i.e. around 5.67 kN) from the cases with stiffness proportional damping between 0.005% and 0.5% is found to be very close to that from the test data (i.e. around 5.94kN), with an error of 5%. In view of that, the range between 0.005% and 0.5% is a safe interval for the stiffness proportional damping ratio ξ_β in the simulations of Specimen III-1 from Yao et al. (2005).

Table 4.5 The values of stiffness proportional damping coefficient β and its corresponding damping ratio ξ_β for Specimen III-1

Stiffness proportional damping ratio ξ_β	0.0005%	0.005%	0.05%	0.5%	5%	50%
Stiffness proportional damping coefficient β	1×10^{-9}	1×10^{-8}	1×10^{-7}	1×10^{-6}	1×10^{-5}	1×10^{-4}

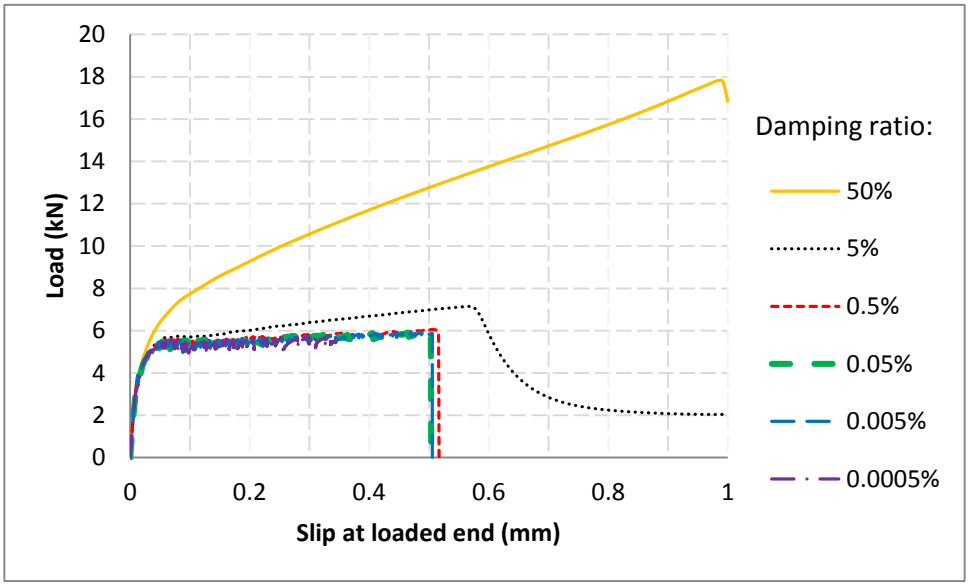

Figure 4.18 Effect of stiffness proportional damping ratio ξ_β in simulation of Specimen III-1

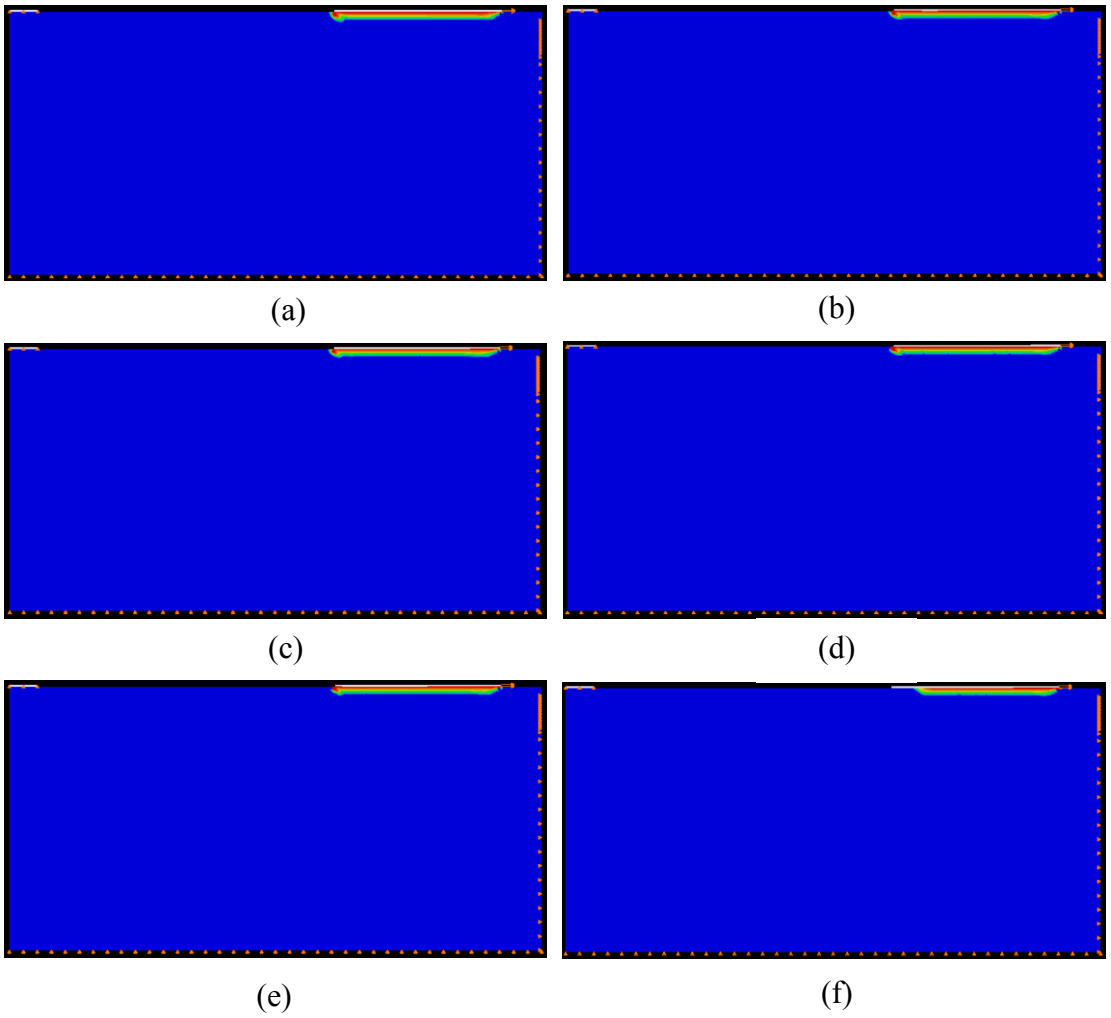

Figure 4.19 Damage contours of Specimen III-1 with stiffness proportional damping ratio ξ_β set to a value of (a) 50%, (b) 5%, (c) 0.5%, (d) 0.05%, (e) 0.005%, and (f) 0.0005%

2. CPF failure mode

With reference to Specimen III-6 from Yao et al. (2005), different values of stiffness proportional damping ratio ξ_β are used to investigate its effect on the mechanical behaviour in simulations. The value of stiffness proportional damping ratio ξ_β varies from 0.0005% to 50% at a multiple of 10.

With the fundamental frequency of 9973 rad/s in this reference case, through Eq. (4.2) the values of stiffness proportional damping coefficient β are calculated from the

desired different values of damping ratio ξ_β, as shown in Table 4.6. Subsequently, these values are used alone to assign Rayleigh damping ratio ξ in the simulations of this reference case.

Eventually, the load-displacement curves from these simulation results are shown in Figure 4.20, and their damage contours are shown in Figure 4.21. It is found that there are very few or even no differences in terms of load-displacement curves amongst the cases with different values of damping ratio ξ_β in the range of 0.05% to 5% (i.e. which means that the mechanical behaviour is converged in this range). However, it is found that the ultimate load in the case with damping ratio of 50% is much higher than that in the other cases. Furthermore, the difficulty of convergence is also found when the damping ratio ξ_β is lower than a value of 0.005%, even though in the early loading stage the simulation is still converged due to the presence of the inherent damping system in HHT-α method (HILBER et al., 1977; ABAQUS, 2011; Chen et al., 2015). It is for this reason that the FRP is only partially debonded from concrete part, as shown in Figure 4.21 (e), whereas in Figure 4.21 (f) it is found that under-damping in stiffness proportional damping leads to a more serious situation that the damage contour in the damage area has become vague. Of course, in the other cases (see Figure 4.21 (a), (b), (c) and (d)) it is found that concrete prism is cracked beyond FRP free end, a damage contour that conforms to that observed in physical tests.

In addition, the ultimate load (i.e. around 16.37 kN) from the cases with stiffness proportional damping ratio ξ_β between 0.05% and 5% is found to be close to that from its corresponding test data (i.e. around 15.75 kN), with an error of 4%. In view of that, the range between 0.05% and 5% is a safe interval for stiffness proportional damping ratio ξ_β in simulations of Specimen III-6 from Yao et al. (2005).

Table 4.6 The values of stiffness proportional damping coefficient β and its corresponding damping ratio ξ_β for Specimen III-6

Stiffness proportional damping ratio ξ_β	0.0005%	0.005%	0.05%	0.5%	5%	50%

Stiffness proportional damping coefficients β	1×10^{-9}	1×10^{-8}	1×10^{-7}	1×10^{-6}	1×10^{-5}	1×10^{-4}

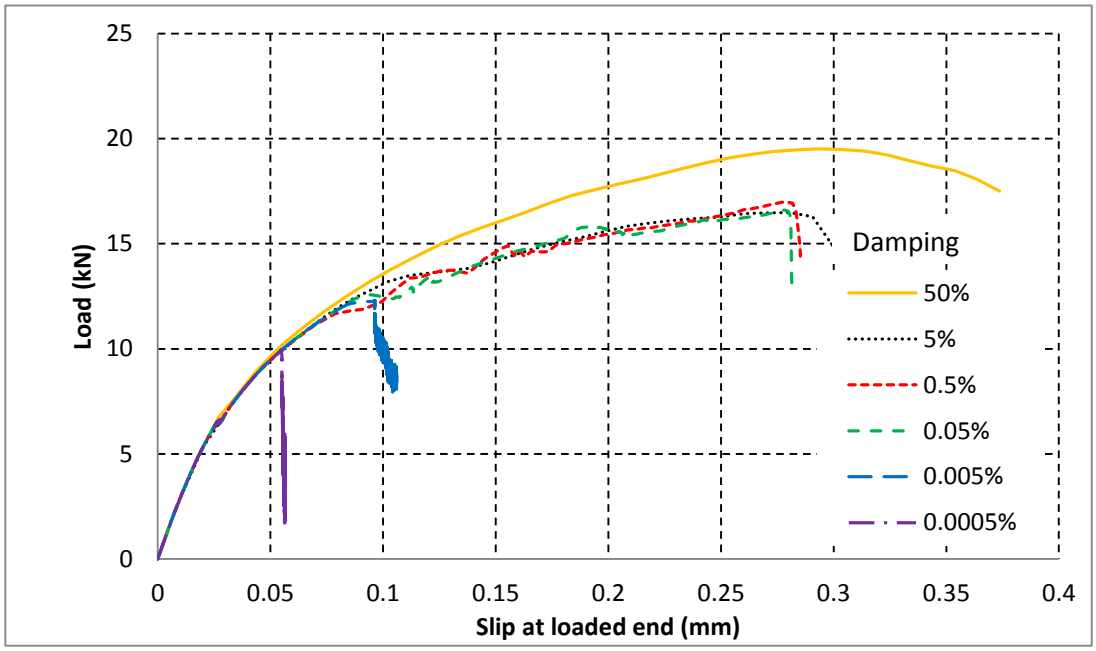

Figure 4.20 Effect of stiffness proportional damping ratio ξ_β in simulation of Specimen III-6

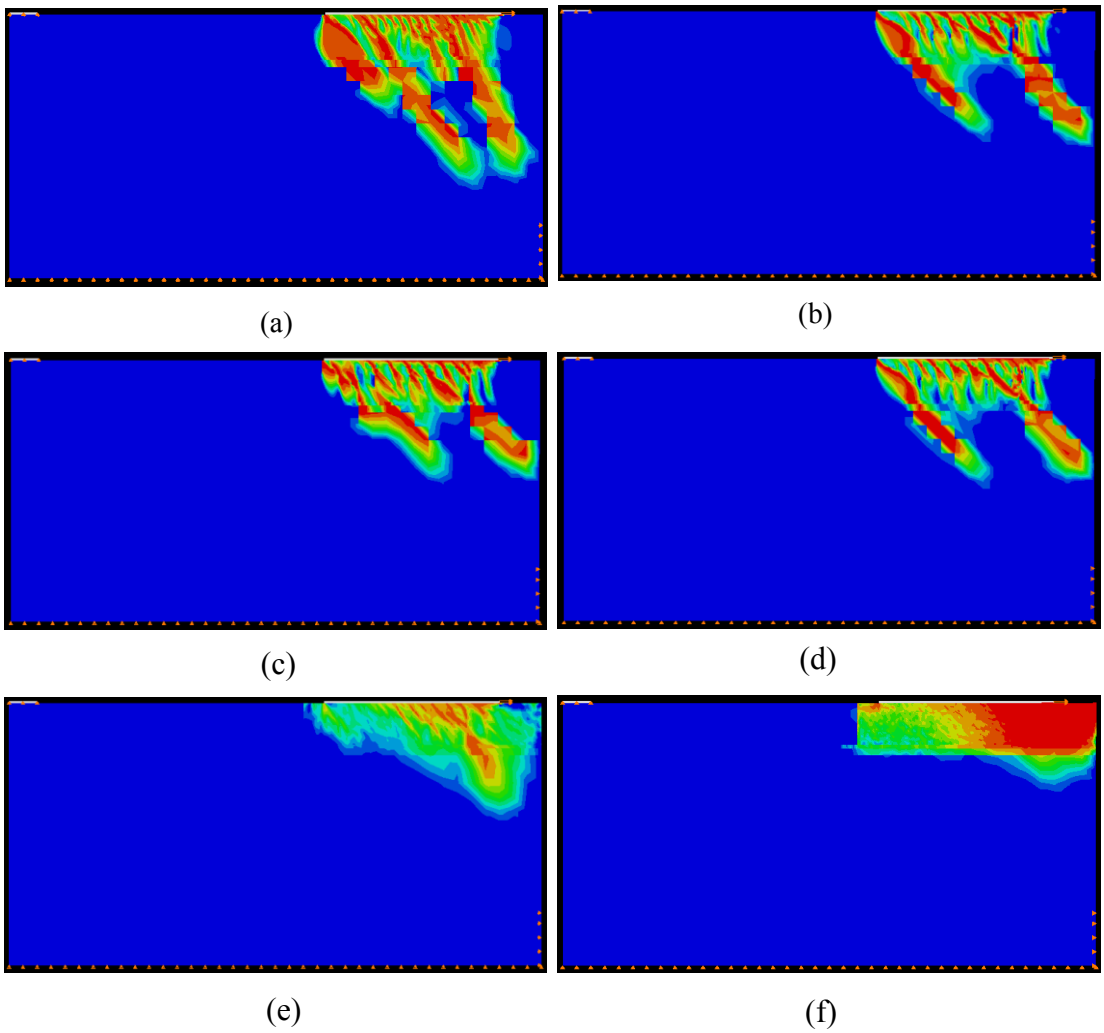

Figure 4.21 Damage contours of Specimen III-6 with stiffness proportional Rayleigh damping ratio ξ_β set to a value of (a) 50%, (b) 5%, (c) 0.5%, (d) 0.05%, (e) 0.005%, and (f) 0.0005%

4.4 Discussions

The equilibrium employed in simulations with dynamic approaches is given as

$$M\ddot{q}(t) + C\dot{q}(t) + Kq(t) = F \tag{4.3}$$

where, M, C, and K are mass, damping and stiffness matrices respectively, along with their corresponding acceleration $\ddot{q}(t)$, velocity $\dot{q}(t)$, displacement $q(t)$ and force F.

Accordingly, $M\ddot{q}(t)$ is the inertia force and $C\dot{q}(t)$ is the damping force. In such an analysis, both considerable energy dissipation and inertia effect are only used to provide stability to regularise and improve convergence behaviour to obtain an essentially static solution (ABAQUS 2011).

By contrast, the equilibrium employed in simulations with static approaches is given as

$$Kq(t) = F \tag{4.4}$$

Through comparisons between Eqs. (4.3) and (4.4), it is found that some errors may be introduced into simulations with dynamic approaches, due to the presence of inertia force $M\ddot{q}(t)$ and damping force $C\dot{q}(t)$. In this thesis a ramp loading type is recommended to be adopted in simulations, as introduced in Chapter 3, so the effect of inertia force $M\ddot{q}(t)$ on the accuracy could be ignored here, due to that the acceleration induced by external loads is almost equal to zero.

As stated in Section 4.2.1, damping force is comprised of the mass and stiffness proportional damping forces. In FE analysis (ABAQUS 2011), the mass proportional damping force is caused by absolute acceleration and given as

$$F = \alpha m a \tag{4.5}$$

where, m is the mass matrix in FE analysis, and a is the acceleration. In the previous studies, it has been shown that the value of mass proportional damping coefficient α has no effect on the mechanical behaviour. However, it is not effective for structures under Mode II or a Mode II-dominated loads, whose response frequency is dominated by higher frequency vibrations. In such simulations, mass proportional damping ratio ξ_α is not capable to remove the oscillations induced by dynamic loads. The element test under Mode II fracture mode and FRP-concrete bonded interfacial simulations are the examples for such a case (see Figure 4.9, Figure 4.13 and Figure 4.16). Even so, in the early loading stage of these cases, the simulation result is still in a satisfactory level, especially in the element test under Mode II fracture mode. That is because implicit dynamic method (HHT-α method) itself provides some degrees of damping, which

could automatically damp out high frequency response as stated in Chen et al. (2015) although they could not make it completely in these cases. Besides, the success of the simulations of element test under Mode I and Mode II fracture modes with zero damping ratio could be also attributed to the presence of the inherent numerical damping in implicit dynamic method (HHT-α method).

The stiffness proportional damping stress σ_{d} is related to the strain rate $\dot{\varepsilon}$ through

$$\sigma_{\mathrm{d}} = \beta D^{\mathrm{el}} \dot{\varepsilon} \tag{4.6}$$

where, $\dot{\varepsilon}$ is the strain rate and D^{el} is defined as an elastic stiffness matrix in the strain-free state in FE analysis. In stiffness proportional Rayleigh damping system, the elastic stiffness matrix in the strain-free state is used to replace the stiffness matrix in the damaging process of concrete to avoid the cases that the tangent stiffness matrix may have negative eigenvalues, which would imply negative damping (i.e. this is not possible in physical sense). However, the use of such an elastic stiffness matrix in severe damage state may make some significant negative effects on accuracy of simulation results, a phenomenon that has also been confirmed in Sections 4.2 and 4.3. Specifically, the element test under Mode II fracture mode with damping ratios of 5%, and 50% (see Figure 4.5), FRP-concrete bonded interfacial simulations with damping ratio of 5% and 50% for debonding failure mode (see Figure 4.18) and with damping ratio 50% for CPF failure mode (see Figure 4.20) are all the examples of such a case. Furthermore, the jagged shapes in these cases, arising from the stress releasing in the debonding process at FRP-concrete bonded interface, have also completely disappeared, a phenomenon that mismatches that observed in physical tests.

Another less attractive feature of stiffness proportional Rayleigh damping system (Serway and Jewett 2005) is that its damping ratio decreases with the decrease of response frequency (as shown in Figure 4.1), a frequency that decreases with the cracking propagation of the model, as indicated in

$$\omega = \sqrt{\frac{k}{m}} \tag{4.7}$$

where, m is the mass of object and k is the spring stiffness. This feature requires users to set the stiffness proportional damping coefficient β to a larger value to satisfy the requirement of model when crack is propagated in simulations. The issue is also observed in the simulation of FRP-concrete bonded interface with CPF failure mode. Specifically, in the damage process a large volume of concrete is torn off as shown in Figure 4.21 (d), a phenomenon that makes the mass of the already debonded FRP becomes larger and makes the frequency become smaller, as indicated in Eq. (4.7). It is for this reason that stiffness proportional damping ratio ξ_β in the CPF case requires a magnitude order larger than that in debonding case, when the frequencies of them are almost the same, like the cases with debonding and CPF failure modes in Section 4.3.2.

Of course, a much lower value in the stiffness proportional damping ratio is not effective to remove oscillations in simulations. The element test under Mode II fracture mode with damping ratio of 0.05% and 0.00%, FRP-concrete bonded interfacial simulations with damping ratio of 0.0005% for debonding failure mode and with damping ratio 0.005% and 0.0005% for CPF failure mode are all the examples of such a case. Apart from that, the issues arising from under-damping of high frequency response in simulations of FRP-concrete bonded interface are more serious than that in element test under Mode II fracture mode. Specifically, in simulations of FRP-concrete bonded interface with debonding failure mode, the convergence issues are experienced (see the curve from the case with damping ratio of 0.0005% in Figure 4.18 and damage contour in Figure 4.19 (f)). By contrast, in simulations of FRP-concrete bonded interface with CPF failure mode, not only convergence issues are experienced (see the curve from the case with damping ratio of 0.0005% Figure 4.20), but also damage contour are seen vague (see Figure 4.21 (f)).

In view of that, it is found that stiffness proportional damping coefficient β plays a delicate but pivotal role in such simulations but is essential to set to damp higher frequency response. It is for this reason that a safe interval for stiffness proportional damping ratio ξ_β is needed in simulations to avoid the aforementioned issues induced by both over-damping and under-damping of high frequency response. Specifically,

for FRP-concrete bonded interface with debonding failure mode the range between 0.5% and 0.005% is the safe interval for stiffness proportional damping ratio ξ_β, whereas for FRP-concrete interface with CPF failure mode the range between 5% and 0.05% is the safe interval.

Moreover, it is also found that the issues arising from dynamic loads in the element test under Mode II fracture mode are generally not as serious as that in simulations of FRP-concrete bonded interface. Specifically, in element test oscillations in the load-displacement curves are observed only when the element nearly loses its capacity (i.e. the stress in the element is steeply dropping to zero), as shown in Figure 4.9. Thus, the occurrence of such oscillations has no effect on the ultimate load in simulations so it has long been neglected, although it may have been observed in some simulations of traditional structural components. On the other hand, in simulations of FRP-concrete bonded interface oscillations are observed in the loading plateau of load-displacement curves (see Figure 4.18) or when the loading is increasing (see Figure 4.20) so they may directly affect the success of simulations. That is because FRP-concrete bonded interface is not wholy involved in the debonding behaviour when FRP is long enough. On the contrary, the whole load is only resisted by a part of the interface, which is called effective length (Chen and Teng 2001; Ben Ouezdou et al. 2009). When the entire load is taken to a certain level, localised debonding occurs, a phenomenon that makes the active zone shift to another new zone. At this time point, in the old zone some oscillations may be generated because the stress in this zone is dropping to zero, whereas in the new zone the stress is still increasing. Therefore, oscillations affect the value of the ultimate load in simulations of FRP-concrete bonded interface to a greater degree than that in element tests under Mode II fracture mode.

In addition, it has also been found that response frequency of structure is highly connected to its loading modes and constraints, and determines which term in Rayleigh damping should be used in simulations loaded with dynamic approaches.

4.5 Conclusions

In this chapter, the effect of Rayleigh damping ratio is investigated through different values of mass and stiffness proportional ratios with reference to an element bar loaded under Mode I and Mode II fracture modes and Specimens III-1 and III-6 from Yao et al. (2005).

Through the relevant investigations, it is found that the mass proportional damping ratio has no negative effect in simulations, whereas the stiffness proportional damping ratio has some negative effects on in simulations. Specifically, the accuracy of the result may be affected when the damping ratio is larger than this safe range, on the other hand it is not effective when the damping ratio is smaller than this safe interval. However, only the stiffness proportional damping ratio is capable of removing the oscillations occurring in the models with high frequency response.

Furthermore, in the element test with Mode I fracture mode no vibration is observed, whereas in the element test with Mode II fracture mode there are some oscillations when stress is dropping to zero. By contrast, such oscillations lead to more serious effect in simulations of FRP-concrete bonded interface. Specifically, if the value of the stiffness proportional damping ratio ξ_β is lower than the minimum value in its safe interval, it is so difficult to converge that the FRP is only partially torn off concrete part. Of course, the ultimate load in simulation result is shown larger than it should be when the damping ratio is larger than the maximum value of the safe interval, similar to that in element test under both Mode I and Mode II fracture modes. In addition, in simulations of FRP-concrete bonded interface, the unreasonably large value in stiffness proportional Rayleigh damping ratio ξ_β leads to the disappearance of the jagged shapes in global load-displacement curves, generated in the process of FRP debonding.

In view of that, a procedure is recommended to find out a safe interval for the stiffness proportional damping ratio ξ_β to accurately simulate the debonding behaviour at FRP-concrete bonded interface and avoid the aforementioned issues induced by both over-

damping and under-damping of high frequency response. These procedures will be used in the subsequent simulations of FRP-concrete bonded interface, if its stiffness proportional damping coefficient β needs to be determined.

Specifically, the procedure is stated as follows:

1. Identify the fundamental circular frequency of the model with its own boundary conditions;
2. Calculate β value for the desired damping ratio ξ_β, which varies from 0.0005% to 50% with a multiple of 10;
3. Use these obtained values alone to assign Rayleigh damping ratio ξ_β respectively in different simulations;
4. Run these simulations with different Rayleigh damping ratios ξ_β, and then extract the load-displacement curves from these simulations when the computation is accomplished;
5. Collect together the curves and then pick out the curves that share the similar results, amongst which the minimum and maximum damping ratio ξ_β form the safe interval for stiffness proportional damping ratio ξ_β. Any value in this interval is capable of removing the noises induced by dynamic effect without sacrificing any accuracy in simulations.

In summary, the above procedure will help researchers avoid these over-damping and under-damping issues in simulations with high frequency responses, although it is a little bit laborious and time-consuming. In view of that, these procedures will be used in subsequent simulations in this thesis, if their stiffness proportional damping coefficient β needs to be determined.

Chapter 5
A critical evaluation of concrete damage models

5.1 Introduction

Concrete, as a kind of composite material, is made of cement, mortar and aggregates, so it contains numerous micro-cracks even before the application of any external loads. These inherent micro-cracks mainly exist at the aggregate-cement interface, due to shrinkage and thermal expansion in the cement paste and aggregates. Damage in concrete is primarily caused by the propagation and coalescence of these micro-cracks. The growth of these micro-cracks during loading causes reduction in both strength and stiffness. Therefore, it is essential to consider crack initiation and propagation in the numerical analysis of specimen associated with concrete.

To model damage in concrete, a number of empirical models have been proposed (e.g. Brencich and Gambarotta (2001); Tao and Phillips (2005))； these present a reduction of stiffness in different ways. These models can be classified as either anisotropic damage models (e.g. Chaboche (1993); Chow and Wang (1988)) or isotropic damage models (e.g. Brencich and Gambarotta (2001); Tao and Phillips (2005)).

Anisotropic damage models make use of tensor damage variables, to present the damage behaviour of concrete under loading. In this approach, different levels of damage are associated with different directions. This has been done using a symmetric second-order tensor (Murakami 1983, 1988; Ortiz 1985), or fourth order damage tensor (Chaboche 1993; Chaboche et al. 1995). Obviously, it is very difficult to do comparison of damage-induced anisotropy to its corresponding experimental data, since there are very few 3D experimental facilities currently available to detect concrete damage level in different directions under loading (Taqieddin 2008). As a consequence, many researchers are resorting to simple isotropic damage models.

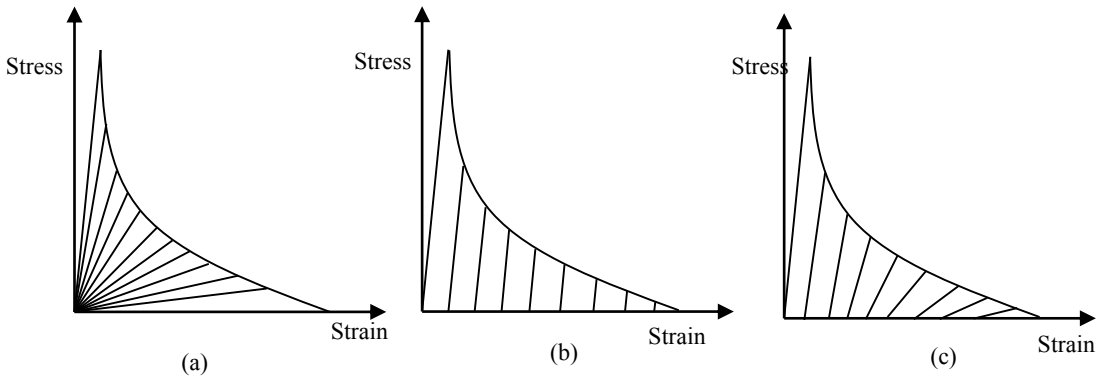

Figure 5.1 Unloading Response of (a) elastic damage, (b) elastic plastic, and (c) elastic plastic damage model

The isotropic damage models can be further categorised as shown in Figure 5.1. Figure 5.1 (a) shows exclusive damage model without plasticity wherein there is no real strain upon the loading. Figure 5.1 (b) shows entirely plastic model in which there is stiffness degradation and Figure 5.1 (c) is a combination of plasticity and damage. In the pure damage model all the unloading paths lead to the origin point. In the pure plasticity model, all the unloading paths are parallel with the initial loading path. In reality, concrete exhibits both damage and plasticity (e.g. Armero and Oller (2000); Lubliner (1989)). In view of this, the damaged plasticity model provides the appropriate theoretical framework. In the damaged plasticity model, as shown in Figure 5.1 (c), scalar damage variables are employed to describe the deteriorated stiffness behaviour of concrete while loading. The scalar damage variables are coupled with the plastic deformation in concrete constitutive formulations and they can be calibrated with the experimental results.

Damage states, such as tensile cracking and compressive failure, are employed to account for damage process in the concrete body. Isotropic damage models are incorporated using scalar damage variable. The simplest form is to include only a single damage variable for both tension and compression; other approaches make use of two separate variables to describe tensile and compressive damage. Obviously, the latter one is more reasonable.

In addition, damage models are often combined with plasticity for more accurate representation of material behaviour. Once again, a wide range of plasticity models are available for application in conjunction with damage. As discussed earlier in this study, the damaged plasticity model available in ABAQUS (2011) is employed.

In this chapter, eight empirical damage models are comprehensively reviewed using concrete damaged plasticity. These are used to compare damage states under cyclic loads. Both qualitative differences and comparison with physical experiments are considered.

Investigation is first conducted with single element tests to examine the constitutive response of different damage models. This is then followed by the simulations of debonding at FRP-concrete bonded interface with different damage models. Furthermore, different values of upper limit in damage model are employed to investigate the effect of the damage variable on the ultimate debonding load at FRP-concrete bonded interface.

5.2 Review of damage models

As discussed in introduction, the scalar damage approach is the most widely used to describe the degradation behaviour of concrete via stiffness reduction (Figure 5.2) due to simplicity of implementation and ease of calibration with experimental results.

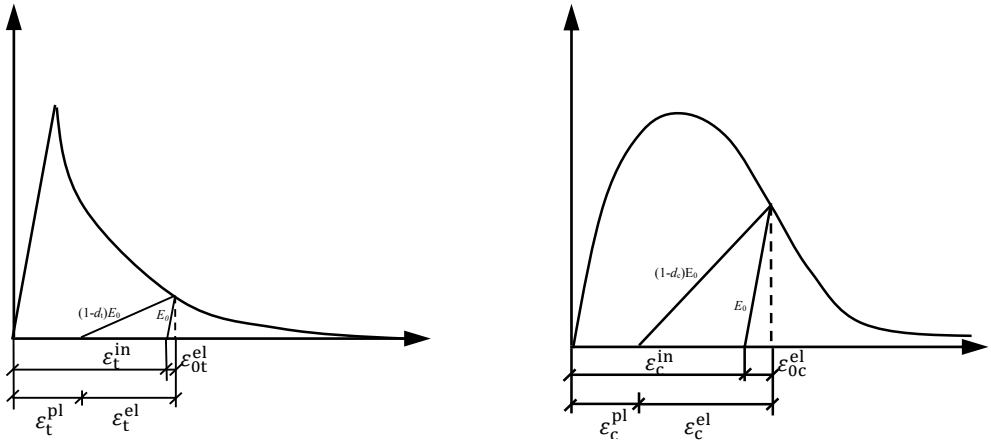

(a) Tension (b) Compression

Figure 5.2 Degradation behaviour of concrete via stiffness reduction

In the scalar damage approach, the stress is represented as

$$\sigma \stackrel{\text{def}}{=} (1 - d_x)\bar{\sigma} = (1 - d_x)D_0^{\text{el}}\colon\left(\varepsilon - \varepsilon^{\text{pl}}\right) \tag{5.1}$$

where, d_x is the scalar stiffness degradation variable (which can be d_c or d_t depending on the stress state), which can take the value in the range from zero (undamaged material) to one (fully damaged material). D_0^{el} is the initial (undamaged) elastic stiffness of the material. $\bar{\sigma}$ is the effective stress and ε and ε^{pl} are total strain and plastic strain respectively.

It can be hypothesised that different damage models may make significant differences in the terms of the mechanical behaviour in the numerical model, as effective stress $\bar{\sigma}$ is scaled down on the basis of damage variables, as shown in Eq. (5.1).

In the following paragraphs, eight different empirical formulae are considered. In these, E_c represents the elastic modulus of concrete. These models use uniaxial stress and strain terms to define damage. Damage formulation can be different in tension or compression. In the formulations that follow the subscript x has been used, which can be either c for compression or t for tension. σ_x is the uniaxial stress; ε_x is uniaxial strain; $\varepsilon_x^{\text{in}}$ is the inelastic strain; $\varepsilon_x^{\text{pl}}$ is the plastic strain; ε_x^0 is the strain at peak stress; ε_x^{u} is

the ultimate strain, beyond which the stress is assumed as zero; and f_x is the strength of concrete.

1. **Birtel and Mark's (2006) model**

The variation of damage is denoted by d_x which varies from zero (no damage) to one (complete damage). As per this model, d_x varies as

$$d_x = 1 - \frac{\sigma_x / E_c}{\varepsilon_x^{pl}(1/b_x - 1) + \sigma_x / E_c} \tag{5.2}$$

where, b_x is a parameter, indicating the ratio of plastic strain ε_x^{pl} to inelastic strain ε_x^{in} either under compression or tension. Eq. (5.2) can be rewritten as

$$d_x = \frac{\varepsilon_x^{in}(1 - b_x)}{\varepsilon_x^{in}(1 - b_x) + \sigma_x / E_c} \tag{5.3}$$

In Birtel and Mark (2006), b_x is typically taken as 0.7.

2. **Nechnech et al.'s (2002) model**

$$d_x = 1 - \exp(-c_x \varepsilon_x^{in}) \tag{5.4}$$

where, $c_x = \frac{\ln(1-\bar{D}_x)}{-\kappa_{xm}}$. In tension, $\bar{D}_t = 0.3$ and κ_{tm} is the strain corresponding to the stress of $f_t/2$. Likewise, in compression, $\bar{D}_c = 0.25$ and κ_{cm} is the hardening parameter at which the yielding stress f_c is at its maximum absolute value.

3. **Labadi and Hannachi's (2005) model**

$$d_x = 1 - \frac{\varepsilon_x^0}{\varepsilon_x^{in} + \varepsilon_x^0} \exp(-b_x \varepsilon_x^{in}) \tag{5.5}$$

where, $b_x = (\frac{g_f \rho_0 E}{f_x^2} - \frac{1}{2})^{-1}$. Here g_f is the strain energy in either compression or tension, ρ_0 is the specific mass of the specimen. In addition, d_x is defined in the strain interval $[\varepsilon_x^0, \infty]$. So at $\varepsilon_x = \varepsilon_x^0$, $d_x = 0$ (which means that the material remains undamaged until the peak stress is attained) and at $\varepsilon_x = \infty$, $d_x = 1$.

4. **Chen et al.'s (2012) model**

$$d_x = \frac{\varepsilon_x^{\mathrm{in}}}{(\varepsilon_x^{\mathrm{in}} + \sigma_x/E_{\mathrm{c}})} \tag{5.6}$$

It needs to be pointed out that this model is a purely damage mechanics model, since that plastic strain always remains zero

$$\varepsilon_x^{\mathrm{pl}} = \varepsilon_x^{\mathrm{in}} - \frac{d_x}{1-d_x} \cdot \frac{\sigma_x}{E_{\mathrm{c}}} = 0 \tag{5.7}$$

5. de Borst et al.'s (1995) model

This damage model is a linear model, in which damage factor increases linearly with inelastic strain in the strain interval $[\varepsilon_x^0, \varepsilon_x^{\mathrm{u}}]$.

$$d_x = \begin{cases} 0, & \text{if } \varepsilon_x \le \varepsilon_x^0 \\ \dfrac{\varepsilon_x^{\mathrm{u}}(\varepsilon_x - \varepsilon_x^0)}{\varepsilon_x(\varepsilon_x^{\mathrm{u}} - \varepsilon_x^0)}, & \text{if } \varepsilon_x^0 < \varepsilon_x < \varepsilon_x^{\mathrm{u}} \\ 1, & \text{if } \varepsilon_x^{\mathrm{u}} \le \varepsilon_x \end{cases} \tag{5.8}$$

6. Jirásek's (2004) model

This model is nonlinear in which damage factor increases nonlinearly with inelastic strain as

$$d_x = \begin{cases} 0, & \text{if } \varepsilon_x \le \varepsilon_x^0 \\ 1 - \dfrac{\varepsilon_x^0}{\varepsilon_x} \exp\left(-\dfrac{\varepsilon_x - \varepsilon_x^0}{\varepsilon_x^{\mathrm{u}} - \varepsilon_x^0}\right), & \text{if } \varepsilon_x^0 < \varepsilon_x < \varepsilon_x^{\mathrm{u}} \\ 1, & \text{if } \varepsilon_x^{\mathrm{u}} \le \varepsilon_x \end{cases} \tag{5.9}$$

7. Yu et al.'s (2010) model

The model proposed by Yu et al. (2010) is linear in which the damage factor increases linearly with decreasing post-peak stress in the interval $[\varepsilon_x^0, \infty]$.

$$d_x = \begin{cases} 0, & \text{if } \varepsilon_x \le \varepsilon_x^0 \\ 1 - \dfrac{\sigma_x}{f_x}, & \text{if } \varepsilon_x^0 < \varepsilon_x \end{cases} \tag{5.10}$$

8. Tao and Chen's (2014) model

Tao and Chen's (2014) model is a modification of the model proposed by Birtel and Mark (2006) with damage defined as

$$d_x = \begin{cases} \dfrac{\varepsilon_x^{\text{in}}(1-b_x)}{\varepsilon_x^{\text{in}}(1-b_x)+\sigma_x/E_c}, & \text{if } \dot{\bar{\varepsilon}}^{\text{p}} \geq 0 \\ \dfrac{\varepsilon_x^{\text{in}}-(\varepsilon_x-\bar{\varepsilon}_{x\text{r}}^{\text{e}})}{\varepsilon_x^{\text{in}}-(\varepsilon_x-\bar{\varepsilon}_{x\text{r}}^{\text{e}})+\sigma_x/E_c}, & \text{if } \dot{\bar{\varepsilon}}^{\text{p}} < 0 \end{cases} \tag{5.11}$$

Here $b_x = \sigma_x/f_x$, as in Yu model (Yu et al. 2010). The second formula in Eq. (5.11) is for situations when the plastic strain rate, $\dot{\bar{\varepsilon}}^{\text{p}}$, becomes negative. The term $\bar{\varepsilon}_{\text{cr}}^{\text{e}}$ is set as a constant with the value of the elastic strain when the situation starts to be happening (at $\dot{\bar{\varepsilon}}^{\text{p}} = 0$).

5.3 Comparison of empirical damage model with test data

In this section, the empirical scalar damage models are compared with test data on short plain concrete columns or cylinders cyclically loaded under either compression (Karsan and Jirsa 1969; Sinha et al. 1964) or tension (Gopalaratnam and Shah 1985; Reinhardt and Cornelissen 1984) loads. In general, the experimental results show that the envelope of stress-strain response is similar to the stress-strain curve for monotonic tests, bounding the unloading and reloading paths (Jowkarmeimandi and Aslani 2012). In testing, it is found that the unloading and reloading paths are traced in two different ways: unloading path follows a convex nonlinear curve, which possesses a higher stiffness at the beginning but becomes flat as the stress level decreases to a lower level, as shown in Figure 5.3; the reloading path shows a curve with a double curvature.

For the sake of simplicity, a straight line is usually employed to represent the unloading path either in tension or in compression. The same straight line is adopted for the reloading branch. The plastic strains in the damage models are used to define the slope of the unloading/reloading line.

In view of the significance of plastic strain in the damage models, it is compared with that reported for the test data. Figure 5.3 compares the reviewed damage models with the experimental studies of Sinha et al. (1964). These studies are conducted under

cyclic compression. Plastic strains predicted by different models were compared with those obtained from the test data at different points, Pt1 to Pt8 (Figure 5.3) and these are provided in Table 5.1. In each case, an error is reported as a percentage. Similar comparisons are made using the compression test data of Karsan and Jirsa (1969) (Figure 5.4 and Table 5.2), the tension test data of Gopalaratnam and Shah (1985) (Figure 5.5 and Table 5.3) and the tension test data of Reinhardt and Cornelissen (1984) (Figure 5.6 and Table 5.4).

A visual inspection of Figure 5.3, shows that Birtel and Mark's (2006) model resembles the test well. Chen et al.'s (2012) model, which is obviously pure damage model, has unloading/reloading paths, which are very different from the test data. This is borne out by the errors evaluated in Table 5.1. A comparison with compression test data of Karsan and Jirsa (1969) (Figure 5.4 and Table 5.2) also suggests that Jirásek's (2004) model, de Borst et al.'s (1995) model and Birtel and Mark's (2006) model all perform reasonably well. An overall good concordance with tension test data of Gopalaratnam and Shah (1985) is also observed in the charts of Tao and Chen's (2014) model, Birtel and Mark's (2006) model, de Borst et al.'s (1995) model and Jirásek's (2004) model in Figure 5.5, and further reinforced by the relevant data in Table 5.3. In addition, the curves of unloading/reloading paths, obtained from Labadi and Hannachi's (2005) model, Jirásek's (2004) model, de Borst et al.'s (1995) model and Birtel and Mark's (2006) model, are generally in line with that from the test data of Reinhardt and Cornelissen (1984). Considering the aforementioned comparisons, it is evident that Birtel and Mark's (2006) model appears as the best model to describe the damage behaviour of concrete under cyclic load with the least average error (Table 5.6).

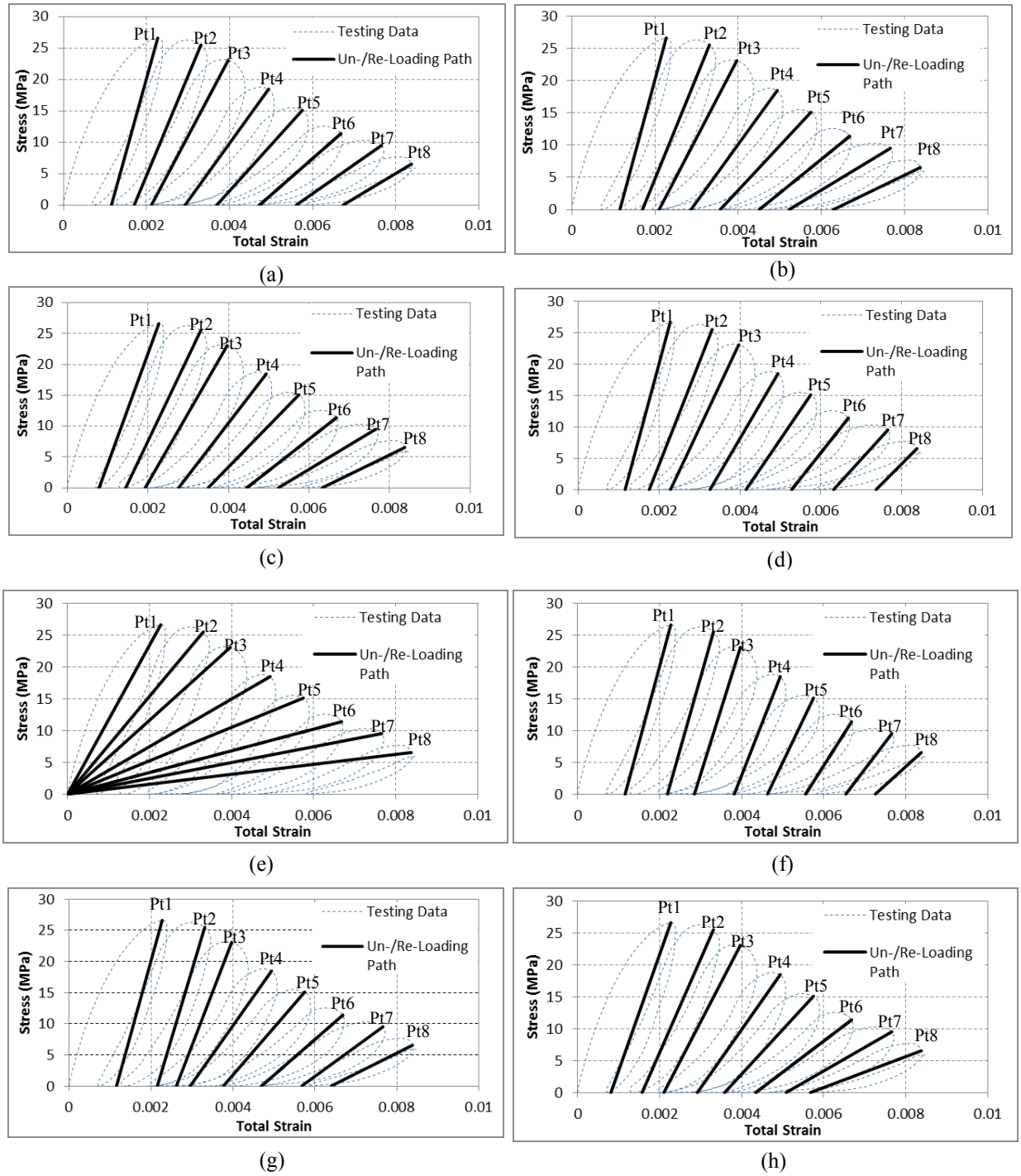

Figure 5.3 (a) Jirásek's (2004) model, (b) de Borst et al.'s (1995) model, (c) Nechnech et al.'s (2002) model, (d) Labadi and Hannachi's (2005) model, (e) Chen et al.'s (2012) model, (f) Yu et al.'s (2010) model, (g) Tao and Chen's (2014) model and (h) Birtel and Mark's (2006) model, compared with stress-strain history for concrete subjected to cyclic compression load (data from Sinha et al. (1964) as presented by Chen and Han (1988))

Table 5.1 Plastic strains and the corresponding errors for different models evaluated from Figure 5.3 for different unloading/reloading paths for cyclic test conducted by Sinha et al. (1964)

	Pt1		Pt2		Pt3		Pt4		Pt5		Pt6		Pt7		Pt8		
	Plastic strain ($\times 10^{-4}$)	Error (%)	Plastic strain ($\times 10^{-4}$)	Error (%)	Plastic strain ($\times 10^{-4}$)	Error (%)	Plastic strain ($\times 10^{-4}$)	Error (%)	Plastic strain ($\times 10^{-4}$)	Error (%)	Plastic strain ($\times 10^{-4}$)	Error (%)	Plastic strain ($\times 10^{-4}$)	Error (%)	Plastic strain ($\times 10^{-4}$)	Error (%)	Average error (%)
Testing	8.26	0	12.8	0	20.9	0	29.7	0	36.8	0	39.9	0	51.6	0	59.6	0	
Jirásek's (2004) model	11.6	39.9	17	33.1	21.2	1.39	29.3	1.42	36.9	0.28	47.2	18.3	56	8.61	67.3	12.9	14.5
de Borst et al.'s (1995) model	11.6	39.9	17	32.7	21	0.39	28.6	3.6	35.7	3.09	45.1	12.9	52.2	1.17	62.8	5.42	12.4
Nechnech et al.'s (2002) model	7.85	5.01	14.4	12.9	19.3	7.7	27.6	7.1	34.9	5.11	44.5	11.5	52.3	1.43	63.2	6.07	7.1
Labadi and Hannachi's (2005) model	11.6	40	17.5	37	22.8	9.04	32.6	9.63	41.5	12.7	52.8	32.3	63.2	22.4	73.7	23.6	23.3
Chen et al.'s (2012) model	0	100	0	100	0	100	0	100	0	100	0	100	0	100	0	100	100
Yu et al.'s (2010) model	11.6	39.9	22	71.6	28.5	36.5	38.3	28.8	46.4	26	55.7	39.5	65.5	26.9	72.7	21.9	36.4
Tao and Chen's (2014) model	11.6	39.9	21.5	68.1	26.2	25.2	29.6	0.49	37.7	2.32	47	17.7	56.8	9.99	64	7.31	21.4
Birtel and Mark's (2006) model	8.09	2.04	15.7	22.6	21	0.53	29.2	1.79	35.8	2.64	43.4	8.84	50.8	1.49	56.7	4.79	5.59

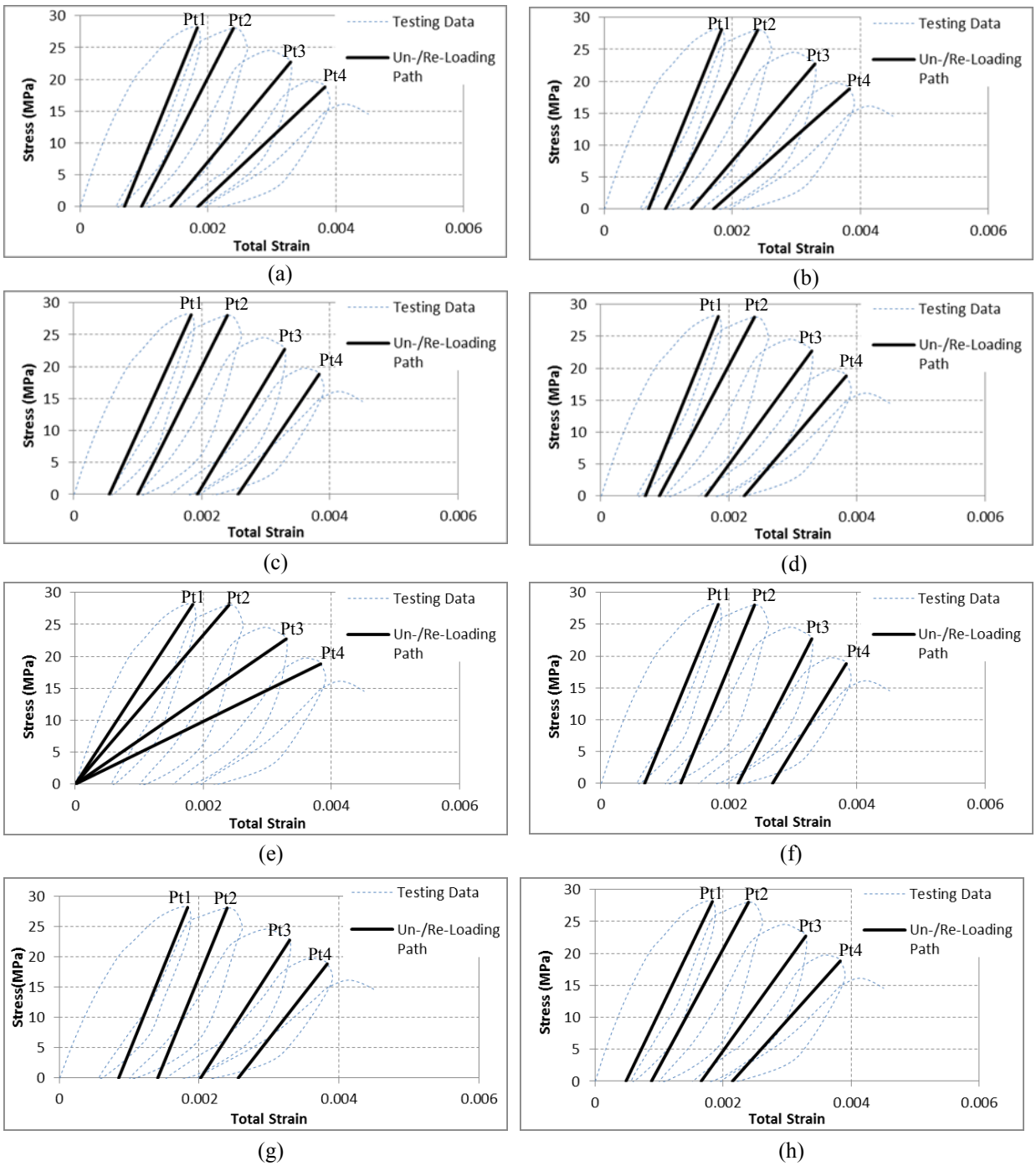

Figure 5.4 (a) Jirásek's (2004) model, (b) de Borst et al.'s (1995) model, (c) Nechnech et al.'s (2002) model, (d) Labadi and Hannachi's (2005) model, (e) Chen et al.'s (2012) model, (f) Yu et al.'s (2010) model, (g) Tao and Chen's (2014) model and (h) Birtel and Mark's (2006) model, compared with stress-strain history for concrete subjected to cyclic compression load (data from Karsan and Jirsa (1969))

Table 5.2 Plastic strains and the corresponding errors for different models evaluated from Figure 5.4 for different unloading/reloading paths for cyclic test conducted by Karsan and Jirsa (1969)

	Pt1		Pt2		Pt3		Pt4		
	Plastic strain ($\times 10^{-4}$)	Error (%)	Plastic strain ($\times 10^{-4}$)	Error (%)	Plastic strain ($\times 10^{-4}$)	Error (%)	Plastic strain ($\times 10^{-4}$)	Error (%)	Total error (%)
Testing	5.69		10.1		15.1		19.5		
Jirásek's (2004) model	6.94	22	9.6	5.2	14.2	6.23	18.4	5.48	9.72
de Borst et al.'s (1995) model	6.94	22	9.57	5.52	13.6	9.99	17.1	12.4	12.5
Nechnech et al.'s (2002) model	5.56	2.37	9.99	1.37	19.3	27.8	25.7	31.6	15.8
Labadi and Hannachi's (2005) model	6.94	22	9.13	9.88	16.4	8.47	22.4	14.7	13.8
Chen et al.'s (2012) model	0	100	0	100	0	100	0	100	100
Yu et al.'s (2010) model	6.83	20	12.5	23.1	21.4	41.8	26.8	37.5	30.6
Tao and Chen's (2014) model	8.49	49.2	14.1	38.9	20.2	33.7	25.6	31.2	38.2
Birtel and Mark's (2006) model	4.86	14.6	8.84	12.8	16.6	9.91	21.5	10.2	11.9

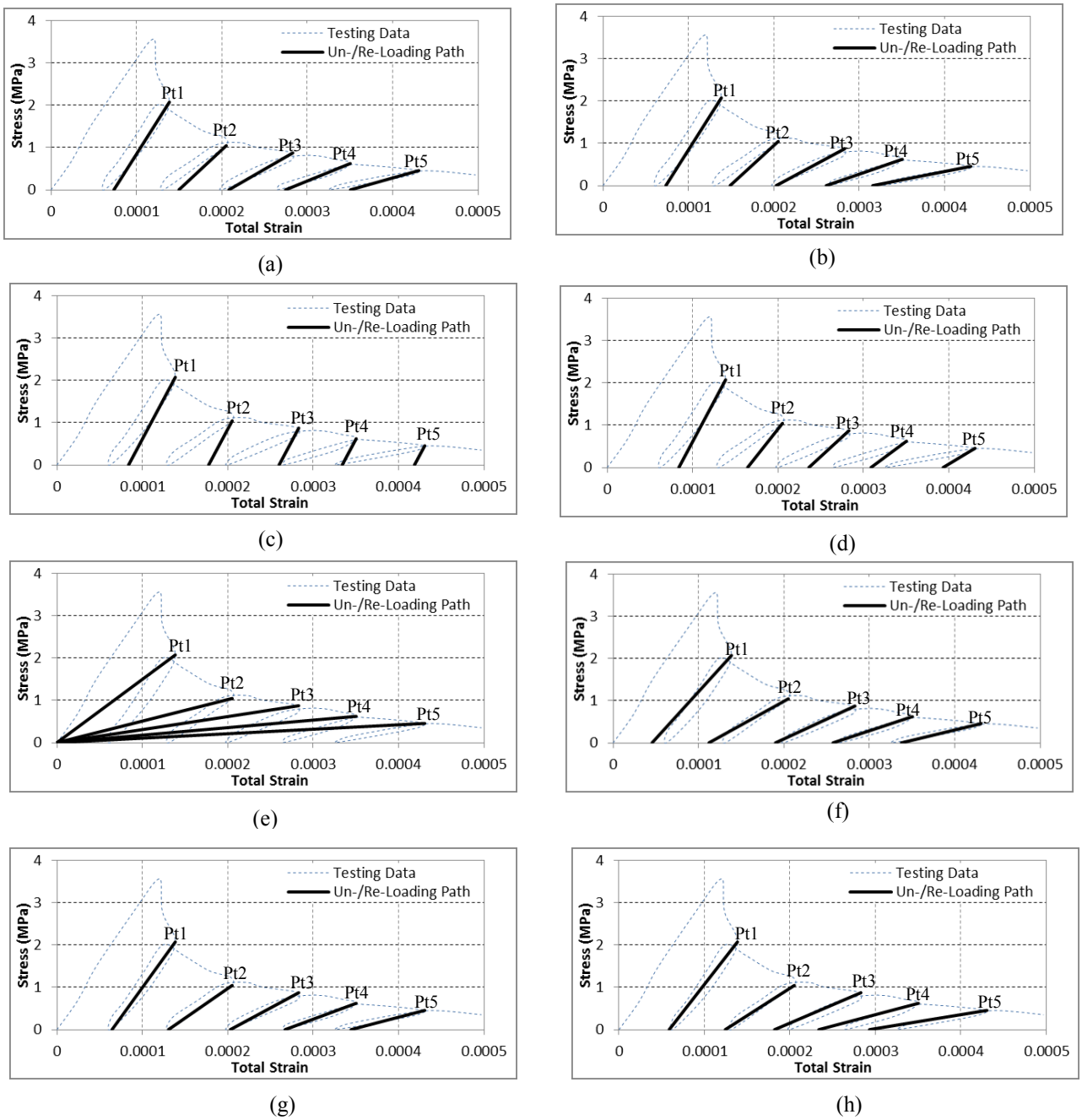

Figure 5.5 (a) Jirásek's (2004) model, (b) de Borst et al.'s (1995) model, (c) Nechnech et al.'s (2002) model, (d) Labadi and Hannachi's (2005) model, (e) Chen et al.'s (2012) model, (f) Yu et al.'s (2010) model, (g) Tao and Chen's (2014) model and (h) Birtel and Mark's (2006) model, compared with stress-strain history for concrete subjected to cyclic tension load (data from Gopalaratnam and Shah (1985))

Table 5.3 Plastic strains and the corresponding errors for different models evaluated from Figure 5.5 for different unloading/reloading paths for cyclic test conducted by Gopalaratnam and Shah (1985)

	Pt1		Pt2		Pt3		Pt4		Pt5		Total error
	Plastic strain (×10-5)	Error (%)	Plastic strain (×10-5)	Error (%)	Plastic strain (×10-5)	Error (%)	Plastic strain (×10-5)	Error (%)	Plastic strain (×10-5)	Error (%)	
Testing	6.25		13.1		20		66.50		32.7		
Jirásek's (2004) model	7.36	17.8	14.97	14.3	20.82	4.1	27.46	58.7	35.05	7.2	20.4
de Borst et al.'s (1995) model	7.36	17.7	14.88	13.6	20.28	1.38	26.14	60.7	31.57	3.45	19.4
Nechnech et al.'s (2002) model	8.39	34.2	17.76	35.6	26.00	30	33.40	49.8	41.86	28	35.5
Labadi and Hannachi's (2005) model	8.39	34.2	16.43	25.5	23.60	18	30.88	53.6	39.33	20.3	30.3
Chen et al.'s (2012) model	0	100	0	100	0	100	0	100	0	100	100
Yu et al.'s (2010) model	4.56	27.1	11.22	14.4	19.01	4.97	25.74	61.3	33.76	3.23	22.2
Tao and Chen's (2014) model	6.45	3.15	13.06	0.32	20.30	1.48	26.72	59.8	34.43	5.29	14
Birtel and Mark's (2006) model	5.87	6.08	12.43	5.1	18.20	8.98	23.38	64.8	29.30	10.4	19.1

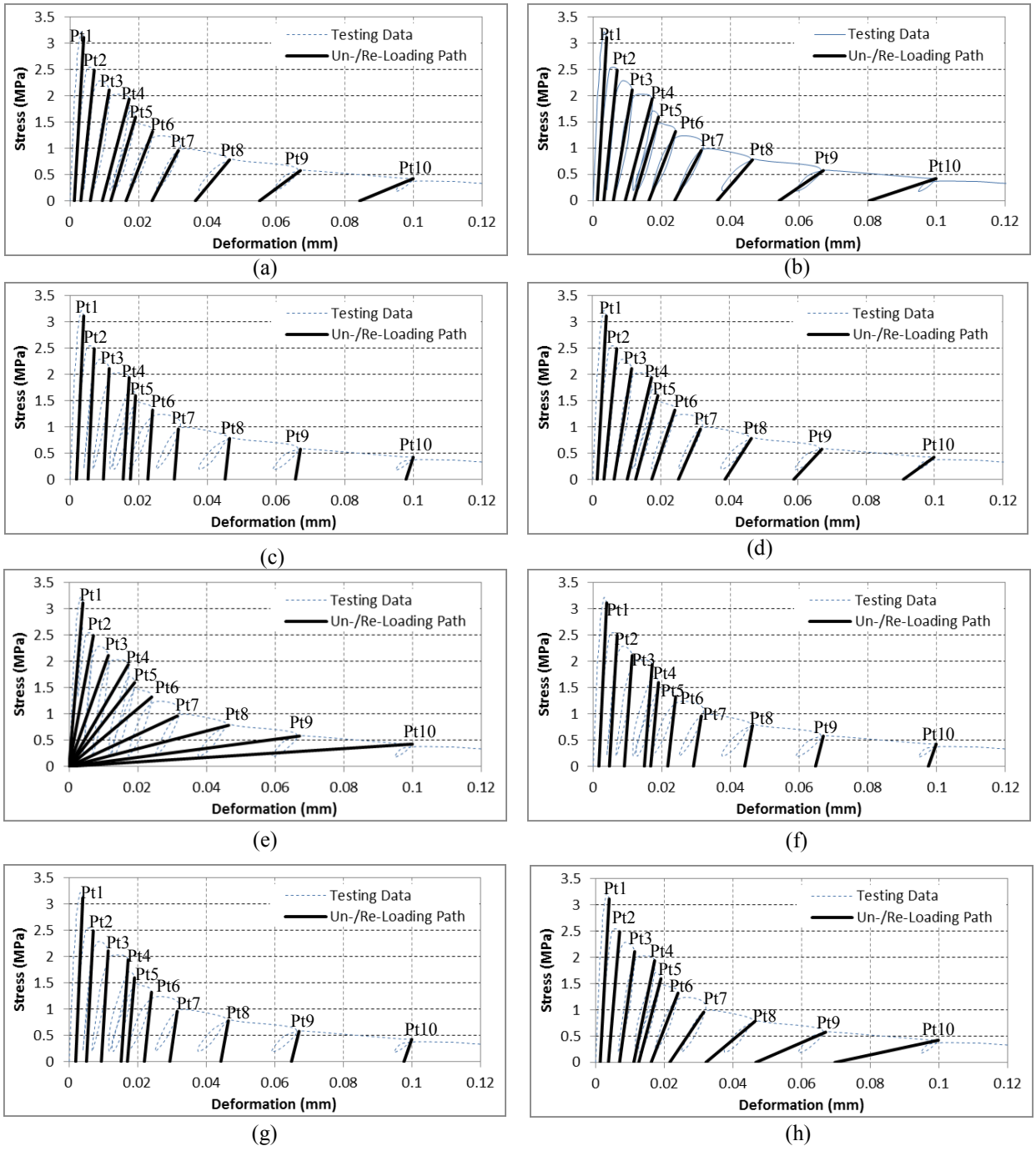

Figure 5.6 (a) Jirásek's (2004) model, (b) de Borst et al.'s (1995) model, (c) Nechnech et al.'s (2002) model, (d) Labadi and Hannachi's (2005) model, (e) Chen et al.'s (2012) model, (f) Yu et al.'s (2010) model, (g) Tao and Chen's (2014) model and (h) Birtel and Mark's (2006) model, compared with stress-strain history for concrete subjected to cyclic tension load (data from Reinhardt and Cornelissen (1984))

Table 5.4 Plastic strains for different models evaluated from Figure 5.6 for different unloading/reloading paths for cyclic test conducted by Reinhardt and Cornelissen (1984)

	Plastic Deformation ($\times 10^{-3}$ mm)									
	Pt1	Pt2	Pt3	Pt4	Pt5	Pt6	Pt7	Pt8	Pt9	Pt10
Testing	1.3	4.3	6.4	11.2	12.3	16.2	23.5	35.8	55.9	91.6
Jirásek's (2004) model	1.3	3.2	6.0	9.4	11.9	16.4	23.9	36.5	55.2	84.3
de Borst et al.'s (1995) model	1.3	3.2	6.0	9.4	11.9	16.3	23.8	36.1	54.1	80.3
Nechnech et al.'s (2002) model	1.9	5.3	9.8	15.5	17.6	22.7	30.4	45.1	65.6	97.8
Labadi and Hannachi's (2005) model	1.4	3.3	6.3	10.1	12.6	17.3	25.1	38.7	58.8	90.9
Chen et al.'s (2012) model	0.0	0.0	0.0	0.0	0.0	0.0	0.0	0.0	0.0	0.0
Yu et al.'s (2010) model	1.8	4.8	9.2	15.0	16.8	21.8	29.3	44.2	64.8	97.6
Tao and Chen's (2014) model	2.0	5.1	9.4	15.2	17.0	22.0	29.4	44.3	64.8	97.6
Birtel and Mark's (2006) model	1.4	3.8	7.1	11.2	12.6	16.2	21.6	32.2	46.7	69.7

Table 5.5 The corresponding errors for different models evaluated from Figure 5.6 for different unloading/reloading paths for cyclic test conducted by Reinhardt and Cornelissen (1984)

	Error (%)										Average Error (%)
	Pt1	Pt2	Pt3	Pt4	Pt5	Pt6	Pt7	Pt8	Pt9	Pt10	
Testing	-	-	-	-	-	-	-	-	-	-	-
Jirásek's (2004) model	2.8	25.0	6.3	15.6	3.2	0.9	1.8	2.0	1.3	8.0	6.7
de Borst et al.'s (1995) model	2.8	25.0	6.4	15.8	3.4	0.6	1.4	1.1	3.1	12.3	7.2
Nechnech et al.'s (2002) model	43.6	24.3	53.2	38.8	43.1	40.0	29.4	26.3	17.4	6.7	32.3
Labadi and Hannachi's (2005) model	1.6	21.5	1.0	9.2	2.6	6.8	7.0	8.3	5.3	0.8	6.4
Chen et al.'s (2012) model	100.0	100.0	100.0	100.0	100.0	100.0	100.0	100.0	100.0	100.0	100.0
Yu et al.'s (2010) model	30.4	13.1	43.8	34.0	36.8	34.4	24.7	23.5	15.9	6.5	26.3
Tao and Chen's (2014) model	48.5	20.6	48.2	36.1	38.6	35.6	25.3	23.8	16.1	6.5	29.9
Birtel and Mark's (2006) model	4.9	9.8	10.7	0.2	2.8	0.3	7.8	10.1	16.5	23.9	8.7

Table 5.6 Summary of the comparison results between test data and empirical models in terms of plastic deformation errors under cyclic test

	Sinha et al. (1964) %	Karsan and Jirsa (1969) %	Gopalaratnam and Shah (1985) %	Reinhardt and Cornelissen (1984) %	Average %
Jirásek's (2004) model	14.5	9.7	20.4	6.7	12.8
de Borst et al.'s (1995) model	12.4	12.5	19.4	7.2	12.9
Nechnech et al.'s (2002) model	7.1	15.8	35.5	32.3	22.7
Labadi and Hannachi's (2005) model	23.3	13.8	30.3	6.4	18.5
Chen et al.'s (2012) model	100.0	100.0	100.0	100.0	100.0
Yu et al.'s (2010) model	36.4	30.6	22.2	26.3	28.9
Tao and Chen's (2014) model	21.4	38.2	14.0	29.9	25.9
Birtel and Mark's (2006) model	5.6	11.9	19.1	8.7	11.3

5.4 Single element tests with concrete damaged plasticity

The discussion on the damage in the previous section was limited to uniaxial tension or compression. However, concrete specimens, in general, experience triaxial stress state. It is for this reason that this study has adopted a general concrete damaged plasticity (CDP) model.

This section first considers whether the CDP model is capable of capturing the uniaxial loading, unloading and reloading behaviour expected from damage models. More complex loading states are considered in later section.

All the tests are conducted using a single square plane stress element (i.e. with four integration points (CPS4)) with an arbitrarily selected size of 100 mm. The material properties are as discussed in Chapter 3. A compressive strength of 23 MPa and tensile strength of 1.8 MPa are assigned. The key variations considered here relates to the description of damage and loading.

It is important to note that the CDP model requires definition of evolving damage with increasing inelastic deformation. Based on the formulation discussed earlier, the variation of damage factor in tension, d_t, is shown in Figure 5.7 (a); the variation of damage factor in compression, d_c, is shown in Figure 5.7 (b).

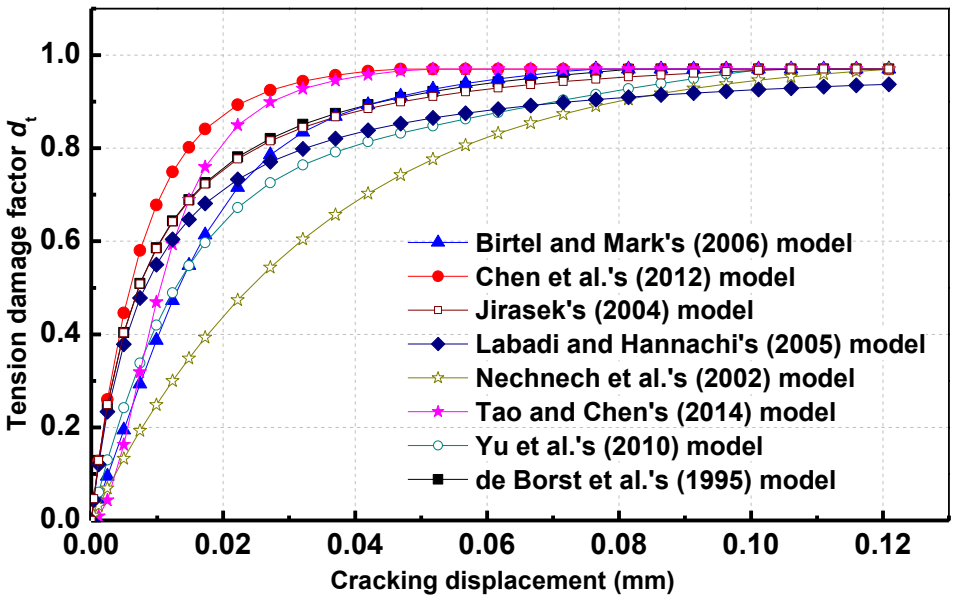

(a)

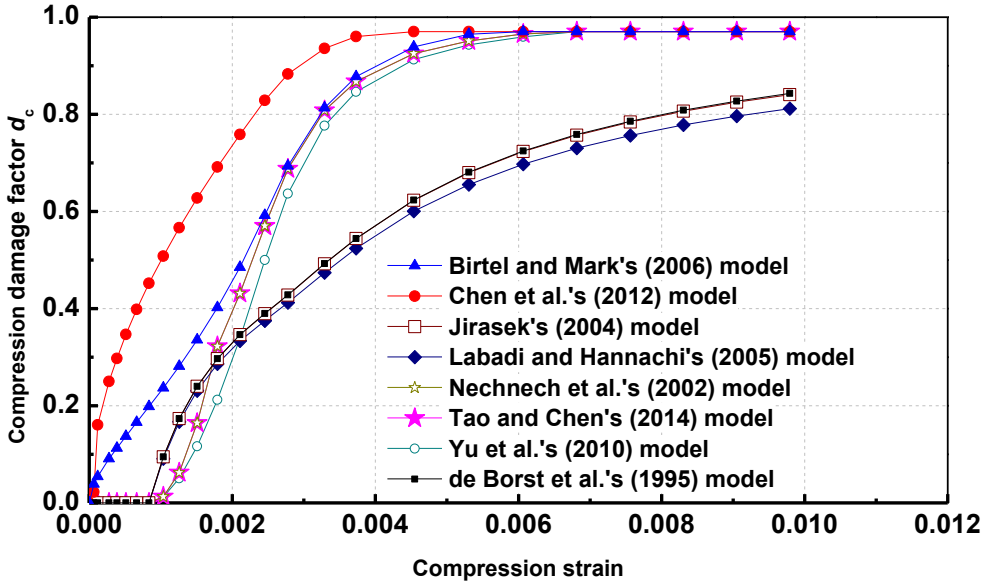

(b)

Figure 5.7 Damage factor versus inelastic strain relationships for different damage models (a) in tension and (b) in compression

5.4.1 Uniaxial cyclic loading

In order to demonstrate that the CDP criterion is able to simulate stiffness degradation arising from a tension or compression damage, cyclic tests are conducted using Birtel and Mark's (2006) model for damage. Boundary conditions in compression and tension are set respectively as shown in Figure 5.8.

(a) (b)

Figure 5.8 Geometrical model and constraints for the numerical example for (a) uniaxial tension load and (b) uniaxial compression load

The loading scheme for both compression and tension comprises of a monotonic loading, and unloading then reloading using the displacement control. In tension, unloading was initiated at the displacements of 0.017mm, 0.026mm, 0.04mm and 0.07mm. The stress-strain curve is extracted from the aforementioned analysis for vertical normal stresses and strains. The results for the uniaxial cyclic tension loading are showing in Figure 5.9 (a). It can be seen that the stiffness reduces with increasing deformation in the post-peak stress zone as illustrated by the unloading and reloading lines in Figure 5.9 (a). The stiffness degradation of Birtel and Mark's (2006) model is faithfully reproduced by the CDP criterion.

A similar test is conducted under uniaxial compression. In this case, the unloading is initiated at the displacements of 0.175 mm, 0.218 mm, 0.26 mm, 0.3 mm to 0.4 mm. Once again, the unloading behaviour demonstrates (Figure 5.9 (b)) the stiffness

degradation with the increasing inelastic deformation as expected from Birtel and Mark's (2006) model.

In summary, in both tension and compression, the unloading stiffness is found to decrease with increasing inelastic strain, which corresponds to the definition of damage in Eq. (5.1). Also, this stiffness reduction reflects the damage evolution under cyclic load in simulations.

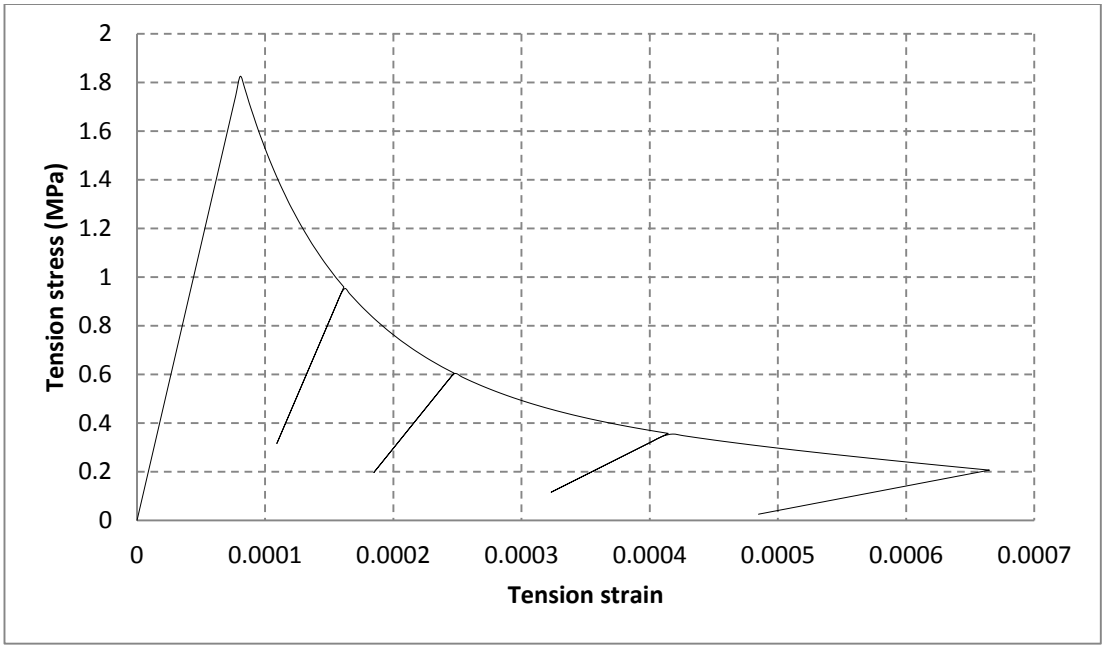

(a)

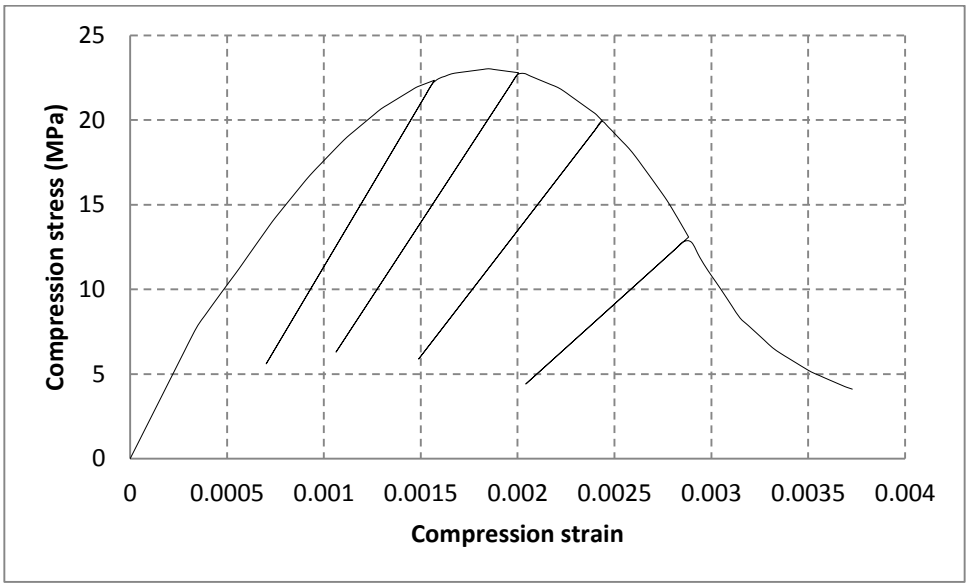

Figure 5.9 The unloading/reloading paths of stress-strain curve under different loading levels in (a) tension and (b) compression

5.4.2 Test with monotonic loading

It is a common conception that no effect of damage on the monotonic loading. This section considers this belief for different monotonic loading scenarios. In each loading case, the full range of damage models discussed earlier are considered.

Monotonic tests are first conducted under uniaxial tension and compression; then more complex loading scenarios are applied. To prevent numerical problems or non-convergence of simulations, the upper limit of 0.97 is set for damage parameters in both compression and tension. Other material properties are as discussed in Chapter 3.

5.4.2.1 Uniaxial monotonic loading

In order to examine the effect of the damage under monotonic uniaxial loading, tests are conducted using the damage models discussed in Section 5.2. The boundary conditions used are shown in Figure 5.8.

The vertical normal stress-strain curves in uniaxial tension for different tension damage models are shown in Figure 5.10. As expected, the choice of damage model makes no difference under monotonic uniaxial tension. It is also important to note that the monotonic uniaxial tension response is not influenced by the choice of damage model in compression.

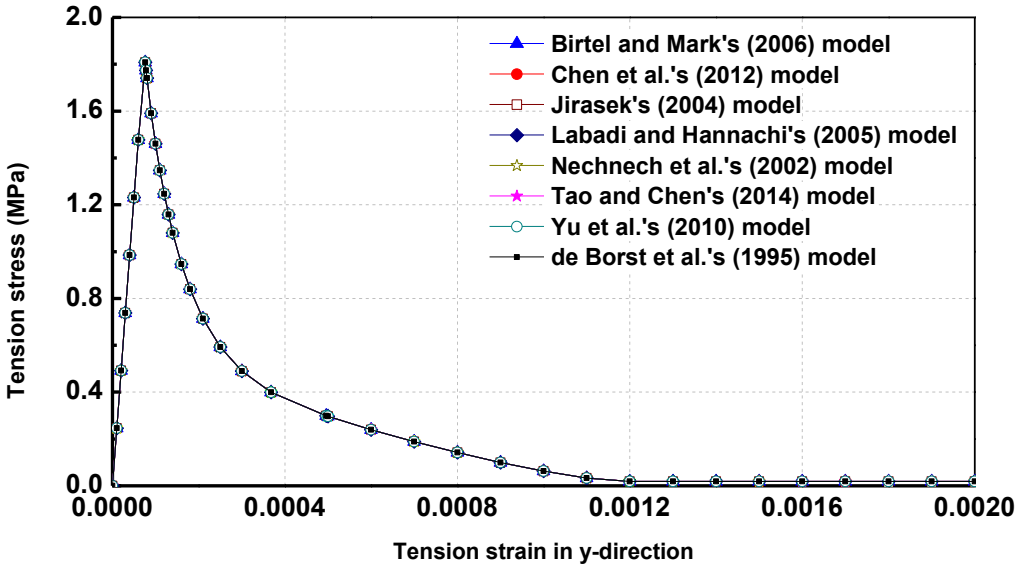

Figure 5.10 Stress-strain relationships from the numerical element tests in tension, for different tension damage models

Similar tests are conducted under monotonic uniaxial compression. And the results are shown in Figure 5.11. Once again, it can be seen that the choice of damage model in compression has no effect on the response as all curves are identical. Also, the choice of damage model in tension has no effect under uniaxial compression. It can be concluded that the common conception that the effect of damage models is absent in monotonic loading is true for uniaxial loading scenarios.

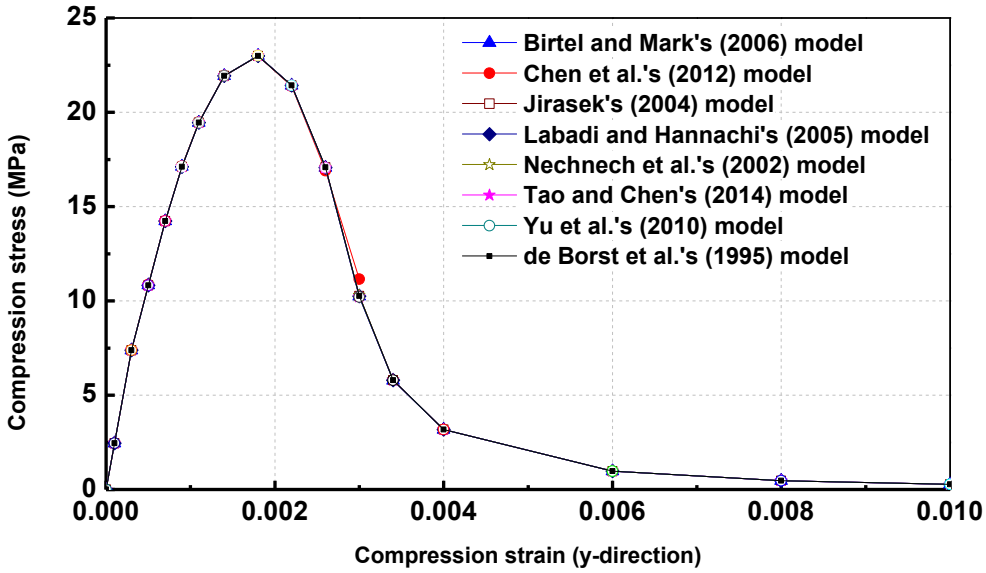

Figure 5.11 Stress-strain relationships from the numerical element tests in compression, for different compression damage models

5.4.2.2 Monotonic complex loading

It can be hypothesised that since CDP model is triaxial, response under complex monotonic loading scenarios will be influenced by the choice of damage model. To investigate this, a range of biaxial tests are performed. The biaxial tests are performed in three quadrants: biaxial compression, biaxial compression-tension and biaxial tension. In this study, four loading conditions are considered with the corresponding boundary conditions, as illustrated in Figure 5.12. It may be noted that Figure 5.12 (d) represents shear, which is also biaxial tension and compression.

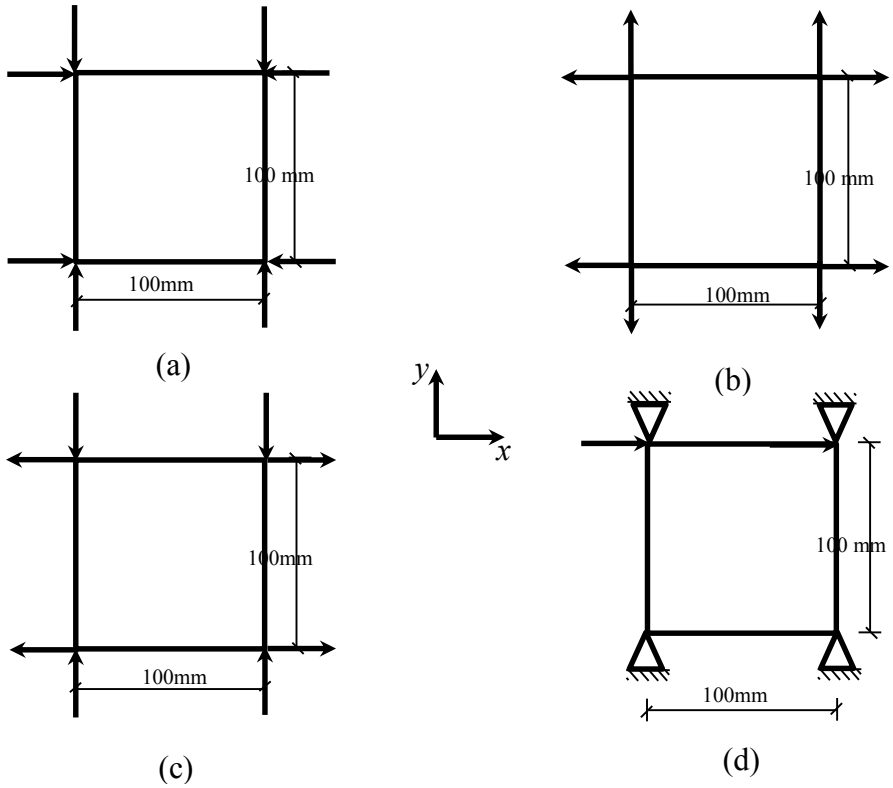

Figure 5.12 Geometrical model and constraints for the numerical example under (a) biaxial compression load, (b) biaxial tension load, (c) biaxial load with one direction in compression and the other direction in tension, and (d) shear load

For the biaxial loading scenarios, shown in Figure 5.12 (a), (b) and (c), monotonically increasing displacement were applied in the directions shown; the magnitude in the two directions was kept equal.

Figure 5.13 compares the stress-strain curves in the y-direction for biaxial compression (Figure 5.12 (a)) for different damage models in compression. Once again it can be seen that under biaxial compression there is no difference in the response.

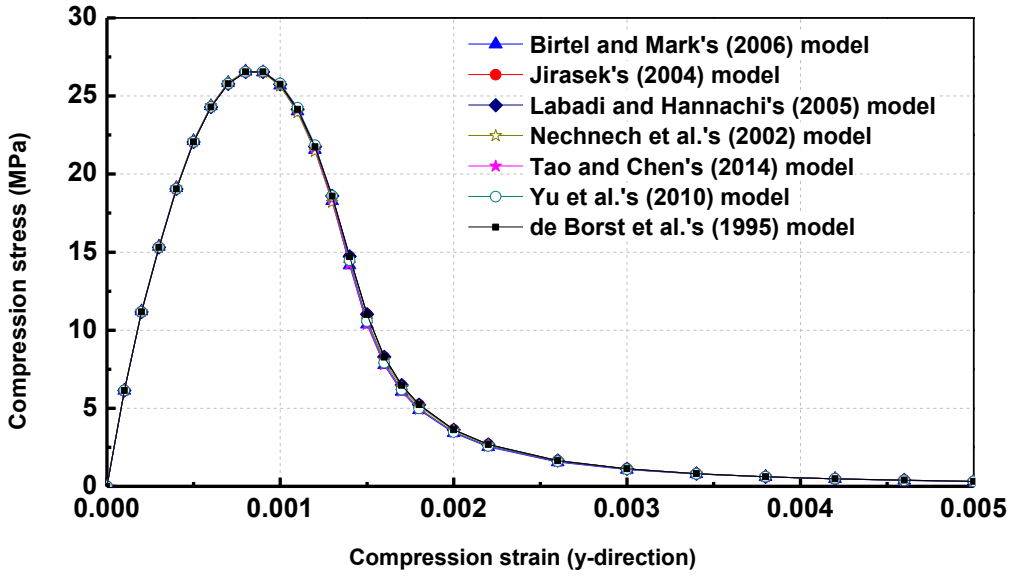

Figure 5.13 Stress-strain relationships from numerical element tests under the biaxial compression load, for different compression damage models

Similarly, in biaxial tension, the tension stress-strain curves in y-direction are compared in Figure 5.14; these show that the variation in damage parameter does not affect the response in biaxial tension-tension.

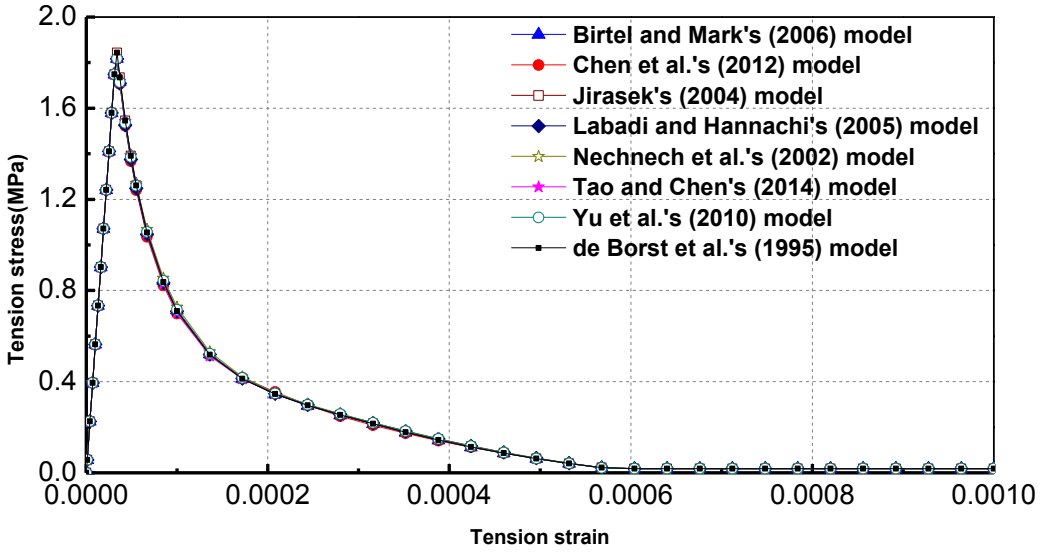

Figure 5.14 Stress-strain relationships from element test under the biaxial tension load for different tension damage models

Biaxial compression-tension loading as shown Figure5.12 (c) is next considered. As mentioned earlier, the displacement magnitude in x- and y-direction are kept the same and stress-strain curves in the y-direction are compared for different damage models.

For biaxial compression-tension loading, the stress-strain response from the different damage models compared in both x- and y- directions as shown in Figure 5.15-Figure 5.16. It can be seen that even under monotonic loading, there is still considerable effect of the damage model chosen. This is because of the complex interaction between damage and plasticity in the tension-compression zone. It can be seen that Tao and Chen's (2014) and Nechnech et al.'s (2002) models provide the highest and lowest peak stresses respectively.

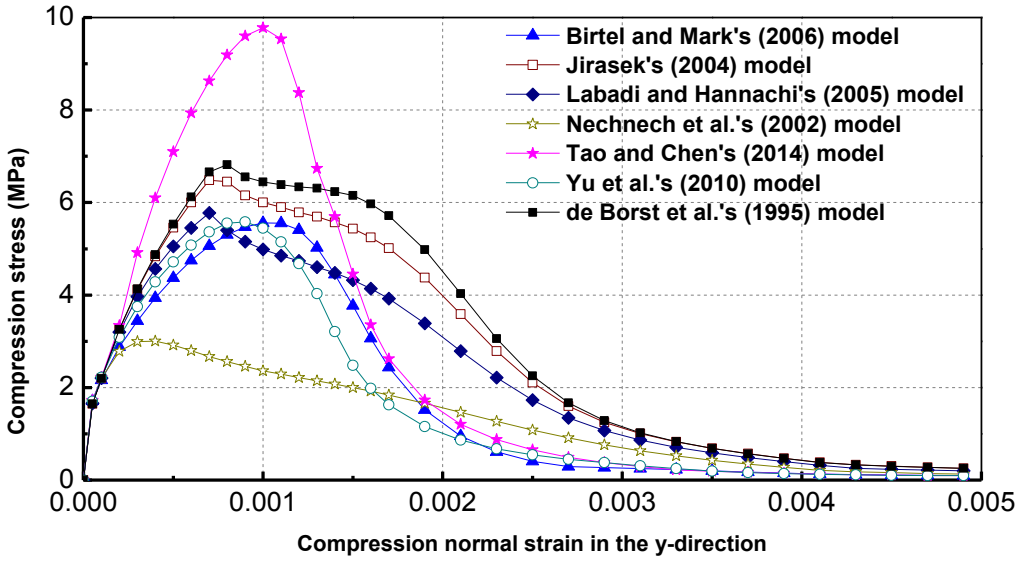

Figure 5.15 Stress-strain relationships from element test under biaxial compression-tension load in the y-direction with different damage models

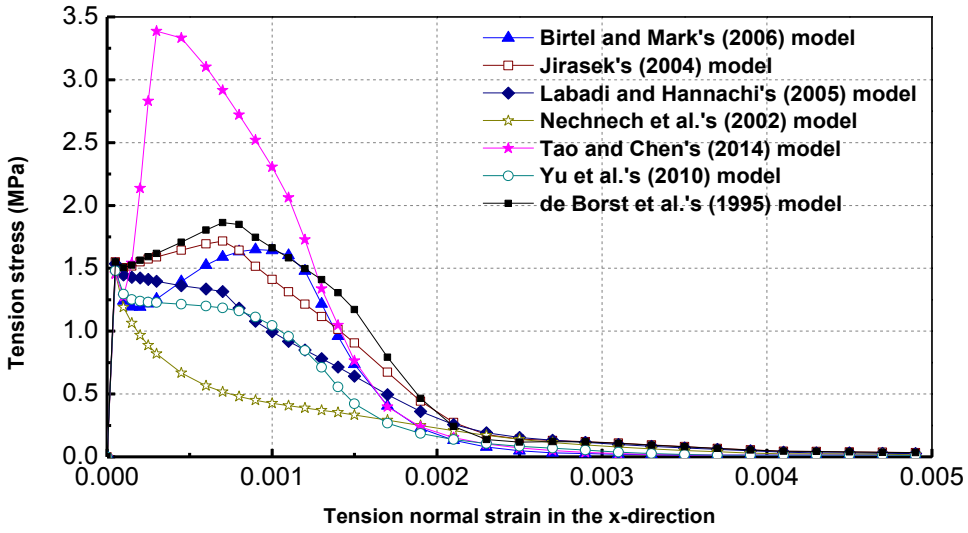

Figure 5.16 Stress-strain relationships from element test under biaxial compression-tension load in the x-direction with different damage models

In addition, the single element test was also conducted under shear load, in which a horizontal displacement (along x-direction) was applied to the top surface of the element as shown in Figure 5.12 (d). The shear stress-strain curves for different damage models are compared in Figure 5.17. Once again, it can be seen that different damage models result in significantly different responses. Also, Tao and Chen's (2014) and Nechnech et al.'s (2002) models provide the highest and lowest peak stresses respectively.

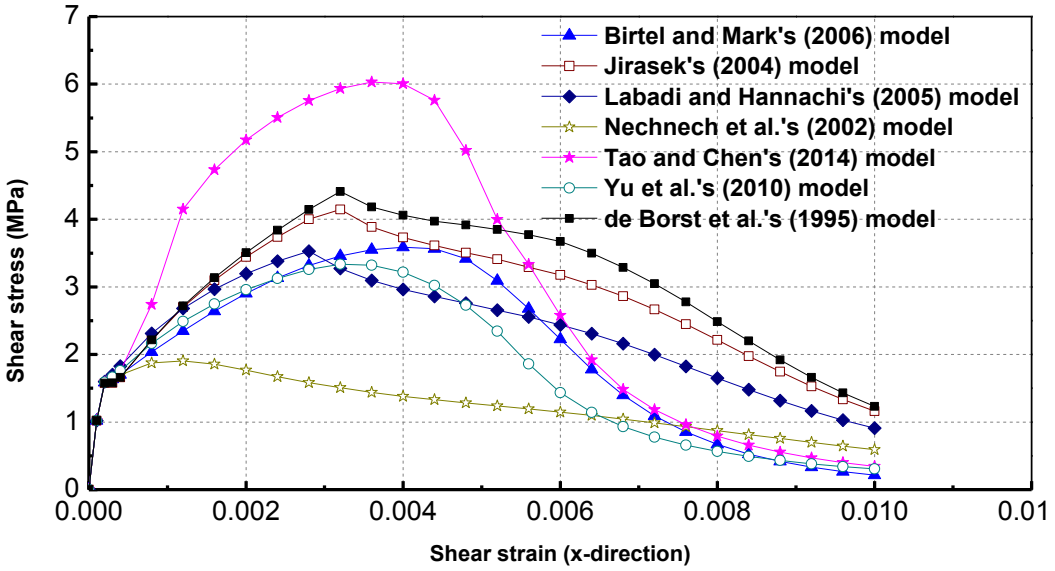

Figure 5.17 Shear stress-strain relationships from the element test under shear load for different tension damage models

From the above results, it can be seen that the response from the element test with Birtel and Mark's (2006) model is somewhat in the middle. It is important to recall from section 5.2 that the results of Birtel and Mark's (2006) model are very close to physical experiments. In the results shown so far, Birtel and Mark's (2006) model was employed with b_c=0.7 and b_t=0.7 (see Eq. (5.2)). As Birtel and Mark's (2006) model permits, application of different values for parameter b_x, the effect of changing this parameter is further investigated.

The parameter b_x was set to different values ranging from 0.1 to 0.9 at an interval of 0.2. The resulting variation of damage factors in tension and compression are shown in Figure 5.18.

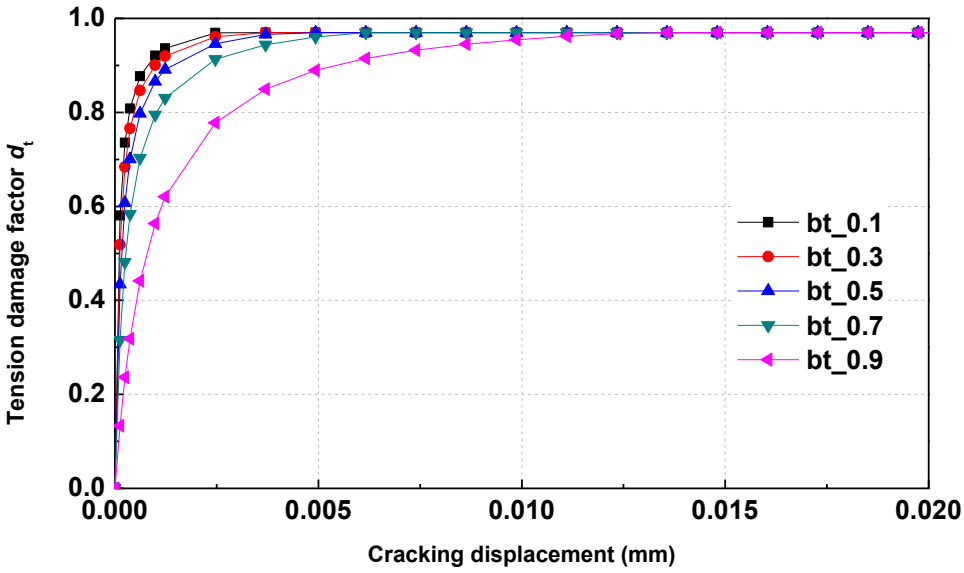

(a)

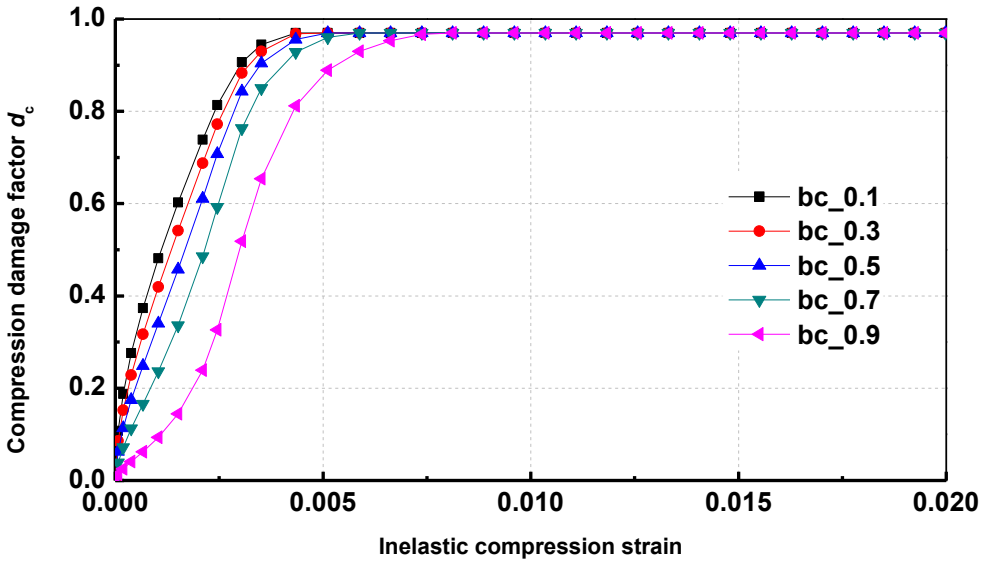

(b)

Figure 5.18 The Birtel damage model with the different values of the parameter (a) b_c, and (b) b_t

The effect of the variation in tension damage model is first investigated under the biaxial compression-tension test. In this case, the parameter b_c was set to a value of 0.7 while b_t was varied. The normal stress-strain curves in the vertical direction are shown in Figure 5.19 (a). Similarly, b_c was varied when the parameter was set to 0.7. The resulting normal stress-strain curves in the vertical direction are shown in Figure 5.19 (b). It can be seen that even in the same model, simple change of parameter b_x results in significant response variation in biaxial compression and tension.

For the sake of completeness, a similar study was conducted under shear, in which b_t was varied when b_c was kept constant and then b_c was varied when b_t was kept constant. The resulting shear stress and shear strain curves are shown in Figure 5.20. Once again, the change of parameter b_x results in significant variation in response.

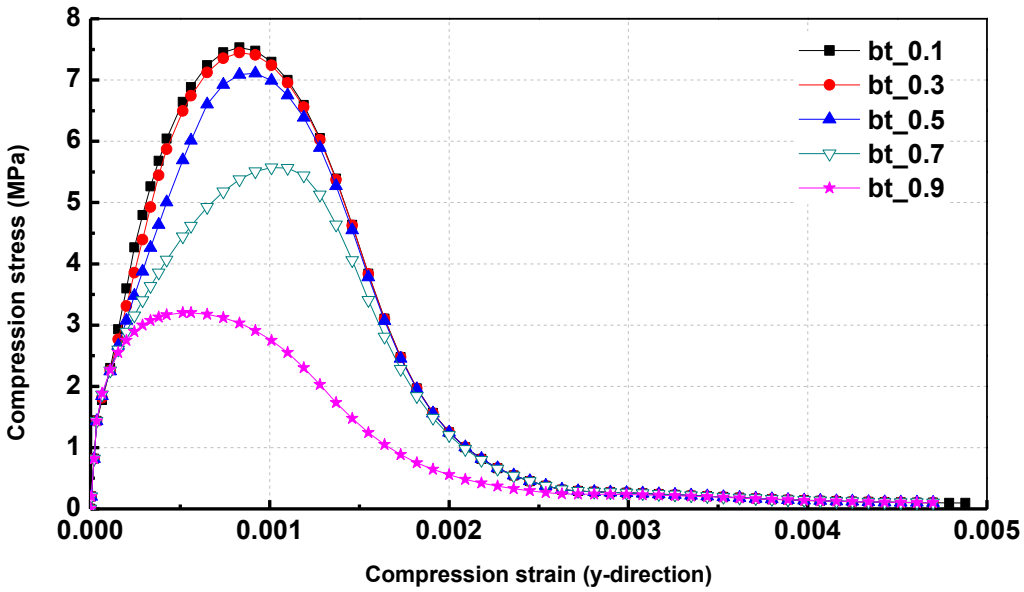

(a)

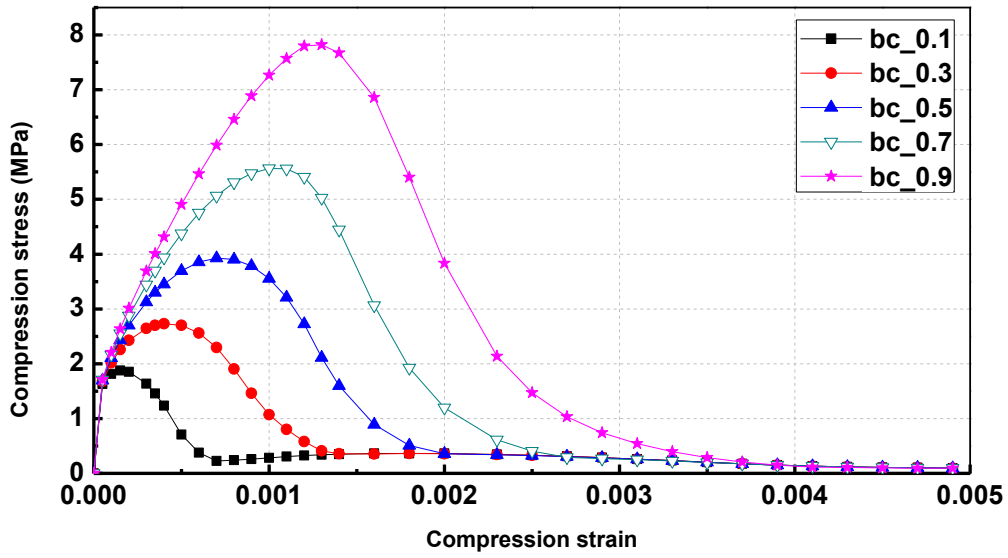

(b)

Figure 5.19 Stress-strain relationships from numerical element test under the biaxial load with one direction in compression and the other direction in tension, for different values of (a) b_t and for (b) b_c in Birtel and Mark's (2006) model

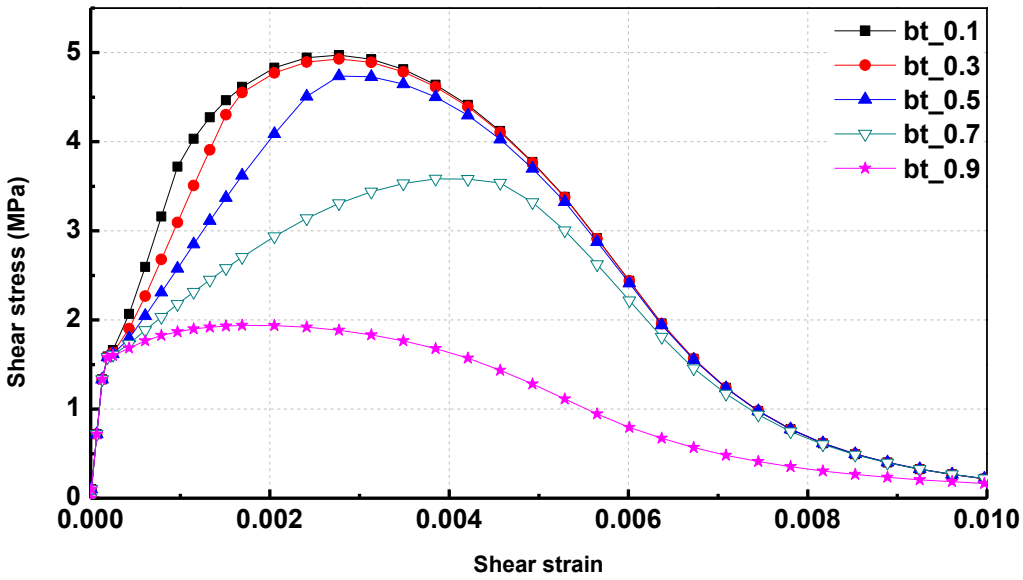

(a)

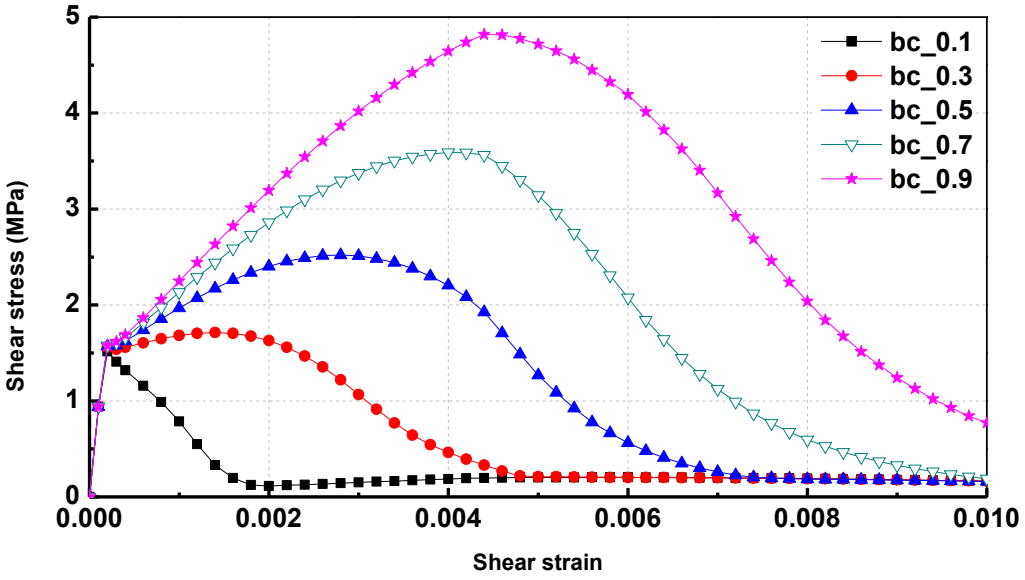

(b)

Figure 5.20 Shear stress-strain relationships from numerical element tests under shear load, for different values of (a) b_t and (b) b_c in Birtel and Mark's (2006) model

5.5 Effect of damage models on the FRP-concrete interfacial response

To examine the influence of the damage models on FRP-concrete interfacial response, Specimen I-3 in Yao et al. (2005) is employed as the reference case. The compressive and tensile strengths of 23 MPa and 1.83 MPa respectively are used. The geometrical model and the material properties assignments are as discussed earlier. The only variation is the damage models used.

Four damage models, viz Birtel and Mark's (2006), Nechnech et al.'s (2002), Tao and Chen's (2014) and Yu et al.'s (2010) models, are considered in this investigation.

Firstly, the effect of the tension damage factor is investigated using these four models. To maintain an element similarity, Birtel and Mark's (2006) model (b_c=0.7) is used to

describe the damage behaviour in compression. The load versus displacement curves are shown in Figure 5.21. The shapes of these response curves are similar in all of these cases. The Birtel and Mark's (2006) and Tao and Chen's (2014) models predict a significantly higher peak load than the other two models considered. The jagged response is related to progressive interfacial failure.

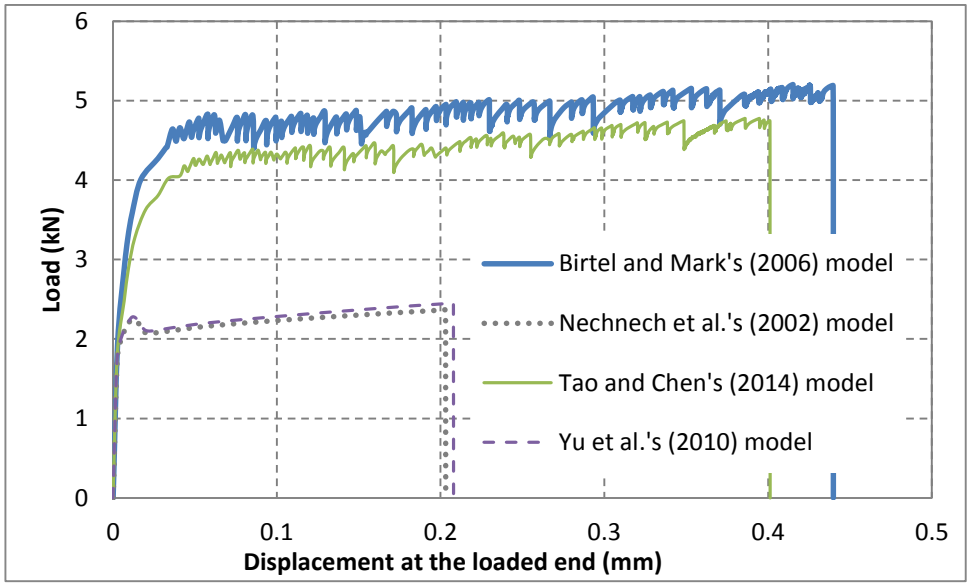

Figure 5.21 Load-displacement curves of Specimen I-3 with different tension damage models

Secondly, the effect of the compression damage factor is investigated using the same four damage models. In this case, Birtel and Mark's (2006) model is again used to describe the damage behaviour in tension. The load versus displacement curves from these numerical analyses are shown in Figure 5.22. It is found that the difference in the ultimate load in simulation arising from the variation in compression damage models is not as significant as that seen from different tension damage models. The ultimate load from Yu et al.'s (2010) model with lower value of damage factor at the same inelastic strain (see Figure 5.7 (b)) is higher than that from Nechnech et al.'s (2002) model with higher value of damage factor (see Figure 5.7 (b)).

These findings observed in this section, have further confirmed the conclusion drawn from the element tests under shear and biaxial compression-tension load. Despite of

that, the further simulation is still in need, due to the crossing issues amongst different damage models, as shown in Figure 5.7.

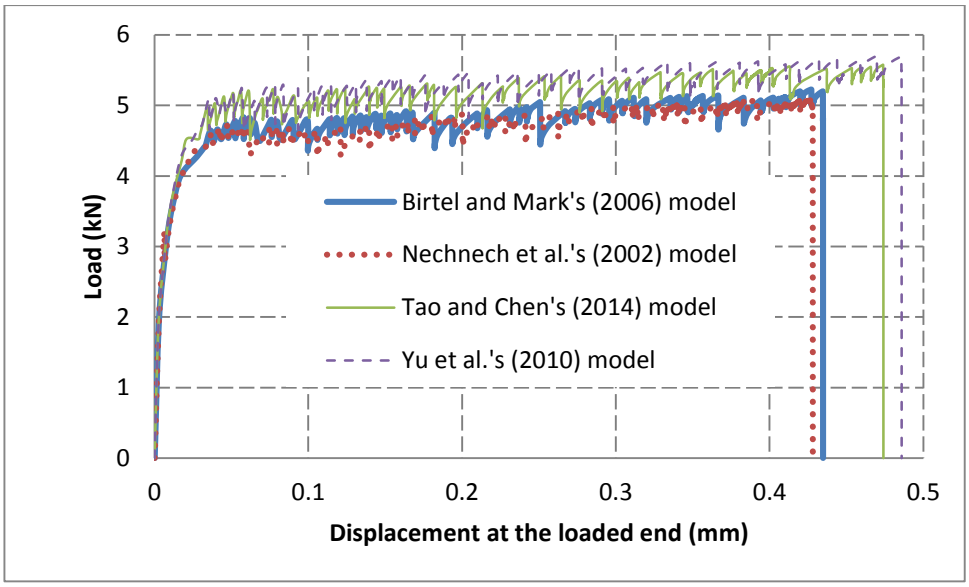

Figure 5.22 Load-displacement curves of Specimen I-3 from Yao et al. (2005) with different compression damage models

The interfacial failure problem was next analysed with Birtel and Mark's (2006) model with varied values b_x. In the first analysis, Birtel and Mark's (2006) model with the parameter b_t varied from 0.3 to 0.9 at an interval of 0.2 was considered while b_c was set to 0.7. The load versus displacement curves are extracted from these numerical analyses, as shown in Figure 5.23. As earlier it is found that higher value of tension damage factor, which decreases with the parameter b_t (see Figure 5.18 (a)), leads to higher value in the ultimate load in simulation (see Figure 5.23).

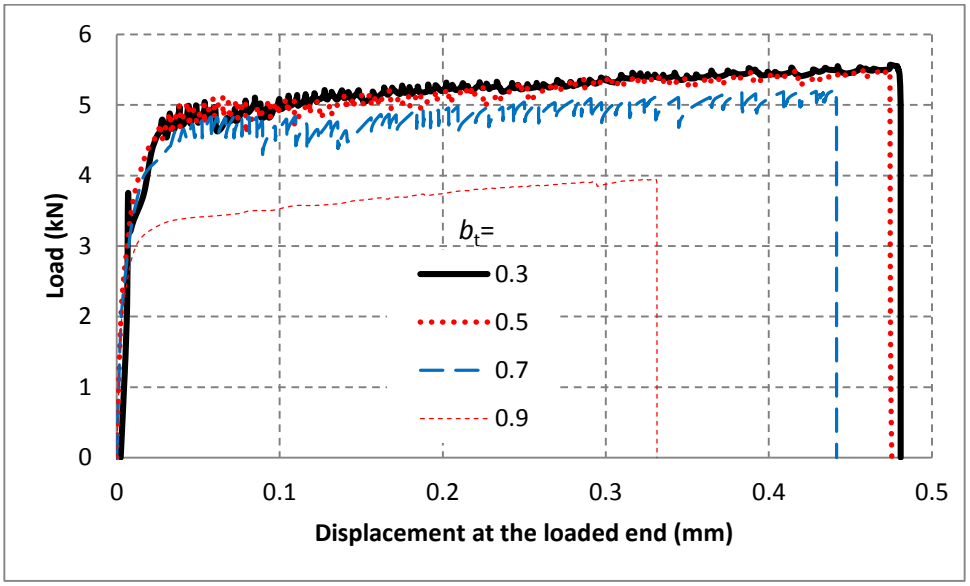

Figure 5.23 Load-displacement curves of Specimen I-3 with different values of b_t in Birtel and Mark's (2006) model

Next, the b_c parameter of Birtel and Mark's (2006) model is varied while b_t is set to 0.7. The load versus displacement curves are shown in Figure 5.24. It is found that lower value of compression damage factor, which decreases with the parameter b_c (see Figure 5.18 (b)), leads to higher value in the ultimate load in simulation (see Figure 5.24). These findings are similar to those drawn from the single element test under shear and biaxial compression-tension loads.

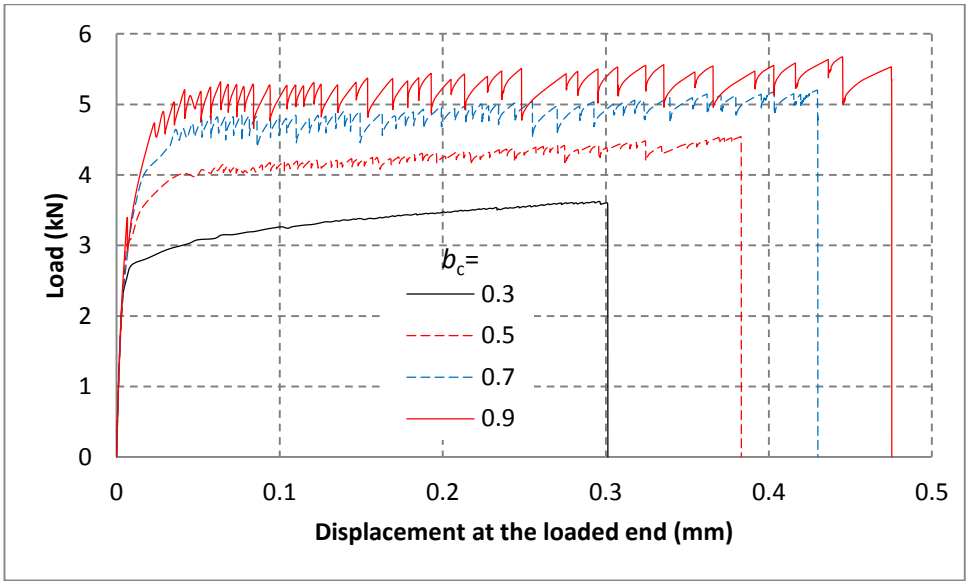

Figure 5.24 Load-displacement curves with different values of b_c in Birtel and Mark's (2006) model

The ultimate load from the simulations is compared with that found experimentally by Yao et al. (2005) for their Specimen I-3. It is found that the simulations with Birtel and Mark's (2006) model are closest to experimental results.

Table 5.7 Summary of the ultimate load of the simulation of Specimen I-3 from Yao et al. (2005) with different damage models

		Test	Birtel and Mark's (2006) model (b_x=0.7)	Nechnech et al.'s (2002) model	Tao and Chen's (2014) model	Yu et al.'s (2010) model
Tension damage model	Load (kN)	5.76	5.23	2.37	4.78	2.46
	Error (%)	-	9%	59%	17%	57%
Compression damage model	Load (kN)	5.76	5.23	5.09	5.58	5.71
	Error (%)	-	9%	12%	3%	1%
	Average error	-	9%	35.5%	10%	29%

In summary, the choice of the damage model affects the response significantly in the numerical analysis for FRP-concrete interfacial debonding even under monotonic load. Birtel and Mark's (2006) model, which is found to best replicate cyclic experiments, is again found to provide the response to interfacial debonding problem.

5.6 The effect of the upper limit of the damage factor

In theory, damage factor could be set to unity in simulations, when material is completely damaged. In this situation, the elastic modulus of material *E* becomes zero as

$$E = (1 - d)\, E_{\mathrm{c}} \tag{5.12}$$

Excessive damage resulting in extreme low value of *E*, can affect convergence. It is important to balance computation efficiency (i.e. the convergence rate) with the computation accuracy. In order to examine the effect of the upper limit of the damage factor, a number of tests are conducted with the FRP-concrete interface debonding problem, which has already been discussed in this chapter.

5.6.1 The upper limit for the tension damage factor

Birtel and Mark's (2006) model is employed with different values of the upper limit in the tension damage model (Table 5.8), and with a value of 0.97 as the upper limit in compression damage model. The geometrical modelling and the assignments of all the other material properties are all as discussed earlier.

Table 5.8 The effect of tension damage upper limit on ultimate load

Upper limit	0.5	0.7	0.9	0.97	0.99
Ultimate load (kN)	3.36	3.67	5.04	5.86	6.00

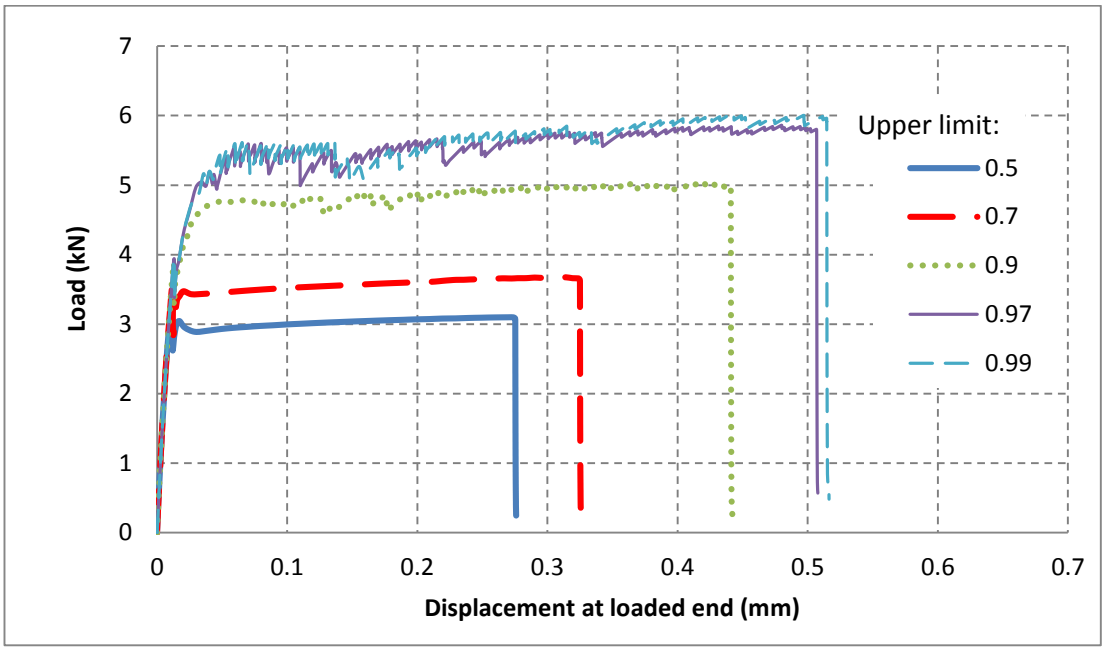

Figure 5.25 Load-displacement curves for Specimen III-1 from Yao et al. (2005) with different tension damage factor upper limits

The load-displacement curves from these models are shown in Figure 5.25 and the ultimate loads are summarised in Table 5.8. As seen in Figure 5.25, the ultimate load from the simulation of FRP-concrete interface is found to increase with an increasing upper limit in the tension damage model, a phenomenon that conforms to the prediction obtained from Sections 5.4 and 5.5. The difference between the ultimate loads at damage factor upper limits at 0.97 and 0.99 is around 2%. To aid convergence, the value of 0.97 is adopted for subsequent simulations.

5.6.2 The upper limit for the compression damage factor

Once again, Birtel and Mark's (2006) model is employed with different values for the upper limit in the compression damage model (Table 5.9), and with a value of 0.97 as the upper limit in the tension damage model.

Table 5.9 The effect of compression damage upper limit on ultimate load

	D1	D2	D3	D4	D5
Upper limit	0.5	0.7	0.9	0.97	0.99
Ultimate load (kN)	6.163	6.122	6.105	6.058	5.963

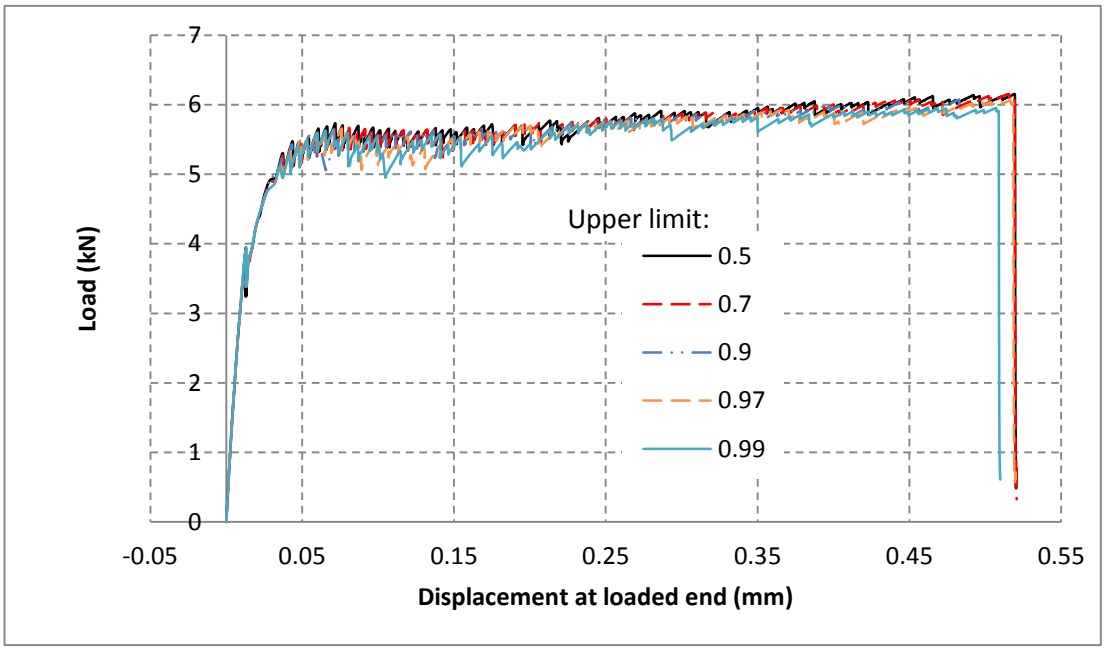

Figure 5.26 Load-displacement curves for Specimen III-1 from Yao et al. (2005) with different compression damage factor upper limits

The load-displacement curves from these models are shown in Figure 5.26 and the ultimate loads are summarised in Table 5.9. In this case, the differences between the responses are imperceptible, as seen in Figure 5.26. Despite of that, as demonstrated in Figure 5.26, it is found that the peak load from the simulation of FRP-concrete interface drops slightly with the increasing value of upper limit in compression damage model, a phenomenon which was seen in Sections 5.4 and 5.5.

For the subsequent simulations, the value of 0.97 is adopted as the upper limit in the compression damage model.

5.7 Conclusions

The scalar approach has been the most widely used to describe the damage behaviour of concrete. In this chapter, eight empirical damage models have been reviewed. In order to examine the constitutive performance of these damage models in predicting the unloading/reloading paths, they are compared with the test data in compression and tension. It is found that Birtel and Mark's (2006) model is in the best agreement with that test data.

A series of simulations are conducted under cyclic loads to demonstrate the role of damage factors in simulations using concrete damaged plasticity. In monotonic uniaxial loading, biaxial compression loading and biaxial tension loading, the response is not affected by the choice of the damage model. In biaxial compression-tension load, it is found that the higher value in the tension damage factor leads to higher value in the ultimate load; while the lower value in the compression damage factor leads to higher value in the ultimate load.

The effect of damage model on FRP-concrete interfacial response is examined and compared with the test data from Yao et al. (2005). It is found that Birtel and Mark's (2006) model provides the best match with the ultimate load.

The effect of upper limit of damage factor in tension and compression is considered for the debonding problem. It is found that the maximum value in tension damage makes a significant difference to the response; whereas the upper limit of compression damage has little influence on the response.

Chapter 6
Effects of CDP model parameters on FRP-concrete interfacial behaviour

6.1 Introduction

In Chapter 5, the damage model, as a bridge between the effective stress and Cauchy's stress, was found to play a significant role in the concrete damaged plasticity (CDP) model and have a significant effect on the ultimate load even under monotonic static loading. Through a series of investigations in Chapter 5, Birtel and Mark (2006) model was selected as the damage model in the CDP model to describe the damage behaviour of concrete for simulations hereinafter in this thesis.

Apart from the damage model, the CDP model also requires the definition of concrete tension stress-cracking displacement and compression stress-strain relationships depicting the damaged plasticity behaviour of concrete under tension and compression respectively.

As discussed in Chapter 2, in most cases, the failure at the FRP-concrete interface occurs in the concrete body (Gdoutos et al. 2000; Smith and Teng 2001). It is for this reason that the definitions of damage and plasticity of concrete are of high significance in the simulation of FRP-concrete interface.

In this chapter, the effect of concrete fracture energy and compression strain energy are explored in detail, using Specimens III-1 and III-5 in Yao et al. (2005) as reference cases.

6.2 Effect of tensile fracture energy

In this section, the effect of tensile fracture energy on FRP-concrete interfacial behaviour is investigated in two ways: varying the fracture energy with the tensile stress-strain shape either changed or remaining unchanged. They are called shape-

change approach and constant shape approach hereafter. The same material and geometrical properties are used as in Chapter 3 unless stated otherwise. The only variation is the tensile stress versus cracking displacement relationship. The tensile stress versus cracking displacement relationship is changed to vary the tensile fracture energy from 0.5 to 2 G_f, with G_f = 0.0698 N/mm being the tensile fracture energy for concrete with a strength of 27.1 MPa (Specimen III-1 in Yao et al (2005)). Accordingly, $2G_f$ = 0.1397 N/mm.

6.2.1 Shape-change approach

In this section, the shape-change approach is employed to vary the tensile fracture energy in simulation of Specimens III-1 and III-5 in Yao et al. (2005). The cracking displacement is changed by multiplying a factor to achieve the desired fracture energy (area under the curve) while keeping the tension stress constant, as shown in Figure 6.1.

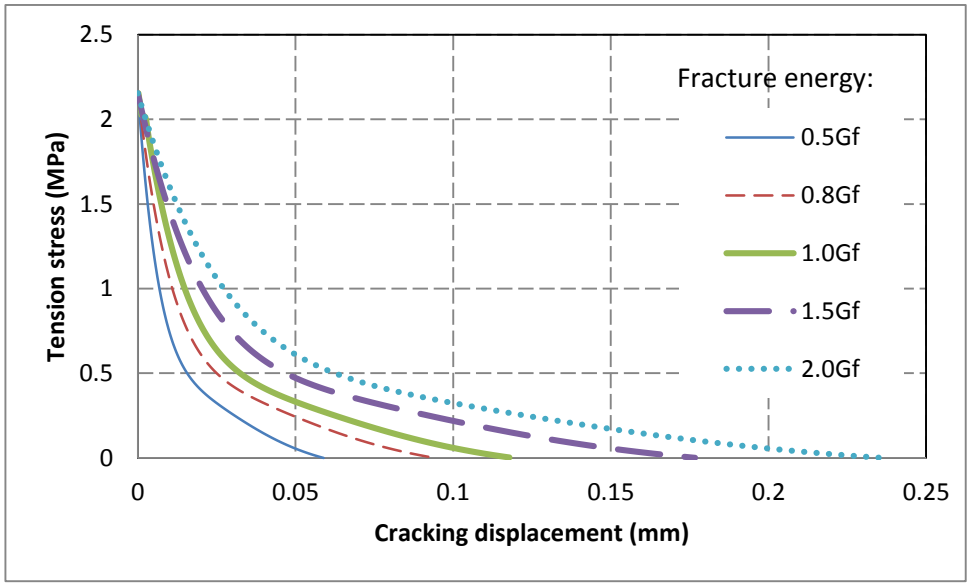

Figure 6.1 Shape-change approach: displacement varied to give different fracture energies

Debonding failure mode

As introduced earlier, Specimen III-1 in Yao et al. (2005) is employed as the reference case for debonding failure mode and the effect of the concrete fracture energy is investigated on the ultimate load of the FRP-concrete bonded interface.

When the concrete tensile fracture energy is varied from 0.5 to $2G_f$, the predicted load-displacement curves are compared in Figure 6.2. The ultimate loads for these cases are plotted in Figure 6.3 and also shown in Table 6.1. It is seen that the ultimate load of the FRP-concrete interface is reduced by about 6% when the concrete tensile fracture energy is halved from the reference case (i.e. its tensile fracture energy is $1.0G_f$), and increased by about 2% when the fracture energy is doubled. Within the range investigated, the failure mode does not change and remains as debonding failure as shown in Figure 6.4.

It may therefore be concluded that the tensile fracture energy of concrete does not play a critical role in the debonding behaviour of FRP-concrete bonded interface.

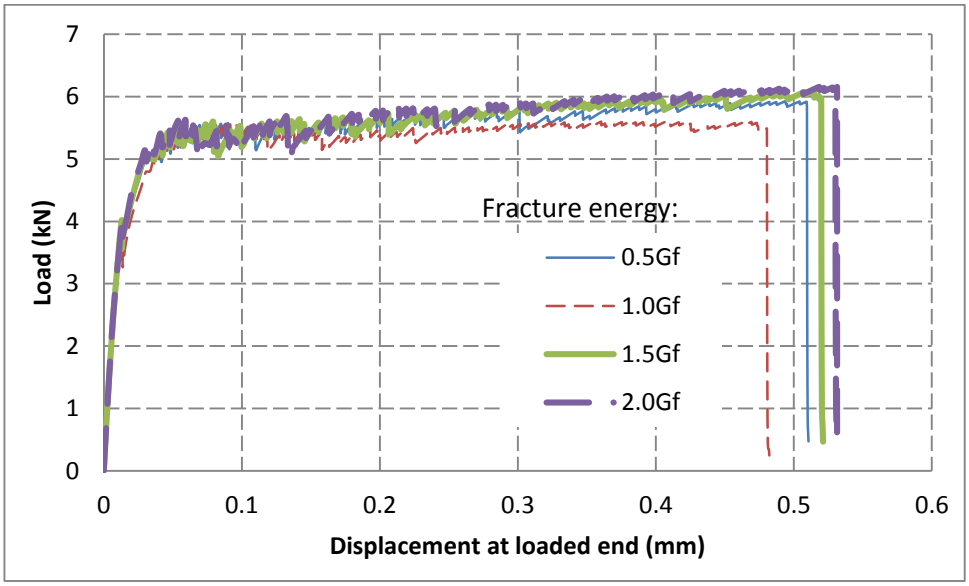

Figure 6.2 Shape-change approach: predicted load versus displacement curves with Specimen III-1 in Yao et al. (2005) as the reference case

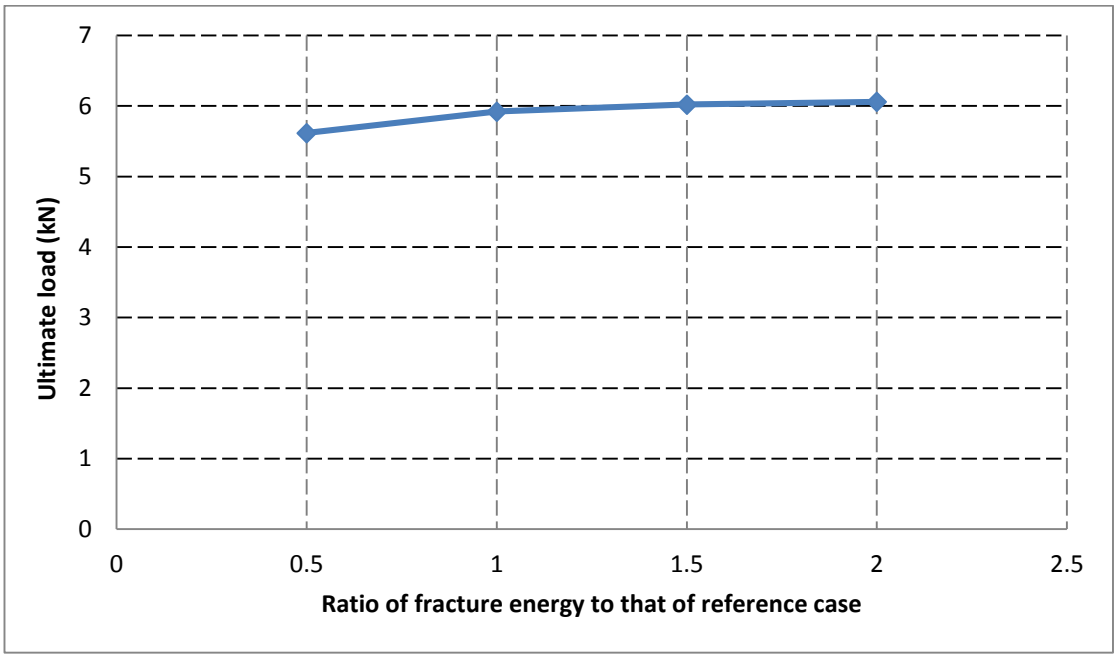

Figure 6.3 Shape-change approach: effect of tensile fracture energy on the ultimate load

Table 6.1 Shape-change approach: predicted ultimate load (with Specimen III-1 in Yao et al. (2005) as the reference case)

Fracture energy (N/mm)	Ratio of fracture energy to that of reference case	Ultimate load (kN)
0.0349 (0.5G_f)	0.5	5.6
0.0698 (1.0G_f)	1.0	5.9
0.1048 (1.5G_f)	1.5	6.0
0.1397 (2.0G_f)	2.0	6.1

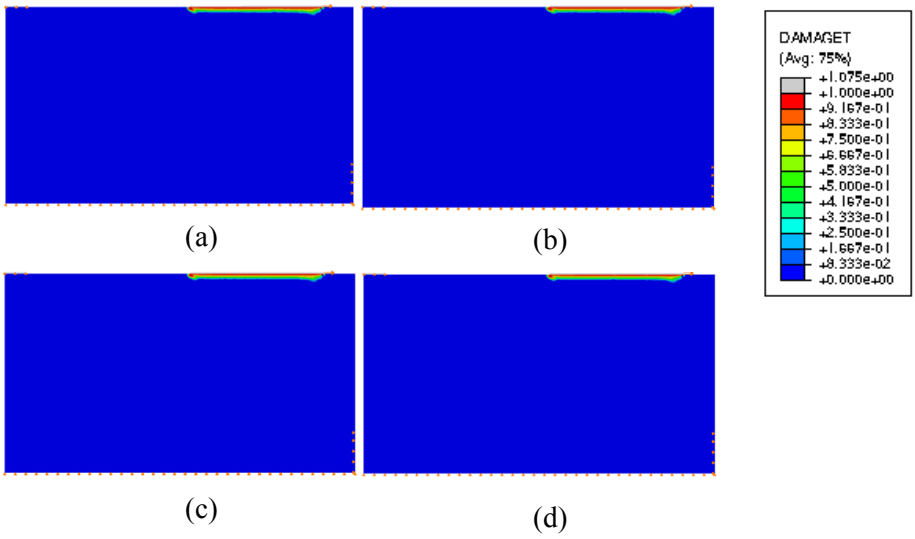

Figure 6.4 Shape-change approach: predicted failure modes when ratio of fracture energy to that of reference case of Specimen III-1 in Yao et al. (2005) is equal to (a) 0.5, (b) 1.0, (c) 1.5, and (d) 2.0

CPF failure mode

Specimen III-5 in Yao et al. (2005) is used as the reference case for the CPF failure mode. It is investigated with different values of concrete tensile fracture energy for their effect on the ultimate load of FRP-concrete interface.

The load-displacement curves from these analyses are compared in Figure 6.5. The relationship between the ultimate load and fracture energy ratio is shown in Figure 6.6 and Table 6.2.

In Figure 6.6 and Table 6.2, it is found that the ultimate load increases with the increase of fracture energy before the fracture energy reaches a critical value (the fracture energy of the reference test in this case). That is because the CPF mode is dominated by tensile cracking behaviour of concrete, which is reflected by the tensile fracture energy. A change of failure mode occurs in this case at the critical fracture energy, as will be discussed below.

As the fracture energy increases further, the ultimate load reduces. The failure is FRP debonding in these cases, with the cracks at the interface becoming shallower as the tensile fracture energy increases.

The predicted failure mode is shown in Figure 6.7. The failure is CPF when the fracture energy is less than or equal to the value of the reference case. A 50% increase or more changes the failure mode to FRP debonding.

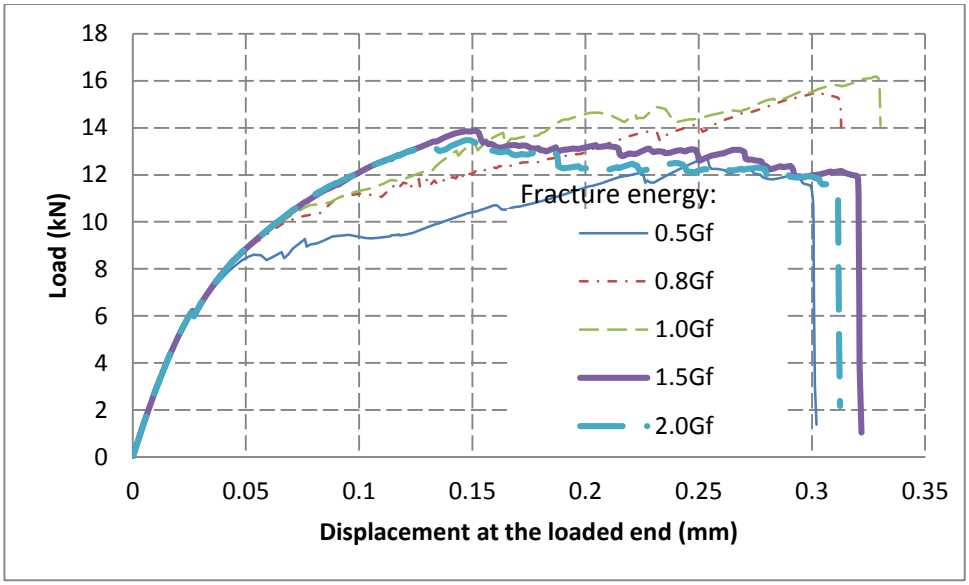

Figure 6.5 Shape-change approach: predicted load versus displacement curves with Specimen III-5 in Yao et al. (2005) as the reference case

Table 6.2 Shape-change approach: predicted ultimate load (with Specimen III-5 in Yao et al. (2005) as the reference case)

Fracture energy (N/mm)	Ratio of fracture energy to that of reference case	Ultimate load (kN)
0.0349($0.5G_f$)	0.5	14.8
0.05584($0.8G_f$)	0.8	15.5
0.0698($1.0G_f$)	1.0	15.9
0.1048($1.5G_f$)	1.5	13.6

0.1397(2.0G_f)	2.0	12.4

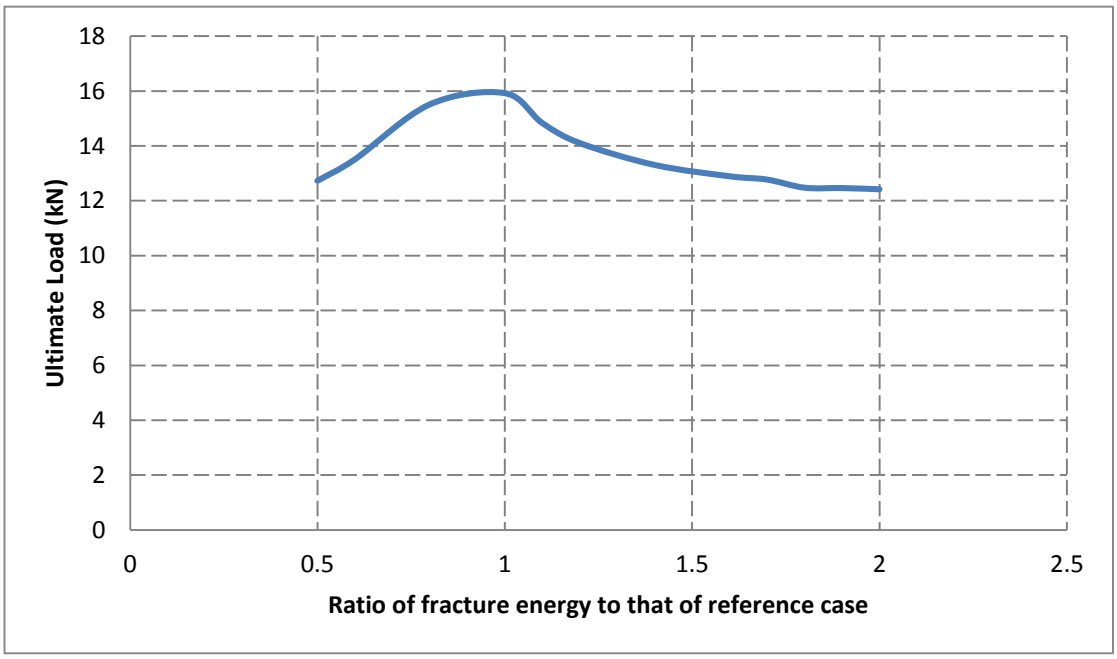

Figure 6.6 Shape-change approach: effect of tensile fracture energy on the ultimate load (with Specimen III-5 in Yao et al. (2005) as the reference case)

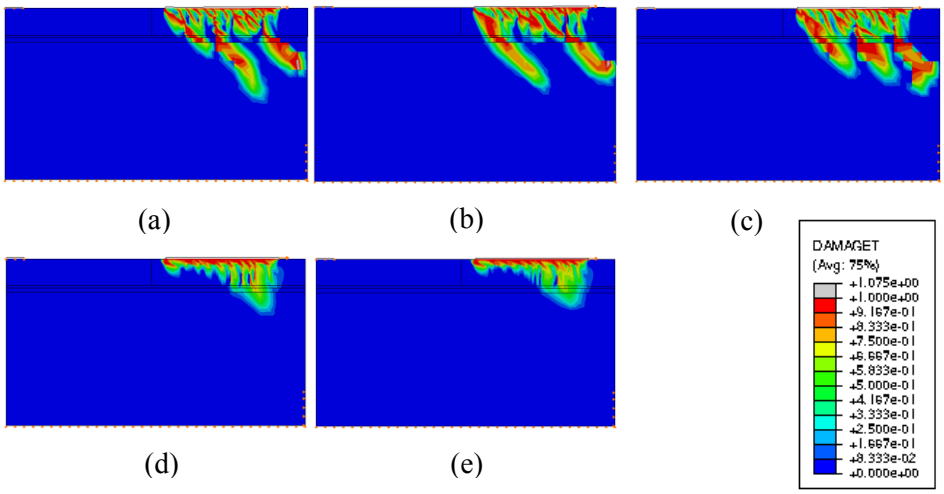

Figure 6.7 Shape-change approach: predicted failure modes when ratio of fracture energy to that of reference case of Specimen III-5 in Yao et al. (2005) is equal to (a) 0.5, (b) 0.8, (c) 1.0, (d) 1.5, and (e) 2.0

6.2.2 Constant shape approach

In this section, the constant shape approach is employed to vary the tensile fracture energy in simulations of Specimens III-1 and III-5 in Yao et al. (2005). The tensile stress and the cracking displacement are multiplied with a factor to achieve the desired fracture energy while keeping the shape constant, as shown in Figure 6.8.

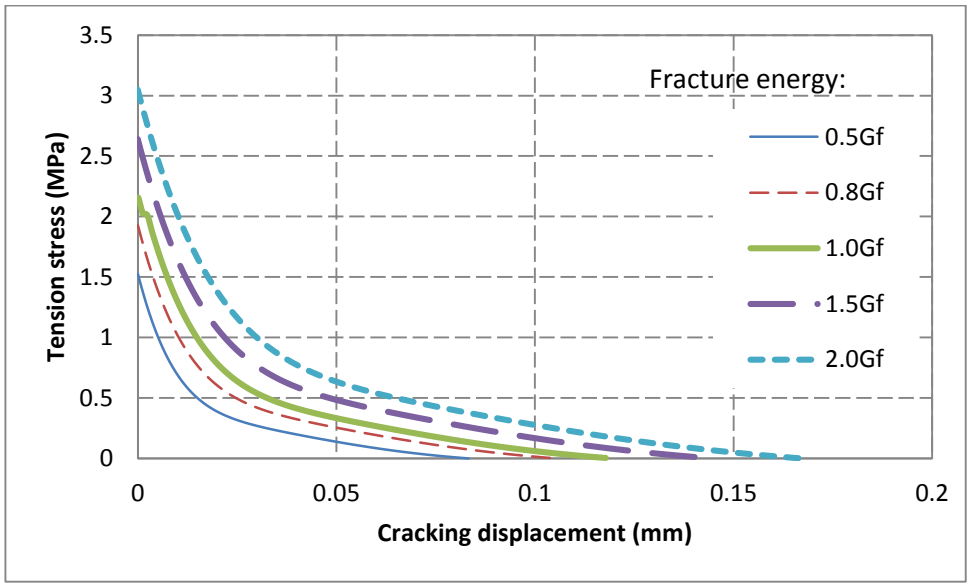

Figure 6.8 Constant shape approach: stress and displacement varied proportionately to give different fracture energies

Debonding failure mode

Once again, Specimen III-1 in Yao et al. (2005) is employed as the reference case for debonding failure mode and the effect of the concrete fracture energy is investigated on the ultimate load of the FRP-concrete bonded interface.

When the concrete tensile fracture energy is varied from 0.5 to 2G_f, the predicted load-displacement curves are compared in Figure 6.9. The ultimate loads for these cases are plotted in Figure 6.10 and also shown in Table 6.3. Similarly, it is seen that the ultimate load of the FRP-concrete bonded interface is reduced by about 6% when the concrete tensile fracture energy is halved from the reference case, and increased by about 4%

when the fracture energy is doubled. Within the range investigated, the failure mode also does not change and remains as debonding failure as shown in Figure 6.11.

Similarly, it may therefore be concluded that the tensile fracture energy of concrete does not play a critical role in the debonding behaviour of FRP-concrete bonded interface.

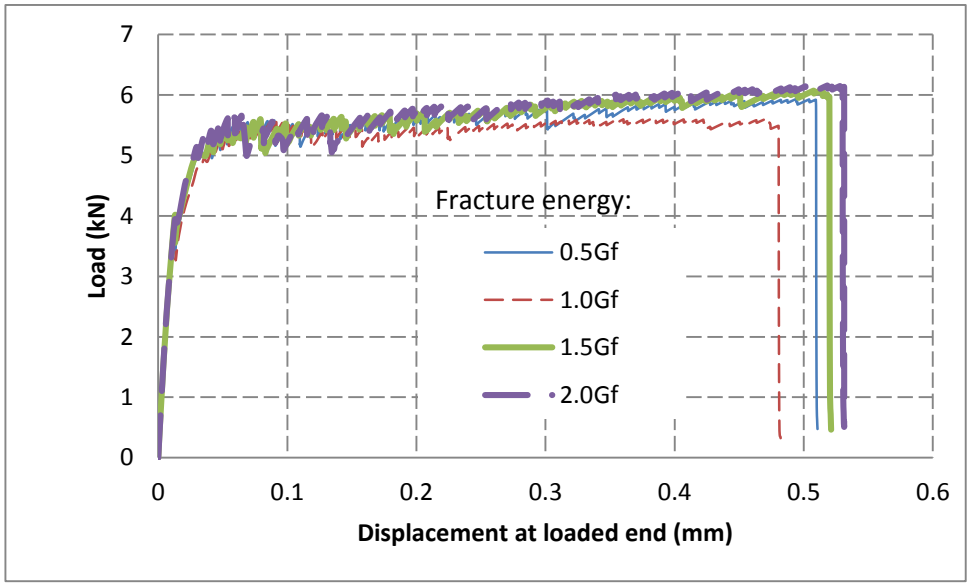

Figure 6.9 Constant shape approach: predicted load versus displacement curves with Specimen III-1 in Yao et al. (2005) as the reference case

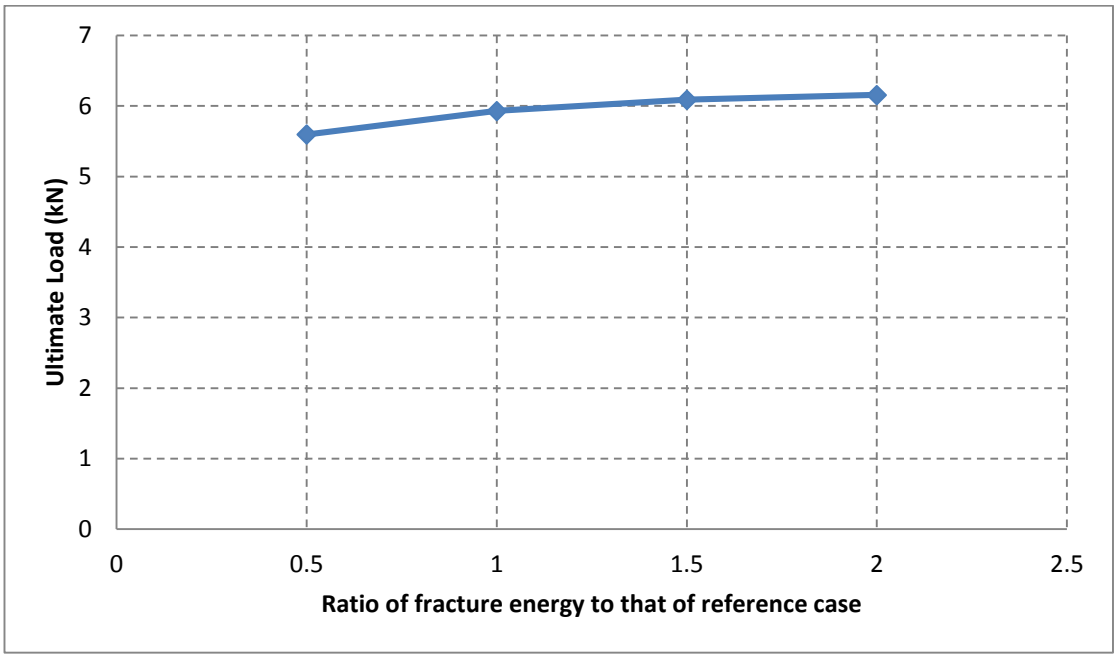

Figure 6.10 Constant shape approach: effect of tensile fracture energy on the ultimate load

Table 6.3 Constant shape approach: predicted ultimate load (with Specimen III-1 in Yao et al. (2005) as the reference case)

Fracture energy (N/mm)	Coefficient for fracture energy	Ultimate load (kN)
0.0349(0.5G_f)	0.5	5. 60
0.0698(1.0G_f)	1	5.93
0.1048(1.5G_f)	1.5	6.09
0.1397(2.0G_f)	2.0	6.16

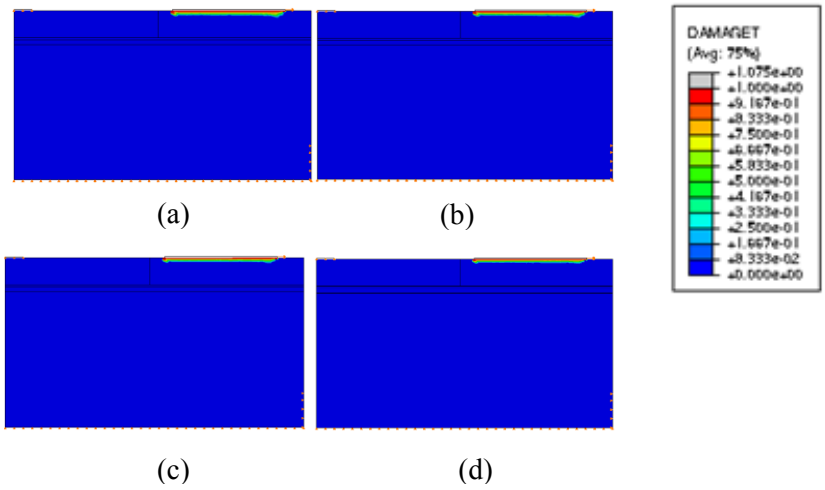

Figure 6.11 Constant shape approach: predicted failure modes when ratio of fracture energy to that of reference case of Specimen III-1 in Yao et al. (2005) is equal to (a) 0.5, (b) 1.0, (c) 1.5, (d) 2.0

CPF failure mode

Once again, Specimen III-5 in Yao et al. (2005) is used as the reference case for the CPF failure mode. It is investigated with different values of concrete tensile fracture energy for their effect on the ultimate load of FRP-concrete bonded interface.

The load-displacement curves from these analyses are compared in Figure 6.12. The relationship between the ultimate load and fracture energy ratio is shown in Figure 6.13 and Table 6.4.

In Figure 6.13 and Table 6.4, it is also found that the ultimate load increases with the increase of fracture energy before the fracture energy reaches a critical value (the fracture energy of the reference test in this case). That is because the CPF mode is dominated by tensile cracking behaviour of concrete, which is reflected by the tensile fracture energy. A change of failure mode also occurs in this case at the critical fracture energy, as will be discussed below.

As the fracture energy increases further, the ultimate load is also found to reduce. The failure is FRP debonding in these cases, with the cracks at the interface becoming shallower as the tensile fracture energy increases.

The predicted failure mode is shown in Figure 6.14. The failure is CPF when the fracture energy is less than or equal to the value of the reference case. A 50% increase or more changes the failure mode to FRP debonding.

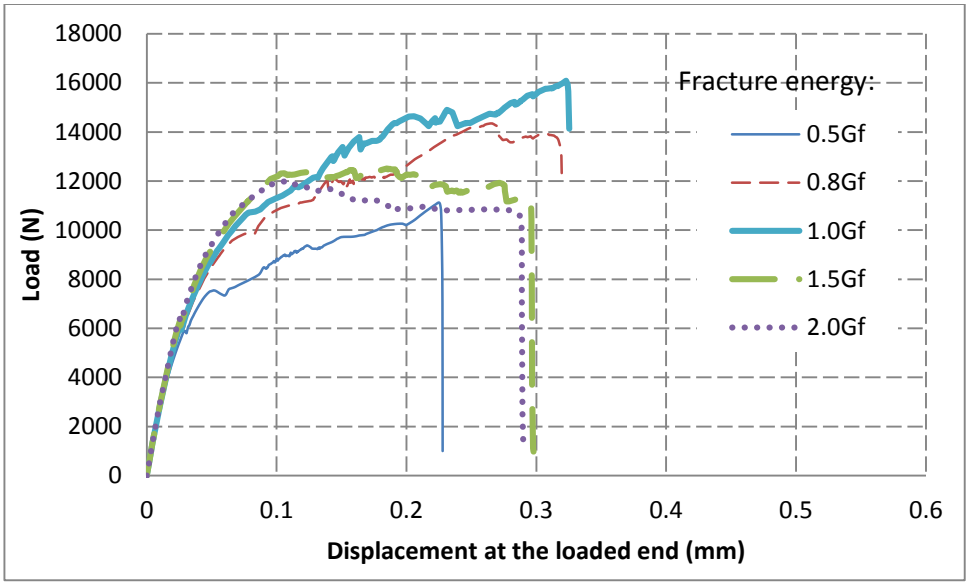

Figure 6.12 Constant shape approach: predicted load versus displacement curves with Specimen III-1 in Yao et al. (2005) as the reference case

Table 6.4 Constant shape approach: predicted ultimate load (with Specimen III-5 in Yao et al. (2005) as the reference case)

Fracture energy(N/mm)	Coefficient for fracture energy	Ultimate load(N)
0.0349($0.5G_f$)	0.5	11.038
0.05584($0.8G_f$)	0.8	14.352
0.0698($1.0G_f$)	1	16.250
0.1048($1.5G_f$)	1.5	12.512

0.1397(2.0G_f)	2.0	11.991

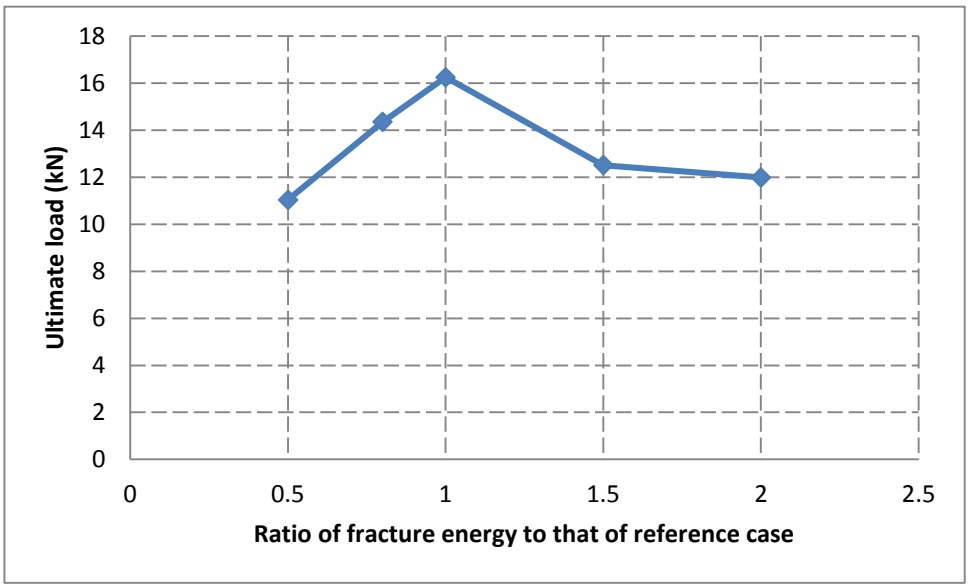

Figure 6.13 Constant shape approach: effect of tensile fracture energy on the ultimate load

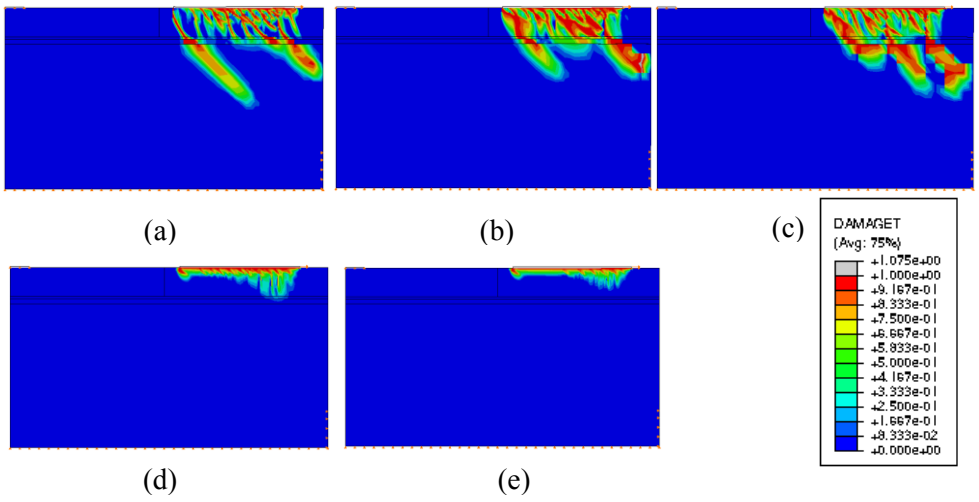

Figure 6.14 Constant shape approach: failure modes when ratio of fracture energy to that of reference case of Specimen III-5 in Yao et al. (2005) is equal to (a) 0.5, (b) 0.8, (c) 1.0, (d) 1.5, and (e) 2.0

6.3 Effect of compression hardening strain energy

In this section, the effect of compression hardening strain energy on FRP-concrete interfacial behaviour is also investigated in two ways: varying the hardening strain energy with the compression stress-inelastic strain shape either changed or remaining constant. They are called shape change approach and constant shape approach hereafter again. The same material and geometrical properties are used as in Chapter 3 unless stated otherwise. The only variation is the concrete compression stress versus inelastic strain relationship. This relationship is changed to vary the compression hardening strain energy from 0.5 to $2g_c$, with g_c = 0.339 MPa being the compression strain energy for concrete with a strength of 27.1 MPa (Specimen III-1 in Yao et al (2005)). Accordingly, $2g_c$ = 0.678 MPa.

6.3.1 Shape-change approach

In this section, the shape-change approach is employed to vary the compression hardening strain energy in simulations of Specimens III-1 and III-5 in Yao et al. (2005). The inelastic strain is changed by multiplying a factor to achieve the desired hardening strain energy (area under the curve) while keeping the compression stress constant, as shown in Figure 6.15.

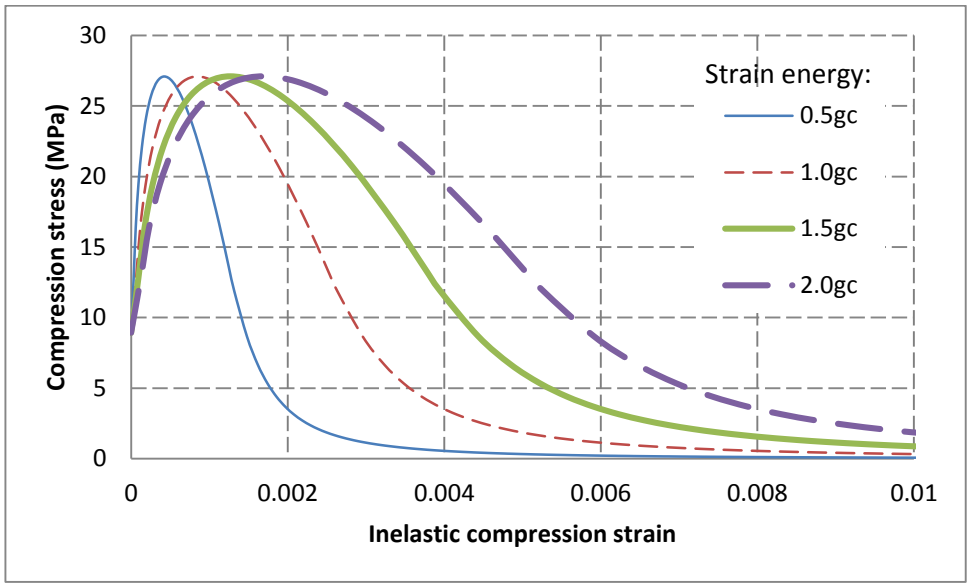

Figure 6.15 Shape-change approach: inelastic strain varied to give different hardening strain energies

Debonding failure mode

Specimen III-1 in Yao et al. (2005) is again employed as the reference case for debonding failure mode and the effect of the concrete hardening strain energy is investigated on the ultimate load of the FRP-concrete bonded interface.

When the concrete hardening strain energy is varied from 0.5 to $2g_c$, the predicted load-displacement curves are compared in Figure 6.16. The ultimate loads for these cases are plotted in Figure 6.17 and also shown in Table 6.5. It is seen that the ultimate load of the FRP-concrete interface increases with the increase of compression hardening strain energy. In spite of that, within the range investigated, the failure mode also does not change and remains as debonding failure as shown in Figure 6.18.

It may therefore be concluded that the debonding behaviour at the FRP-concrete bonded interface is highly related to compression hardening strain energy of concrete.

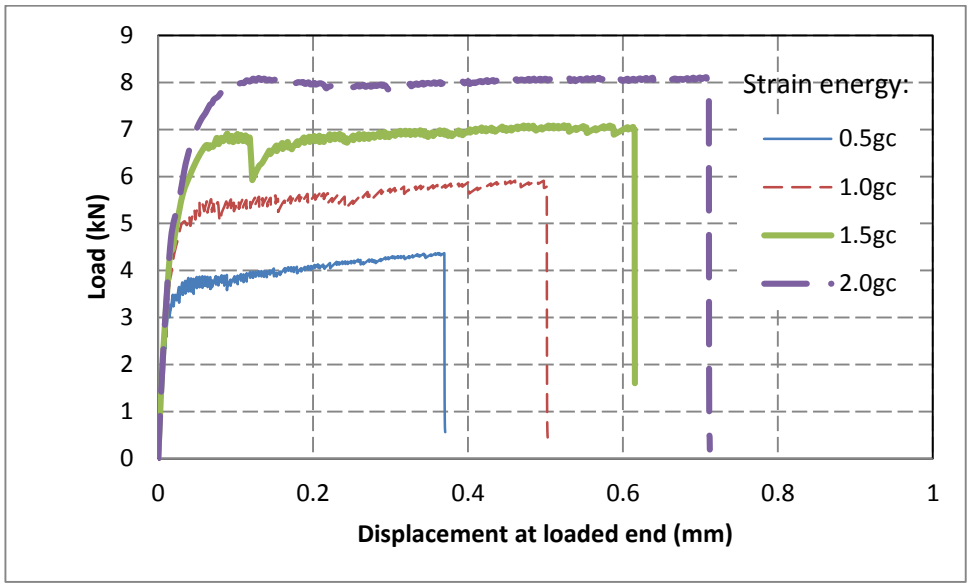

Figure 6.16 Shape-change approach: predicted load versus displacement curves with Specimen III-1 in Yao et al. (2005) as the reference case

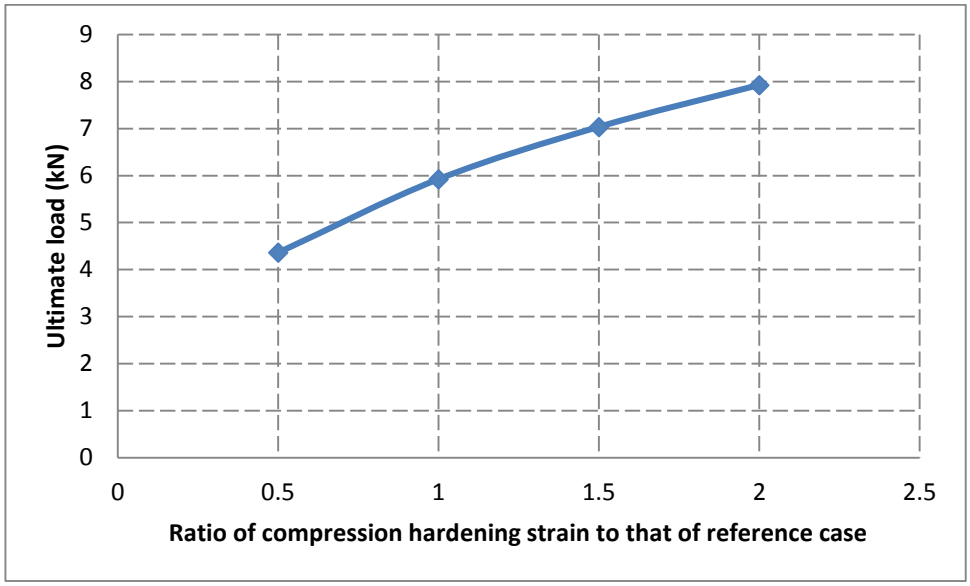

Figure 6.17 Shape-change approach: effect of compression hardening strain energy on the ultimate load

Table 6.5 Shape-change approach: predicted ultimate load (with Specimen III-1 in Yao et al. (2005) as the reference case)

Hardening strain energy (MPa)	Ratio of strain energy to that of reference case	Ultimate load (kN)
0.1695 ($0.5g_c$)	0.5	4.37
0.339 ($1.0g_c$)	1.0	5.92
0.5085 ($1.5g_c$)	1.5	7.09
0.678 ($2.0g_c$)	2.0	8.12

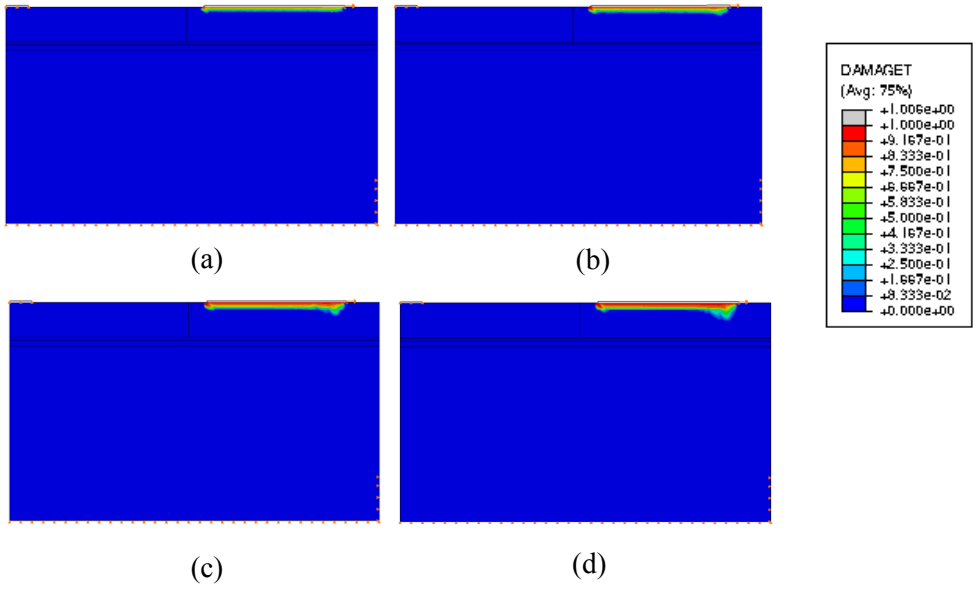

Figure 6.18 Shape-change approach: predicted failure modes when ratio of compression hardening strain energy to that of reference case of Specimen III-1 in Yao et al. (2005) is equal to (a) 0.5, (b) 1.0, (c) 1.5, and (d) 2.0

CPF failure mode

Similarly, Specimen III-5 in Yao et al. (2005) is used as the reference case for the CPF failure mode. It is investigated with different values of compression hardening strain energy of concrete for their effect on the ultimate load of FRP-concrete.

The load-displacement curves from these analyses are compared in Figure 6.19. The relationship between the ultimate load and hardening strain energy ratio is shown in Figure 6.20 and Table 6.6.

In Figure 6.20 and Table 6.6, it is found that the ultimate load increases with the increase of compression strain energy before the compression strain energy reaches a critical value (i.e. the hardening strain energy of the reference test in this case $1.0g_c$). That is because the debonding mode is dominated by compression strain energy, as discussed before, while CPF mode is dominated by tensile cracking behaviour of concrete, which is reflected by the tensile fracture energy. The FRP would be debonded from the concrete prism when the compression hardening strain energy is insufficient, as that has occurred in the case of $0.5g_c$.

A change of failure mode occurs in this case at the critical fracture energy, as will be discussed below.

As the hardening strain energy increases further, the ultimate load almost is kept constant. The failure is CPF in these cases, with the concrete prism cracked from the FRP end, before its complete debonding.

The predicted failure mode is shown in Figure 6.21. The failure is FRP debonding when the hardening strain energy is less than or equal to the value of the reference case. A 50% increase or more changes the failure mode to CPF.

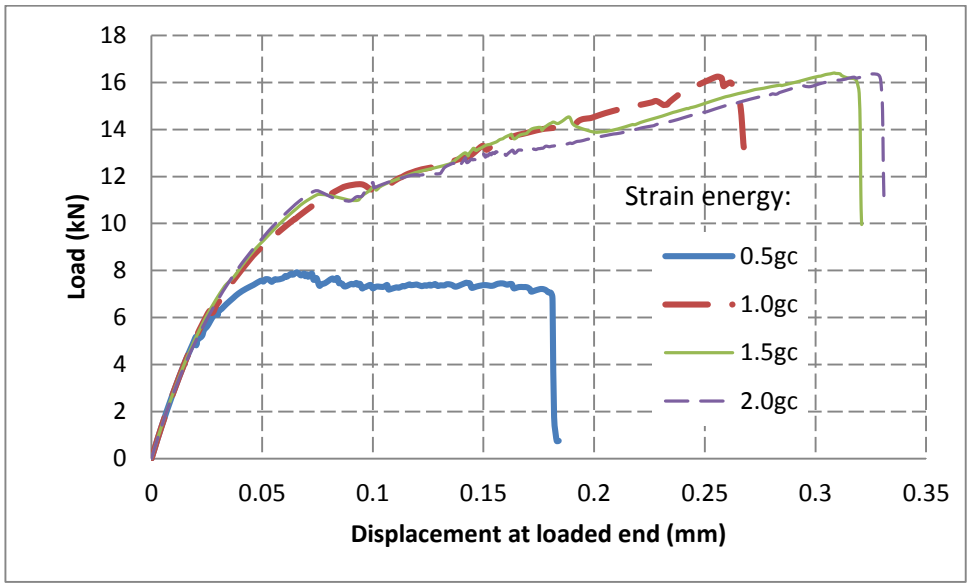

Figure 6.19 Shape-change approach: predicted load versus displacement curves with Specimen III-5 in Yao et al. (2005) as the reference case

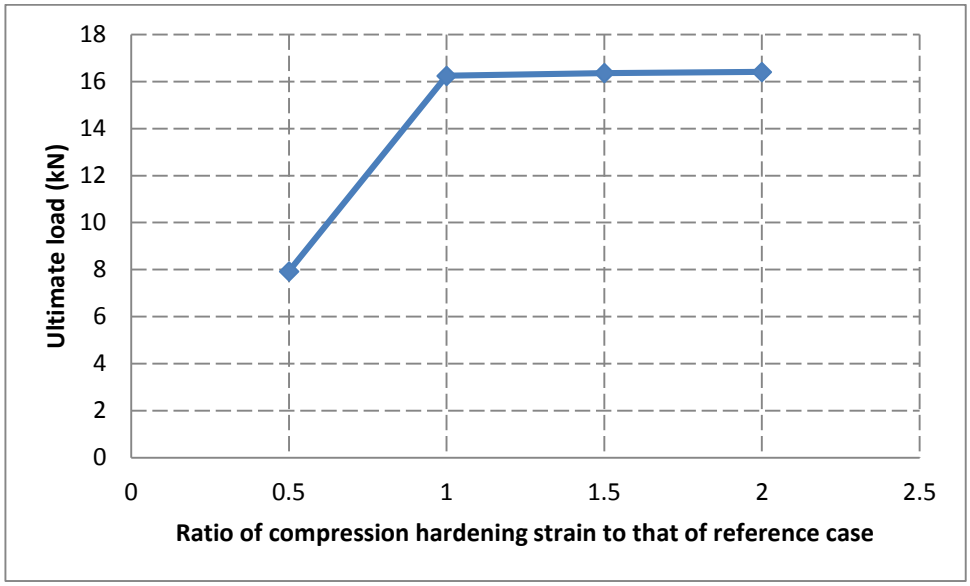

Figure 6.20 Shape-change approach: effect of compression hardening strain energy on the ultimate load

Table 6.6 Shape-change approach: predicted ultimate loads (with Specimen III-5 in Yao et al. (2005) as the reference case)

Hardening strain energy in compression (MPa)	Ratio of hardening strain energy to that of reference case	Ultimate load (kN)
0.1695($0.5g_c$)	0.5	7.93
0.339($1.0g_c$)	1	16.25
0.5085($1.5g_c$)	1.5	16.36
0.678($1.0g_c$)	2.0	16.41

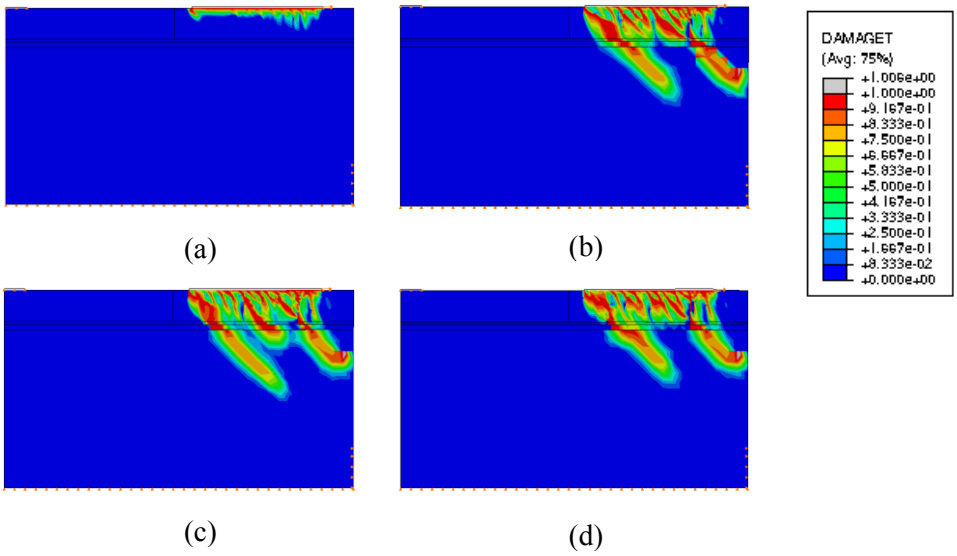

Figure 6.21 Shape-change approach: predicted failure modes when ratio of compression hardening strain energy to that of reference case of Specimen III-5 in Yao et al. (2005) is equal to (a) 0.5, (b) 1.0, (c) 1.5, and (d) 2.0

6.3.2 Constant shape approach

Here the constant shape approach is employed to vary the compression hardening strain energy in simulations of Specimens III-1 and III-5 in Yao et al. (2005). The stress and inelastic strain are changed proportionately by multiplying a factor simultaneously to achieve the desired hardening strain energy (area under the curve) while keeping the shape constant, as shown in Figure 6.22.

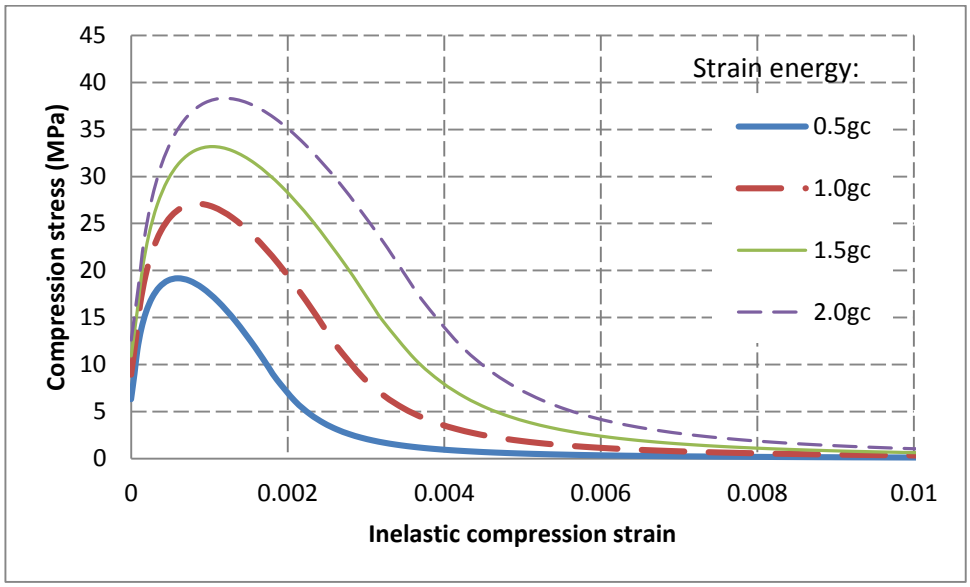

Figure 6.22 Constant shape approach: stress and inelastic strain varied proportionately to give different hardening strain energies

Debonding failure mode

As introduced earlier, Specimen III-1 in Yao et al. (2005) is again employed as the reference case for debonding failure mode and the effect of the concrete hardening strain energy is investigated on the ultimate load of the FRP-concrete bonded interface.

When the concrete hardening strain energy is varied from 0.5 to $2g_c$, the predicted load-displacement curves are compared in Figure 6.23. The ultimate loads for these cases are plotted in Figure 6.24 and also shown in Table 6.7. It is also seen that the ultimate load of the FRP-concrete bonded interface almost increases linearly with the increase of compression strain energy. In spite of that, within the range investigated, the failure mode also does not change and remains as debonding failure as shown in Figure 6.25.

It may therefore be inferred that the debonding behaviour at the FRP-concrete interface is highly related to concrete compression strain energy.

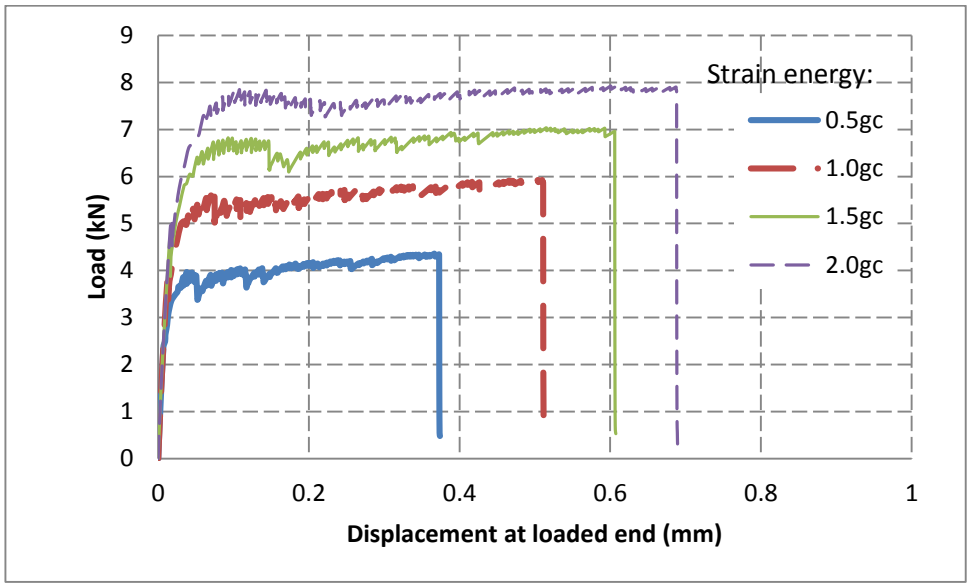

Figure 6.23 Constant shape approach: predicted load versus displacement curves with Specimen III-1 in Yao et al. (2005) as the reference case

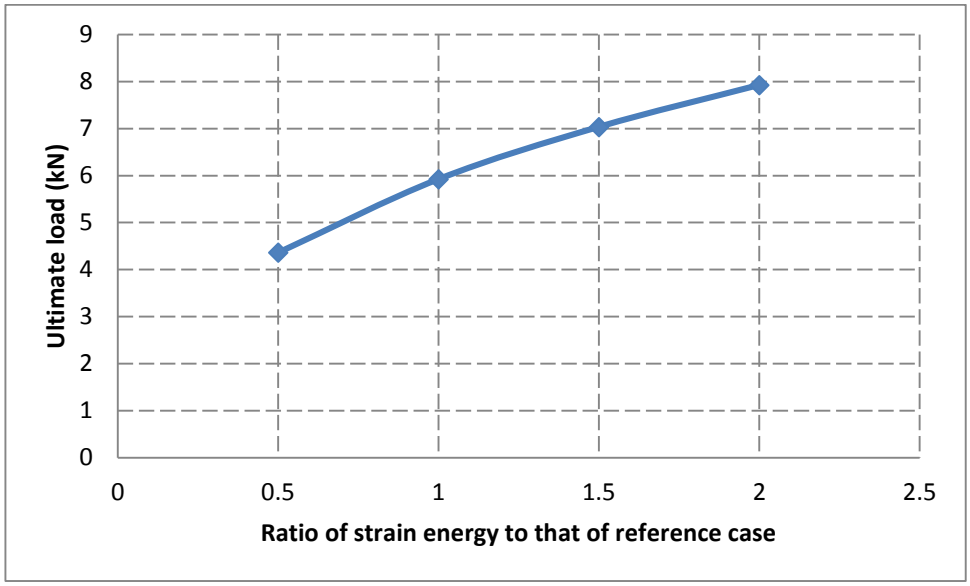

Figure 6.24 Constant shape approach: effect of compression hardening strain energy on the ultimate load

Table 6.7 Constant shape approach: predicted ultimate loads (with Specimen III-5 in Yao et al. (2005) as the reference case)

Hardening strain energy in compression (MPa)	Ratio of hardening strain energy to that of reference case	Ultimate load (kN)
0.1695($0.5g_c$)	0.5	4.36
0.339($1.0g_c$)	1	5.92
0.5085($1.5g_c$)	1.5	7.03
0.678($2.0g_c$)	2.0	7.92

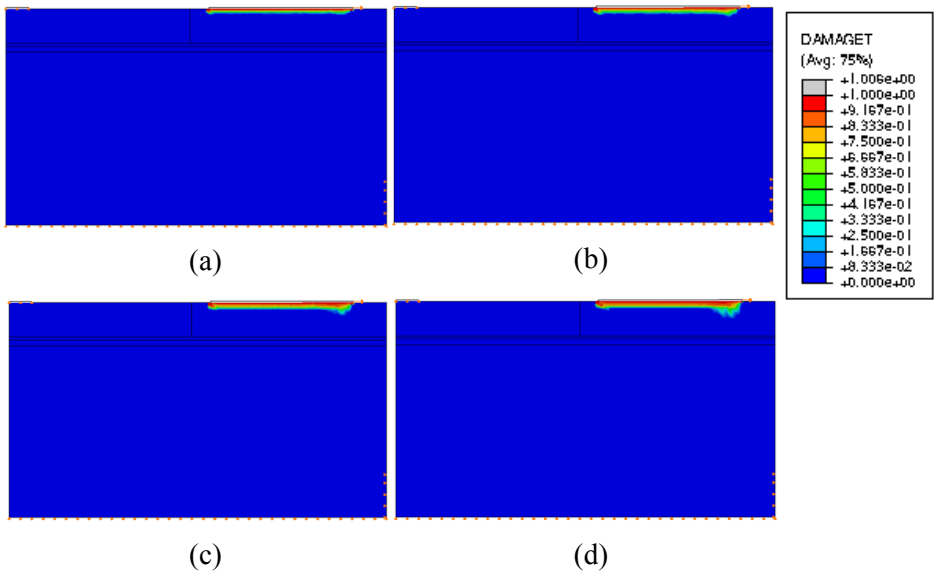

Figure 6.25 Constant shape approach: predicted failure modes when ratio of compression hardening strain energy to that of reference case of Specimen III-1 in Yao et al. (2005) is equal to (a) 0.5, (b) 1.0, (c) 1.5, and (d) 2.0

CPF failure mode

Similarly, Specimen III-5 in Yao et al. (2005) is used as the reference case for the CPF failure mode. It is investigated with different values of compression hardening strain

energy of concrete for their effect on the ultimate load of FRP-concrete bonded interface.

The load-displacement curves from these analyses are compared in Figure 6.26. The relationship between the ultimate load and compression strain energy ratio is shown in Figure 6.27 and Table 6.8.

In Figure 6.27 and Table 6.8, it is found that the ultimate load increases with the increase of compression hardening strain energy before the compression strain energy reaches a critical value (i.e. the compression hardening strain energy of the reference test in this case). That is because the debonding mode is dominated by compression strain energy, as discussed before, while CPF mode is dominated by tensile cracking behaviour of concrete, which is reflected by the tensile fracture energy. The FRP would be debonded from the concrete prism when the compression hardening strain energy is insufficient, as that has occurred in the case of $0.5g_c$.

A change of failure mode occurs in this case at the critical fracture energy, as will be discussed below.

As the hardening strain energy increases further, the ultimate load is almost kept constant. The failure is CPF failure mode in these cases, with the concrete prism cracked from the FRP end before its complete debonding.

The predicted failure mode is shown in Figure 6.28. The failure is FRP debonding when the hardening strain energy is less than or equal to the value of the reference case. A 50% increase or more changes the failure mode to CPF.

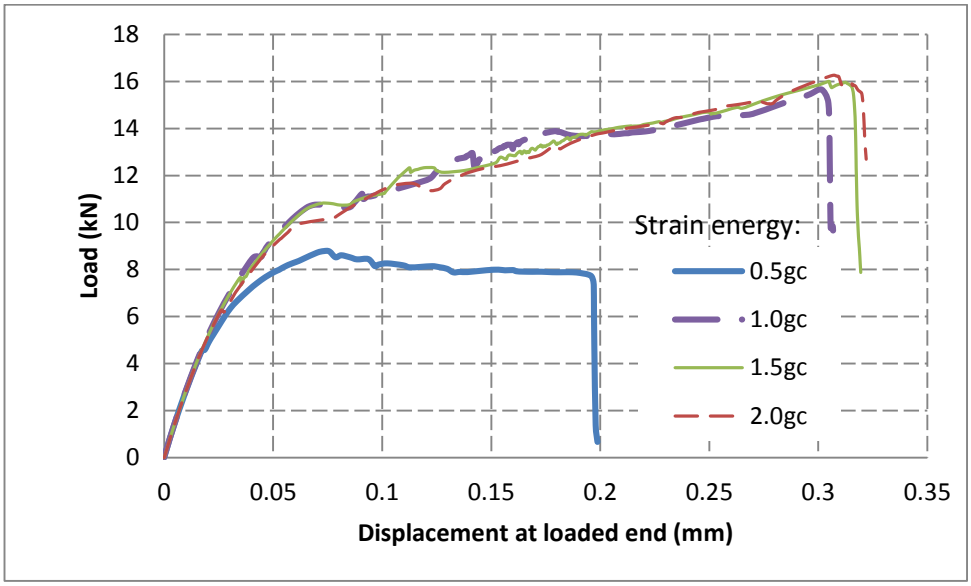

Figure 6.26 Constant shape approach: predicted load versus displacement curves with Specimen III-1 in Yao et al. (2005) as the reference case

Table 6.8 Constant shape approach: predicted ultimate loads (with Specimen III-5 in Yao et al. (2005) as the reference case)

Hardening strain energy in compression (MPa)	Ratio of strain energy to that of reference case	Ultimate load (kN)
0.1695($0.5g_c$)	0.5	8.78
0.339($1.0g_c$)	1	15.66
0.5085($1.5g_c$)	1.5	16.01
0.678($2.0g_c$)	2.0	16.26

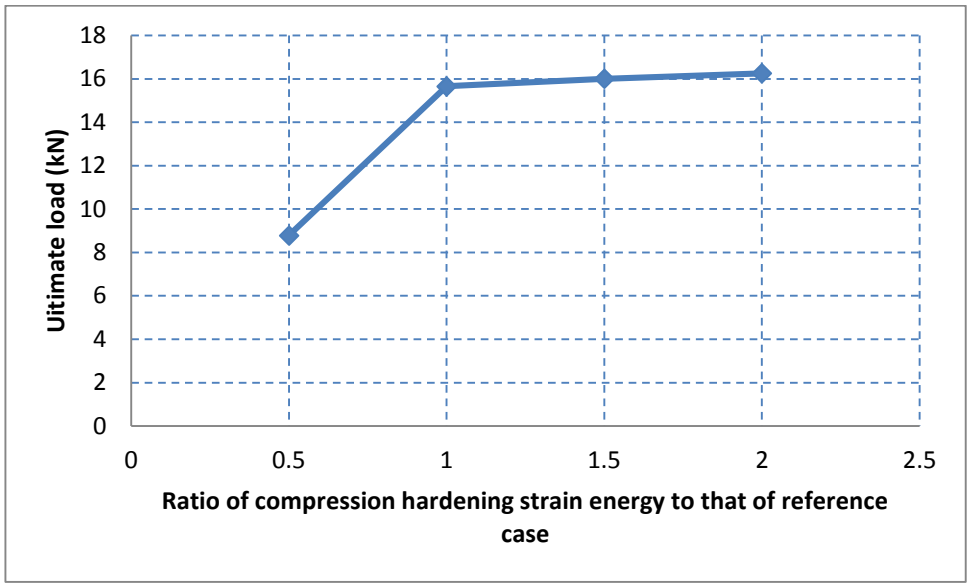

Figure 6.27 Constant shape approach: effect of compression hardening strain energy on the ultimate load

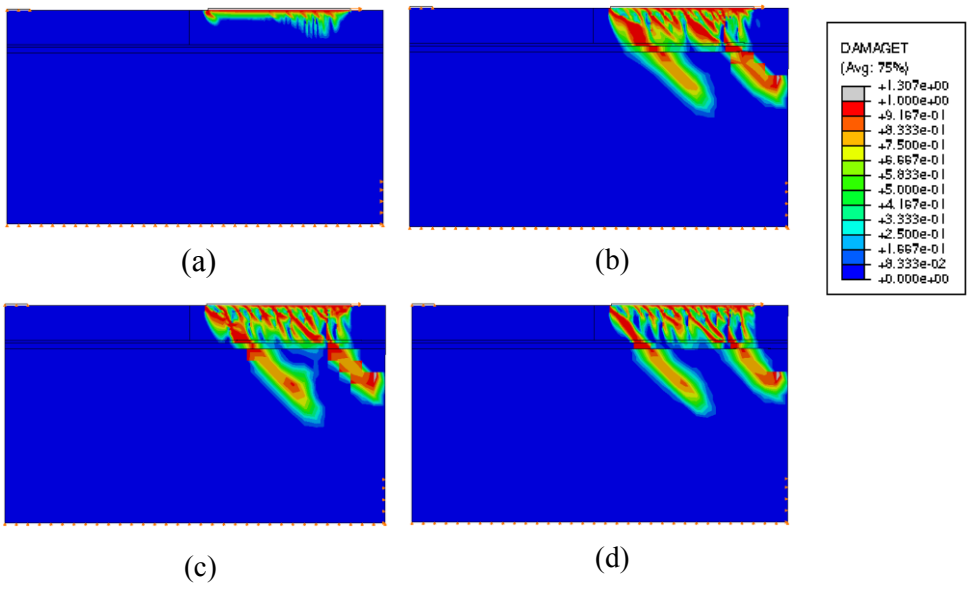

Figure 6.28 Constant shape approach: predicted failure modes of Specimen III-5 in Yao et al. (2005) when ratio of compression hardening strain energy to that of reference case is equal to (a) 0.5, (b) 1.0, (c) 1.5, and (d) 2.0

6.4 Further discussions about failure process in debonding and CPF cases

It has been found earlier in this chapter that the ultimate load decreases with the increase of fracture energy (see Figure 6.6 and Figure 6.13), once the ratio of fracture energy to that of reference case reaches a critical value (the fracture energy of the reference test in this case). Cases with $1.0G_f$ and $1.5G_f$ in shape-change approach are employed in simulations of Specimen III-5 to explain this abnormal phenomenon.

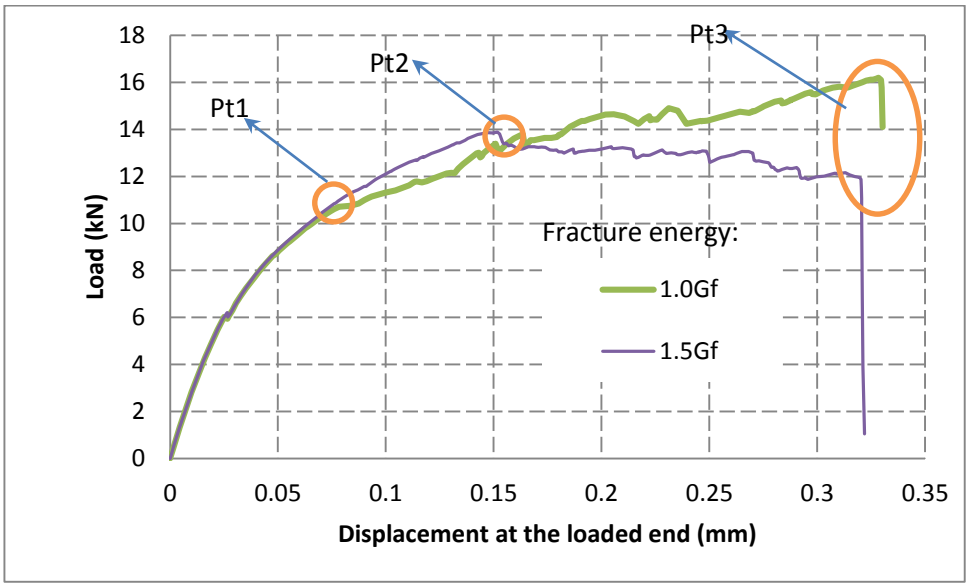

Figure 6.29 Load-displacement curves of Specimen III-5 in Yao et al. (2005) in the cases of $1.0G_f$ and $1.5G_f$ in shape-change approach

Load-displacement curves from $1.0G_f$ and $1.5G_f$ cases are shown in Figure 6.29, with three critical points to divide the whole loading process into three stages, via Stage 1 (from origin point to Pt1), Stage 2 (from Pt1 to Pt2) and Stage 3 (from Pt2 to Pt3). The failure modes of $1.0G_f$ and $1.5G_f$ cases at these three critical points are shown in Figure 6.30-Figure 6.32, respectively.

In Stage 1, only a few cracks are observed in both cases. No significant difference is found between them (see Figure 6.30), due to the fact that in this stage their mechanical

behaviour at the interface is both dominated by the debonding behaviour at the interface, which is governed by the compression strain energy of concrete.

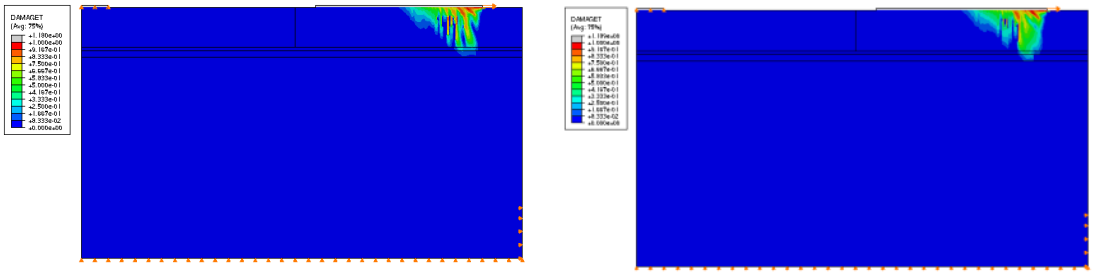

(a) (b)

Figure 6.30 Damage contours at Pt1 for the cases of (a) 1.0G_f and (b) 1.5G_f

In Stage 2, with many more cracks produced at the interface due to dedonding, the fracture energy is starting to take effect. In the case of 1.0G_f (i.e. with lower fracture energy), it is found that more cracks are observed (see Figure 6.31) with a lower load (see Figure 6.29) due to a small value of tensile fracture energy. At the end of stage 2, a crack is found to be initiated at the FRP end, a phenomenon that indicates that the CPF mode is occurring in this case. In the case of 1.5G_f, the peak value of ultimate load is achieved at the end of this stage, because the crack at the interface will become shallower in the later stage than that in this stage 2 after this point. What is worth pointing out is that the ultimate loads of these two cases at stage 2 are almost at the same level.

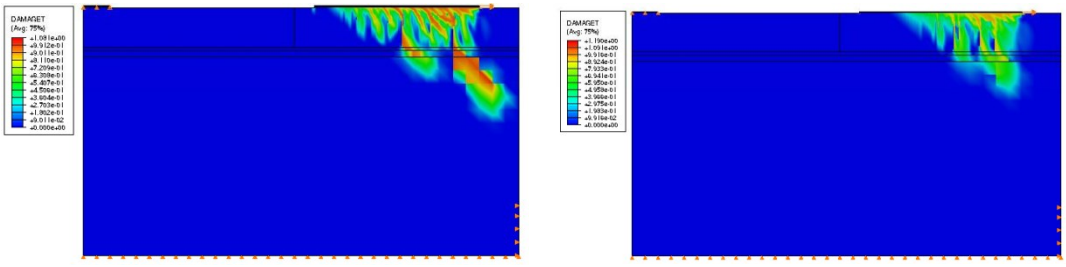

(a) (b)

Figure 6.31 Damage contours at Pt2 for the cases of (a) 1.0G_f and (b) 1.5G_f

In Stage 3, a significant difference is made between these two cases. In the case of $1.0G_f$, the cracks are propagated along the crack initiated at the FRP end. In the damage process, the crack is becoming deeper than that in the earlier stage, as shown in Figure 6.32 (a), a phenomenon that indicates the lever arm of the resistance force is always increasing. It is for this reason that the load in $1.0G_f$ increases until complete failure is achieved, as shown in Figure 6.29. In the case of $1.5G_f$, the load is decreasing since the end of stage 2 because the cracks produced in this stage becomes shallow with the increase of the applied load as shown in Figure 6.32 (b), a phenomenon that indicates that the loading arm of the resistance force is becoming smaller.

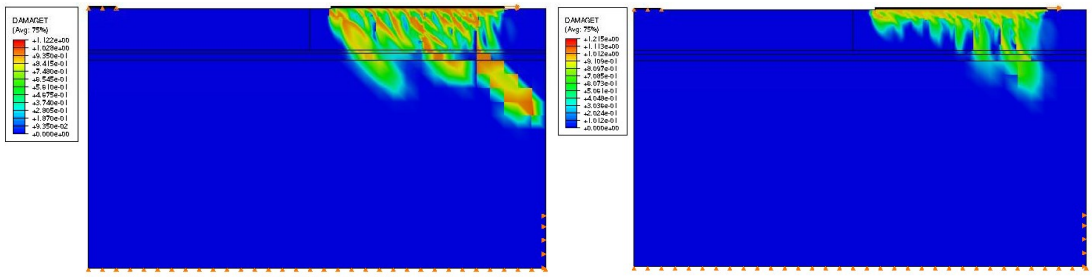

(a) (b)

Figure 6.32 Damage contours at Pt3 for the cases of (a) $1.0G_f$ and (b) $1.5G_f$

Through the aforementioned comparisons it is explained that the ultimate load in $1.5G_f$ case (i.e. a reference case of debonding mode) is lower than that in $1.0G_f$ case (i.e. a reference case of CPF mode), although the tensile fracture energy of concrete used in $1.5G_f$ case is 50% larger than that in $1.0G_f$ case.

To further validate this, the test data of the specimens with CPF failure mode in Yao et al. (2005) are compared to the corresponding values obtained from the bond strength model, proposed by Chen and Teng (2001) on the basis of a large scale of test data from the experiments of FRP-concrete bonded interface. This empirical model has been found as the best one in the existing bond strength models (Kalfat and Al-Mahaidi 2014). This model is given as

$$P_{\mathrm{u}} = 0.427\beta_{\mathrm{p}}\beta_{\mathrm{L}}\sqrt{f_{\mathrm{c}}'}b_{\mathrm{p}}L_{\mathrm{e}} \tag{6.1}$$

where,

$$L_{\mathrm{e}} = \sqrt{\frac{E_{\mathrm{p}}t_{\mathrm{p}}}{\sqrt{f_{\mathrm{c}}'}}} \tag{6.2}$$

$$\beta_{\mathrm{L}} = \begin{cases} \sin\dfrac{\pi L}{2L_{\mathrm{e}}}, & L < L_{\mathrm{e}} \\ 1, & L \geq L_{\mathrm{e}} \end{cases} \tag{6.3}$$

$$\beta_{\mathrm{p}} = \sqrt{\frac{2 - b_{\mathrm{p}}/b_{\mathrm{c}}}{1 + b_{\mathrm{p}}/b_{\mathrm{c}}}} \tag{6.4}$$

In Yao et al. (2005), for the specimens with CPF failure mode, the test data deviate from the predicted value using Chen and Teng's (2001) bond strength model, with an average error of 16%, as shown in Table 6.9. By contrast, in Yao et al. (2005), a very good prediction is conducted for the specimens with debonding failure mode, with an average error of 2.7%.

Table 6.9 Test and predicted results of the specimens with CPF failure mode from Yao et al. (2005)

	Test load (kN)	Predicted load (kN)	P_{test}/P_{pred}
III-5	15.08	13.42	1.12
III-6	15.75	14.16	1.11
V-7	14.27	12.28	1.16
V-8	13.78	12.28	1.12
V-9	13.56	12.88	1.05

V-10	15.66	12.88	1.22
V-11	15.57	13.30	1.17
V-12	17.43	13.30	1.31
Average			1.16

It is concluded that the debonding and CPF failure modes are two different failure modes, with different damage mechanical mechanisms. This bond strength model, proposed by Chen and Teng (2001), is only applicable to predict the ultimate load in debonding failure mode. The ultimate load in CPF failure mode is much higher than that in the assumed debonding failure mode.

6.5 Conclusions

In this chapter, the effects of the concrete tensile fracture energy and the compression hardening strain energy have been investigated using two approaches, namely shape change and constant shape approaches. Both CPF and debonding failure modes are considered.

In the CPF mode, the ultimate load of the model is controlled by tensile fracture energy in both shape-change and constant shape approaches, but is not affected by the compression hardening strain energy, as shown in section 5.3.2. On the other hand, in the debonding failure mode, the ultimate load of FRP-concrete bonded interface is governed by the compression hardening strain energy in both shape-change and constant shape approaches, but not governed by the tensile fracture energy as was thought before (Ouezdou et al., 2009; Li et al., 2011; Lu et al., 2005). The ultimate load in CPF failure mode is much higher than that in debonding failure mode. Thus, maybe the CPF failure mode is more preferable, especially in real application when concrete is reinforced with high strength steel bar.

Few significant differences are found between both shape-change and constant shape approaches in both debonding and CPF modes.

In summary, compression hardening strain energy is of high importance for the debonding behaviour in the simulation of FRP-concrete interface and it is determined by the compression stress-strain model. Therefore, in the next chapter, a careful study is carried out to select an appropriate concrete compression stress-strain model for the hereafter simulations.

Chapter 7

Effect of concrete compressive stress-strain model on the ultimate load of FRP-concrete bonded interface

7.1 Introduction

As discussed in Chapter 6, concrete compression hardening strain energy (i.e. the area enclosed by compressive stress-inelastic strain curve and the x-axis), which is determined by the concrete compressive stress-strain curve, is found to have a significant effect on the ultimate load of FRP-concrete bonded interface. A large number of concrete compressive stress-strain models have been proposed based on experimental tests (Popovics 1970). In general, they have similar ascending branches, but have widely different descending branches (Tulin and Gerstle 1964; Wang et al. 1978).

In traditional RC structural components, the effect of such a difference is not shown significant because the cracks are restrained by the reinforcements once they are formed; whereas at FRP-concrete bonded interface there is no reinforcement to restrain the already cracked concrete. It is for this reason that the descending branch of concrete compressive stress-strain relationship is of high significance to the debonding behaviour of FRP-concrete bonded interface. An appropriate concrete compressive stress-strain model thus is required for simulations of FRP-concrete bonded interface.

In this chapter different compressive stress-strain relationships for concrete are reviewed first. It is followed by a comparison of these models to test data of plain concrete short cylinders with a wide range of strengths. These models are used respectively in simulations of FRP-concrete bonded interface to test their performances in simulations. Lastly, effect of the cut-off threshold in the compressive stress-strain model is investigated on the ultimate load of FRP-concrete bonded interface.

7.2 Review of compressive stress-strain models

A comprehensive review of concrete compressive stress-strain models is presented in this section. In the models reviewed below, σ_0 is the peak stress, ε_0 is the strain at the peak stress, E_0 is the tangent elastic modulus of concrete, E_1 is the secant modulus from the origin to the peak stress, f_c' is standard cylinder strength of concrete.

1. The Madrid parabola (Owen and Figueiras, 1984;Abbasi et al., 1993)

The Madrid parabola is a classical formula for concrete compression behaviour based on the assumption that $E_0 = 2E_1$ which was recommended by the European Concrete Committee (1964). It is given as

$$\sigma = E_0\varepsilon(1 - \varepsilon/2\varepsilon_0) \tag{7.1}$$

$E_1 = \frac{\sigma_0}{\varepsilon_0}$, as implied in the definition of scant modulus E_1. Considering the assumption that $E_0 = 2E_1$, it can also be rewritten as

$$\frac{\sigma}{\sigma_0} = \frac{\varepsilon}{\varepsilon_0}\left(2 - \frac{\varepsilon}{\varepsilon_0}\right) \tag{7.2}$$

which is referred as the parabola part in Hognestad et al.'s (1955) model.

2. Saenz's (1964) model 1

In real testing, the assumption of $E_0 = 2E_1$ does not always hold. In view of that, a more complicated but more exact equation is proposed by Saenz (1964) by discarding this assumption and given as

$$\sigma = E_0\varepsilon\left[1 + \left(\frac{3E_1}{E_0} - 2\right)\left(\frac{\varepsilon}{\varepsilon_0}\right) + \left(1 - \frac{2E_1}{E_0}\right)\left(\frac{\varepsilon}{\varepsilon_0}\right)^2\right] \tag{7.3}$$

Therefore, Saenz's (1964) model 1 is the general case of the Madrid parabola.

3. Desayi and Krishnan's (1964) model

Similar to the Madrid model, by assuming $E_0 = 2E_1$, Desayi and Krishnan's (1964) model is given as

$$\sigma = \sigma_0 \frac{2\left(\frac{\varepsilon}{\varepsilon_0}\right)}{1+\left(\frac{\varepsilon}{\varepsilon_0}\right)^2} \tag{7.4}$$

Considering the assumption that $E_0 = 2E_1$, it can be written as

$$\sigma = \frac{E_0\varepsilon}{1+\left(\frac{\varepsilon}{\varepsilon_0}\right)^2} \tag{7.5}$$

4. Saenz's (1964) model 2

Similar to Saenz's (1964) model 1, by discarding the assumption of $E_0 = 2E_1$, a general model of Desayi and Krishnan's (1964) model is proposed by Saenz (1964) and given as

$$\sigma = \frac{E_0\varepsilon}{1+\left(\frac{E_0}{E_1}-2\right)\left(\frac{\varepsilon}{\varepsilon_0}\right)+\left(\frac{\varepsilon}{\varepsilon_0}\right)^2} \tag{7.6}$$

5. Elwi and Murray's (1979) model

Based on Saenz's (1964) model 2, Elwi and Murray (1979) proposed a new model:

$$\sigma = \frac{\varepsilon}{A + B\varepsilon + C\varepsilon^2 + D\varepsilon^3} \tag{7.7}$$

in which constants *A*, *B*, *C* and *D* are obtained through the following conditions:

a) Origin of the curve, i.e. $\varepsilon = 0$, $\sigma = 0$;

b) Tangent stiffness at the origin of the curve, i.e. $\varepsilon = 0$, $\frac{\mathrm{d}\sigma}{\mathrm{d}\varepsilon} = E_0$;

c) Value of the peak stress of the curve: i.e. $\varepsilon = \varepsilon_0$, $\sigma = \sigma_0$;

d) Derivative at the peak stress of the curve: $\varepsilon = \varepsilon_0$, $\frac{\mathrm{d}\sigma}{\mathrm{d}\varepsilon} = 0$;

e) Ultimate strength when concrete specimen collapses: $\varepsilon = \varepsilon_u$, $\sigma = \sigma_u = k\sigma_0$.

Through these conditions, the constants *A*, *B*, *C* and *D* are obtained and the resulting equation is given as

$$\sigma = \frac{E_0 \varepsilon}{1 + \left(R + \frac{E_0}{E_1} - 2\right)\left(\frac{\varepsilon}{\varepsilon_0}\right) - (2R - 1)\left(\frac{\varepsilon}{\varepsilon_0}\right)^2 + R\left(\frac{\varepsilon}{\varepsilon_0}\right)^3} \tag{7.8}$$

in which

$$R = \frac{E_0/E_1(\sigma_0/\sigma_\mathrm{u} - 1)}{(\varepsilon_\mathrm{u}/\varepsilon_0 - 1)^2} - \frac{1}{(\varepsilon_\mathrm{u}/\varepsilon_0 - 1)} \tag{7.9}$$

6. Sargin's (1971) model

Through a modification of Saenz's (1964) model 2, Sargin's (1971) model is given as

$$\sigma = k_3\sigma_0 \frac{A\left(\frac{\varepsilon}{\varepsilon_0}\right) + (D - 1)\left(\frac{\varepsilon}{\varepsilon_0}\right)^2}{1 + (A - 2)\frac{\varepsilon}{\varepsilon_0} + D\left(\frac{\varepsilon}{\varepsilon_0}\right)^2} \tag{7.10}$$

where, $A=E_0/E_1$; $\sigma_0=k_3 f_c'$ is the normalised stress of confined concrete at the strain ε_0 (i.e. k_3=1 for unconfined plain concrete), D is a parameter which mainly affects the descending branch of the model with little effect on the ascending branch.

Additionally, assuming A=2, D=0 and k_3=1 yields the Madrid parabola (see Eq.(7.1)), which is also referred as the parabola part in Hognestad et al.'s (1955) model; substituting A=2, D=1 and k_3=1 into Eq.(7.10) results in Desayi and Krishnan's (1964) model (see Eq.(7.4)); assuming D=1 and k_3=1, this equation reduces to Saenz's (1964) model 2 (see Eq. (7.6)).

7. CEB-FIP Model Code 1990 model

Sargin's (1971) model with D=0 and k_3=1 is introduced into the CEB-FIP Model Code 1990 (Béton 1993) and given as

$$\frac{\sigma}{\sigma_0} = \begin{cases} \dfrac{k\left(\frac{\varepsilon}{\varepsilon_0}\right) - \left(\frac{\varepsilon}{\varepsilon_0}\right)^2}{1 + (\mathrm{k} - 2)\left(\frac{\varepsilon}{\varepsilon_0}\right)} & \text{for} \quad \varepsilon \le \varepsilon_{\mathrm{c,lim}} \\ \left[\left(\dfrac{1}{\varepsilon_{\mathrm{c,lim}}/\varepsilon_0}\xi - \dfrac{2}{(\varepsilon_{\mathrm{c,lim}}/\varepsilon_0)^2}\right)\left(\dfrac{\varepsilon}{\varepsilon_0}\right)^2 + \left(\dfrac{4}{\varepsilon_{\mathrm{c,lim}}/\varepsilon_0} - \xi\right)\dfrac{\varepsilon}{\varepsilon_0}\right]^{-1} & \text{for} \quad \varepsilon > \varepsilon_{\mathrm{c,lim}} \end{cases} \tag{7.11}$$

where, $k = E_0/E_1$

and

$$\xi = \frac{4\left[\left(\frac{\varepsilon_{c,lim}}{\varepsilon_0}\right)^2\left(\frac{E_0}{E_1}-2\right)+2\frac{\varepsilon_{c,lim}}{\varepsilon_0}-\frac{E_0}{E_1}\right]}{\left[\frac{\varepsilon_{c,lim}}{\varepsilon_0}\left(\frac{E_0}{E_1}-2\right)+1\right]^2} \tag{7.12}$$

with the strain $\varepsilon_{c,lim}$ at $\sigma_{c,lim} = 0.5\sigma_c$ calculated from

$$\frac{\varepsilon_{c,lim}}{\varepsilon_0} = \frac{1}{2}\left(\frac{1}{2}\frac{E_0}{E_1}+1\right)+\left[\frac{1}{4}\left(\frac{1}{2}\frac{E_0}{E_1}+1\right)^2-\frac{1}{2}\right]^{1/2} \tag{7.13}$$

This model is called CEB-FIP (1990) model for brevity in this thesis.

8. Eurocode (2004) model

The Eurocode (EN 1992-1-1 2004), adopts the same expression as the CEB-FIP (1990) model (the first equation in Eq. (7.11)) but with a constant *k* set to $1.05E_0/E_1$.

9. Smith and Young's (1955) model

In Smith and Young's (1955) model, the relationship between compressive stress σ and strain ε for short-term axial loading is independently proposed without any connections to previous models and given as

$$\sigma = \sigma_0\left(\frac{\varepsilon}{\varepsilon_0}\right)e^{1-\left(\frac{\varepsilon}{\varepsilon_0}\right)} \tag{7.14}$$

In some literature, this model is also expressed in the form of

$$\sigma = E_0\varepsilon e^{\left(-\frac{\varepsilon}{\varepsilon_0}\right)} \tag{7.15}$$

with the assumption that $\frac{E_0}{E_1} = e$.

10. Umemura and Aoyama's (1970) model

In Umemura and Aoyama's (1970) model, the compressive stress σ relates to the strain ε through

$$\sigma = 6.75\left(\mathrm{e}^{-0.812\left(\frac{\varepsilon}{\varepsilon_0}\right)} - \mathrm{e}^{1.218\left(\frac{\varepsilon}{\varepsilon_0}\right)}\right) \tag{7.16}$$

11. Young's (1960) model

In Young's (1960) model, the relationship between compressive stress σ and strain ε for short-term axial loading is independently proposed without any connections with previous models and given as

$$\frac{\sigma}{\sigma_0} = \sin\left(\frac{\pi}{2}\frac{\varepsilon}{\varepsilon_0}\right) \tag{7.17}$$

12. Tulin and Gerstle's (1964) model

In Tulin and Gerstle's (1964) model, the relationship between compressive stress σ and strain ε for short-term axial loading is independently proposed without any connections to previous models and given as

$$\sigma = \frac{E_0\varepsilon}{2 + (\varepsilon/\varepsilon_0)^3} \tag{7.18}$$

13. Hognestad et al.'s (1955) model

In this model, the ascending branch is depicted with parabolic curve, and the descending branch is depicted with a straight line. It is expressed as

$$\frac{\sigma}{\sigma_0} = \begin{cases} 2\left(\frac{\varepsilon}{\varepsilon_0}\right) - \left(\frac{\varepsilon}{\varepsilon_0}\right)^2 & \text{for} \quad \varepsilon \le \varepsilon_0 \\ 1 - 0.15\left(\frac{\varepsilon - \varepsilon_0}{\varepsilon_u - \varepsilon_0}\right) & \text{for} \quad \varepsilon_0 < \varepsilon \le \varepsilon_u \end{cases} \tag{7.19}$$

In the post-peak zone of this model, the stress linearly drops to ultimate stress σ_u (i.e. 0.85 σ_0) from peak stress σ_0. The model was originally proposed for RC structures, in which the effect of the softening branch could be neglected. However, in simulations of FRP-concrete interface, this effect may not be neglected. In view of that, a cut-off branch is considered to reduce compressive stress to a value approaching zero. Otherwise, the stress in element will be assumed as σ_u (i.e. 0.85 σ_0) once the computed

strain is beyond ε_u, which will generate an unacceptable error in simulation results, as discussed in Section 7.5.

Thus, in Hognestad's (1955) model, the concrete compressive stress-strain curve is comprised of three parts, namely ascending, descending and cut-off branches, as shown in Figure 7.1. Through different cut-off methods in this model, three different curves are obtained, namely Hognestad et al.'s (1955) model with 1% cut-off, Hognestad et al.'s (1955) model with 10% cut-off and Hognestad et al.'s (1955) model with natural cut-off. In all three curves, the stress linearly drops to zero from the ultimate stress σ_u, using the elastic modulus calculated from

$$\tilde{E}_u = \frac{\sigma_u - 0}{\varepsilon_u - \varepsilon_{cu}} \tag{7.20}$$

In fact, the cut-off branch in this model is determined by the parameter ε_{cu}, as shown in Figure 7.1, which is obtained through

For Hognestad et al.'s (1955) model with 1% cut-off, $\varepsilon_{cu} = \varepsilon_u \times 1\% + \varepsilon_u$;

For Hognestad et al.'s (1955) model with 10% cut-off, $\varepsilon_{cu} = \varepsilon_u \times 10\% + \varepsilon_u$;

For Hognestad et al.'s (1955) model with natural cut-off, $\varepsilon_{cu} = \varepsilon_0 - \frac{\sigma_0}{\sigma_0 - \sigma_u}(\varepsilon_0 - \varepsilon_u)$.

14. Comparison of concrete compression models

According to the similarities of the curves, the above concrete compression models are classified into five groups, as listed in Table 7.1 and drawn in Figure 7.2-Figure 7.6. To further compare the difference amongst these groups, Saenz's (1964) model 2 is selected as a representative for the models in the first group, Umemura and Aoyama's (1970) model for the second group, CEB-FIP (1990) model for the third group, Young's (1960) model for the fourth group, Hognestad et al.'s (1955) model for the fifth group, as shown in Figure 7.7. It is found that the main difference amongst them mainly lies in the softening branch of the compressive stress-strain curves. From the first group to the fourth group, the stiffness in the softening branch of the compressive stress-strain curves becomes steeper with the increase of the group number.

Table 7.1 Classification of the empirical models of concrete in compression

Group Number	Concrete Model
1st Group	Desayi and Krishnan's (1964) model
	Sargin's (1971) model (i.e. D=1.0)
	Saenz's (1964) model 2
	Tulin and Gerstle's (1964) model
2nd Group	Smith and Young's (1955) model
	Umemura and Aoyama's (1970) model
3rd Group	CEB-FIP (1990) model
	Elwi and Murray's (1979) model
4th Group	Eurocode (2004) model
	Sargin's (1971) model (i.e. D=0.0)
	The Madrid parabola
	Saenz's (1964) model 1
	Young's (1960) model
5th Group	Hognestad et al.'s (1955) model with 1% cut-off
	Hognestad et al.'s (1955) model with 10% cut-off
	Hognestad et al.'s (1955) model with natural cut-off

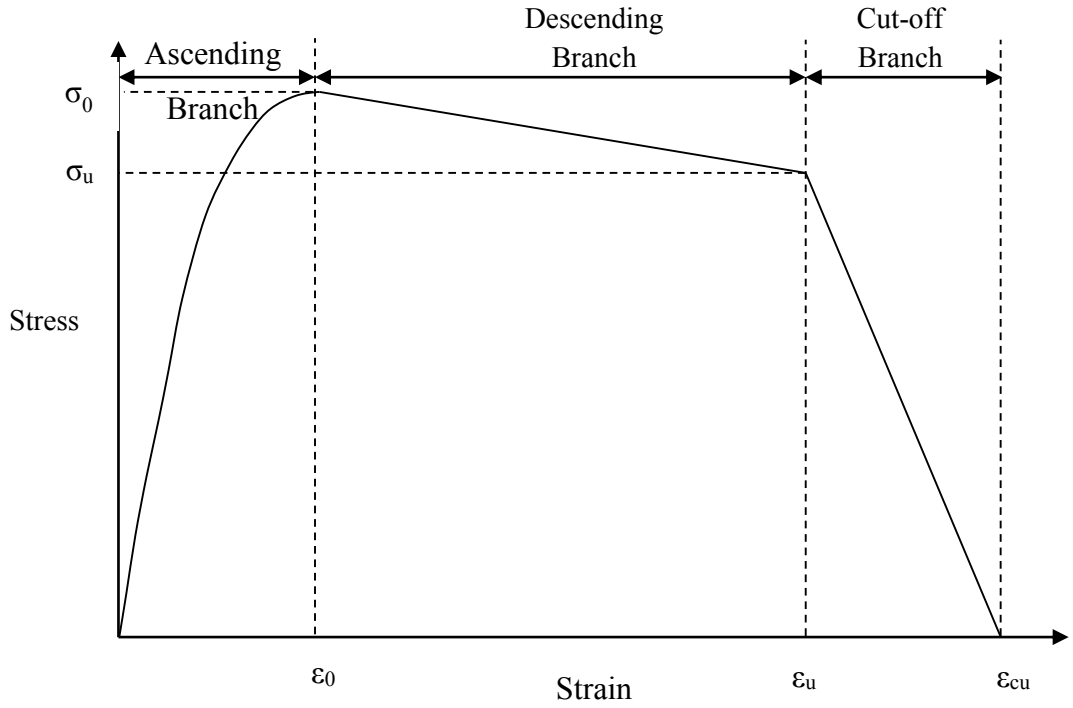

Figure 7.1 Diagrammatic sketch for compressive stress-strain relationship in Hognestad et al.'s (1955) model

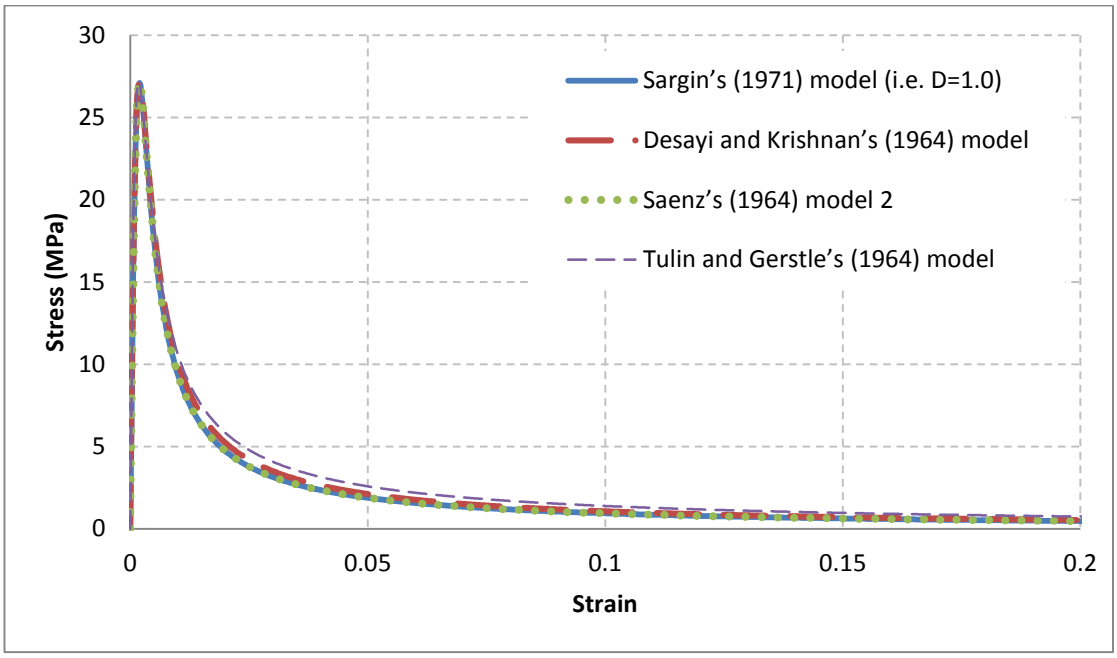

Figure 7.2 Compressive stress-strain curves of the models in the 1st group

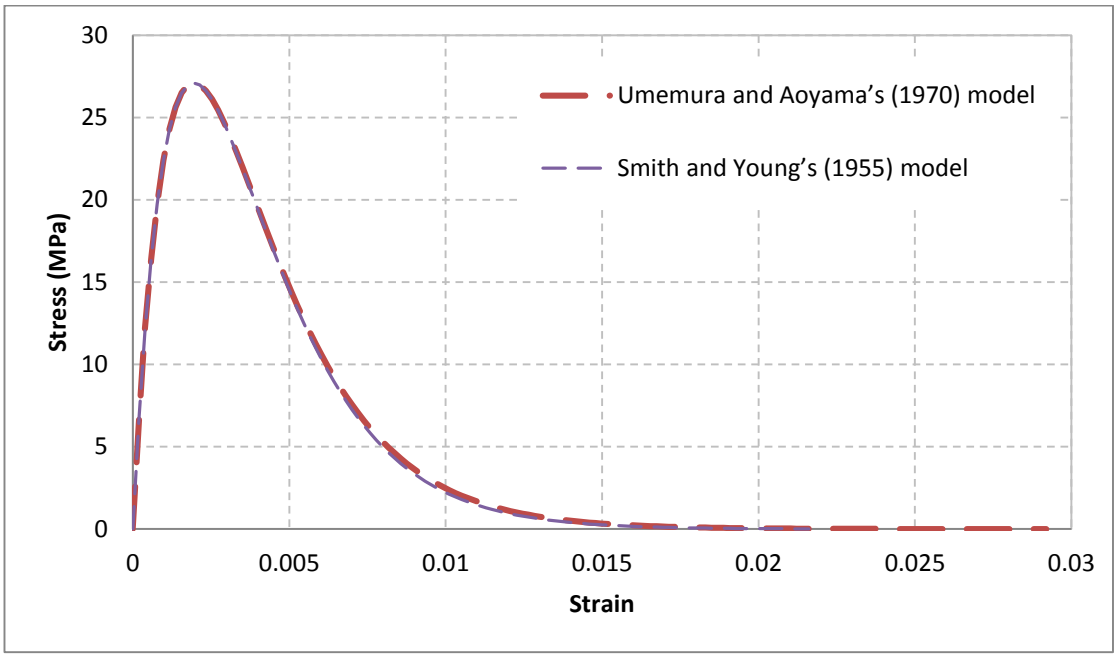

Figure 7.3 Compressive stress-strain curves of the models in the 2nd group

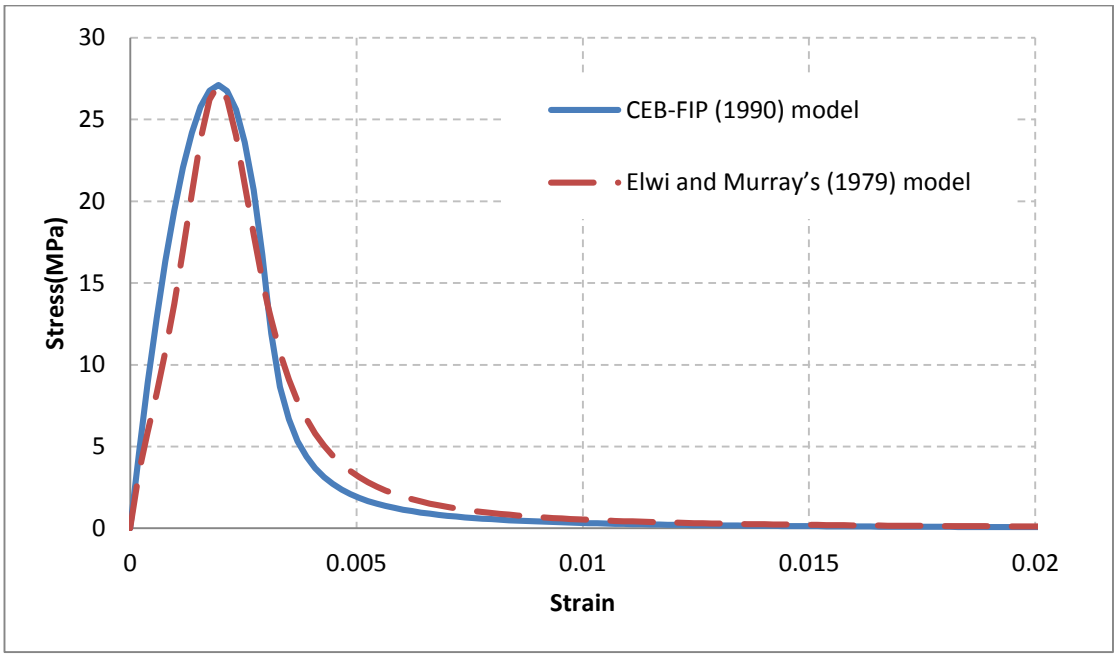

Figure 7.4 Compressive stress-strain curves of the models in the 3rd group

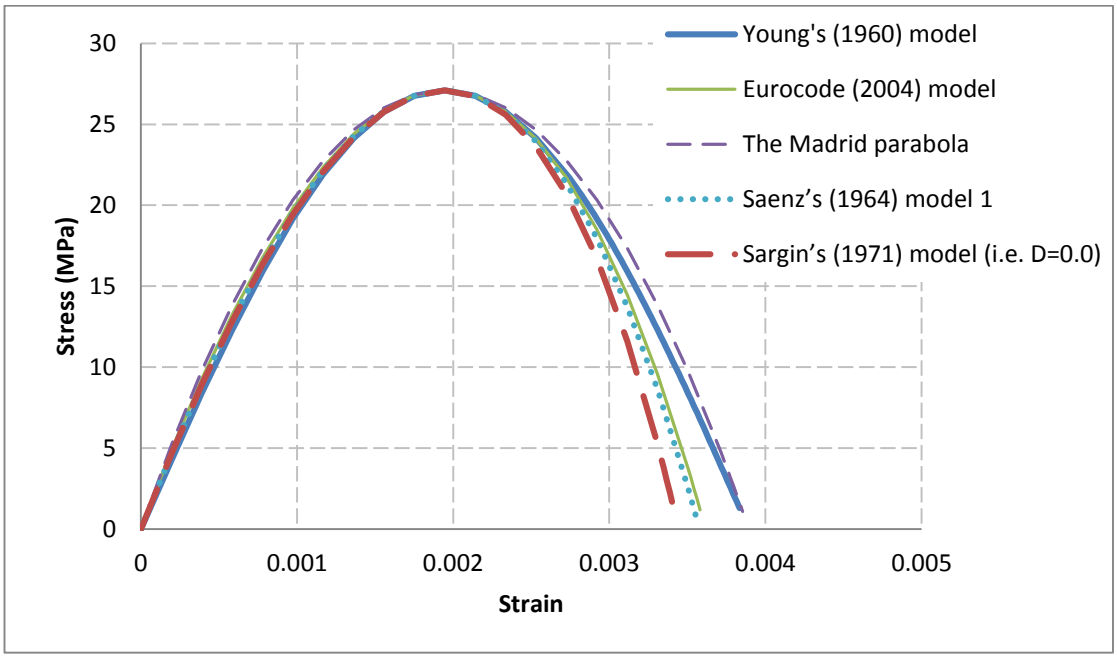

Figure 7.5 Compressive stress-strain curves of the models in the 4th group

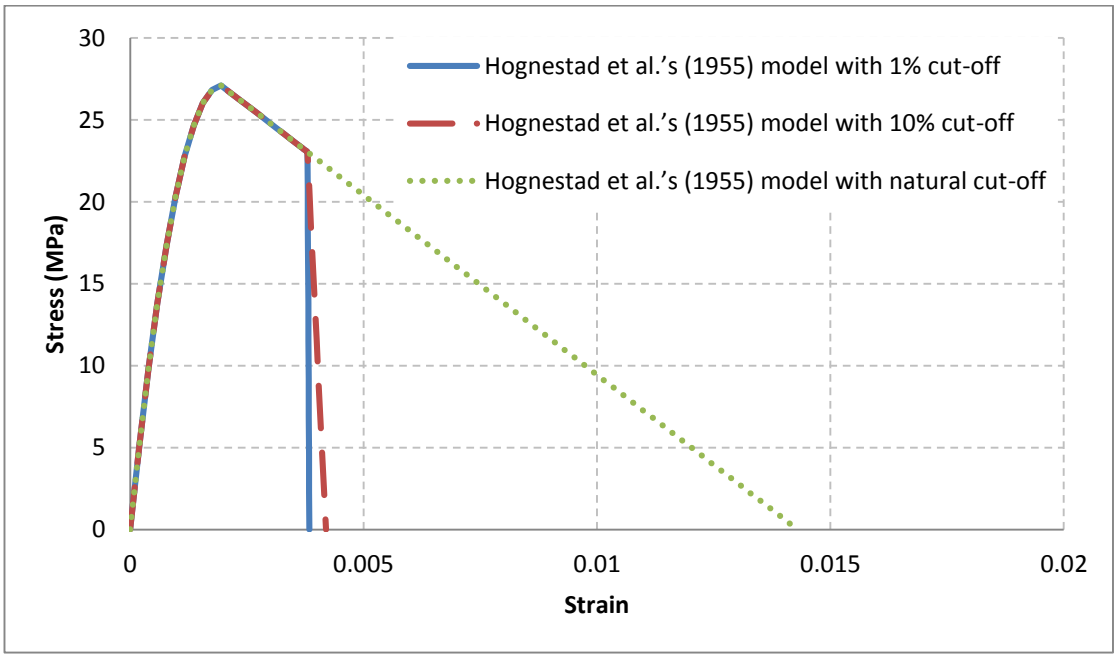

Figure 7.6 Compressive stress-strain curves of the models in the 5th group

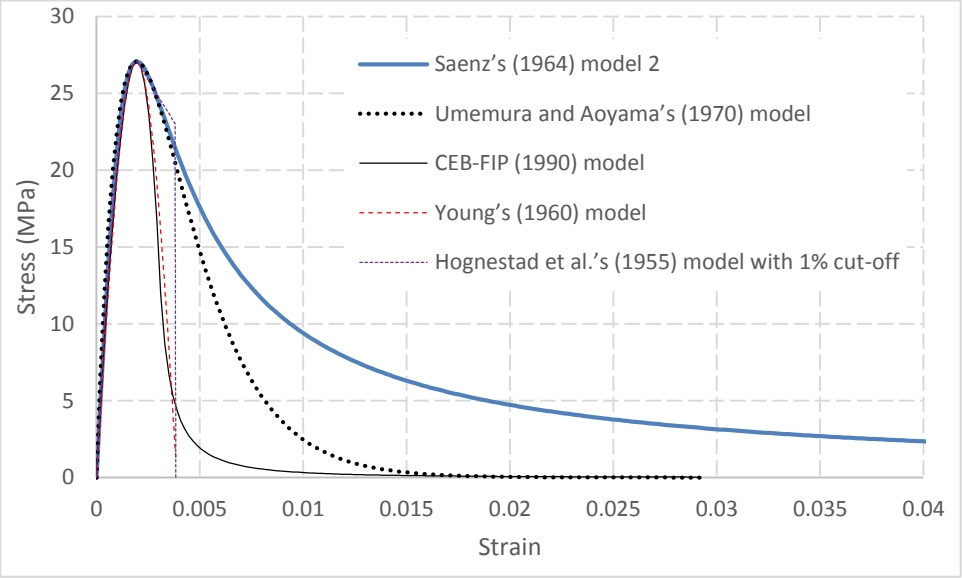

Figure 7.7 Compressive stress-strain curves of the representative models of these five groups

7.3 Comparison of concrete compression model with test data

As discussed above, all the reviewed concrete compressive stress-strain models are categorised into five different groups, according to the similarity of the curves. As the representative models of these five groups, Saenz's (1964) model 2, Umemura and Aoyama's (1970) model, CEB-FIP (1990) model, Young's (1960) model, and Hognestad et al.'s (1955) model are compared to test data on plain concrete short columns under compression load (Chen et al. 2010; Samani and Attard 2012; Wang et al. 1978), with concrete strength ranging from 23 MPa to 73 MPa.

Visual inspections of Figure 7.8-Figure 7.14 show the main difference amongst these models only lies in the descending branch while in the ascending branch there are only small difference. It appears that for the descending branch Young's (1960) and CEB-FIP (1990) models provide the best match with the test data. Between Young's (1960) and CEB-FIP (1990) models, the latter one is more preferable, because more accurate softening behaviour is taken into account in this model. It is for this reason that CEB-

FIP (1990) model, as a representative mode in the 3rd group, is regarded as the best model used in the rest of the thesis to describe the mechanical behaviour of concrete.

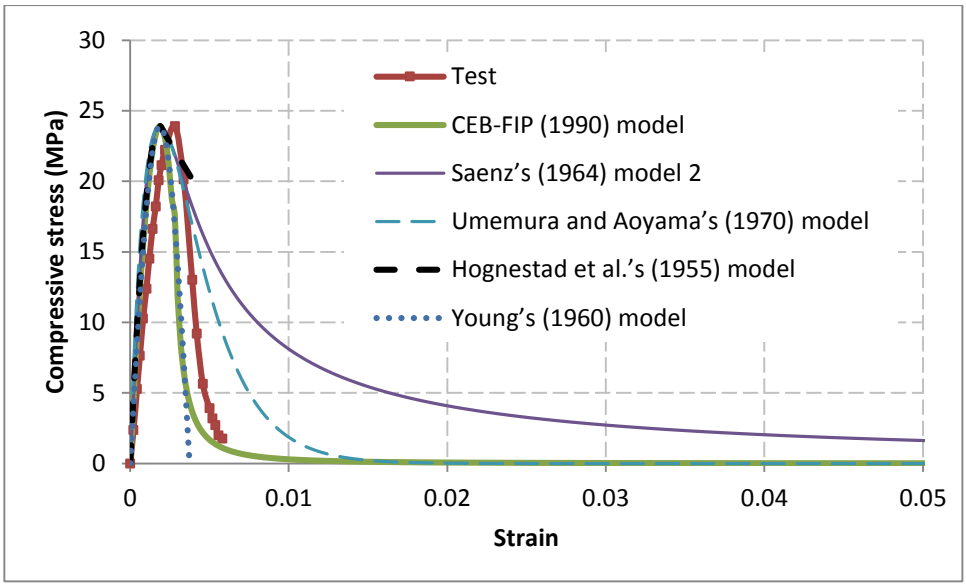

Figure 7.8 Comparison of experimental stress-strain curve with concrete strength of 23 MPa (Wang et al. 1978) **with the representative models**

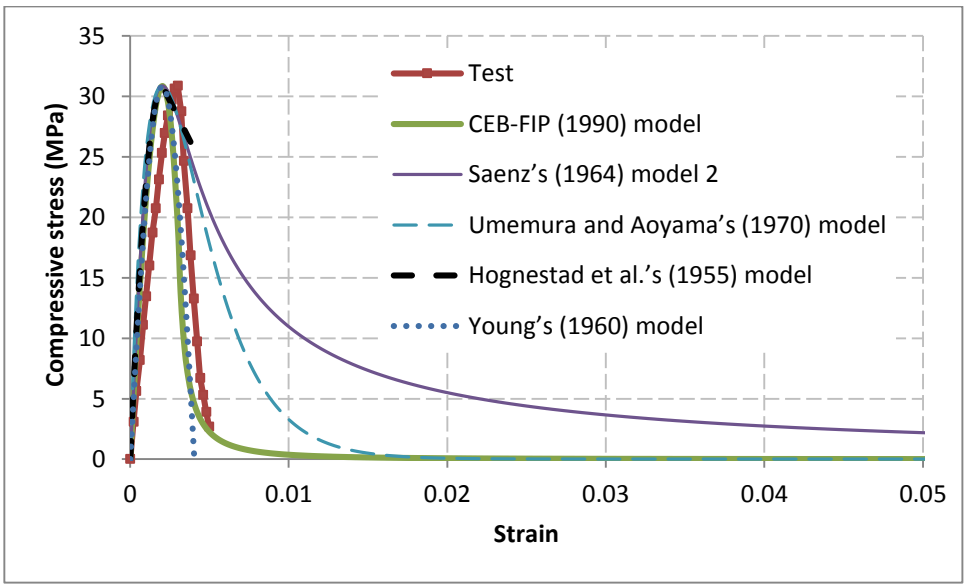

Figure 7.9 Comparison of experimental stress-strain curve with concrete strength of 31 MPa (Wang et al. 1978) **with the representative models**

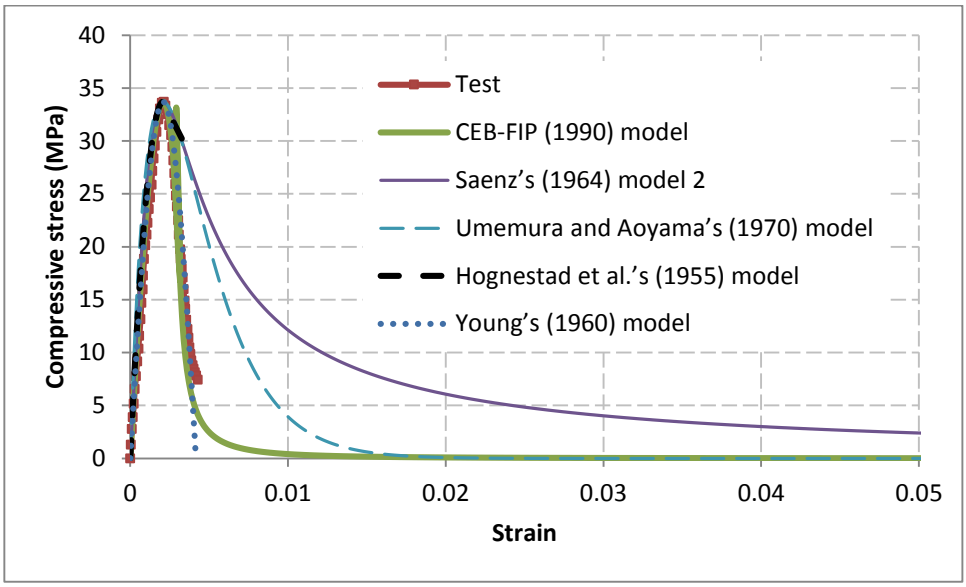

Figure 7.10 Comparison of experimental stress-strain curve with concrete strength of 33 MPa (Chen et al. 2010) **with the representative models**

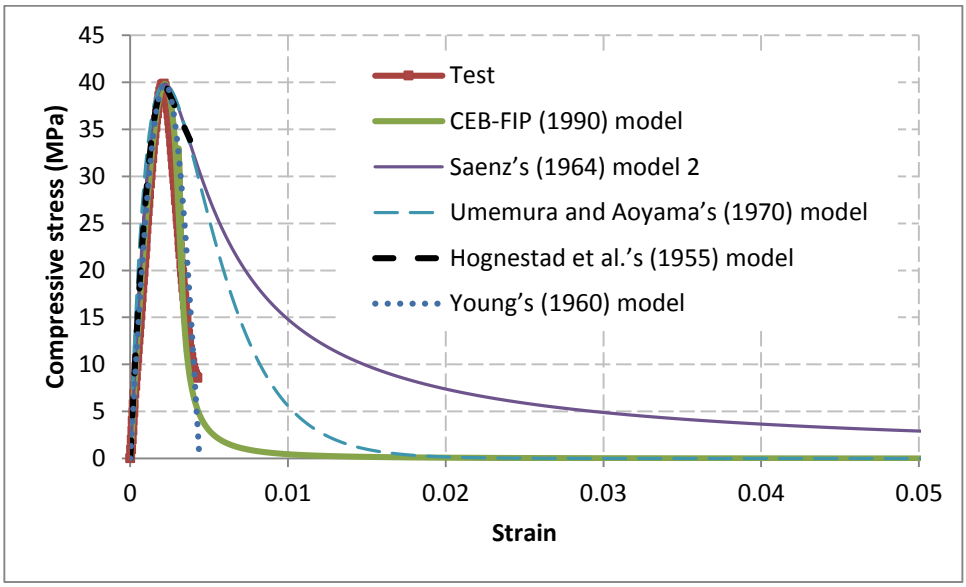

Figure 7.11 Comparison of experimental stress-strain curve with concrete strength of 39 MPa (Chen et al., 2010) with the representative models

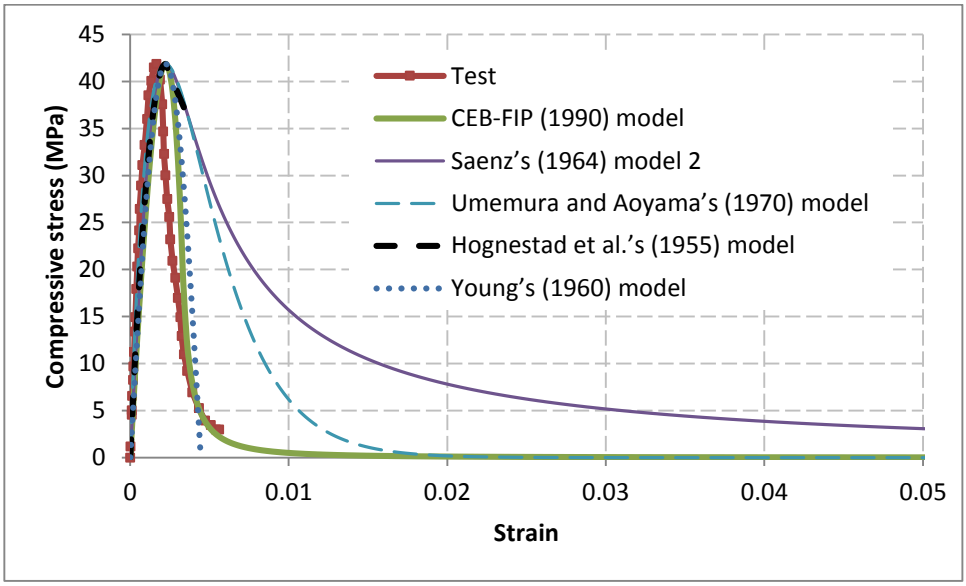

Figure 7.12 Comparison of experimental stress-strain curve with concrete strength of 41 MPa (Samani and Attard 2012) **with the representative models**

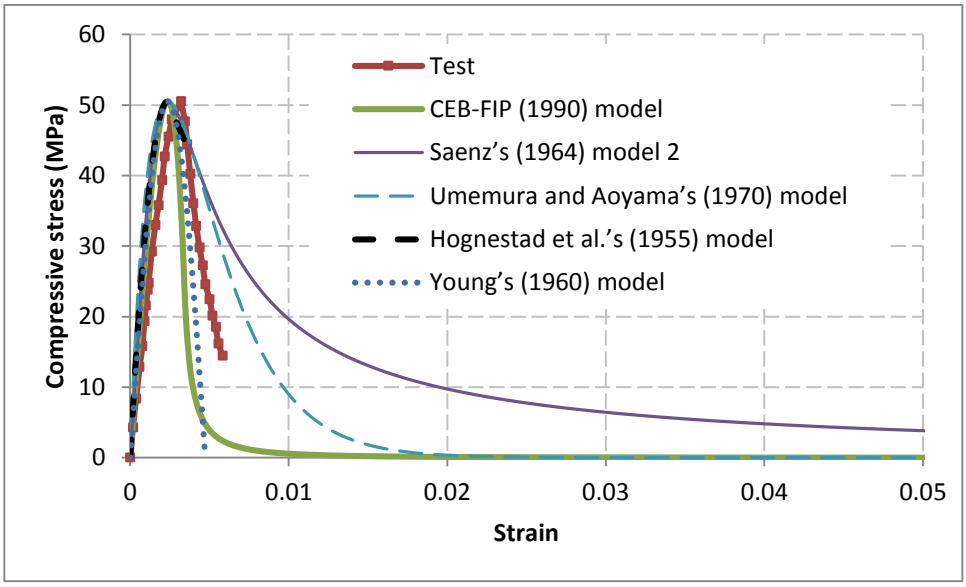

Figure 7.13 Comparison of experimental stress-strain curve with concrete strength of 50 MPa (Wang et al. 1978) **with the representative models**

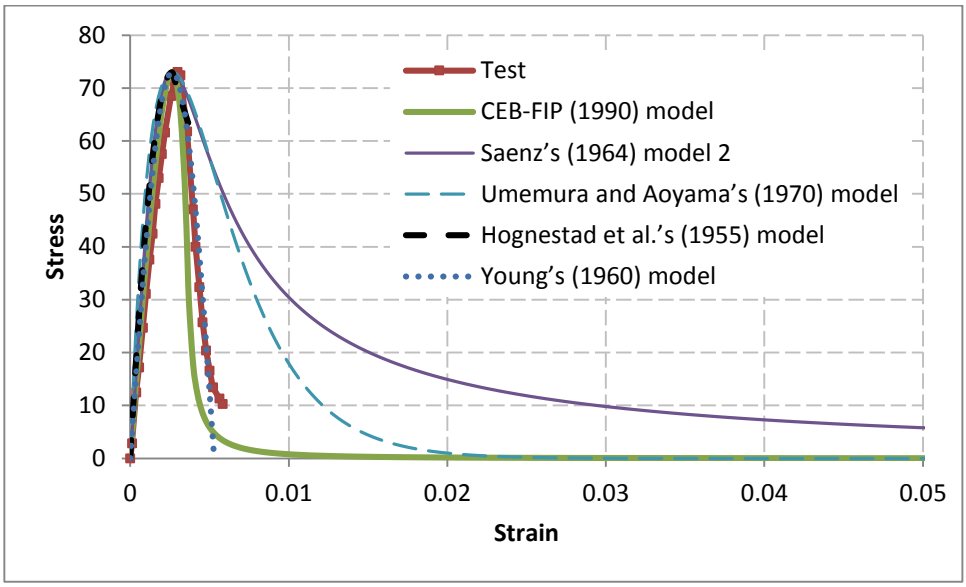

Figure 7.14 Comparison of experimental stress-strain curve with concrete strength of 72 MPa (Wang et al. 1978) **with the representative models**

7.4 Effect of compressive stress-strain model on FRP-concrete interface behaviour

In Chapter 6, the compressive strain energy has been found to have a significant effect on the ultimate load in simulations of FRP-concrete bonded interface. The effect of the compressive stress-strain model is investigated here. Specimen III-1 in Yao et al. (2005) is employed as the reference case. The same material and geometrical properties are used as in Chapter 3 unless stated otherwise. The only variation is the concrete compressive stress versus inelastic strain relationship, which is derived from concrete compressive stress-strain model.

In this section, all the models reviewed in Section 7.2 are used with their corresponding residual stresses in the model. Specifically, the residual stresses in the first three groups in Table 7.2 are set to 0.02 % of the peak stress, while in the remaining two groups, they are set to 5 % of the peak stress due to convergence issues in their simulations.

The results from these analyses with different concrete stress-strain models are summarised in Table 7.2, together with test and predicted loads with Chen and Teng's

(2001) bond strength model. The results with the models from the same group almost are very close, except the fifth group. Within these first four groups, the predicted loading capacity decreases with the increase of Group number until the third group. In the fourth group the models with 5% of peak stress as residual stress were used due to convergence issues, a procedure that makes the compression strain energy larger than that it should be. The effect of residual stress is discussed in detail in Section 7.5.

In addition, good agreement is found between test and simulation results with the models in the third group (i.e. with an error of approximately 1% for CEB-FIP (1990) and 4% for Elwi and Murray's (1979) models). Therefore, the CEB-FIP (1990) model is deemed to be reasonable and used in the subsequent simulations.

Table 7.2 Results for simulations with different concrete compression models

Group No.	Name of models	Load (kN)	Residual stress, MPa	Failure mode	P_{sim}/P_{test}	P_{sim}/P_{pred}
Test load		5.94		debonding		
Predicted load		6.27				
1st	Desayi and Krishnan's (1964) model	10.03	0.005	debonding	1.69	1.60
1st	Sargin's (1971) model (i.e. D=1.0)	10.20	0.005	debonding	1.72	1.63
1st	Saenz's (1964) model 2	10.24	0.005	debonding	1.72	1.63
1st	Tulin and Gerstle's (1964) model	10.34	0.005	debonding	1.74	1.65
2nd	Smith and Young's (1955) model	8.69	0.005	debonding	1.46	1.39
2nd	Umemura and Aoyama's (1970) model	8.75	0.005	debonding	1.47	1.40
3rd	CEB-FIP (1990) model	6.02	0.005	debonding	1.01	0.96
3rd	Elwi and Murray's (1979) model	6.16	0.005	debonding	1.04	0.98

4th	BSEN (2004) model	8.99	1.355	debonding	1.51	1.43
4th	Sargin's (1971) model (i.e. D=0.0)	8.38	1.355	debonding	1.41	1.34
4th	The Madrid parabola	9.74	1.355	debonding	1.64	1.55
4th	Saenz's (1964) model 1	8.97	1.355	debonding	1.51	1.43
4th	Young's (1960) model	9.68	1.355	debonding	1.62	1.54
5th	Hognestad et al.'s (1955) model with 1% cut-off	10.16	1.355	debonding	1.71	1.62
5th	Hognestad et al.'s (1955) model with 10% cut-off	10.57	1.355	debonding	1.78	1.69
5th	Hognestad et al.'s (1955) model with natural cut-off	12.36	1.355	debonding	2.08	1.97

Note: P_{sim}/P_{test} is the ratio of simulation results with different compressive stress-strain models to the test load; P_{pred}/P_{test} is the ratio of simulation results with different compressive stress-strain models to the predicted load with Chen and Teng's (2001) bond strength model.

7.5 Effect of residual stress in compressive stress-strain model on simulation results

In simulations of traditional structural components, such as beams, columns or joints, the residual stress in concrete compressive stress-strain models has little effect on the ultimate load of specimens, because of the restraint on the cracked concrete from reinforcing bars. Thus, in simulations of such traditional structural components, the effect of residual stress in concrete compressive stress-strain curve is never paid attention to.

However, in simulations of FRP-concrete bonded interface, residual stress in compressive stress-strain curves can have a very significant effect on the ultimate load. In the whole damaging process of FRP-concrete bonded interface, the load is resisted

only by a part of such an interface. With the increase of the load, concrete in the loaded end of interface is cracking, a mechanical behaviour that shifts the active zone to a new zone farther away from the loading point. The length of the active zone is called effective length in the study of FRP-concrete bonded interface (Chen and Teng 2001). This kind of shift is continuous until the interface is completely debonded.

The stress in the already debonded zone shall be zero if complete separation has occurred. In simulations the stress in this zone is not zero but a finite value related to the value of residual stress in concrete compressive stress-strain model. This value is usually set to a small but finite value to avoid convergence difficulties in simulations. However, if this value is significant it may lead to an inaccurate prediction.

In view of that, an appropriate value is needed to determine for the residual stress in compressive stress-strain model on the balance of computational efficiency and accuracy.

In this section, the effect of residual stress in Young's (1960) model is investigated with a single element first. It is followed by the analysis of FRP-concrete interfacial behaviour using Young's (1960) and CEB-FIP (1990) models but with different residual stresses, with reference to Specimens III-1 and III-5 in Yao et al. (2005).

7.5.1 Effect of residual stress using a single element

In this subsection, a single square element with side length of 1 mm is loaded under uniaxial compression to investigate the effect of residual stress in Young's (1960) model. The material property in the element test is defined with CDP model as in Chapter 3, except that the compressive stress-inelastic strain is defined through Young's (1960) model.

Young's (1960) model is cut off at two different thresholds, obtaining different curves named Young_ResidualStress1 and Young_ResidualStress2 respectively, as shown in Figure 7.15. In the case of Young_ResidualStress1, the concrete compressive stress-strain curve is cut off at a compressive stress of 0 MPa; by contrast, in the case of

Young_ResidualStress2, the concrete compressive stress-strain curve is cut off at a compressive stress of 1.7 MPa, as shown in Figure 7.15.

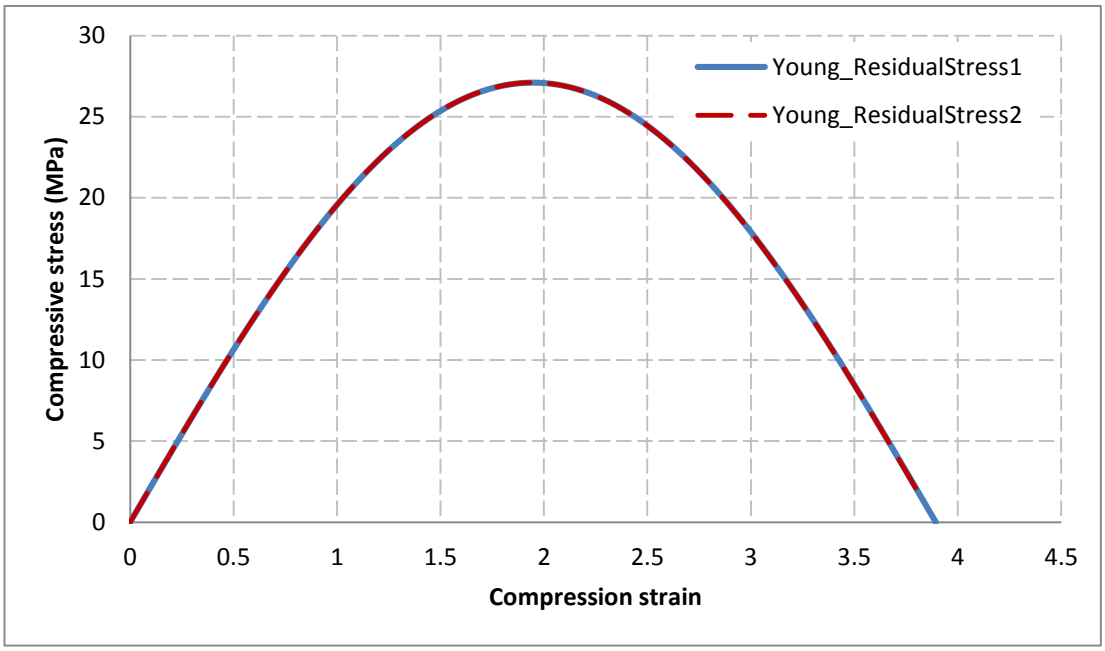

Figure 7.15 Young's (1960) compressive stress-strain model with different residual stresses

The resulting compressive stress-strain curves from the simulations with different residual stresses are compared in Figure 7.16. Through a visual inspection of Figure 7.16, it is found that each of these curves is followed by a horizontal line. The main difference between them lies in the fact that the horizontal line is located at different loading levels, which is caused by different values of residual stress obtained through different cut-off thresholds. Thus, it could be inferred that larger value of residual stress results in a higher compressive strain energy, due to the fact that the stress is assumed as the value of the stress at cut-off position (i.e. residual stress) in simulations once the computed strain is beyond that at cut-off position, as shown in Figure 7.16.

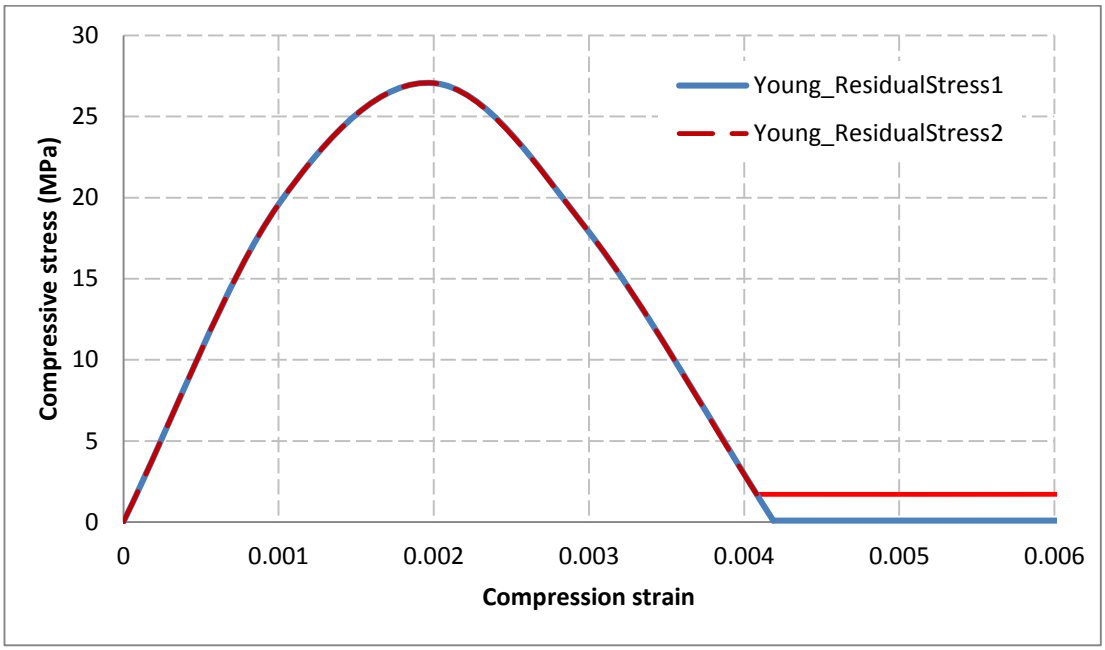

Figure 7.16 Stress-strain curves from the results with different residual stresses

7.5.2 Effect of residual stress in compressive stress-strain model on the simulation results of FRP-concrete bonded interface

Once again, the effect of residual stress in compressive stress-strain models is investigated with reference to Specimen III-1 and III-5 from Yao et al. (2005). The same material and geometrical properties used in Chapter 3 are employed here except the concrete compressive stress-inelastic strain curve, which is derived from concrete compressive stress-strain model.

First, Young's (1960) model is employed as the compressive stress-strain model with different residual stresses as shown in Table 7.3. The relevant results from these analyses are also shown in Table 7.3, together with the test and predicted results with Chen and Teng's (2001) bond strength model. It is found that the simulations did not converge in the case of S1, S2 and S3 due to the inappropriate values of residual stresses in the compressive stress-strain model. On the other hand, an excessive error on the ultimate load is found while comparing the simulation result to test result (i.e.

the ultimate load for Specimen III-1 in Yao et al. (2005) is 5.94kN) when the residual stress is set inappropriate as in the case of S4, although convergence issue has been avoided.

Table 7.3 Predicted results of Specimen III-1 in Yao et al. (2005) with Young's (1960) model cut off at different thresholds

Different schemes	Cut-off threshold		Load (kN)
	Cut-off stress (MPa)	Cut-off strain	
Test			5.940
Predicted load			6.27
S1	0.04	0.00389	Not Converged
S2	0.13	0.00388	Not Converged
S3	0.51	0.00385	Not Converged
S4	1.28	0.00378	9.680

Note: The cut-off threshold in concrete compressive stress-strain model is comprised of cut-off stress and strain. In this study, cut-off stress is also called residual stress.

Of course, Young's (1960) model is only a special case due to its very steep drop to zero, and is inappropriate to describe the plastic behaviour of plain concrete with large strains. Thus, with reference to CEB-FIP (1990) model, the effect of residual stress in its descending branch is investigated again in the simulation of Specimen III-1 in Yao et al. (2005), and the relevant simulation results are listed in Table 7.4, together with test and predicted loads with Chen and Teng's (2001) bond strength model.

In these simulations, no convergence issue is experienced even when the compressive stress-strain model is cut off at the compressive stress lower than 0.03% of the peak stress as such in S1 and S2 cases (see Table 7.4). That is because the softening behaviour is more ductile than that in Young's (1960) model when it is approaching to zero. Thus, ductility may be another important merit of CEB-FIP (1990) model

compared to Young's (1960) model, apart from the good agreement with the corresponding test data as found in Section 7.3.

On the other hand, the ultimate load in the simulation result increases with the value of the cut-off threshold in compression hardening stress-strain model, as such in S1, S2, S3, S4 and S5 cases. That is because the ultimate load at FRP-concrete bonded interface is determined by compression strain energy (i.e. as drawn in Chapter 6), which varies with the value of the cut-off threshold in the same compressive stress-strain model (i.e. as drawn in Section 7.5.1).

Table 7.4 Predicted results of Specimen III-1 in Yao et al. (2005) with CEB-FIP (1990) model cut off at different thresholds

	Cut-off threshold		Load (kN)
	Cut-off stress (MPa)	Cut-off strain	
Test load			5.940
Predicted load			6.27
S1	0.0011	0.148	5.907
S2	0.0075	0.058	5.941
S3	0.5260	0.008	6.937
S4	1.046	0.006	7.463
S5	3.137	0.004	10.682

In addition, the effect of cut-off threshold in CEB-FIP (1990) model is also investigated in CPF failure mode of FRP-concrete bonded interface with reference to Specimen III-5 in Yao et al. (2005). The simulation results with different cut-off schemes are shown respectively in Table 7.5, together with test and predicted loads with Chen and Teng's (2001) bond strength model. In these simulations, it is found that the ultimate load at the FRP-concrete bonded interface with CPF failure mode is not affected by the value of cut-off threshold. That is because the CPF failure mode is

a Mode I crack dominated failure mode, which is determined by the tension properties of concrete rather than compression hardening strain energy, as discussed in Chapter 6.

Table 7.5 The simulation results of Specimen III-5 in Yao et al. (2005) with CEB-FIP (1990) model cut off at different thresholds

	Cut-off threshold		Load (kN)
	Cut-off stress (MPa)	strain	
Test load			15.08
Predicted load			14.16
S1	0.0011/27.1 (0.004%)	0.148	14.767
S2	0.0075/27.1 (0.03%)	0.058	14.909
S3	0.5260/27.1 (1.94%)	0.008	15.014
S4	1.046/27.1 (3.86%)	0.006	15.132
S5	3.137/27.1 (11.57%)	0.004	15.149

7.6 Conclusions

A large number of concrete compressive stress-strain models have been proposed based on various assumptions and tests, as discussed in Section 7.2. There are very significant differences existing amongst them, especially in their descending branches. These differences may have no significant effect on the ultimate load of RC structural components due to the restraint of reinforced bars. However, at FRP-concrete bonded interface it may make a very significant difference on the ultimate load.

This chapter first reviewed different compressive stress-strain models, which are categorised into five different groups and then compared to the test data with different concrete compressive strength. Through such comparisons, it is found that the third

group of concrete models, namely CEB-FIP (1990) and Elwi and Murray's (1979) models, provide the best match with that from the corresponding testing.

The effect of concrete compressive stress-strain models in simulations of FRP-concrete bonded interface is investigated with reference to Specimen III-1 from Yao et al. (2005). It is also found that the results from the simulations with the CEB-FIP (1990) and Elwi and Murray's (1979) models are in the best agreement with the corresponding testing results amongst these models. In view of that, the CEB-FIP (1990) model was deemed to be reasonable and employed in subsequent simulations in this thesis.

In addition, the effect of cut-off threshold in compressive stress-strain model is also investigated with reference to element test and Specimen III-1 in Yao et al. (2005), based on Young's (1960) and CEB-FIP (1990) models. In the element test with Young's (1960) model, it is found that the effect of cut-off threshold is only found in the zone where the computed strain reaches beyond that defined in the cut-off threshold. On the other hand, in the simulations of FRP-concrete bonded interface, cut-off threshold has a very significant effect on ultimate result. Specifically, in simulations with Young's (1960) model, whose descending branch is dropping to zero very steeply, it is very difficult to find an appropriate value for cut-off threshold. Larger value leads to higher predicted ultimate load, but lower value leads to convergence issues in simulation. By contrast, in simulations with CEB-FIP (1990) model, whose descending branch approaches zero very slowly, it is acceptable even when the model is cut off at compressive stress equal to 0.03% of concrete compression strength. Of course, a larger value of residual stress in such simulations also leads a higher value in the ultimate load. Thus, CEB-FIP (1990) model will be cut off at the compressive stress equal to 0.03% of concrete compressive strength in subsequent simulations of FRP-concrete bonded interface.

Chapter 8
2D analysis of 3D FRP-to-concrete bonded systems

8.1 Introduction

Many failure modes of FRP strengthened beams, such as FRP delamination at the end of FRP, intermediate crack-induced debonding and inclined crack-induced debonding, as shown in Figure 1.2, are associated with debonding phenomenon at FRP-concrete bonded interface. In FRP-concrete bonded interface, the dimensions of FRP thickness and the debonding crack near the interface are very small, compared to that of the whole specimen. The width of FRP plate and concrete are usually different in the design of strengthened RC beams with FRP. The difference in width between FRP and concrete means that the behaviour is three dimensional in practice (Chen and Pan 2006). Therefore, 3D modelling is preferable to simulate the debonding behaviour at FRP-concrete bonded interface. However, 3D modelling requires high computational cost. A two dimensional model is much more reasonable and appropriate for simulations of FRP-concrete bonded interface for a balance between accuracy and efficiency in simulations. However, neither plane stress element nor plane strain element is appropriate to accurately describe this 3D debonding behaviour at FRP-concrete bonded interface, and the truth is somewhere in between.

Up to date, mesoscale approach in 2D method has been employed in simulations of FRP-concrete bonded interface (Lu et al. 2005b; Tao and Chen 2015). In this approach (i.e. this approach will be named as *traditional approach* hereafter in this study), FRP is treated as linear elastic material, concrete is simulated with concrete damaged plasticity model (Lubliner 1989) and FRP and concrete are connected with each other by sharing nodes. Apart from that, the out-of-plane thicknesses of FRP and concrete parts were set to a value of unity in this approach, a setting that has neglected the difference in terms of FRP and concrete widths in geometrical modelling. Subsequently, the simulation results are processed with Chen and Teng's (2001) FRP-concrete width ratio formula to reflect the difference in the ultimate load amongst the

cases. However, it is evident that the failure mode at FRP-concrete interface also varies with the FRP-concrete width ratio, a phenomenon that has been excluded in these studies. There are additional issues in this approach as discussed in Chapter 2.

A new mesoscale approach is needed to accurately simulate the mechanical behaviour of FRP-concrete bonded interface. The relationship between the width ratio and ultimate load at FRP-concrete bonded interface is explained through strain changes across FRP section from the specimens with different FRP-concrete width ratios in Yao (2004). Combining with the conclusions obtained in Chapter 6 that concrete compressive strain energy is highly related to the ultimate load at FRP-concrete bonded interface. It is followed by proposing a formula to accurately quantify this FRP-concrete width effect. Subsequently, this formula is introduced into the simulations of the pull-out specimens from Yao et al. (2005), Ali-ahmad et al. (2006) and Mazzotti et al. (2009) to verify validity of the proposed model for different FRP width ratios, FRP lengths, free height supports and concrete cylinder strengths. Additionally, three specimens from Pan and Leung (2007) are also simulated in a similar method to test the performance of the proposed model in simulations of beam test.

8.2 Strain distribution across FRP section at FRP-concrete bonded interface with different width ratios

To explain the relationship between the width ratio and ultimate load at FRP-concrete bonded interface qualitatively, FRP strain distributions across FRP section in specimens with different FRP-concrete width ratios are extracted from Yao (2004) and shown in Figure 8.1-Figure 8.4. In general, some waves are observed across the FRP section in these figures. The presence of these waves indicates that the stress is non-uniform in the transverse direction across the section of FRP, which is also under tension in the transverse direction, when it is loaded with a tension load in the longitudinal direction.

In Figure 8.1-Figure 8.4, it is also found that the average amplitude of the strain change in all cases is around 5000με, although the stress level in FRP decreases with the increase of FRP-concrete ratio. What is more, the number of waves arising from strain change in FRP section increases with FRP-concrete width ratio, a phenomenon that means that the confining effect may be enhanced to some degree.

In addition to the Poisson's effect due to differences in the Poisson's ratio between FRP and concrete, the fact that the concrete prism is usually wider than the FRP plate and the concrete outside of the FRP plate also participates in sharing the load transferred from the FRP (Chen and Pan 2006). Both effects leads to confinement of concrete underneath the FRP, thereby increasing the ultimate load when the concrete to FRP width ratio increases. According to the conclusion obtained in Chapter 6 that the compressive strain energy of concrete is highly related to ultimate load at FRP-concrete bonded interface, a formula is derived to quantify width effect so that the FRP-concrete bonded joint can be modelled more accurately in 2D in the next section.

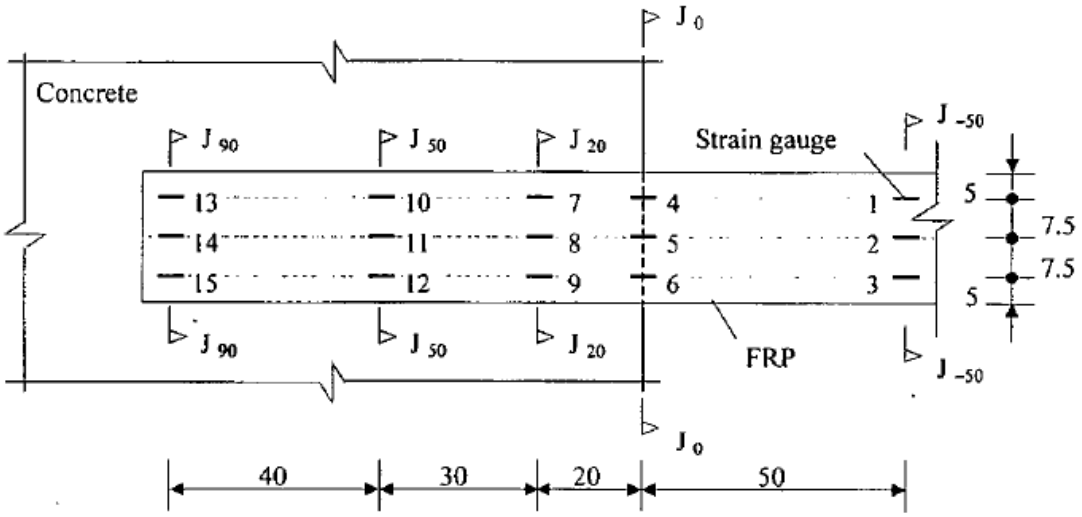

(a) Layout of strain gauges on FRP

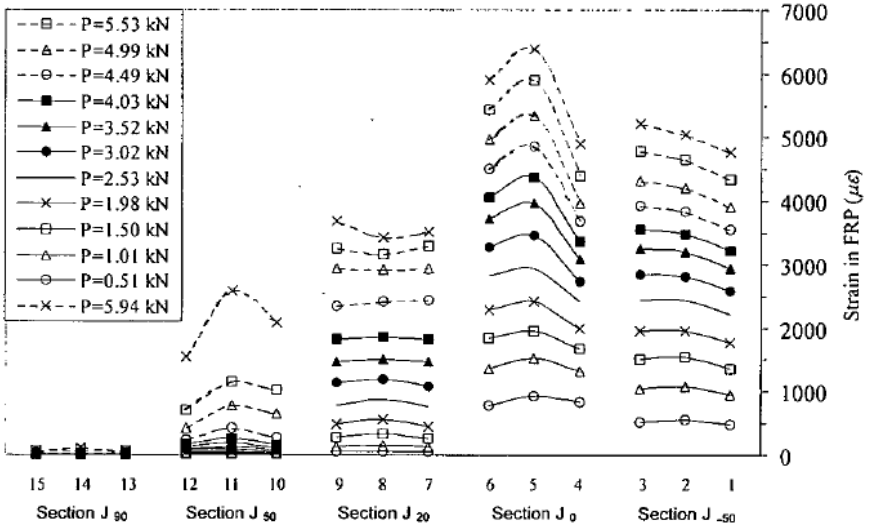

(b) Strain distributions at each section

Figure 8.1 Strain distribution in Specimen III-1 (b_f/b_c=0.167) in Yao (2004)

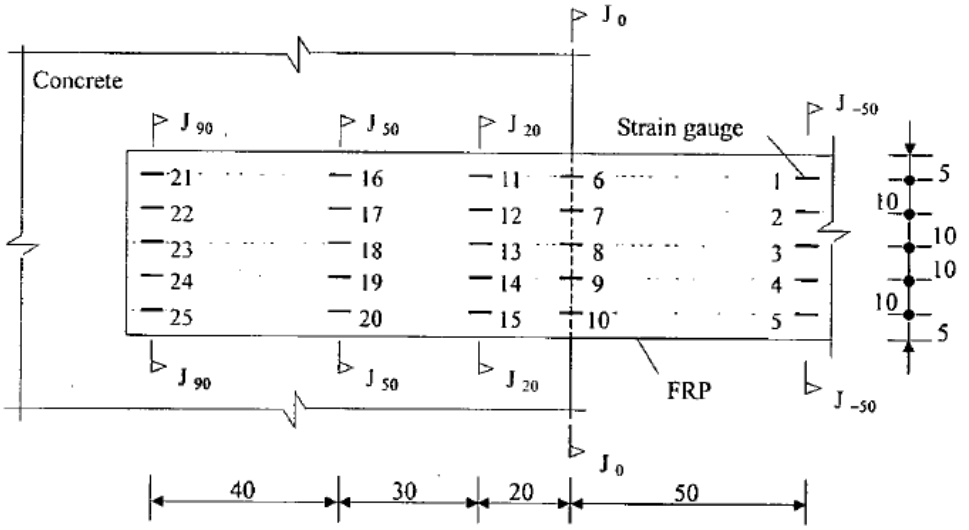

(a) Layout of strain gauges on FRP

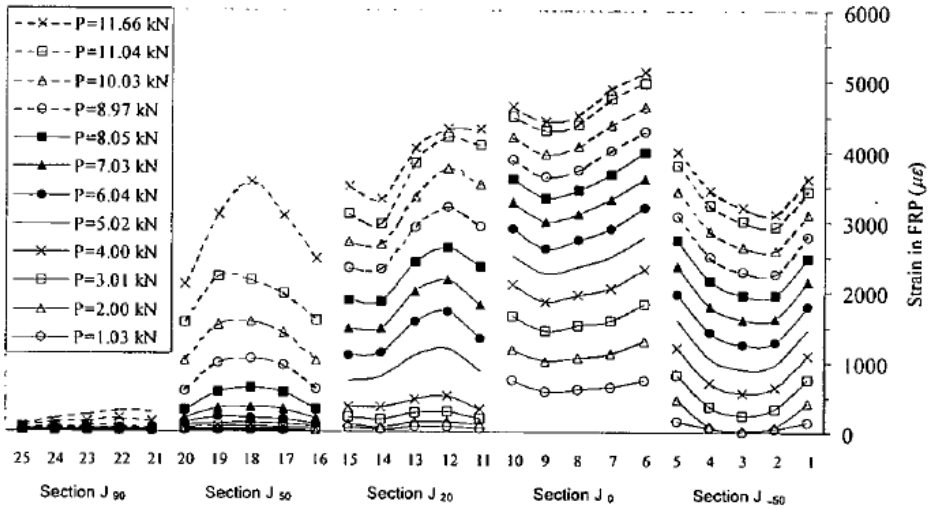

(b) Strain distributions at each section

Figure 8.2 Strain distribution in Specimen III-2 (b_f/b_c=0.333) from Yao (2004)

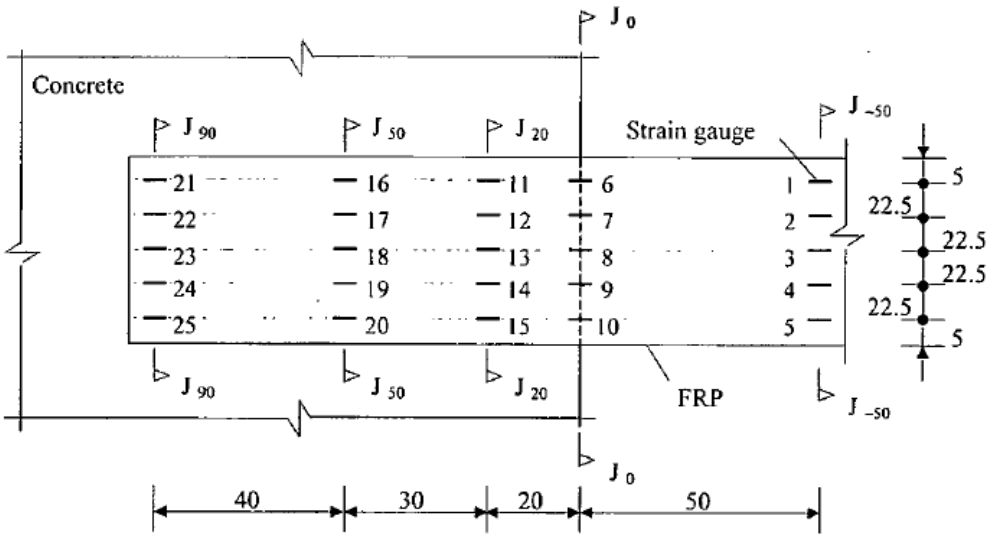

(a) Layout of strain gauges on FRP

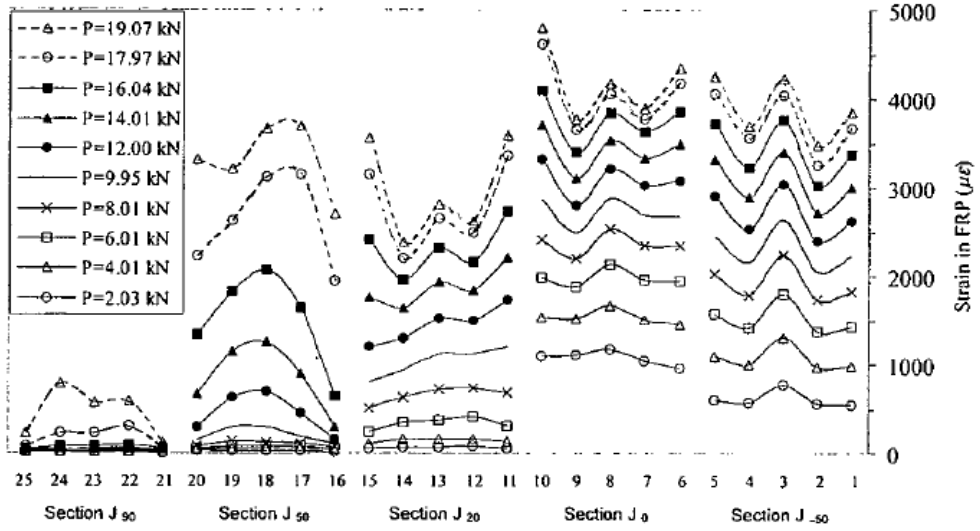

(b) Strain distributions at each section

Figure 8.3 Strain distribution in Specimen III-4 (b_f/b_c=0.667) from Yao (2004)

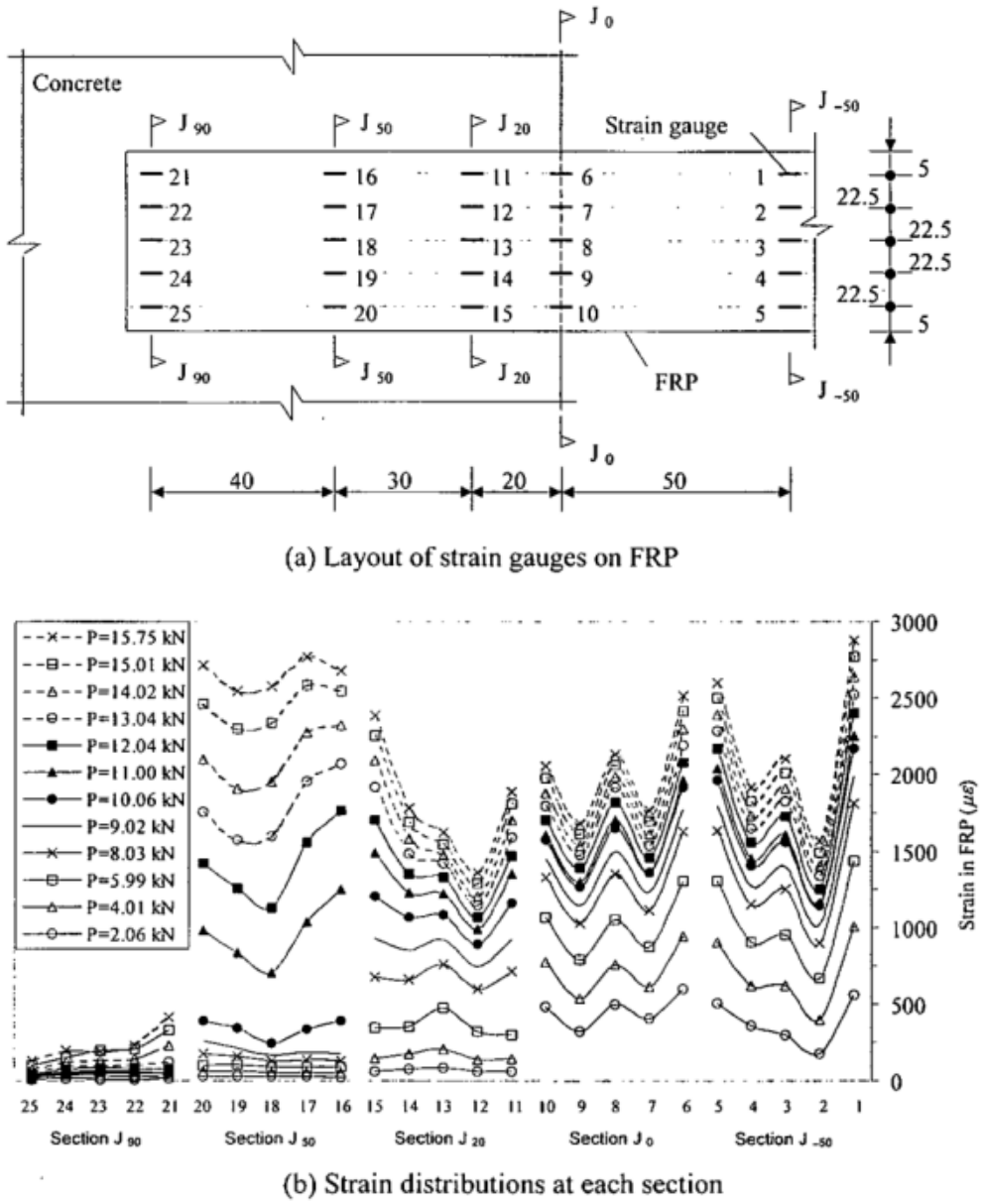

(a) Layout of strain gauges on FRP

(b) Strain distributions at each section

Figure 8.4 Strain distribution in Specimen III-6 (b_f/b_c=1) from Yao (2004)

8.3 Formulation for converting the 3D problem to 2D

A new formula is derived on the basis of the empirical bond strength formula for FRP-concrete bonded interface proposed by Chen and Teng (2001). A mathematical

expression Eq. C (2), as shown in Figure 8.5, can be derived for an effective out-of-plane thickness b_c' for concrete for the cases with different FRP-concrete width ratios.

The debonding ultimate load at FRP-concrete bonded interface is controlled by compressive fracture energy of concrete W_Q as discussed in Chapter 6, which is the product of compressive strain energy and out-of-plane thickness in 2D model. In view of that, alternatively, the compressive strain energy of concrete could be changed through the compressive strain energy rather than the out-of-plane thickness to consider the influence of FRP-concrete width ratio.

The compressive fracture energy W_{Q1} considering the width effect is given as

$$W_{Q1} = A_c'\left(\frac{b_f}{b_c}\right) \cdot b_c'\left(\frac{b_f}{b_c}\right) \tag{8.1}$$

where, $A_c'\left(\frac{b_f}{b_c}\right)$ is the compressive strain energy of concrete (i.e. the area under compressive stress-strain curve); $b_c'\left(\frac{b_f}{b_c}\right)$ is the modified out-of-plane thickness in a 2D model.

Similarly, the compressive strain energy of concrete W_{Q0} in the reference case, whose FRP width b_{f0} is 25 mm and concrete width b_{c0} is 150 mm, is given as

$$W_{Q0} = A_c'\left(\frac{b_{f0}}{b_{c0}}\right) \cdot b_c'\left(\frac{b_{f0}}{b_{c0}}\right) \tag{8.2}$$

The modifier for the compressive fracture energy of concrete is given as

$$h\left(\frac{b_f}{b_c}\right) = W_{Q1}\left(\frac{b_f}{b_c}\right) \Big/ W_{Q0}\left(\frac{b_f}{b_c}\right) = b_c'\left(\frac{b_f}{b_c}\right) \Big/ b_c'\left(\frac{b_{f0}}{b_{c0}}\right) \tag{8.3}$$

with the value of the modifier set to unity in the reference case.

Eventually, the modifier function $h\left(\frac{b_f}{b_c}\right)$ is evolved from Eq. (8.3) and given as

$$h\left(\frac{b_{\mathrm{f}}}{b_{\mathrm{c}}}\right)=\frac{b_{\mathrm{c}}{}'\left(\frac{b_{\mathrm{f}}}{b_{\mathrm{c}}}\right)/b_{\mathrm{c}}}{b_{\mathrm{c}}{}'\left(\frac{25}{150}\right)/150} \tag{8.4}$$

By assuming that compressive stress-strain curve enlarges proportionally, the modifier for compressive stress and strain is given as

$$g\left(\frac{b_{\mathrm{f}}}{b_{\mathrm{c}}}\right)=\sqrt{h\left(\frac{b_{\mathrm{f}}}{b_{\mathrm{c}}}\right)} \tag{8.5}$$

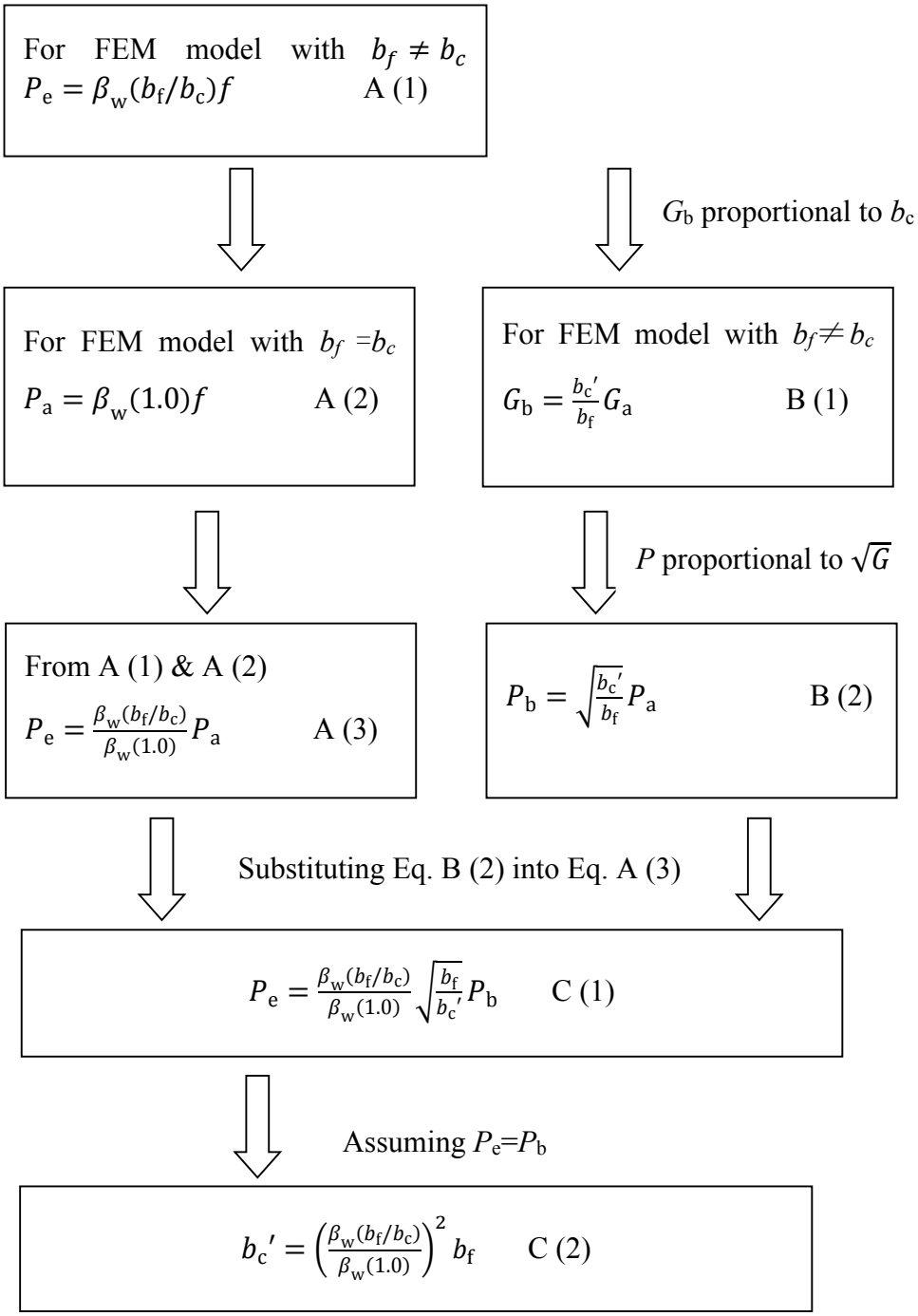

Figure 8.5 The deriving process for an effective width of concrete prism

Note: In Figure 8.5, b_f is the FRP width, b_c is the width of the concrete prism, b_c' is the effective width of concrete prism according to equivalent interfacial fracture

energy, $\beta_w = \sqrt{\frac{2-b_p/b_c}{1+b_p/b_c}}$ is the width factor proposed by in Chen and Teng (2001). G_b, G_a and G are interfacial fracture energy at FRP-concrete bonded interface (Chen and Teng 2001), P_a, P_b, P_e and P are the bond strength of FRP-concrete bonded interface in Chen and Teng (2001). Specifically, P_e is the bond strength with $b_f \neq b_c$; P_a is the bond strength with $b_f = b_c$, and with interfacial fracture energy of G_a; P_b is the bond strength with $b_f \neq b_c$, and with interfacial fracture energy of G_b; and P is used to generally stand for the bond strength. f is the function of bond strength without considering the width factor in Chen and Teng's (2001) bond strength model as in Eq. (2.24) in Chapter 2.

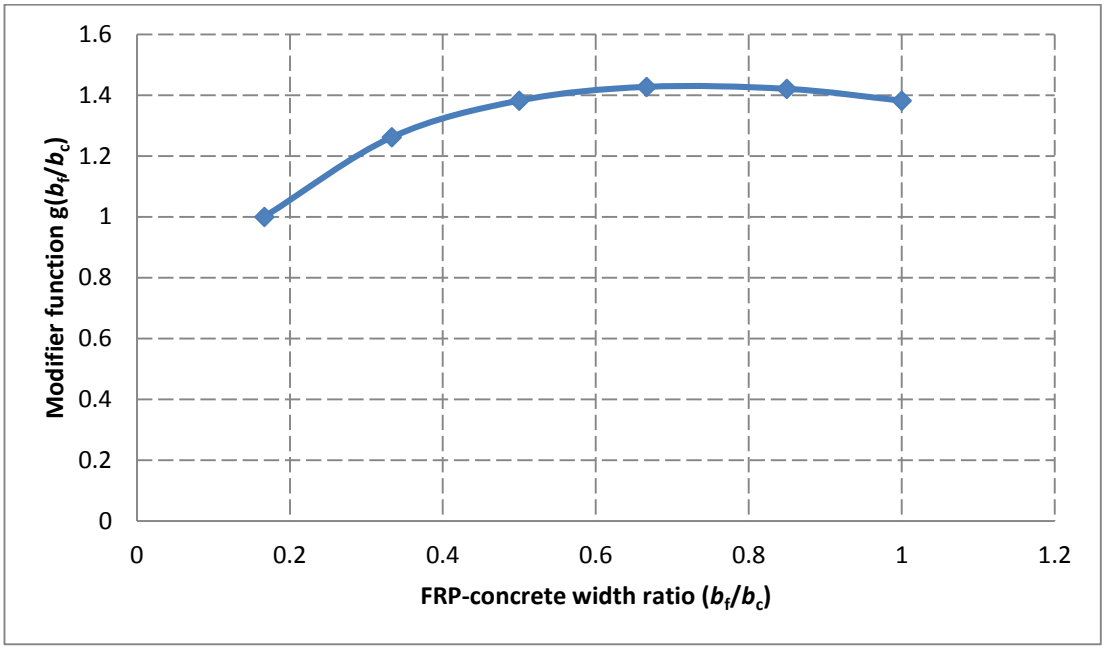

Figure 8.6 The relationship of modifier function g (b_f/b_c) to FRP-concrete width ratio b_f/b_c

Specimens III-1, III-2, III-3, III-4, III-5 and III-6 are taken as examples to demonstrate how the modifier $g(b_f/b_c)$ changes with FRP-concrete width ratio b_f/b_c, which is plotted in Figure 8.6. Generally, it is found that the value of the modifier function $g(b_f/b_c)$ reaches its peak at a value of around 0.67 for FRP-concrete width ratio b_f/b_c. Subsequently, the value of the modifier $g(b_f/b_c)$ decreases a little bit with the increase

of FRP-concrete width ratio b_f/b_c. That is because when the FRP-concrete width ratio reaches a certain value, the contribution on the confinement of concrete from the Poisson's effect may become stable whereas the contribution from the concrete outside of the FRP decreases with the FRP-concrete width ratio until zero when the ratio is equal to unity.

8.4 Validation with experimental data

In this section, the specimens from Yao et al. (2005), Ali-ahmad et al. (2006), Mazzotti et al. (2009) and Pan and Leung (2007) are simulated to validate the proposed method. The use of the specimens from Yao et al. (2005) is to validate the performance of the proposed model in predicting the ultimate loads for different FRP-concrete width ratios. Due to the narrow range of concrete strength in Yao et al. (2005), the specimens from Ali-ahmad et al. (2006) and Mazzotti et al. (2009) are employed as a supplement in terms of concrete strength to further test the performance of the proposed model. Eventually, the specimens from Pan and Leung (2007) are also used to further test the performance of the proposed model in simulation of the combined beam test.

In the simulations, the same geometrical modelling and material properties as in Chapter 3 are used unless stated otherwise. The only variation is that the compressive stress-strain curve in A1 zone. Specifically, in the proposed approach the original A1 zone is vertically divided into two zones, viz confined and normal zones, as shown in Figure 8.7. The compressive stress-strain curve in the normal zone is also set as in Chapter 3. The compressive stress-strain relationship in the confined zone is adjusted with the modifier in Eq. (8.5) to reflect the confining effect caused by the variable FRP-concrete width effect. Usually, the height of confined zone is only set to 5 mm, because this kind of effect, arising from FRP, could only reach that depth.

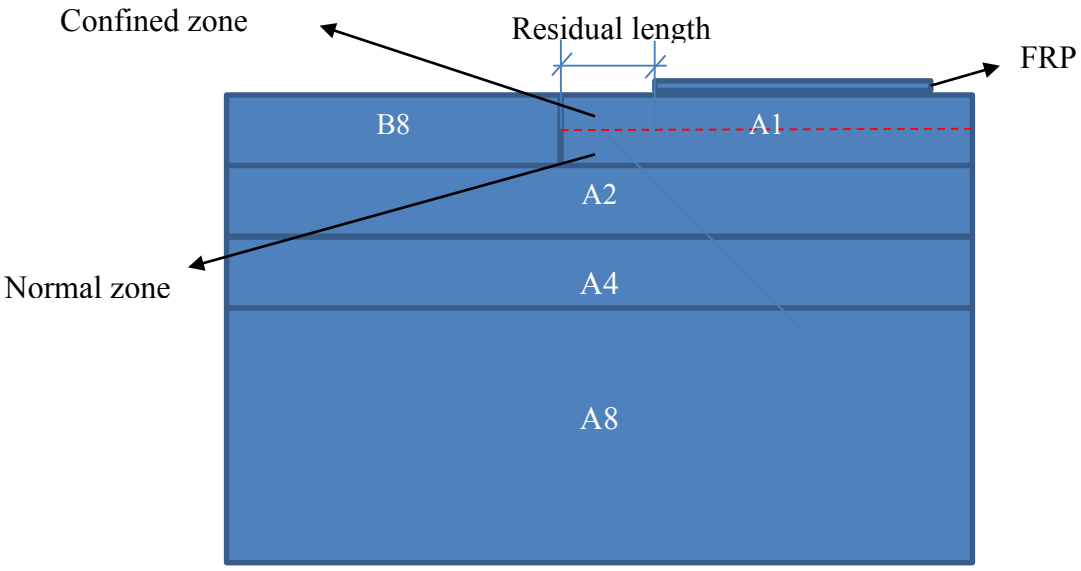

Figure 8.7 Mesh zones in the proposed approach

8.4.1 Simulations of specimens in Yao et al. (2005)

In this subsection, all 72 specimens in Yao et al. (2005) are simulated using the proposed approach. The details of these specimens have been introduced in Chapter 2.

First, series III is used to test the performance of the proposed approach for different FRP-concrete width ratios.

The load-displacement curves from the specimens in series III are shown in Figure 8.8. The ultimate loads from both test and simulation results are listed in Table 8.1. It is found that the simulation results are in good agreement with that in test, not only in terms of ultimate loads, with an average error of 8.7%, but also in terms of failure modes, with each resembling well with that in test, as shown in Figure 8.9.

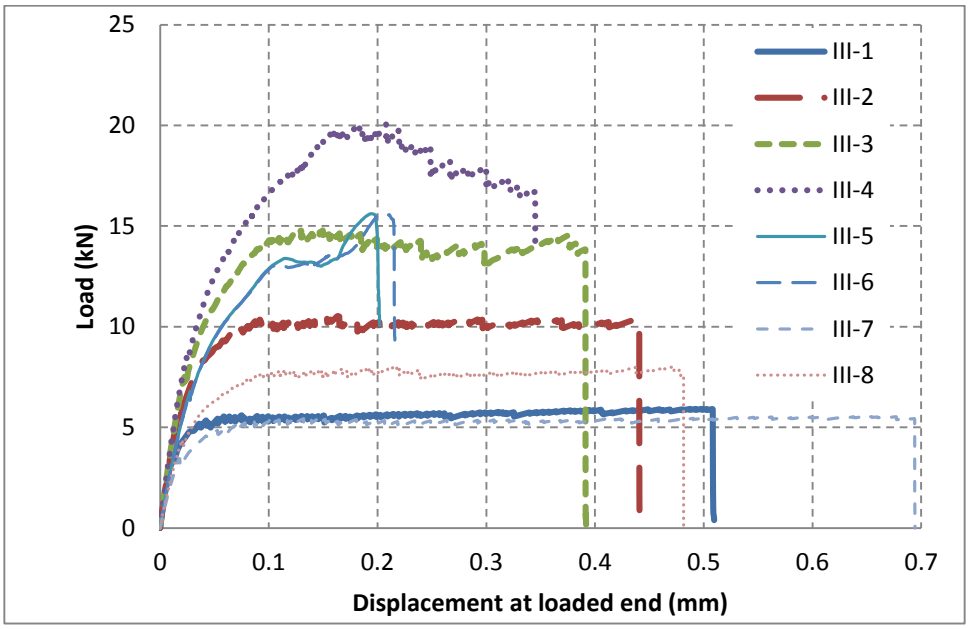

Figure 8.8 Load-displacement curves for the specimens in series III in Yao et al. (2005)

Table 8.1 Comparison of simulation and test results for the specimens from series III in Yao et al. (2005)

Label	Width of concrete prism (mm)	FRP width b_{frp} (mm)	Failure mode in test	Test data (kN)	Failure mode in simulation	Simulation results (kN)	P_{test}/P_{pred}
III-1	150	25	DB	5.94	DB	5.925	1.00
III-2	150	50	DB	11.66	DB	10.283	1.13
III-3	150	75	DB	14.63	DB	14.728	0.99
III-4	150	100	DB	19.07	DB	22.806	0.84
III-5	100	80	CPF	15.08	CPF	14.909	1.01
III-6	100	100	CPF	15.75	CPF	16.253	0.97
III-7	100	25.3	DB	4.78	DB	4.346	1.10
III-8	100	50.6	DB	8.02	DB	7.755	1.03

Average							1.01
CoV							8.7%

Note: (a) DB, debonding in concrete; (b) CPF, Concrete prism failure.

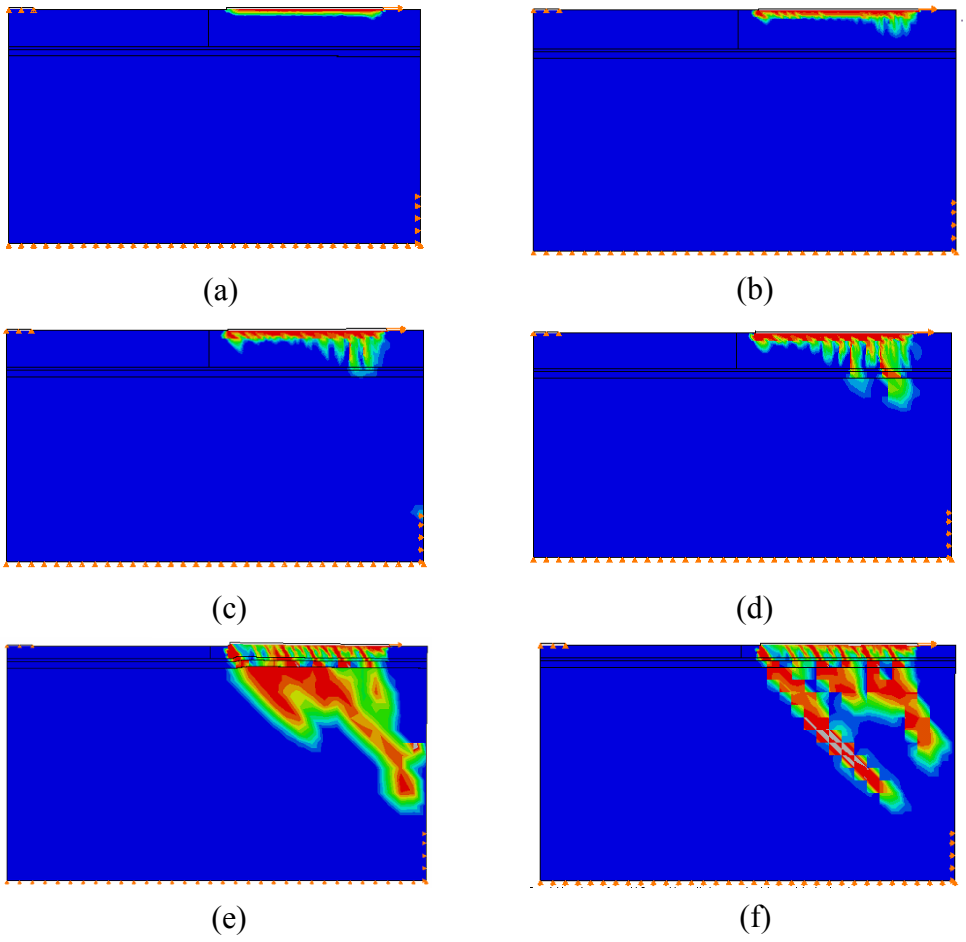

Figure 8.9 Damage contours of Specimens (a) III-1, (b) III-2, (c) III-3, (d) III-4, (e) III-5, and (f) III-6 in Yao et al. (2005)

To further validate the proposed approach in simulations of FRP-concrete bonded interface, all the other 59 specimens in Yao et al. (2005) are taken with concrete strength ranging from 18.1 MPa to 24.9 MPa and different bonded FRP length. For simplicity, both simulation and test results for these cases are plotted in Figure 8.10, in which it is also found that the simulation results are in good agreement with that in test, with an average error of 8.3%.

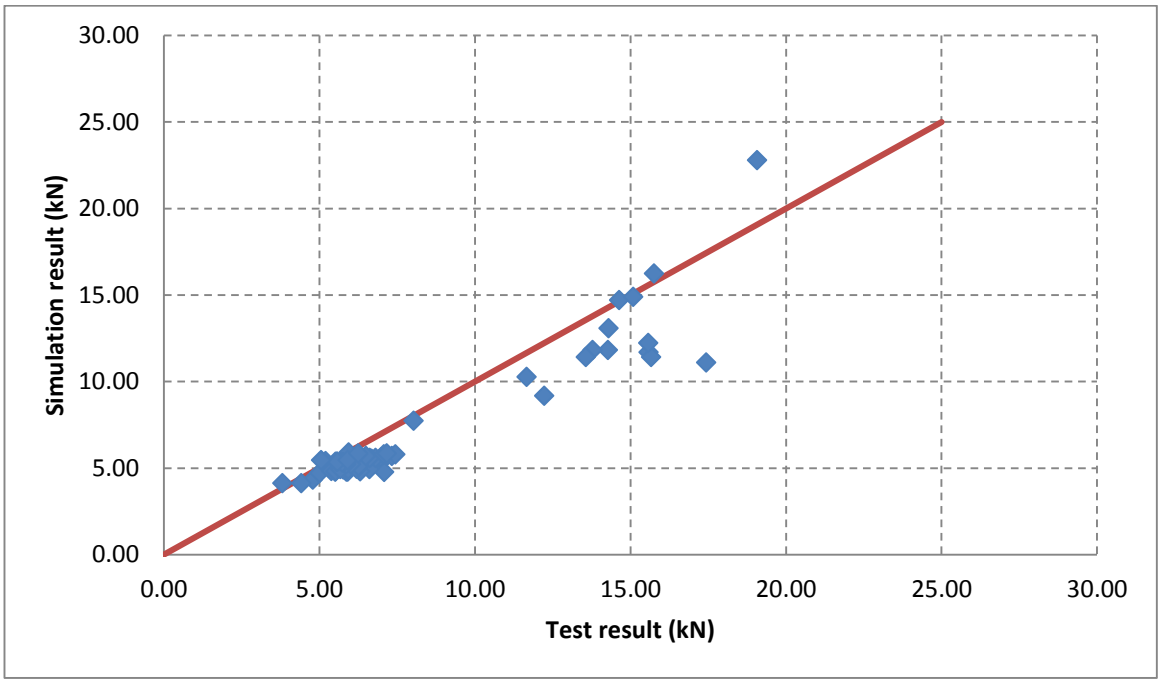

Figure 8.10 Simulation results versus test results

Even so, it is still not enough to justify this proposed model because of the reasons: a) the load-displacement curves in physical tests are not available to be compared to that in simulations; b) the concrete strength is limited in a very small range between 18.9 MPa and 27.1 MPa. For the sake of that, specimens from Mazzotti et al. (2009) and Ali-ahmad et al. (2006) are simulated again with the proposed model.

8.4.2 Simulations of specimens in Ali-ahmad et al. (2006)

In this subsection, Specimen No.5 from Ali-ahmad et al. (2006) is also simulated with the proposed approach. The details about this specimen have also been introduced in Chapter 2.

The load-displacement curves from its simulation and test results are shown in Figure 8.11. It is found that the stiffness in simulation is slightly higher than that in the corresponding test result. That is because of some slight difference existing at the notch tip of FRP-concrete bonded interface between the geometrical modelling and its corresponding physical test. Specifically, in physical test there exists a transition zone

between unbonded and complete bonding regions at FRP-concrete bonded interface, whereas in the simulation such a transient zone is also regarded as perfect bonded. In physical test, the displacement at the loaded end is measured through LVDT installed at the assumed notch tip of FRP-concrete bonded interface. However, the location of the notch tip is very difficult to determine due to the presence of such a transition zone, which results in a lower loading stiffness in experiments, compared to that in its corresponding simulation.

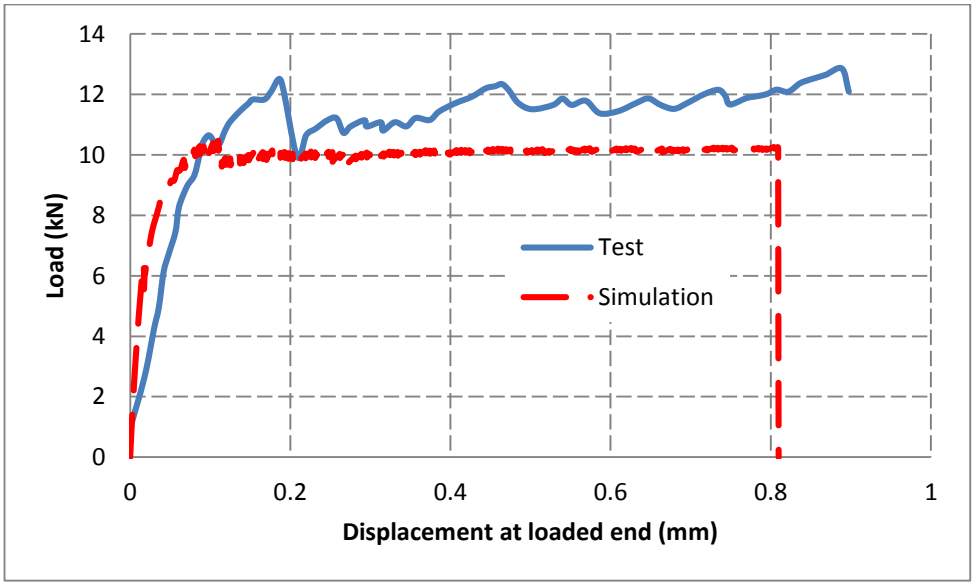

Figure 8.11 Load versus displacement curves from simulation and experimental results for Specimen No. 5 in Ali-ahmad et al.'s (2006) test

In view of that, a 7.74-mm-long FRP at the notch tip was assumed as unbonded in a new simulation of this specimen to reflect the presence of such a transition zone in the physical test. The load versus displacement curves from the new simulation and its corresponding test are compared in Figure 8.12. It is found that the agreement in the stiffness between test and simulation results has been improved to a great degree.

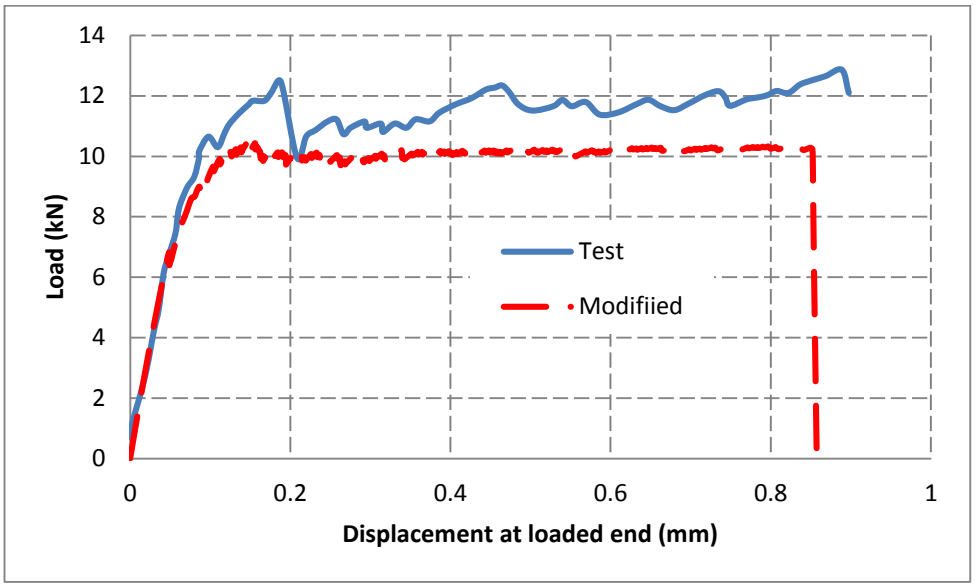

Figure 8.12 Load versus displacement curves from simulation and experimental results for Specimen No. 5 in Ali-ahmad et al.'s (2006) test, with the stiffness in simulation corrected

In addition to the stiffness, there still exist some minor inconsistences between simulation and test results in term of the ultimate load. This may be attributable to the aging of concrete between concrete compressive strength and debonding tests. Specifically, the concrete compressive strength test was conducted at an age of 28 days, whereas the debonding test is conducted at an age of 97 days. This time lapse of 72 days may result in some differences in the ultimate load at FRP-concrete bonded interface.

In view of that, three different time effect models, viz CEBFIP (1993), Guo (1999) and Liu and Xu (2008) models, were employed to predict the concrete strength at an age of 97 days.

In general, the compressive strength of concrete at various age $f_{cm}(t)$ may be estimated from

$$f_{cm}(t) = \beta_{cc} f_{cm} \tag{8.7}$$

$f_{cm}(t)$ is the mean concrete strength at an age of t days,

f_{cm} is the mean concrete strength at an age of 28 days,

$\beta_{\mathrm{cc}}(t)$ is a coefficient which depends on the age of concrete *t*.

The only variation amongst these models lies in the definition of the coefficient $\beta_{\mathrm{cc}}(t)$.

In CEBFIP (1993), for a mean temperature 20 ℃ the coefficient $\beta_{\mathrm{cc}}(t)$ is estimated from

$$\beta_{\mathrm{cc}}(t) = \exp\left\{s\left[1-\left(\frac{28}{t}\right)^{1/2}\right]\right\} \tag{8.8}$$

where

s is a coefficient which depends on the type of cement: *s*=0.20 for rapid hardening high strength cements **RS**, 0.25 for normal and rapid hardening cements **N** and **R**, 0.38 for slowly hardening cements **SL**.

t is the age of concrete (days) adjusted through

$$t = \sum_{i=1}^{n} \Delta t_i \exp\left[13.65 - \frac{4000}{273 + T(\Delta t_i)}\right] \tag{8.9}$$

where

Δt_i is the number of days where a temperature *T* prevails,

$T(\Delta t_i)$ is the temperature (℃) during the time period Δt_i.

For the specimen in Ali-ahmad et al. (2006), Δt_i is 97 days, in accordance with such a statement in its original document that the FRP was attached to the concrete specimen at an age of 90 days, a procedure that is followed by a 7-day curing in the laboratory environment before test. The temperature $T(\Delta t_i)$ was 22 ℃ as stated in Ali-ahmad et al. (2006). The concrete is regarded as normal and rapid hardening cements so *s* = 0.25 as the concrete strength was 38 MPa and the concrete specimens were demoulded 24

hours after casting. Based on the above information, the parameter $\beta_{cc}(t)$ is calculated to be 1.13.

In Guo's (1999) model, concrete strength is related to the age of concrete through Table 8.2.

Table 8.2 Variation of concrete compression strength with the age of concrete (Guo, 1999)

Age/ days		3	7	28	90	360
f_c/N/mm^{-2}	Normal cement	0.4	0.65	1	1.20	1.35
	Rapid hardening cement	0.55	0.75	1	1.15	1.20

For the specimens in Ali-ahmad et al. (2006), the parameter $\beta_{cc}(t)$ in Guo's (1999) model is calculated as 1.20.

In Liu and Xu's (2008) model, concrete strength is related to the age of concrete through

$$\beta_{cc}(t) = \frac{\lg t}{\lg 28} \tag{8.10}$$

For the specimen in Ali-ahmad et al. (2006), parameter $\beta_{cc}(t)$ in Liu and Xu's (2008) model is calculated as 1.38.

The load-displacement curves from the simulations with concrete strength corrected using different age effect models are compared to that from test, as shown in Figure 8.13. The curve from the simulation with concrete strength corrected with Liu and Xu's (2008) model is in the best agreement with that from the test, although the other models also achieved at a reasonably good level.

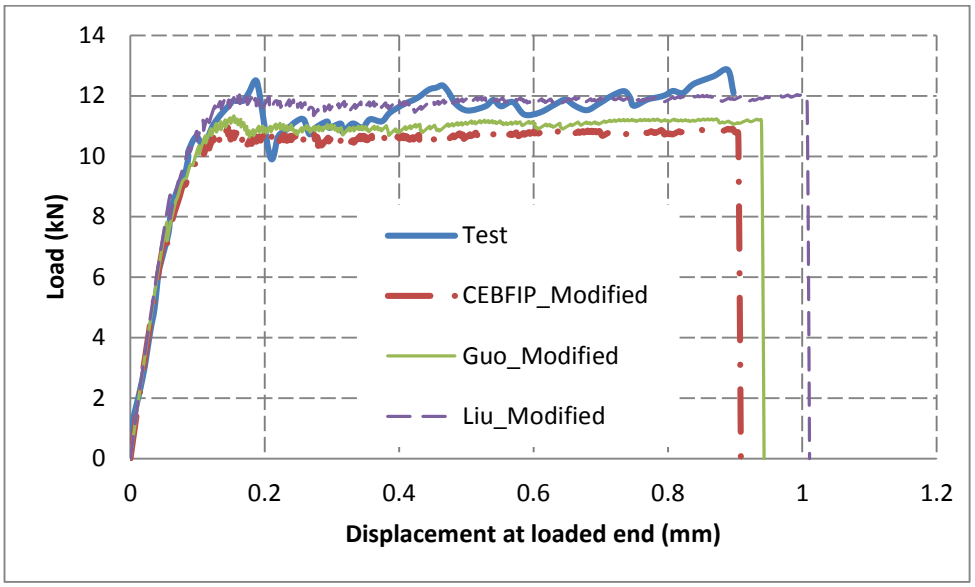

Figure 8.13 The load versus displacement curves from the simulations with concrete strength corrected using different age effect models

8.4.3 Simulations of specimens in Mazzotti et al. (2009)

Once again, Specimens P5A and P9B from Mazzotti et al. (2009) are simulated using the proposed approach. The details about these specimens have also been introduced in Chapter 2.

The ultimate loads from both test and simulation results are listed in Table 8.1. It is found that the simulation results are in good agreement with that in test with an average error of 5.4%. Furthermore, the load-displacement curves from the simulations of these two specimens are compared to their counterpart in the physical tests, as shown in Figure 8.14-Figure 8.15. It is found that the initial stiffness and ultimate load in the simulations are in good agreement with that in the tests. In Figure 8.15, it is found that a relatively good global load versus displacement curve is obtained in the test of Specimen P9B, compared to Specimen P5A. The stiffness in test is a little bit lower than that in its corresponding simulation for a similar reason as stated in Section 8.4.2 that there should exist a transition zone between unbonded and complete bonded zones in the notch tip of FRP-concrete bonded interface. This is inevitable in physical test

but not explicitly stated due to neglect in test. That is because in physical test it is very difficult or almost impossible to detect such a position with a high precision so as to obtain an accurate value of slip by placing an appropriate device (i.e. LVDT) at the surface of FRP, because of an inevitable bonding defect always existing to a different degree, as discussed in Section 8.4.2 but being neglected by this method. Even some high techniques currently are available to accurately detect the positions of the crack tip at the FRP-concrete bonded interface before testing, but it is also very difficult to guarantee the crack tip to keep in line in the transverse direction of FRP (i.e. in the 2D modelling method it is very difficult to consider the difference arising from the mechanical behaviour in the transverse direction of FRP).

Here, a 20-mm-long bonded FRP at the notch tip was assumed as unbonded to reflect the presence of such a transition zone in physical test. Accordingly, the load versus displacement curve from the simulation with the presence of the transition zone considered is also compared to that from its corresponding test result, as shown in Figure 8.15. It is found that the agreement in the loading stiffness between test and simulation results has been improved to a great degree.

The axial strains of FRP along the longitudinal direction at the ultimate load level in simulation of Specimen P5A are compared to that obtained from test, as shown in Figure 8.16. Through visual inspection, it is found that the axial strain from simulation result is consistent with that from test.

In addition, the failure modes of Specimens P5A and P9B, whose difference only lies in the FRP stiffness, are shown in Figure 8.17-Figure 8.18. In general, it is found that the depth of crack at FRP-concrete bonded interface becomes deeper with the increase of FRP axial stiffness.

Table 8.3 Comparison of simulation and test results for the specimens in Mazzotti et al. (2009)

Label	FRP types	Elastic modulus (GPa)	Thickness (mm)	Test data (kN)	Simulation result (kN)	Error
P5A	sheet	230	0.13	16.5	15.45	6.4%
P9B	plate	165	1.2	39.1	40.92	4.4%
					Average	5.4%

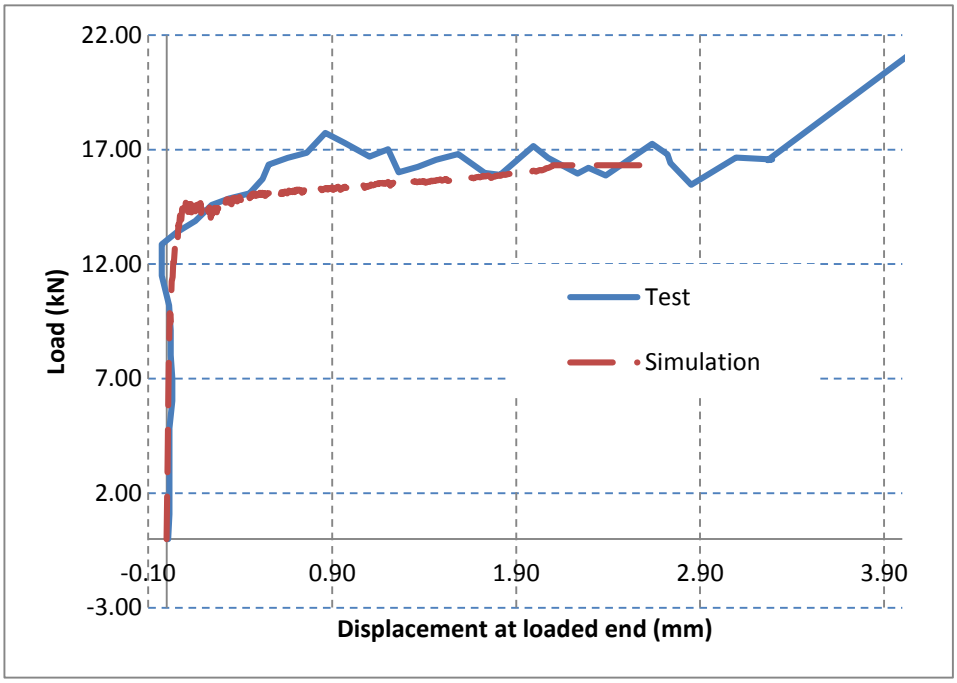

Figure 8.14 Load-displacement curves for Specimen P5A from Mazzotti et al. (2009)

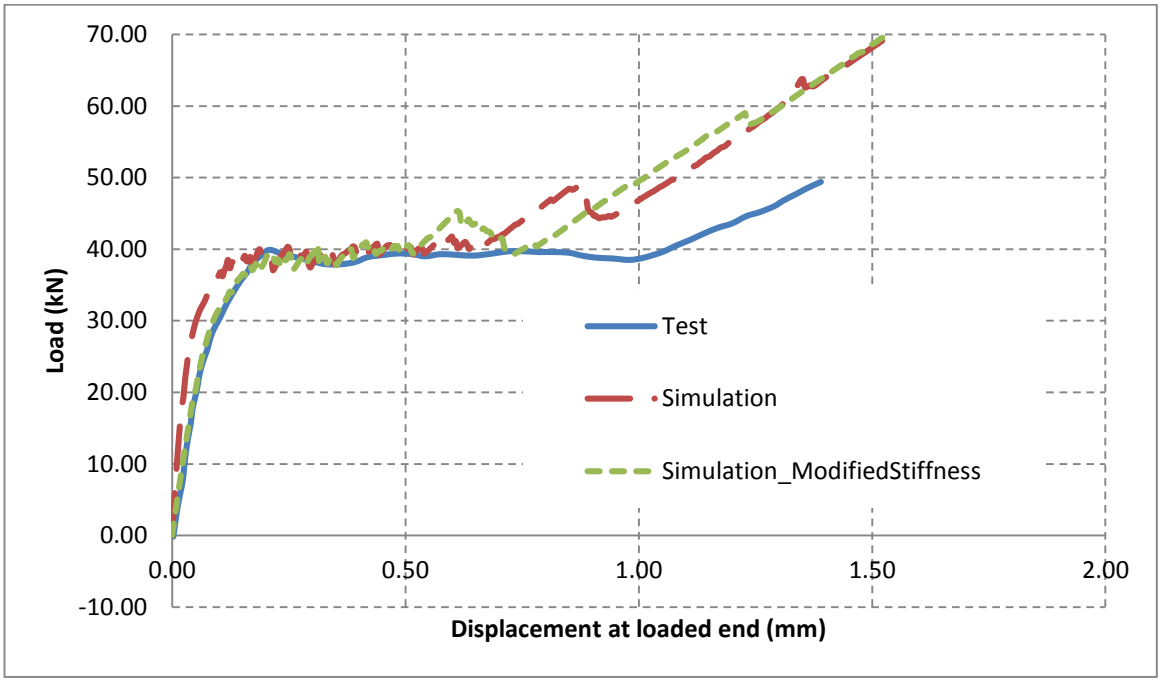

Figure 8.15 Load-displacement curves for Specimen P9B from Mazzotti et al. (2009)

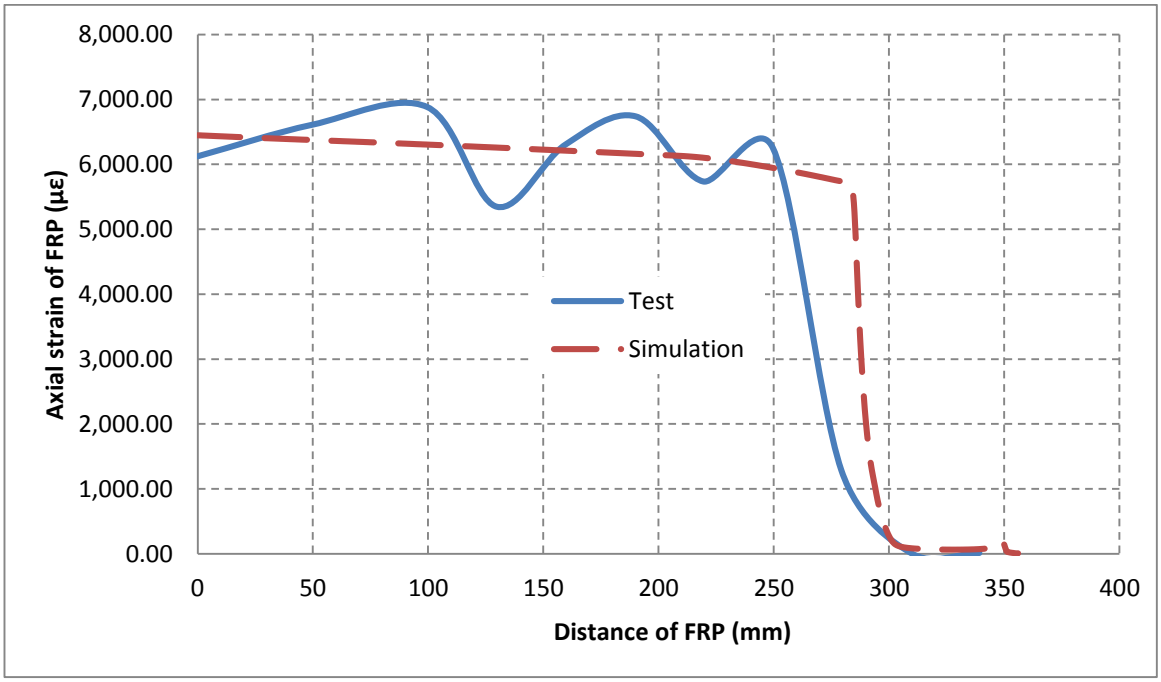

Figure 8.16 Comparison of strains along FRP at peak applied force for Specimen P5A in Mazzotti et al. (2009)

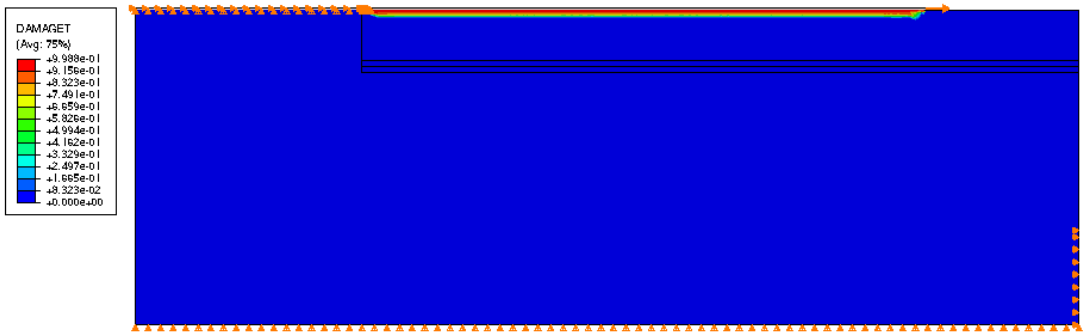

Figure 8.17 Simulated damage contour for Specimen P5A in Mazzotti et al. (2009)

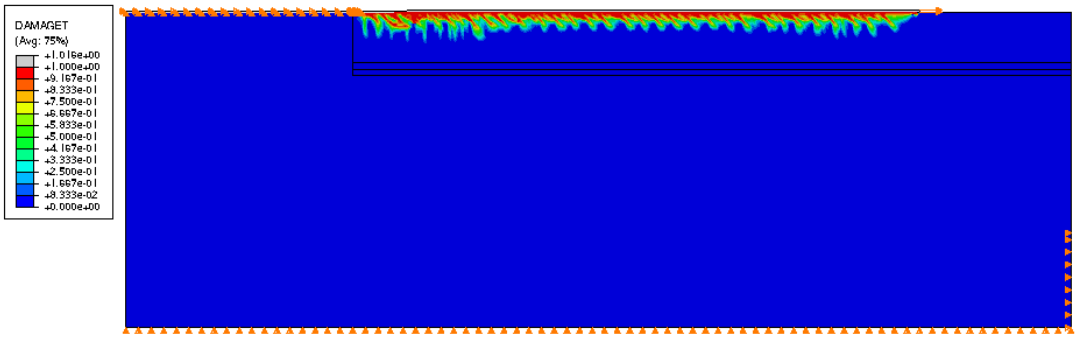

Figure 8.18 Simulated damage contour for Specimen P9B in Mazzotti et al. (2009)

8.4.4 Simulations of specimens in Pan and Leung (2007)

As a supplement of the above studies, three beam tests with different offset displacements from Pan and Leung (2007) have also been simulated using the proposed approach. The details about these specimens were also introduced in Chapter 2. Good agreement is shown between simulation and test results, with an average error of 1.7% (see Table 8.4).

Table 8.4 Comparison of simulation and test results for the specimens in Pan and Leung (2007)

Specimen	Elastic modulus (GPa)	FRP thickness (mm)	FRP length (mm)	Test data (kN)	Simulation results (kN)	Error (%)
B2-150-00	230	0.22	150	11.86	12.307	3.8
B2-150-04	230	0.22	150	10.48	10.586	1.0
B2-150-08	230	0.22	150	6.81	6.83	0.3
					Average	1.7

Note: In the case of B2-150-00, B2 means that two layers of FRP were used in the specimen (the nominal thickness of one layer was 0.11 mm); 150 means that FRP length was 150 mm, 00 means the offset between concrete and steel block was 0 mm.

8.5 Solutions to key issues in simulations with traditional approach

In Chapter 2, four significant issues in the traditional mesoscale model (e.g. Lu et al. (2005); Tao and Chen (2014)) were identified. In Section 8.4, it has proved that the proposed approach has a good performance in predicting the mechanical response at FRP-concrete bonded interface. However, it still remains unknown whether it has completely solved these issues. In view of that, these four issues are explored based on the work in Section 8.4.

Solution to Issue 1: the requirement to post-process the width effect of FRP-concrete bonded interface

In the proposed approach in this study, different failure modes obtained in simulations with different FRP-concrete width ratios, as shown in Figure 8.9 and Table 8.1, resemble that in physical tests. There is no need to do any similar post-processing procedures to that in the traditional approach, because the FRP-concrete width effect has been considered in the definition of the material properties of the confined zone in the FE model, as described in Section 8.3. Therefore, Issue 1 has been completely solved in the proposed approach.

Solution to Issue 2: in physical test the specimen fails as CPF mode, whereas in simulation it fails as debonding mode

In the simulation of Specimen III-6 from Yao et al. (2005) with the proposed approach, the failure mode is not shown as debonding failure like that in the traditional approach, but as CPF failure mode (see Figure 8.19), which is in accord with that observed in physical test (see Figure 2.2). Furthermore, good agreement is also found in comparison between simulation and test results with an error of 3% (see Table 8.1). In summary, Issue 2 appearing in traditional approach has been completely solved in the proposed approach.

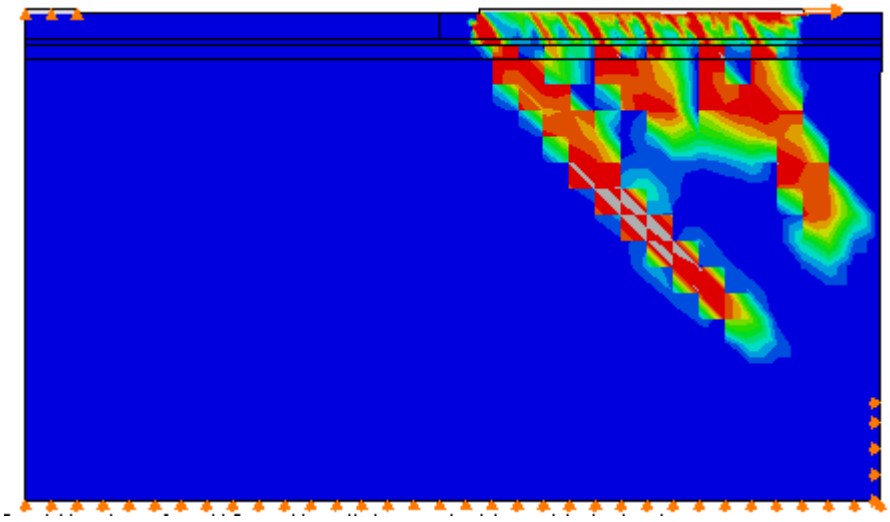

Figure 8.19 Simulated failure mode of Specimen III-6 in Yao et al. (2005)

Solution to Issue 3: in physical test the specimen fails as deboning mode, whereas in simulation fails as CPF mode

This is not an issue anymore in the proposed approach. For example, the failure mode in the simulation of Specimen II-2 in Yao et al. (2005) with the proposed approach is not shown as CPF mode again like that in the traditional approach, but as debonding failure mode, which is in agreement with test as shown in Figure 2.1. Similarly, good agreement is also found in comparison between simulation and test results with an

error of 3.5% in the loading capacity (see Table 8.1). In summary, issue 3 appearing in the traditional approach has been completely solved in the proposed approach.

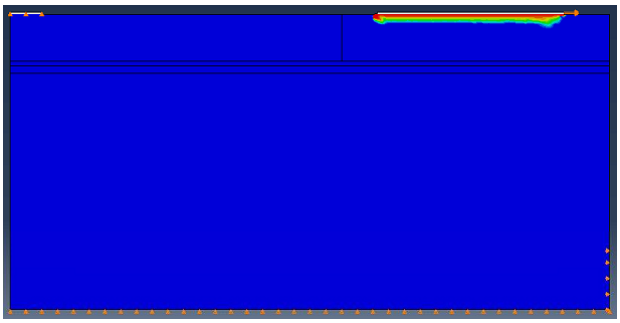

Figure 8.20 Simulated failure mode of Specimen III-2 in Yao et al. (2005)

Solution to Issue 4: in physical beam-type bond test it fails in deboning mode, whereas in simulation it fails as CPF mode

In the simulation of Specimen B2-150-04 from Pan and Leung (2007) using the proposed approach, the failure is a debonding mode, as shown in Figure 8.21, which is in agreement with that observed in physical test as shown in Figure 2.14. A satisfactory level of accuracy is also found in comparison of the simulation result with the proposed method to its corresponding test result, with an error of 4% in loading capacity.

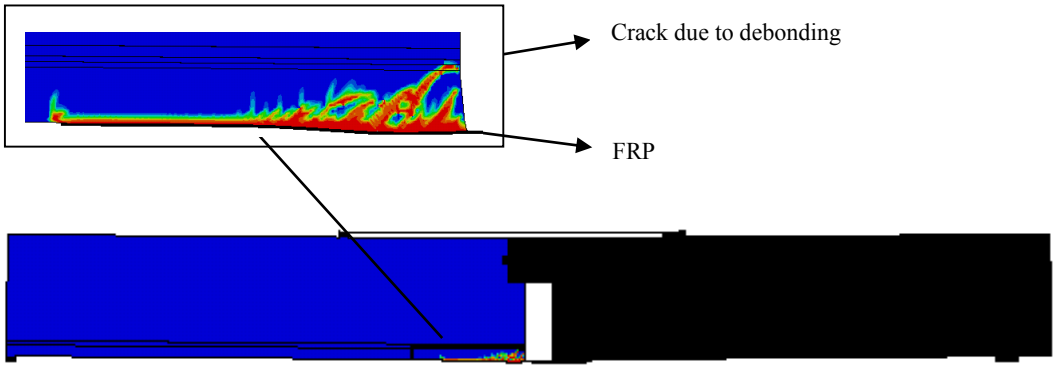

Figure 8.21 Predicted failure mode of Specimen B2-150-04 from Pan and Leung (2007)

In summary, all the key issues in the traditional approach have been solved with failure modes in simulations resembling that observed in their corresponding physical tests, and with a good agreement with the test results in loading capacity.

8.6 Conclusions

In this chapter, strain distribution across FRP section is introduced from Yao (2004) to demonstrate the variation of stress in the transverse direction of FRP, which in turn causes the confinement of concrete adjacent to FRP. Subsequently, a formula (Eq.(8.5)) was proposed to accurately quantify the effect due to different widths between the FRP plate and the concrete prism in an FRP-concrete bonded joint test. Through this formula, the compressive stress-strain curve is enlarged proportionately to reflect confining effect caused by FRP-concrete width ratio, thereby enabling a 2D mesoscale FE model to accurately model FRP-concrete 3D interfacial debonding behaviour.

To validate the reasonability and feasibility of this proposed model, the specimens in Yao et al. (2005) (i.e. from the Hong Kong Polytechnic University), Ali-ahmad et al. (2006) (i.e. from the City University of New York) and Mazzotti et al. (2009) (i.e. from University of Bologna) were employed to test the performance of the proposed approach. In addition, three beam type tests from Pan and Leung (2007) (i.e. Hong Kong University of Science and Technology) were also used to further test the performance of the proposed model in combined beam test. Subsequently, the issues discussed in Chapter 2 are answered respectively on the basis of the simulation results in Section 8.5.

Based on the results presented in this chapter, the following conclusions can be drawn:

1. The load-displacement curves and the strain distributions in FRP from the simulations with proposed approach are in good agreement with that in test results.
2. The proposed approach, combined with the CDP model, is applicable to the simulation of various specimens with FRP-concrete bonded interface, with

variable concrete strength, FRP-concrete width ratio, FRP length, free support height and types of comparison setups.

3. This 2D FE model provides a powerful and economical alternative to laboratory test to gain a better understanding of the behaviour of FRP-concrete interfacial debonding and to generate numerical results for the development of a bond-slip model, which will be discussed in the next chapter.

Chapter 9
Bond–slip models for FRP-concrete interfacial behaviour under monotonic load

9.1 Introduction

This chapter develops a bond-slip model for FRP-to-concrete bonded joints by making use of the 2D mesoscale FE model presented in Chapter 8.

Bond-slip model is the relationship between bond stress (i.e. shear stress) and the relative slip at the FRP-concrete bonded interface. An accurate bond-slip model could accurately model the mechanical behaviour at FRP-concrete bonded interface with the least computation effort, an advantage that makes it possible to simulate large scale structures, whose mechanical behaviours are characterised by debonding at FRP-concrete bonded interface. Thus, a reliable local bond-slip model for the interface is of fundamental importance to the accurate modelling hence in-depth understanding of debonding failures in FRP strengthened concrete structures.

In this chapter, different bond-slip models are reviewed first, followed by an introduction of different methods available in the existing literature to obtain the bond stress and slip for bond-slip models. FE studies employing the mesoscale model developed in Chapter 8 are conducted with different parameters such as FRP stiffness, FRP-concrete width ratio and concrete strength to investigate the effects of these parameters on the bond-slip model, such as its interfacial fracture energy, maximum bond stress and slip at maximum bond stress. On basis of these analyses, a new bond slip relationship is proposed to describe the interfacial behaviour of FRP-concrete bonded interface. The proposed model is then used to simulate the specimens from Yao et al. (2005), Mazzotti et al. (2009) and Ali-ahmad et al. (2006) to test its performance in predicting the mechanical behaviour at FRP-concrete bonded interface.

9.2 Existing bond-slip models

Various bond-slip models have been proposed based on either FRP strains measured in physical tests, global load-slip curves in physical tests, or strain variations in mesoscale FE simulations. Six local bond-slip models have been collected from the existing literature and they are summarised below. In these models, τ (MPa) is the local bond (shear) stress, s (mm) is the local slip, τ_{max} (MPa) is the maximum local bond stress, s_0 (mm) is the slip at the peak bond stress τ_{max}, s_f (mm) is the slip beyond which the local bond stress is assumed zero, β_w is the width ratio factor, f_c' (MPa) is the cylinder compressive strength of concrete, f_t (MPa) is the tensile strength of concrete, E_f is the elastic modulus of FRP, t_f is the thickness of FRP, $K_a=G_a/t_a$ (i.e. G_a is the shear modulus of adhesive and t_a is the thickness of adhesive). The unit for $E_f t_f$ is N/mm while for K_a is MPa/mm, unless stated otherwise.

1. Nakaba et al.'s (2001) model

$$\tau = \tau_{max}\left(\frac{s}{s_0}\right)\left[3\Big/\left(2+\left(\frac{s}{s_0}\right)^3\right)\right] \tag{9.1}$$

where

$$\tau_{max} = 3.5\, {f_c'}^{0.19} \tag{9.2}$$

$$s_0 = 0.065 \tag{9.3}$$

2. Monti et al.'s (2003) model

$$\tau = \begin{cases} \tau_{max}\left(\dfrac{s}{s_0}\right) & \text{for} \quad s \le s_0 \\ \tau_{max}\left(\dfrac{s_f - s}{s_f - s_0}\right) & \text{for} \quad s_0 < s \le s_f \end{cases} \tag{9.4}$$

where

$$\tau_{max} = 1.8\,\beta_w f_t \tag{9.5}$$

$$s_0 = 2.5\tau_{max}\left(\frac{t_a}{E_a} + \frac{50}{E_c}\right) \tag{9.6}$$

$$s_{\mathrm{f}} = 0.33\beta_{\mathrm{w}} \tag{9.7}$$

$$\beta_{\mathrm{w}} = \sqrt{\frac{1.5(2 - b_{\mathrm{f}}/b_{\mathrm{c}})}{1 + b_{\mathrm{f}}/100}} \tag{9.8}$$

3. Savioa et al.'s (2003) model

$$\tau = \tau_{\max}\left(\frac{s}{s_0}\right)\left[2.86/\left(1.86 + \left(\frac{s}{s_0}\right)^{2.86}\right)\right] \tag{9.9}$$

where

$$\tau_{\max} = 3.5\, {f_c}'^{0.19} \tag{9.10}$$

$$s_0 = 0.051 \tag{9.11}$$

4. Dai and Ueda's (2003) model

$$\tau = \begin{cases} \tau_{\max}\left(\dfrac{s}{s_0}\right)^{0.575} & \text{for} \quad s \le s_0 \\ \tau_{\max}\mathrm{e}^{-\beta(s-s_0)} & \text{for} \quad s > s_0 \end{cases} \tag{9.12}$$

where

$$\tau_{\max} = \frac{-1.575\alpha K_{\mathrm{a}} + \sqrt{2.481\alpha^2 K_{\mathrm{a}}^2 + 6.3\alpha\beta^2 K_{\mathrm{a}} G_{\mathrm{f}}}}{2\beta} \tag{9.13}$$

$$s_0 = \tau_{\max}/(\alpha K_{\mathrm{a}}) \tag{9.14}$$

with

$$\alpha = 0.028(E_{\mathrm{f}} t_{\mathrm{f}}/1000)^{0.254} \tag{9.15}$$

$$\beta = 0.0035 K_{\mathrm{a}}(E_{\mathrm{f}} t_{\mathrm{f}}/1000)^{0.34} \tag{9.16}$$

$$G_{\mathrm{f}} = 7.554 K_{\mathrm{a}}^{-0.449}({f_{\mathrm{c}}}')^{0.343} \tag{9.17}$$

5. Dai et al.'s (2005) model

$$\tau = 2BG_{\mathrm{f}}\big(\exp(-Bs) - \exp(-2Bs)\big) \tag{9.18}$$

where

B is given as

$$B = 6.846(E_f t_f)^{0.108} {K_a}^{0.833} \tag{9.19}$$

G_f is given as

$$G_f = 0.446 {K_a}^{-0.352} (f_c')^{0.236} (E_f t_f)^{0.023} \tag{9.20}$$

In this model, the units for $E_f t_f$ is kN/mm, while for K_a is GPa/mm.

6. Lu et al.'s (2005a) model

$$\tau = \begin{cases} \tau_{max} \sqrt{\dfrac{s}{s_0}} & \text{for} \quad s \le s_0 \\ \tau_{max} e^{-\alpha\left(\frac{s}{s_0}-1\right)} & \text{for} \quad s > s_0 \end{cases} \tag{9.21}$$

where

$$\tau_{max} = 1.5 \beta_w f_t \tag{9.22}$$

$$s_0 = 0.0195 \beta_w f_t \tag{9.23}$$

$$G_f = 0.308 \beta_w^2 \sqrt{f_t} \tag{9.24}$$

$$\alpha = \frac{1}{\dfrac{G_f}{\tau_{max} s_0} - \dfrac{2}{3}} \tag{9.25}$$

9.3 Methods for determining bond-slip models

As discussed before, the bond-slip model of FRP-concrete bonded interface comprises of the shear stress and slip so different methods of obtaining the bond stress and slip are reviewed respectively as follows.

9.3.1 Methods for determining the bond stress

In the existing literature there are three methods available to obtain bond stress at FRP-concrete bonded interface: (a) from the variations of the axial stress in FRP strips in mesoscale simulation results (e.g. Lu et al., 2005); (b) from experimental axial strains of the FRP strips measured with closely spaced strain gauges (e.g. Nakaba et al., 2001,

Savioa et al., 2003 and Ali-ahmad et al., 2006); (c) from experimental global load-displacement (i.e. slip at the loaded end) curves measured with loading machine and LVDT (e.g. Dai et al., 2005; Ueda et al., 2003);

Method (a)

In theory, the bond stress could be obtained from the variation of the axial stress in the FRP (Figure 9.1) giving

$$\tau = \frac{\mathrm{d}\sigma_\mathrm{f}}{\mathrm{d}x} t_\mathrm{f} \tag{9.26}$$

where, σ_f is the axial stress in FRP and t_f is the thickness of FRP. From Eq. (9.26), it is found that bond stress τ is the differentiation of the axial stress of FRP σ_f with respect to the distance x.

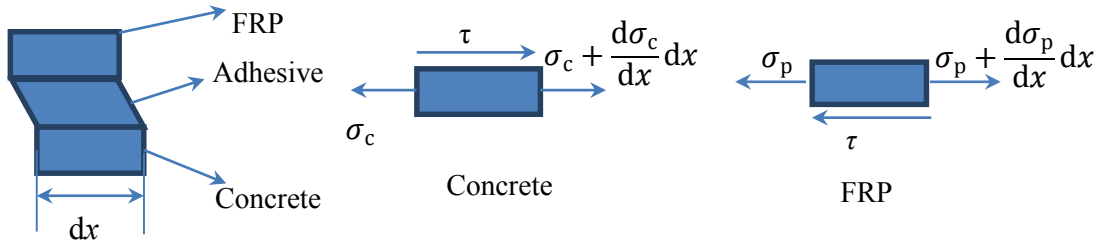

Figure 9.1 Theoretical derivation of bond stress from normal stress

To obtain the bond stress in mesoscale simulations, Eq. (9.26) is approximated as

$$\tau \approx \frac{\Delta\, \sigma_\mathrm{f}}{\Delta\, x} t_\mathrm{f} \tag{9.27}$$

From FE analysis results, the bond stress τ can be obtained through Eq. (9.27) from the normal stress σ_f in two neighbouring elements of FRP, so the shear stress obtained is the average value over the length $\Delta\, x$. In theory, a smaller value $\Delta\, x$ is preferable for the sake of accuracy.

As shown in Figure 9.2, Lu et al.'s (2005) further processed the interfacial bond stress distribution obtained using the above method with a smoothing procedure to remove

oscillations, which were arising from dynamic effect and could be completely avoided through an appropriate setting of dynamic approach as in Chapter 3. However, this smoothing procedure could distort the shape of the bond-slip curve.

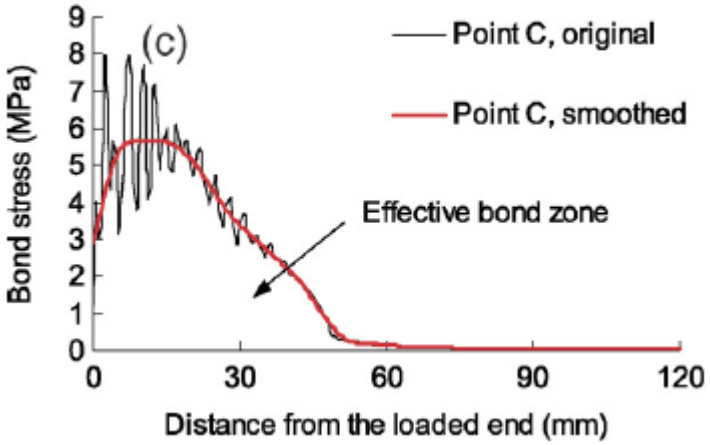

Figure 9.2 bond stress distributions along FRP obtained by Lu et al. (2004)

Method (b)

In the second method, bond stress in bond-slip model is obtained through

$$\tau_i = \frac{E_f t_f (\varepsilon_i - \varepsilon_{i-1})}{\Delta x} \tag{9.28}$$

where, τ_i is the average interfacial bond stress in section *i*; ε_i and ε_{i-1} are strain value measurements at the *i* th and *i*-1 th gauges bonded on the FRP sheets respectively.

This method the same as Eq. (9.27) but uses strain measurements instead. The accuracy of the bond stress obtained in this method can be significantly affected by the Δx value in experiments which cannot be very small for practical reasons. Also the heterogeneity of concrete material (random distribution of coarse aggregates along FRP sheets) may result in violent variations in local bond-slip models (e.g. Dai et al., 2005; Nakaba et al., 2001), as shown in Figure 9.3.

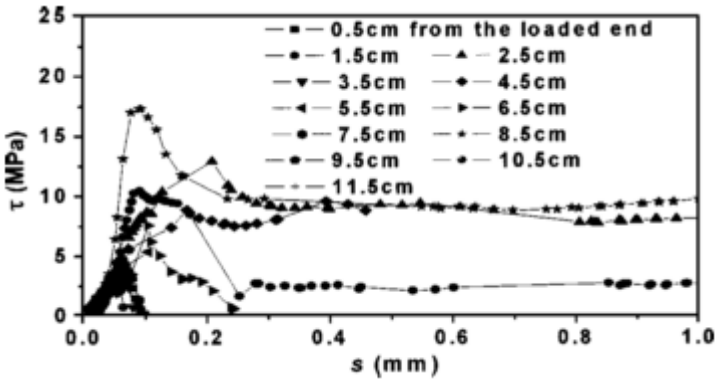

Figure 9.3 Calculated local bond stress-slip relationships at different locations from the loaded end (Dai et al. (2005))

Method (c)

In the third method, the bond-slip model is derived from the global load-slip curve obtained from physical tests, according to the relationship between global load-displacement curve (i.e. the loading stiffness) and its corresponding bond-slip curve. It seems that the model obtained through this method is more plausible than that obtained from axial strain measurement in Method (b) because relatively accurate results about the load and displacement are easier to obtain than the axial strain of FRP in physical tests. However, the accuracy of the global slip in physical tests may not be so easy to be measured, since it is highly sensitive to the position of the crack tip before debonding, as discussed in Chapter 8. Furthermore, in physical test it is very difficult to detect such a position with a high precision so as to obtain an accurate value of slip by placing an appropriate device (i.e. LVDT) at the surface of FRP.

More details about the performance of these bond-slip models in simulations are discussed in Section 9.7.2.

9.3.2 Methods for determining the slip

There are also several different methods to obtain the slip.

In Mazzotti et al. (2009), through assuming perfect bonding (no slip) at the free end of FRP (i.e. s (0) =0) slip at *x* is obtained through

$$s(x) = s(x_i) + \int_{x_i}^{x} \varepsilon(x)\mathrm{d}x = s(x_i) + \frac{(\varepsilon_{i+1} - \varepsilon_i)}{(x_{i+1} - x_i)} \frac{x^2}{2} + \varepsilon_i x \qquad (9.29)$$

where, ε_i and ε_{i+1} are strain value measurements at the *i* th and *i*+1 th gauges bonded on the FRP (i.e. counted from the free end of FRP) respectively; x_i and x_{i+1} are the distances from the *i* th and *i*+1 th gauges to the free end of FRP. Through Eq. (9.29) average slip $s_{i+1/2}$ is computed then based on the assumption that the FRP strain between two neighbouring gauges is linearly distributed.

Similarly, based on the assumption that there is no slip at the free end of FRP, Dai et al. (2005) determined the slip from

$$s_i = \frac{\Delta x}{2}\left(\varepsilon_0 + 2\sum_{j=1}^{i-1}\varepsilon_j + \varepsilon_i\right) \qquad (9.30)$$

where, s_i is local slip between FRP and concrete at the section *i*; ε_0 is the strain of FRP at the free end of the bond area; ε_j is the strain value of the *j* th gauge arranged at the surface of FRP, Δx is the distance between the centroids of two neighbouring strain gauges. Eq. (9.30) is based on the assumption that the strain is constant over the length Δx and that slip of one particular node is equal to the accumulation of the deformation between this node and the node at the free end of FRP.

The main issue, existing in these two methods, lies in the fact that the assumption of zero slip at the free end of FRP is not valid again when the bond length at FRP-concrete bonded interface is very large.

In the mesoscale simulation, slip is obtained directly through difference in node displacements at the two sides of the assumed crack , which is defined by the effective thickness of the concrete t_c as 5 mm (Lu et al. 2005b).

9.4 Influencing factors for determining the bond-slip model from mesoscale FE results

The aim in this section is to find out an appropriate method to extract an appropriate bond-slip model from the simulation results with mesoscale methods through a series of investigations. Different factors are investigated to see how they affect the resulting bond-slip model.

9.4.1 Effect of averaging length

Specimen III-1 in Yao et al. (2005) is used as the reference case. The bond stress is determined by averaging within a small FRP length. The averaging process is described in detail by taking the cases with averaging length of 1 mm and 2 mm as examples, as shown in Figure 9.4. In the case for an averaging length 1mm, the bond stress is obtained through the variation between the two neighbouring elements, as shown in Figure 9.4 (a). The slip is the relative displacement between Node 2 (between the two neighbouring elements in Figure 9.4) and the node located 5 mm right under Node 2 in concrete.

Similarly, in the case of an averaging length 2 mm, the calculation procedure in the case of an averaging length 1 mm is repeated respectively for the element set, which is comprised of element 1 and element 2, and for the element set, which is comprised of element 2 and element 3. Afterwards, the shear stress and slip are averaged respectively at the same time point. Similar procedure is also conducted in the cases of averaging lengths of 5 mm and 10mm through repeating that in the case of an averaging length 1 mm.

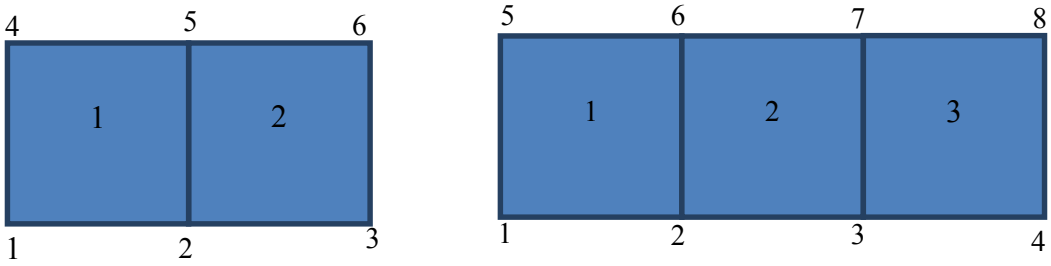

Figure 9.4 Sketch of FRP elements with element and node numbers

Following the aforementioned procedure, the bond stress-slip models are obtained from the mesoscale result using different averaging length Δx, viz 1 mm, 2 mm, 5 mm and 10 mm, as shown in Figure 9.5. It is found that the peak bond stress decreases with an increase of the averaging length Δx, although the initial stiffness and interfacial fracture energy in these cases are almost un-affected.

These bond-slip curves may be used to assign properties for spring elements and simulate the same test specimen using interfacial spring elements. The predicted load-displacement curves using these spring elements are compared to that from the mesoscale result of Specimen III-1 in Yao et al. (2005) as shown in Figure 9.6. Clearly all the shapes of these curves are similar to that from the mesoscale result, in spite of the significant differences amongst the bond-slip curves, as shown in Figure 9.5. The only difference between these cases in Figure 9.6 lies in the area where the load is about to enter the plateau. Generally, the higher value of the bond stress leads to the higher stiffness in this region, which is more close to that in their corresponding mesoscale result.

It appears that the ultimate load in simulations with bond stress-slip models is only determined by interfacial fracture energy, but the softening behaviour in global load versus displacement curve is affected by the counterpart in local bond-slip curve, which is highly connected to the peak bond stress in the bond-slip curve. Furthermore, it is also found that global load-displacement curves from the cases with average

lengths of 1mm and 2mm are very close to each other, as shown in Figure 9.6. A value of $\Delta x = 1$ mm (the element size in the current FE model) is used in the following analysis to obtain bond-slip model from mesoscale simulations.

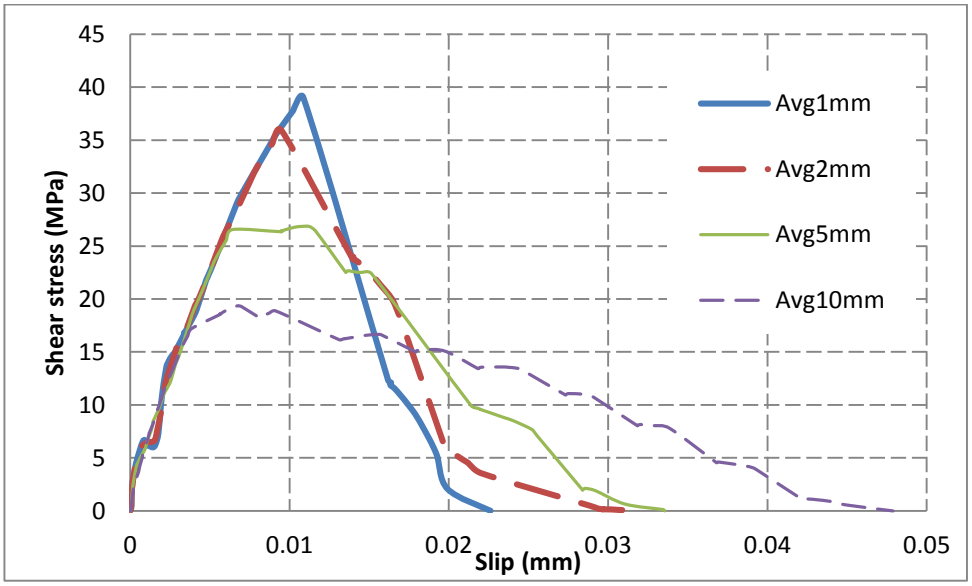

Figure 9.5 Bond stress-slip relationship with averaging length= 1 mm, 2 mm, 5 mm and 10 mm

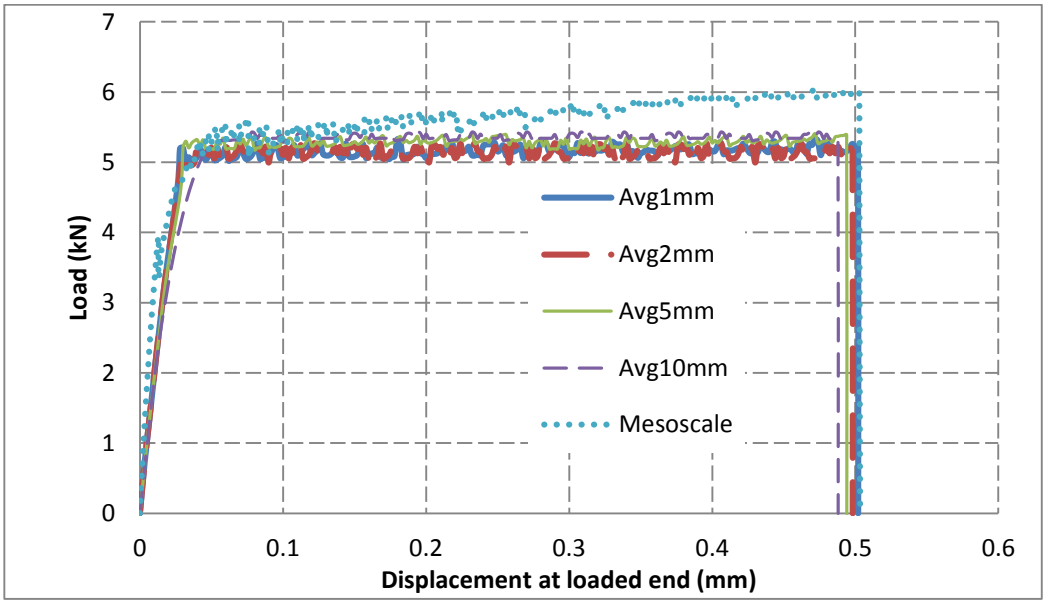

Figure 9.6 Spring element model predicted load-displacement curves using different stress averaging schemes for Specimen III-1 from Yao et al. (2005)

Figure 9.5 shows that some fluctuations are featured in the curves with average lengths of 5 mm and 10 mm. They may be smoothed with a polynomial fit function in a least-squares sense in MATLAB (2014), as shown in Figure 9.7. The load-displacement curves are compared in Figure 9.8 for smoothed and unsmoothed bond-slip curves. In general, there are very little differences between them, except that the global load versus displacement curves from simulations with smoothed model are very smooth while in simulations with original curves experience a lot of oscillations, as shown in Figure 9.8. Therefore, it is acceptable to use an appropriate fit function to remove oscillations in the bond-slip models.

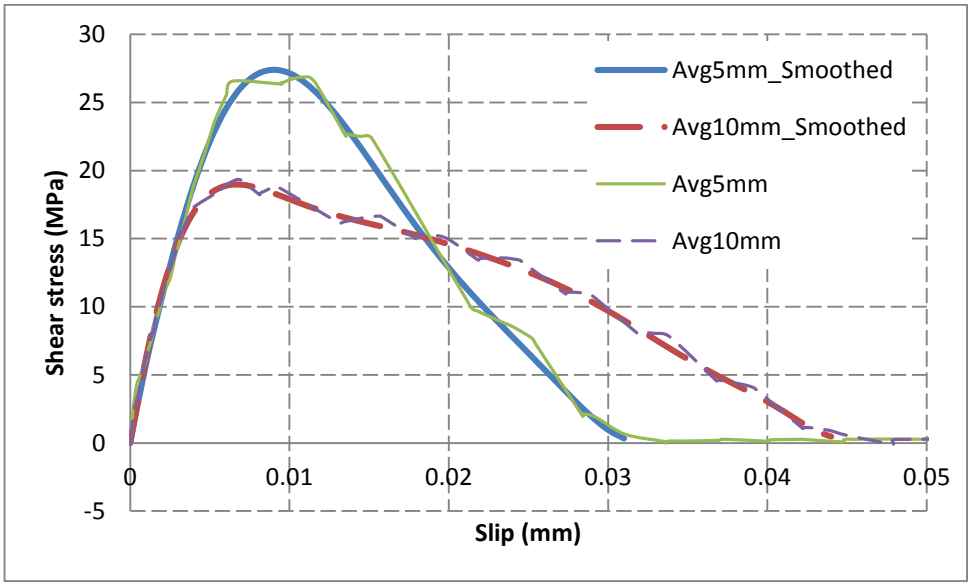

Figure 9.7 The original and smoothed bond-slip models

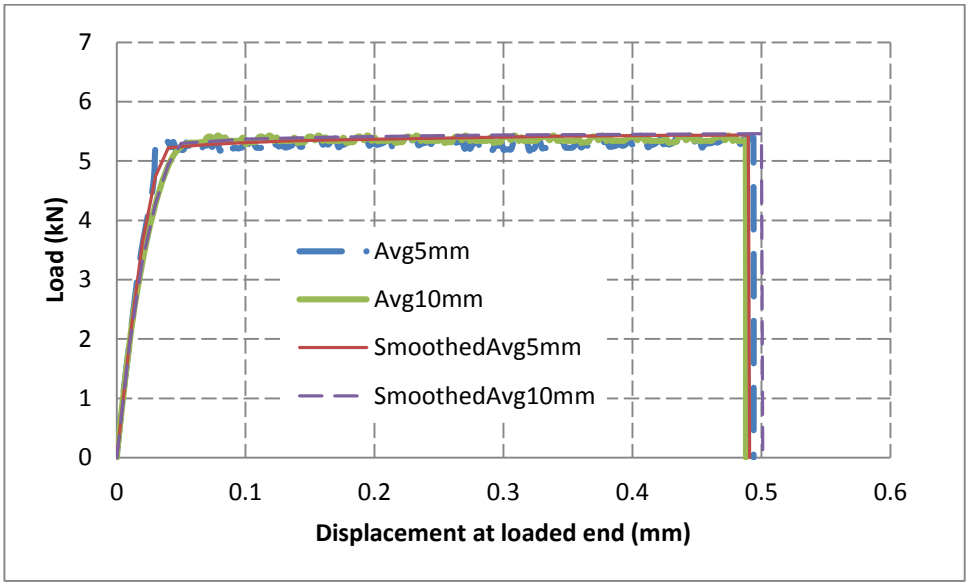

Figure 9.8 Comparison of global load versus displacement curves from the simulations of Specimen III-1 with original and smoothed bond-slip models

9.4.2 Bond stress obtained through virtual strain gauges

In section 9.4.1, it has been found that the average length Δx has a significant effect on the value of the peak stress in bond-slip models, as shown in Figure 9.5. Similar effect may also exist in physical test when obtaining bond stress from strain measurements. Specifically, the bond stress is obtained through axial strains in two neighbouring strain gauges, which in essence are only averaged values over the length of strain gauge bonded to the FRP surface.

With reference to Specimen III-1 in Yao et al. (2005), different bond-slip models are obtained from the mesoscale model by assuming that the strain gauges are bonded to FRP in simulations and imitating the methods employed in physical experiments so as to investigate the effect of the averaged stress on the mechanical behaviour at FRP-concrete bonded interface. Both the length and spacing of strain gauges are varied from 10 mm, 15 mm to 20 mm.

The bond stress-slip relationships with different strain gauge lengths and spacings are obtained from the mesoscale result and compared in Figure 9.9-Figure 9.12. In general,

it is found that the peak value in bond stress decreases with the increase of the strain gauge spacing, as shown in Figure 9.9-Figure 9.11 and with the increase of the strain gauge length, as shown in Figure 9.12. Furthermore, a number of oscillations are observed in these figures, so a polynomial fit function in a least-squares sense is employed to remove them in MATLAB (2014). After the removal of these oscillations, these curves are employed in the simulation of Specimen III-1 in Yao et al. (2005) as the bond-slip model at the FRP-concrete bonded interface (the details about the geometrical modelling and material properties are found in Section 9.7.1).

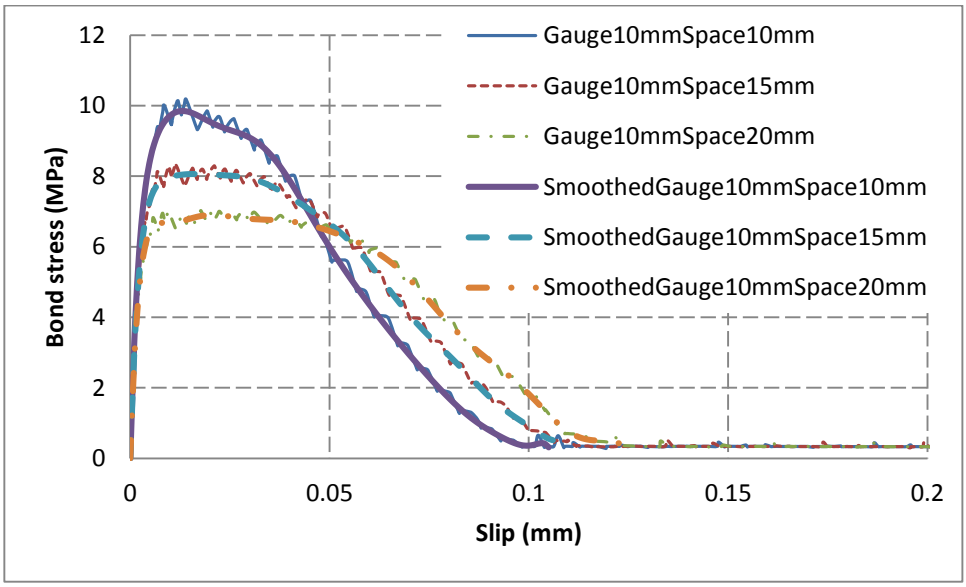

Figure 9.9 Bond stress-slip relationship with 10mm strain gauge length and different spacing rangings

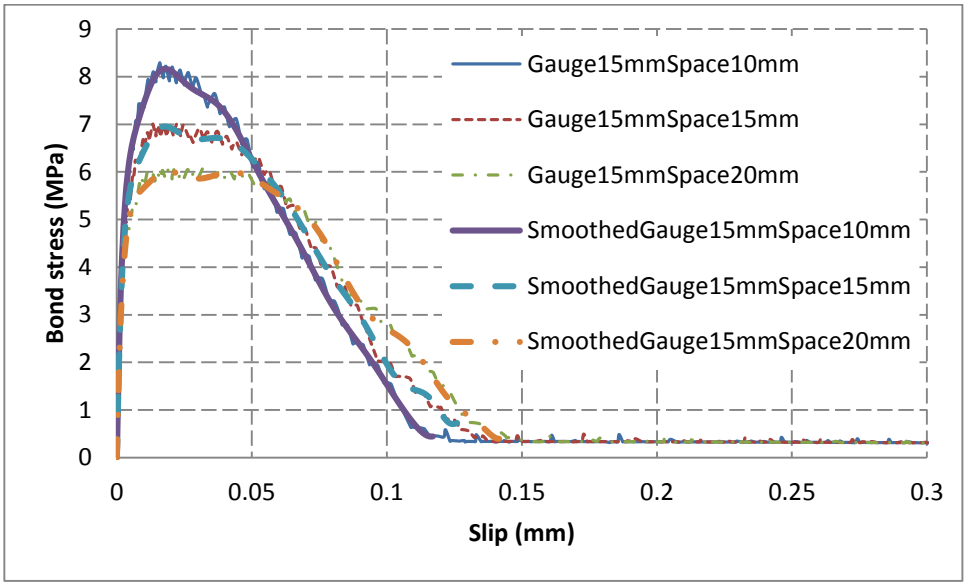

Figure 9.10 Bond stress-slip relationship with 15mm strain gauge length and different spacing rangings

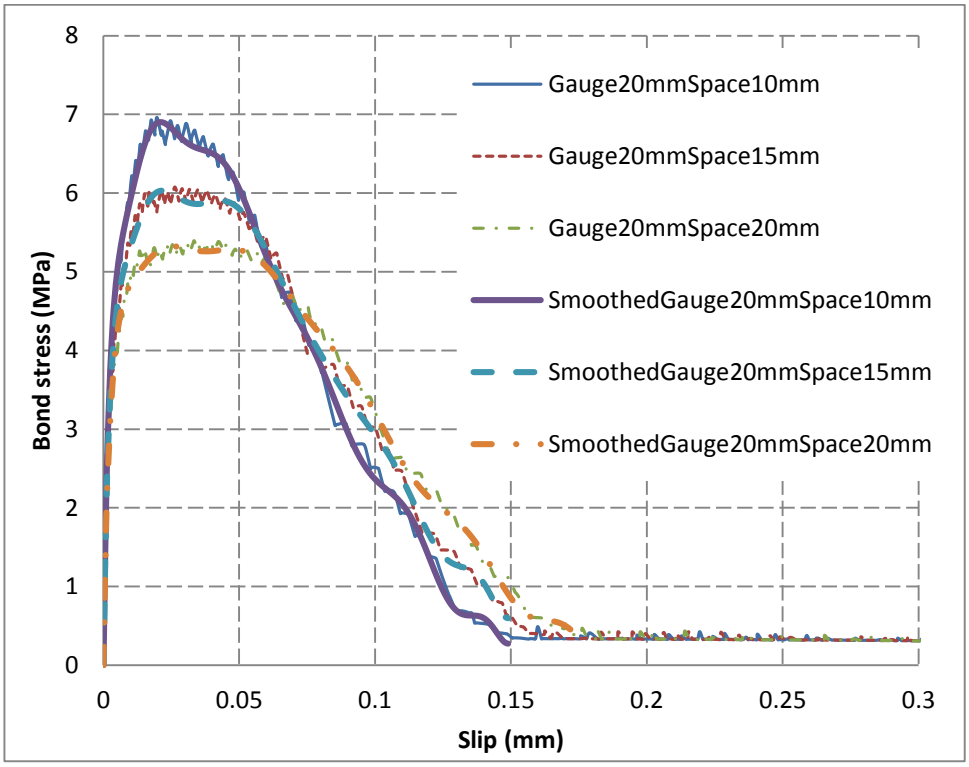

Figure 9.11 Bond stress-slip relationship with 20mm strain gauge length and different spacing rangings

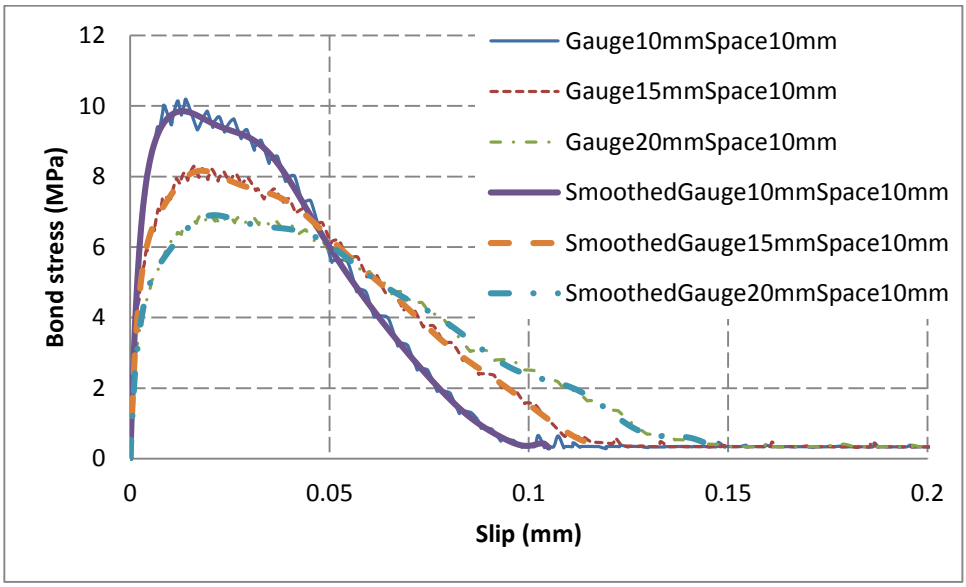

Figure 9.12 Bond stress-slip relationship with 10mm spacing ranging and different strain gauge lengths

Subsequently, the smoothed bond stress-slip curves in Figure 9.9-Figure 9.11 are employed for the simulations of Specimen III-1 in Yao et al. (2005), whose load versus displacement curves are shown in Figure 9.13-Figure 9.16. The curve from the mesoscale FE model is also shown for comparison. In general, it is found that the stiffness in simulation results with these load-slip curves appear significantly lower than that in their corresponding mesoscale results. The use of this quasi-strain gauge approach in this section has shown that the bond stress obtained from the strain measurement in physical test (i.e. similar to Method (b) as discussed in Section 9.3.1) should be treated with care, due to the limitation of strain gauges in their size.

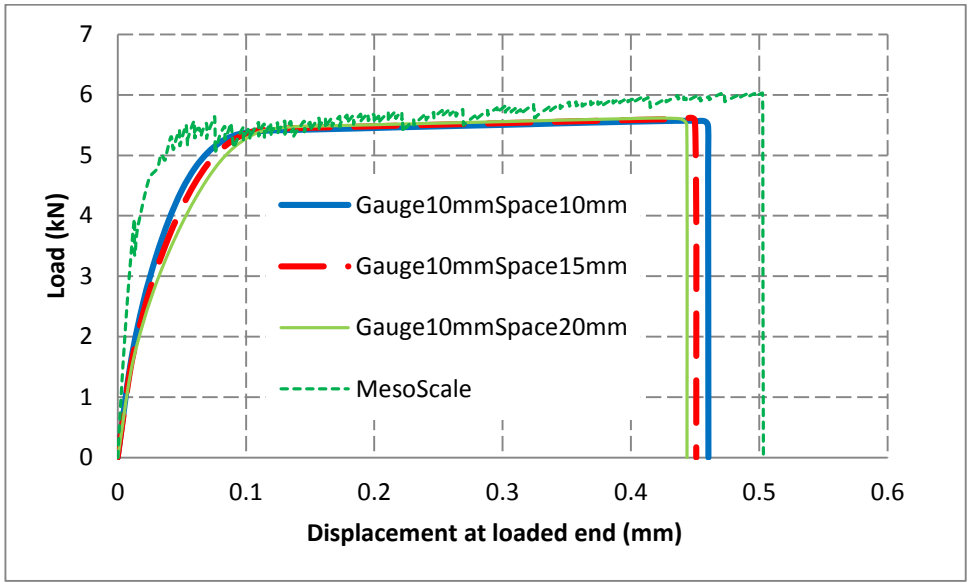

Figure 9.13 Load-displacement curves of Specimen III-1 in Yao et al. (2005) with the bond-slip relationships obtained by assuming strain gauge length of 10 mm with spacing ranging from 10 to 20 mm

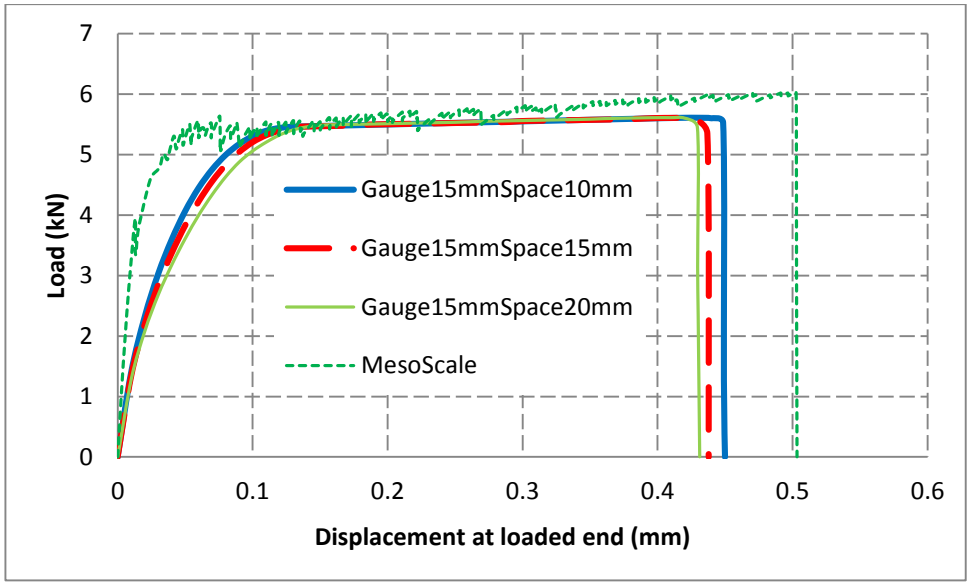

Figure 9.14 Load-displacement curves of Specimen III-1 in Yao et al. (2005) with the bond-slip relationships obtained by assuming strain gauge length of 15 mm with spacing ranging from 10 to 20 mm

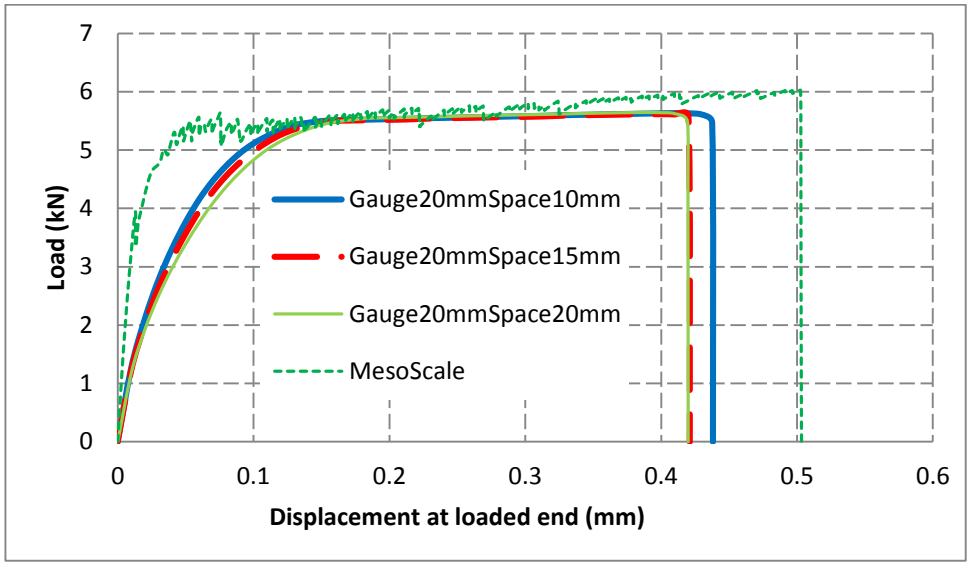

Figure 9.15 Load-displacement curves of Specimen III-1 in Yao et al. (2005) with the bond-slip relationships obtained by assuming strain gauge length as 20 mm with spacing ranging from 10 to 20 mm

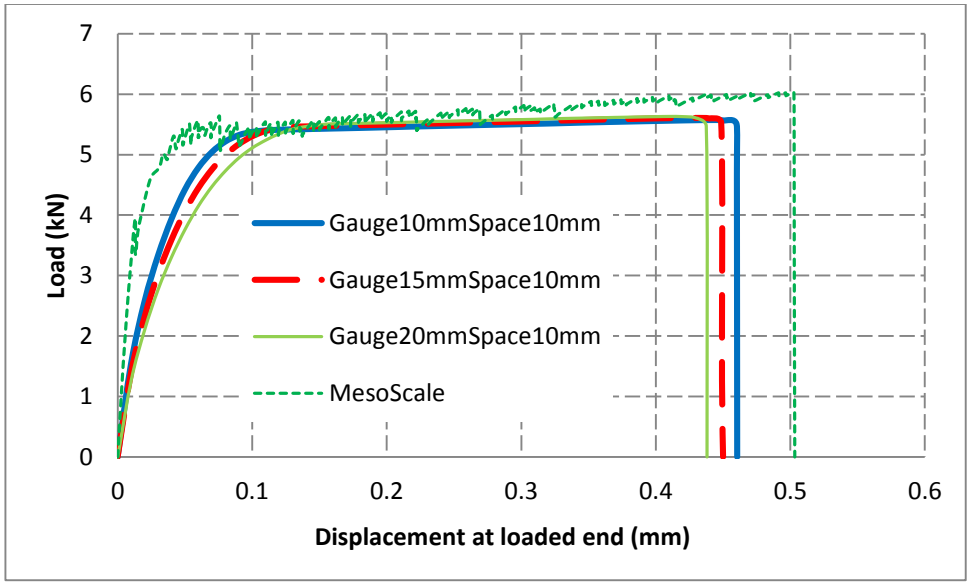

Figure 9.16 Load-displacement curves of Specimen III-1 in Yao et al. (2005) with the bond-slip relationships obtained by assuming spacing as 10 mm with the length of strain gauge ranging from 10 to 20 mm

9.4.3 Effects of concrete elastic deformation on slip

As indicated in its definition, slip is a relative displacement of the two sides of the crack at FRP-concrete bonded interface. Lu et al. (2005) defined an effective thickness of concrete t_c and take the relative displacement at top and bottom of that. They recommended t_c= 5 mm.

Different values of this effective thickness of the concrete t_c, ranging from 1 to 150 mm, are considered to investigate its effect on the stiffness of the bond-slip model, which may affect the global load versus displacement curve in simulation results.

Based on these values of t_c, different bond-slip curves are obtained through Eq. (9.27) with an averaging length of 1 mm, as shown in Figure 9.17. In general, the initial stiffness in bond-slip models decreases with the increase of the effective thickness of concrete t_c, as shown in Figure 9.17. When t_c is greater than 20 mm, there is a deformation (slip) without any stress (Figure 9.17), because the absolute displacement caused by the elastic deformation of in concrete prism is included in the slip. Any such deformation should therefore be removed. It is therefore important to use a value t_c just large enough to account for the plastic deformation within the thin layer of concrete under the FRP. Any elastic deformation can be accounted for in the normal FE model, whether the mesh is coarse or fine.

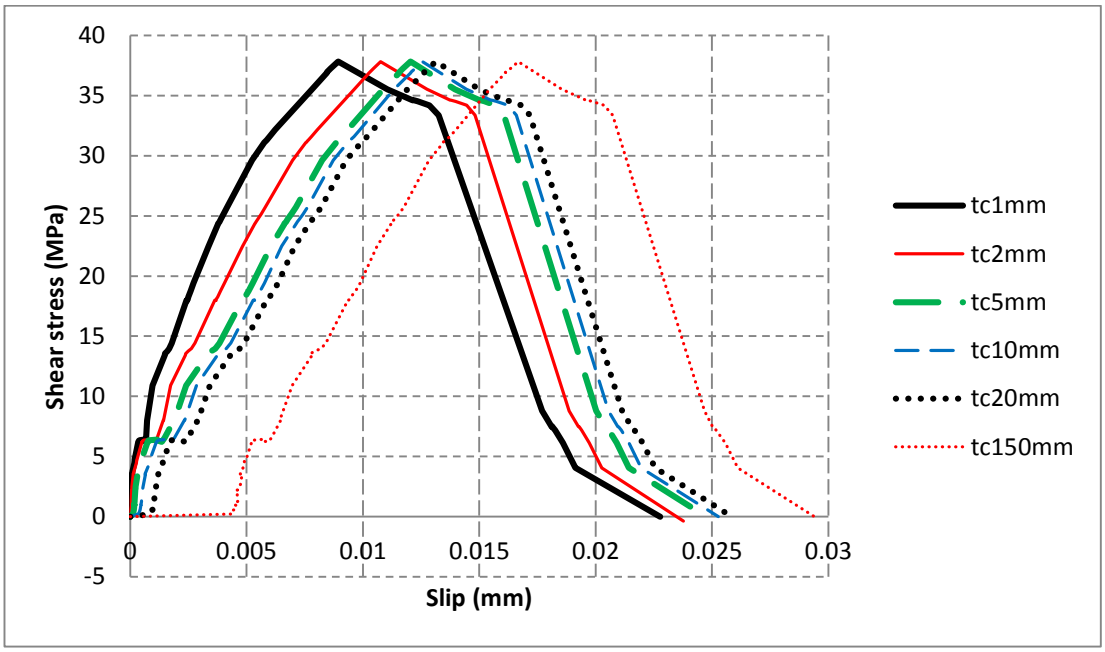

Figure 9.17 Bond stress-slip curves with different effective thicknesses of concrete t_c

The load versus displacement curves with these different values for t_c are compared in Figure 9.18. It is found that the shapes of these curves are generally similar to each other, except for some slight differences around the origin. For instance, the initial loading stiffness in the case with t_c = 150 mm is evidently lower than that in others. The damage contour in concrete shows that the plastic deformation occurs within a thin layer of about 5 mm (see Figure 9.19).

Based on the above discussions, it is reasonable to set the effective thickness of concrete t_c to 5 mm in subsequent simulations.

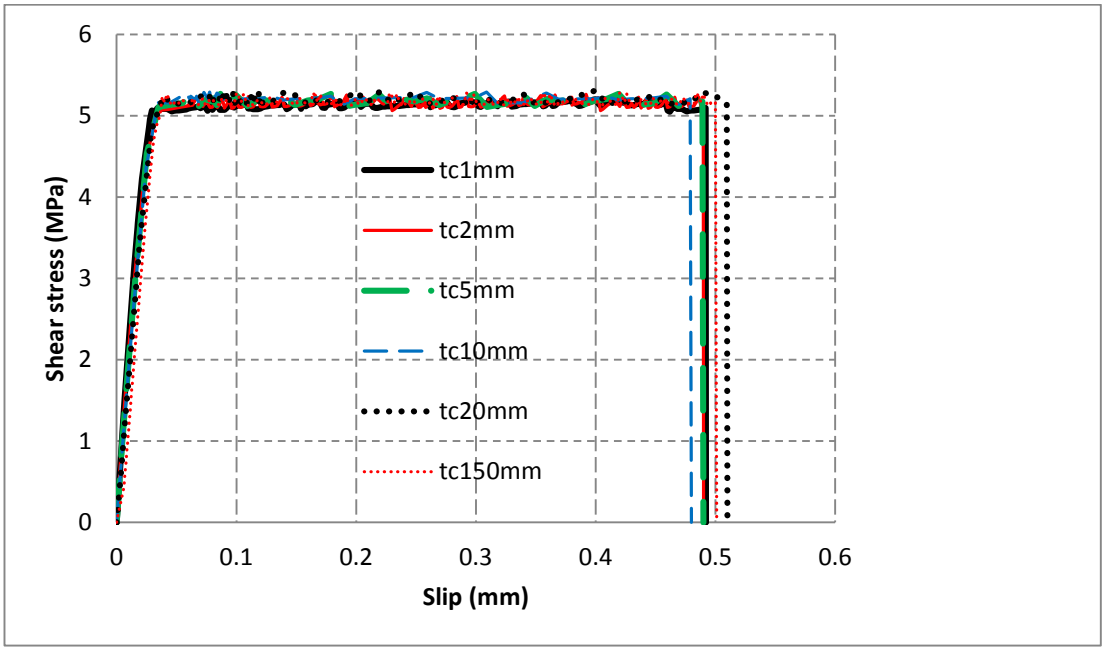

Figure 9.18 Load-displacement curves predicted by spring model with different values of effective thickness of concrete t_c

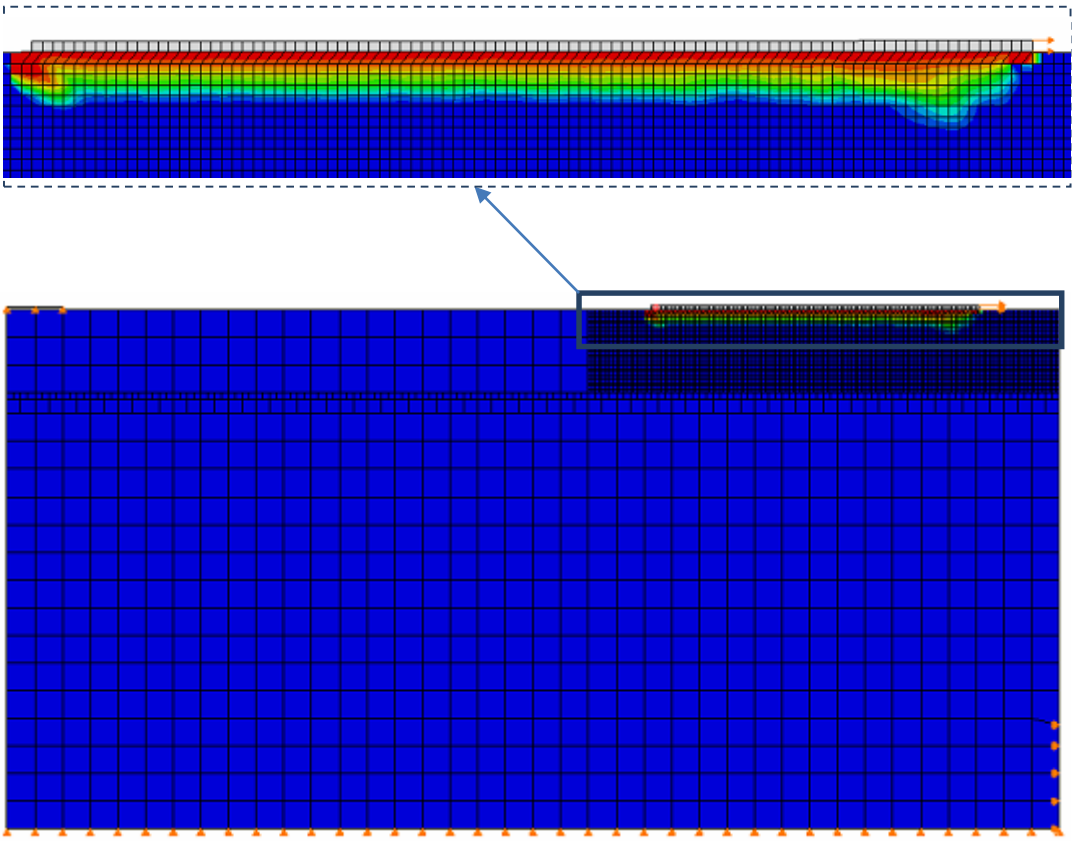

Figure 9.19 Simulated crack band for Specimen III-1 in Yao et al. (2005) with mesoscale model

In summary, the method used in physical tests to obtain bond stress results in a lower stiffness in the bond-slip model. For example, Mazzotti et al. (2009) derived a bond-slip model based on the FRP strain measurements in the physical test, as shown in Figure 9.20. They applied the bond-slip model to simulate the specimens as shown in Figure 9.21. Obviously, the stiffness in the simulation result is lower than that in the corresponding test. Therefore, there are limits for the bond-slip model directly derived from experimental strain measurement and they need to be treated with care.

The method employed by Lu et al. (2005a) is more acceptable, but it has limitations, mainly because a radical smooth tool (i.e. the Fast Fourier Transform) is used to inappropriately filter the oscillations as shown in Figure 9.2, a measure that may change the shape of the bond-slip model .

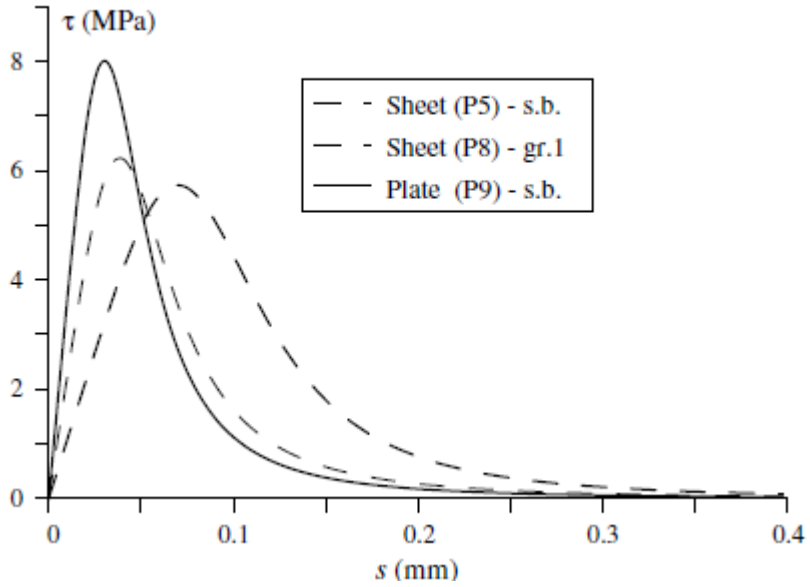

Figure 9.20 Bond-slip models from Mazzotti et al.'s (2009) tests with the same concrete properties but different FRP stiffness

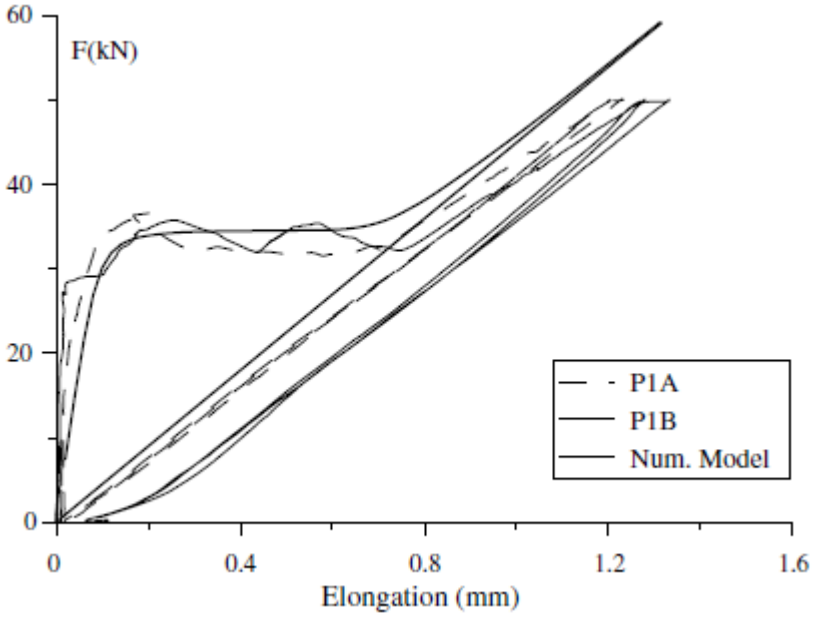

Figure 9.21 Axial force vs. plate elongation: numerical and experimental results from test on Specimens P1A and P1B. (extracted from Mazzotti et al. (2009))

9.5 FE parametric study

FRP-concrete bonded interface is composed of FRP and concrete, so that the ultimate load in mesoscale models may be influenced by the stiffness of FRP, FRP-concrete width ratio and concrete strength. Specimen III-1 in Yao et al. (2005) is taken as the reference case to conduct an FE parametric study to investigate these effects in mesoscale models.

9.5.1 Effect of the stiffness of FRP

In this section, Specimen III-1 in Yao et al. (2005) is taken as the reference case with elastic modulus of 256 GPa, and thickness of 0.165 mm. In the simulations, the geometrical and material properties are the same as those in Chapter 3. The ratio of FRP stiffness (i.e. the product of FRP elastic modulus E and its thickness t_f) to that in reference case k/k_0 is changed from 0.5 to 2.1 at an interval of 0.1 to investigate the effect of FRP stiffness on the maximum bond stress τ_{max}, slip s_0 at maximum bond stress τ_{max} and interfacial fracture energy G_F. The results about the effect of FRP stiffness k on these parameters are summarised in Figure 9.22-Figure 9.24 through the bond stress-slip curves extracted from the mesoscale model results.

In general, it is found that the interfacial fracture energy G_F decreases with increase of the value k/k_0 when the value of k/k_0 remains within the range of 0.4 to 1.7, but remains as constant beyond 1.7 (see Figure 9.22). Such a relationship may be expressed as

$$G_F(E/E_t) = \begin{cases} 0.558\,(k/k_0)^{-0.186} & \text{if } k/k_0 < 1.7 \\ 0.53 & \text{if } k/k_0 > 1.7 \end{cases} \tag{9.31}$$

In Figure 9.23, it is also found that maximum bond stress τ_{max} relates to the ratio of FRP stiffness to that in the reference case k/k_0 through

$$\tau_{max}(k/k_0) = 5.22\,(k/k_0) + 28.5 \tag{9.32}$$

Similarly, in Figure 9.24, it is found that the relationship between the slip s_0 at maximum bond stress τ_{max} and the ratio of FRP stiffness to that in reference case k/k_0 is given as

$$s_0(k/k_0) = 0.0007\ (k/k_0) + 0.0121 \tag{9.33}$$

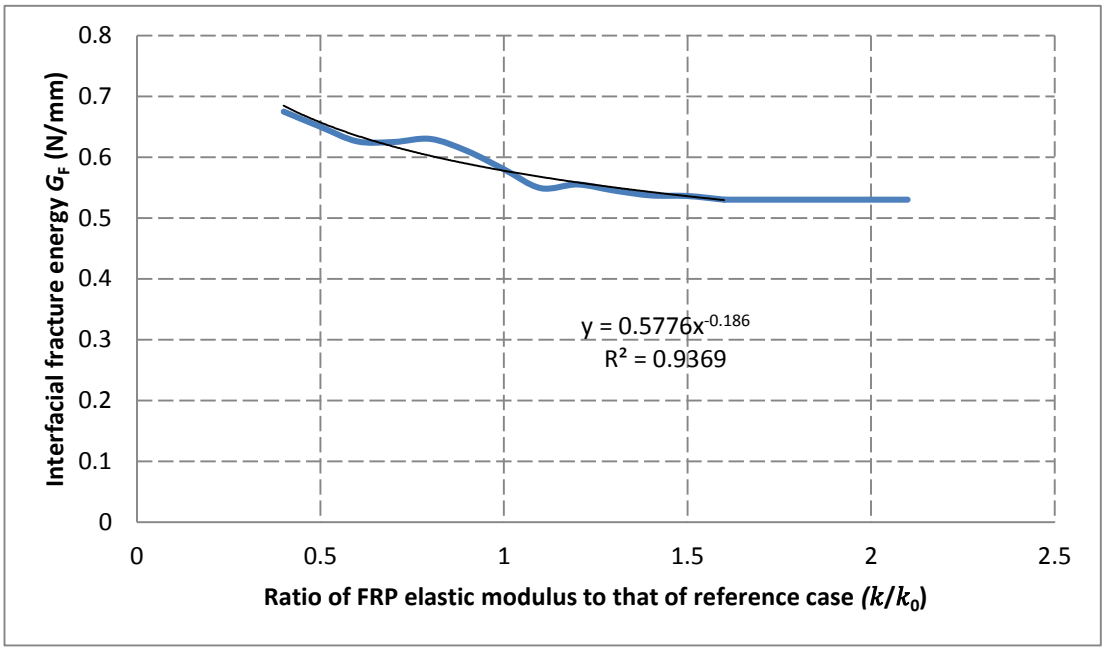

Figure 9.22 Relationship between interfacial fracture energy G_F and normalised FRP stiffness k/k_0

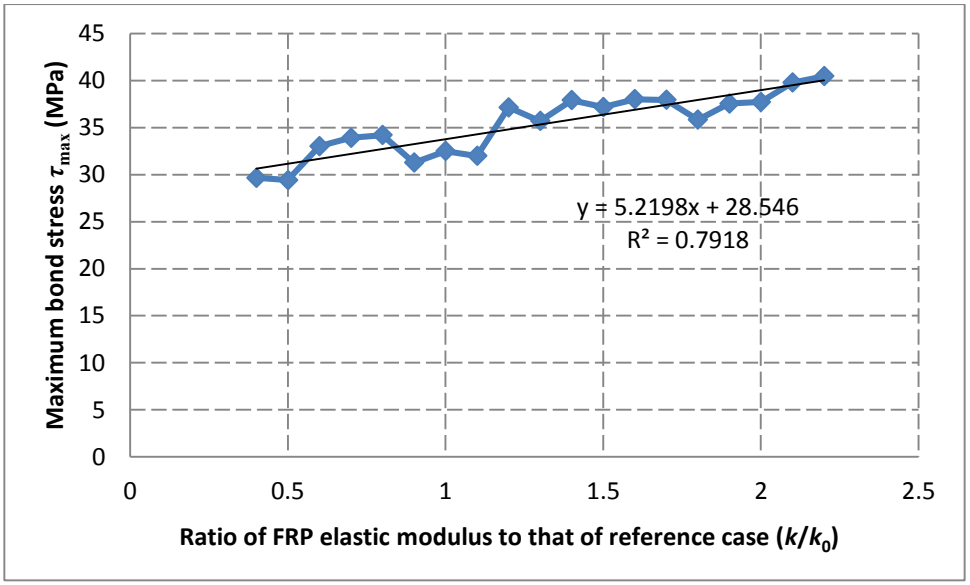

Figure 9.23 The relationship between maximum bond stress τ_{max} and normalised FRP stiffness k/k_0

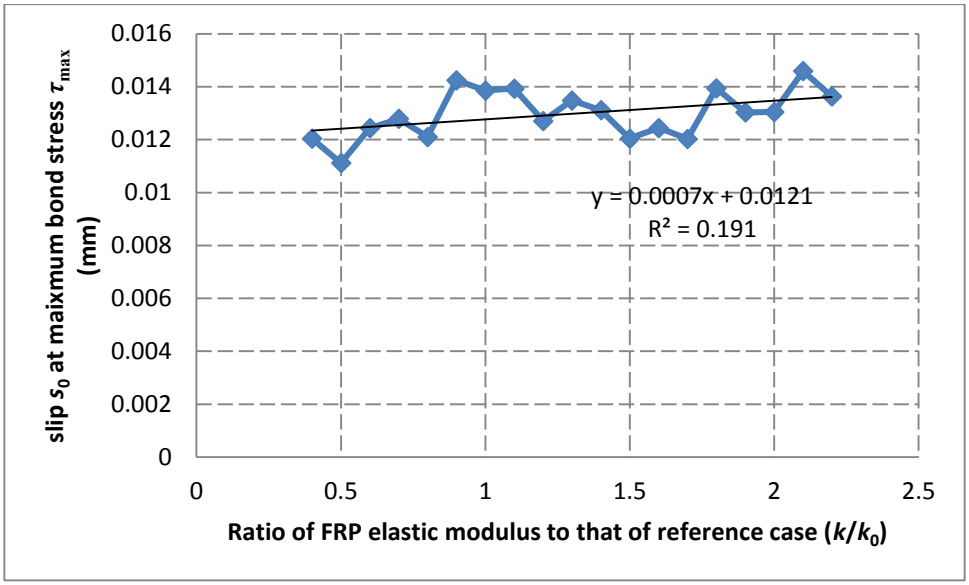

Figure 9.24 Relationship between slip s_0 at the maximum bond stress τ_{max} and the normalised FRP stiffness k/k_0

It seems incredible that the interfacial fracture energy increases with decrease of FRP stiffness, as shown in Figure 9.22, a phenomenon that is not only observed in mesoscale results, but also in physical tests. Specimens P5A and P9B in Mazzotti et al. (2009) are taken as examples to explain this incredible phenomenon. Specifically, Specimen P5A is fabricated with an FRP sheet with the elastic modulus of 230 GPa and the thickness of 0.13 mm while Specimen P9B is fabricated with an FRP plate with the elastic modulus of 165 GPa and the thickness of 1.2 mm. The damage contours of these two specimens are shown in Figure 8.17-Figure 8.18. It is found that the crack in the simulation of Specimen P9B is much deeper than that in Specimen P5A. Accordingly, the interfacial fracture energy obtained in physical test of P9B is a little bit lower than that in P5A as shown in Figure 9.20 (the interfacial fracture energy is still worth trusting although the shape of bond-slip model derived from testing is not, due to the averaging effect of bond stress). That is because the debonding ultimate load is achieved by a row of columns below the FRP-concrete bonded interface. The lengths

of such columns are increased with the FRP stiffness, as illustrated in Figure 8.17-Figure 8.18. Under the same displacement at the top of these columns (i.e. the displacement of FRP strips), the longer column is more prone to be damaged, which results in lower interfacial fracture energy as shown in Figure 9.22.

Moreover, a similar but not the exactly same conclusion is also found in Dai and Ueda's (2003) and Dai et al.'s (2005) models, in which the enhance of the interfacial fracture energy is related to the adhesive property G_a/t_a when FRP and adhesive are separately considered, as shown in Figure 9.25. In general, for the FRPs with the same stiffness bonded to concrete prism, in the case with very thick adhesive layer, the shear behaviour mainly happens in the body of adhesive. FRP is almost debonded at the adhesive-concrete interface or with a very thin layer of concrete, whose failure mode is similar to that in Specimen P5A in Mazzotti et al. (2009) and in which a higher value in interfacial fracture energy is obtained through checking the relative chart in Figure 9.25. On the other hand, in the case with thinner adhesive layer, the shear behaviour mainly happens in the body of concrete. FRP is debonded with a relatively thicker layer of concrete, whose failure mode is similar to that in Specimen P9B in Mazzotti et al. (2009) and in which a lower value in interfacial fracture energy is obtained through checking the relative chart in Figure 9.25.

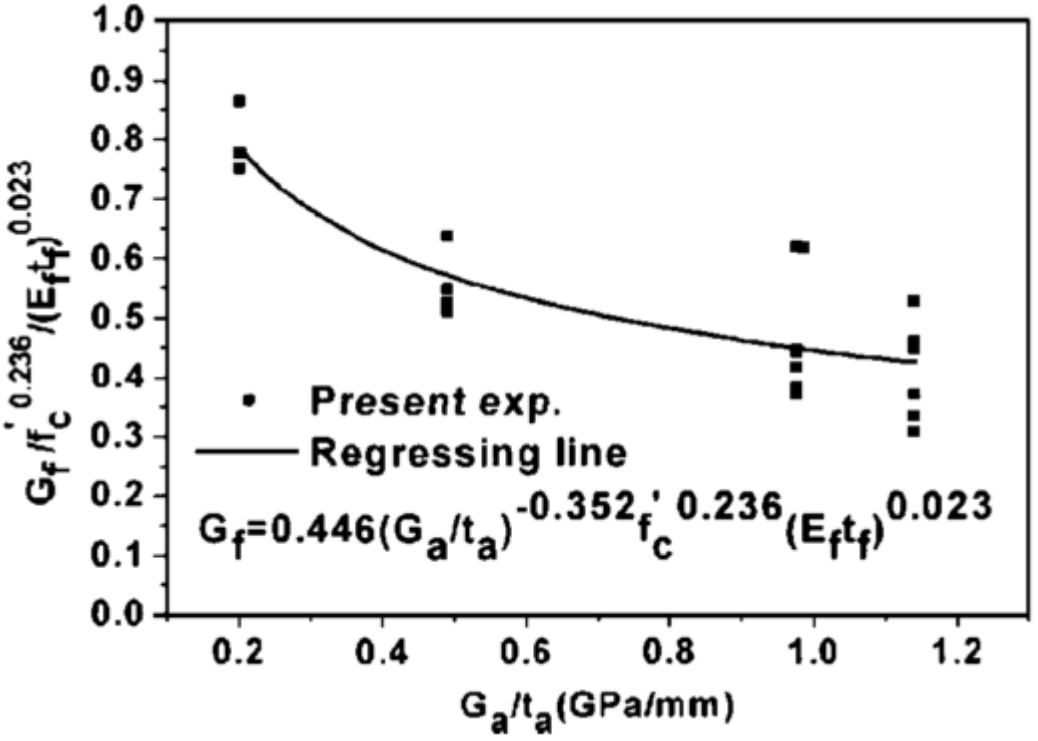

Figure 9.25 Effect of adhesive on the interfacial fracture energy (extracted from Dai et al.'s (2005))

Through the aforementioned analysis, in essence, these two conclusions are in agreement with each other.

9.5.2 Effect of FRP-concrete width ratio

In this section, Specimens III-1, III-2, III-3 and III-4 in Yao et al. (2005) are taken as the reference cases so as to investigate the effect of FRP-concrete width ratio on maximum bond stress τ_{max}, slip s_0 at maximum bond stress τ_{max} and interfacial fracture energy G_F. In these simulations, the geometrical modelling and the material properties assignments are conducted as in Chapter 3. The results about the effect of FRP-concrete width ratio b_f/b_c on these parameters are summarised in Figure 9.26-Figure 9.28 through the bond stress-slip curves extracted from the results of these mesoscale models.

As shown in Figure 9.26, the relationship between FRP-concrete width ratio b_f/b_c and interfacial facture energy G_F is given as

$$G_F(b_f/b_c) = -0.232 \ln(b_f/b_c) + 0.189 \quad (9.34)$$

where, b_f is the width of FRP strips and b_c is the width of concrete.

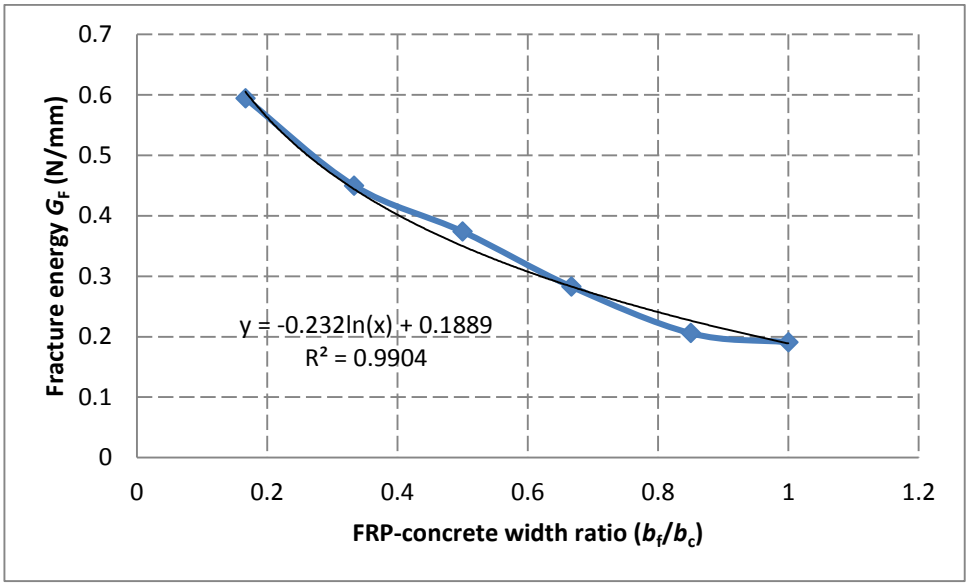

Figure 9.26 The relationship between FRP-concrete width ratio b_f/b_c and interfacial fracture energy G_F

As shown in Figure 9.27, the relationship between FRP-concrete width ratio b_f/b_c and maximum bond stress τ_{max} is given as

$$\tau_{max}(b_f/b_c) = 42.2\,(b_f/b_c)^2 - 82.4\,(b_f/b_c) + 48.5 \quad (9.35)$$

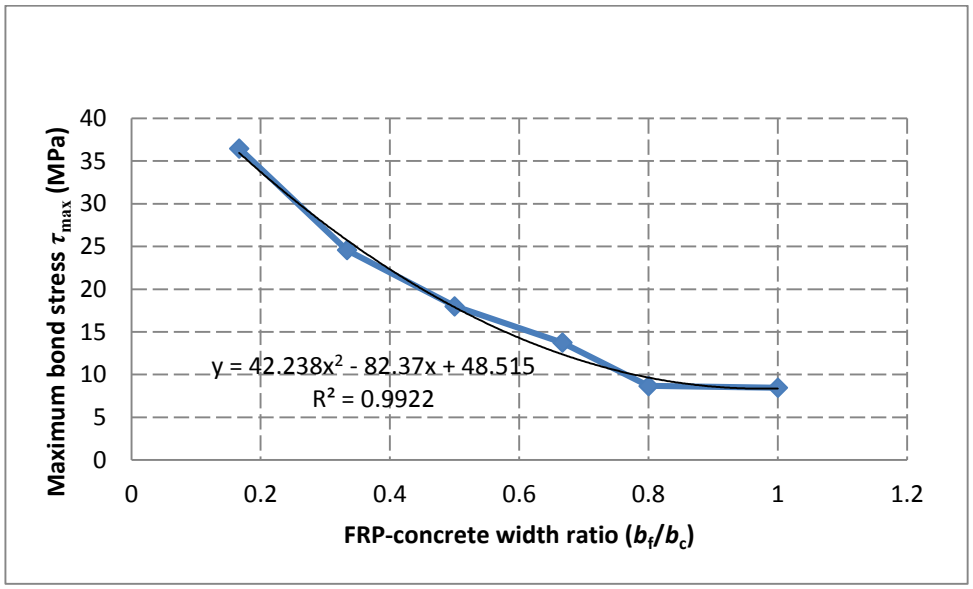

Figure 9.27 The relationship between FRP-concrete width ratio b_f/b_c and maximum bond stress τ_{max}

As shown in Figure 9.28, the relationship between FRP-concrete width ratio b_f/b_c and slip s_0 at maximum bond stress τ_{max} is given as

$$s_0(b_f/b_c) = -0.0256\,(b_f/b_c)^2 + 0.0409\,(b_f/b_c) + 0.0077 \qquad (9.36)$$

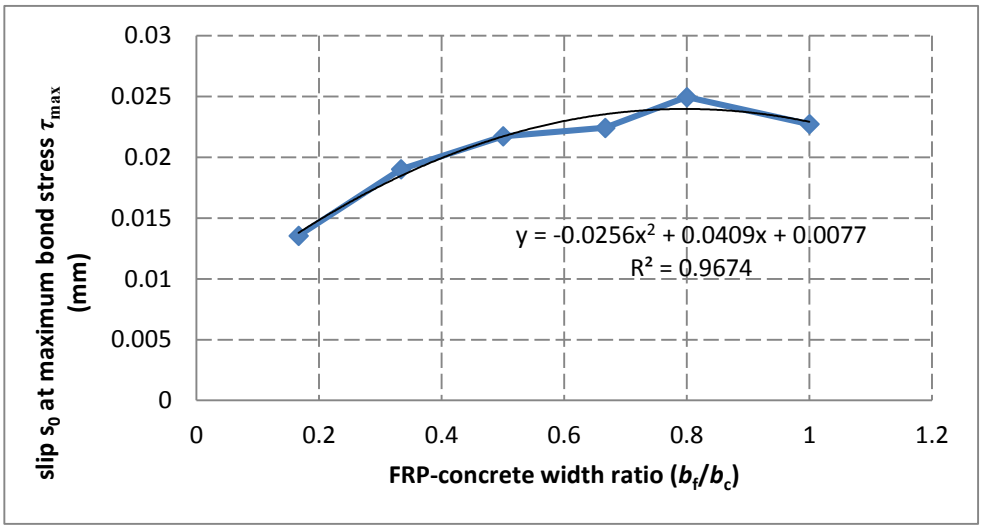

Figure 9.28 The relationship between FRP-concrete width ratio b_f/b_c and slip s_0 at maximum bond stress τ_{max}

9.5.3 Effect of concrete strength

In this section, with reference to Specimen III-1 in Yao et al. (2005), a series of simulations are conducted to investigate the effect of concrete strength f_c' on the maximum bond stress τ_{max}, slip s_0 at maximum bond stress τ_{max} and interfacial fracture energy G_F. In the simulations, the geometrical and material properties are the same as those in Chapter 3. The only variation is that concrete strength f_c' varies from 15 MPa to 60 MPa at an interval of 5 MPa. The results about the effect of concrete strength f_c' on these parameters are summarised in Figure 9.29-Figure 9.31 through the bond stress-slip curves extracted from the results of these mesoscale models.

As shown in Figure 9.29, the relationship between concrete strength f_c' and interfacial facture energy G_F is given as

$$G_F(f_c') = 0.0231\ (f_c') + 0.0044 \tag{9.37}$$

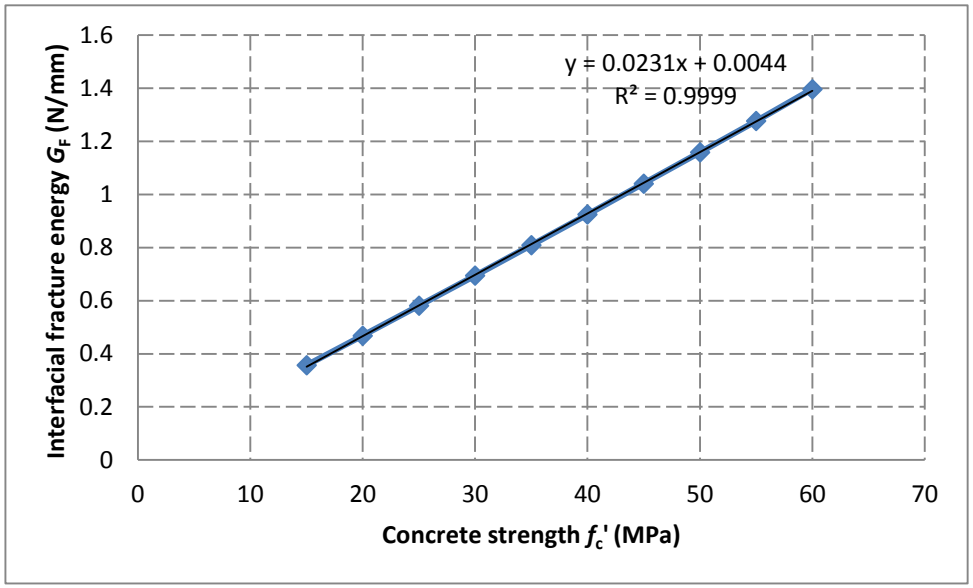

Figure 9.29 The relationship between concrete strength f_c' and interfacial fracture energy G_F

As shown in Figure 9.30, the relationship between concrete strength f_c' and maximum bond stress τ_{max} is given as

$$\tau_{\max}(f_c') = 1.0686\,(f_c') + 7.4867 \tag{9.38}$$

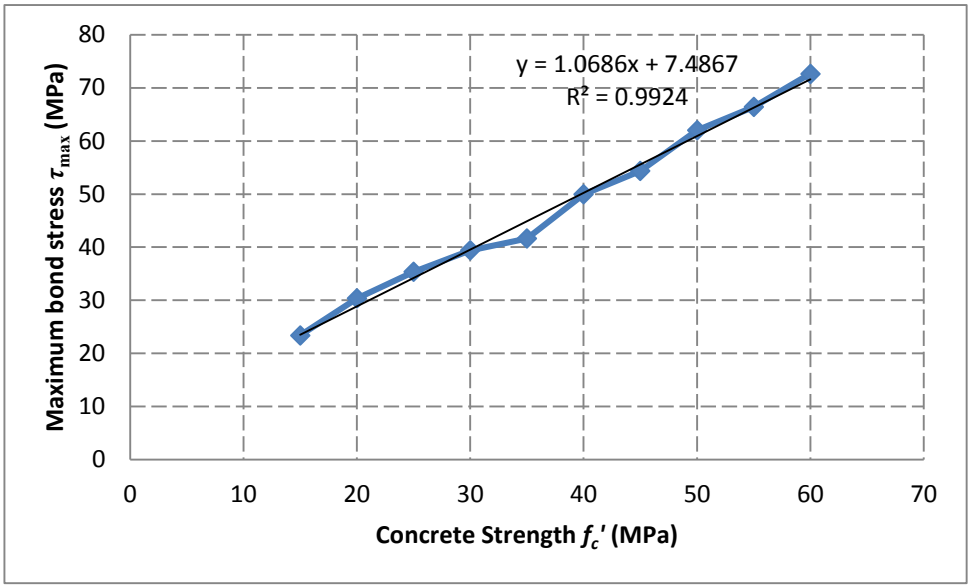

Figure 9.30 The relationship between concrete strength f_c' and maximum bond stress τ_{max}

As shown in Figure 9.31, FRP-concrete width ratio b_f/b_c is related to the slip s_0 at maximum bond stress τ_{max} through

$$s_0(f_c') = 1 \times 10^{-7}\,(f_c')^3 - 1 \times 10^{-5}\,(f_c')^2 + 0.0003\,(f_c') + 0.0109 \tag{9.39}$$

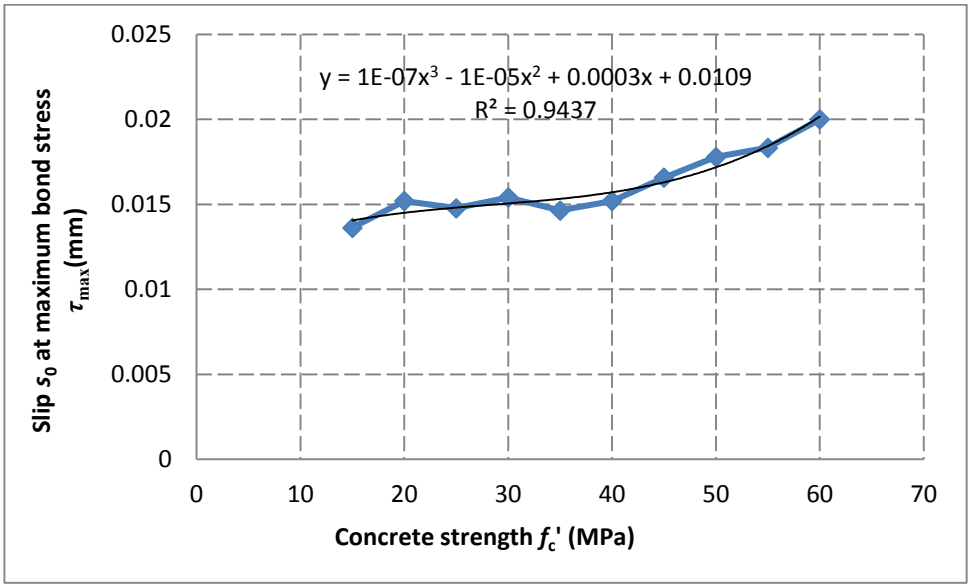

Figure 9.31 The relationship between concrete strength f_c' and slip s_0 at maximum bond stress τ_{max}

9.6 A new bond-slip relationship

In the previous studies, it has been found that the ultimate load of the model is determined by the interfacial fracture energy at FRP-concrete bonded interface and the softening behaviour in the global load-displacement curve is determined by the counterpart in the bond-slip model, which in turn is controlled by the maximum bond stress and slip at the maximum bond stress of the model. Based on the above deliberations, a new bond-slip model is proposed for FRP-concrete bonded interface based on the results from the parametric study presented in Section 9.5.

In general, the shape of the bond-slip model is comprised of an ascending branch and a descending branch. In the ascending branch, the ascending branch in Lu et al. (2005a) is used; while in the descending branch a straight line is used. Specifically, the proposed model is given as

$$\tau = \begin{cases} \tau_{\max}\sqrt{\dfrac{s}{s_0}} & \text{if} \quad s \le s_0 \\ \tau_{\max} - h(s - s_0) & \text{if} \quad s > s_0 \end{cases} \tag{9.40}$$

where h is the stiffness to control the descending branch in the model and is represented as

$$h = \frac{\tau_{\max}^2}{2\left(G_{\mathrm{f}} - \int_0^{s_0} \tau \, \mathrm{d}s\right)} \tag{9.41}$$

The maximum bond stress $\tau_{\max}$ is given as

$$\tau_{\max} = \frac{\tau(f_{\mathrm{c}}')\tau(\frac{b_{\mathrm{f}}}{b_{\mathrm{c}}})\,\tau(k/k_0)}{\tau(\frac{25}{150})\,\tau(k_0/k_0)} \tag{9.42}$$

where, $\tau(f_{\mathrm{c}}')$, $\tau(\frac{b_{\mathrm{f}}}{b_{\mathrm{c}}})$ and $\tau(k/k_0)$ are the functions representing maximum bond stress $\tau_{\max}$ at FRP-concrete bonded interface with regard to concrete strength f_{c}', FRP-concrete width ratio $b_{\mathrm{f}}/b_{\mathrm{c}}$ and ratio of FRP stiffness to that in the reference case k/k_0, respectively, whose details are found in Section 9.5.

The slip s_0 at the maximum bond stress $\tau_{\max}$ is given as

$$s_0 = \frac{s_0(f_{\mathrm{c}}')s_0(\frac{b_{\mathrm{f}}}{b_{\mathrm{c}}})\,s_0(k/k_0)}{s_0(\frac{25}{150})\,s_0(k_0/k_0)} \tag{9.43}$$

where, $s_0(f_{\mathrm{c}}')$, $s_0(\frac{b_{\mathrm{f}}}{b_{\mathrm{c}}})$ and $s_0(k/k_0)$ are the functions representing slip s_0 at the maximum bond stress $\tau_{\max}$ of FRP-concrete bonded interface with regard to concrete strength f_{c}', FRP-concrete width ratio $b_{\mathrm{f}}/b_{\mathrm{c}}$ and ratio of FRP stiffness to that in the reference case k/k_0, respectively, whose details are also found in Section 9.5.

The fracture energy G_{f} is given by

$$G_{\mathrm{f}} = \frac{G_{\mathrm{f}}(f_c')G_{\mathrm{f}}(\frac{b_{\mathrm{f}}}{b_{\mathrm{c}}})\ G_{\mathrm{f}}(k/k_0)}{G_{\mathrm{f}}(\frac{25}{150})\ G_{\mathrm{f}}(k_0/k_0)} \tag{9.44}$$

where, $G_{\mathrm{f}}(f_c)$, $G_{\mathrm{f}}\left(\frac{b_f}{b_c}\right)$ and $G_{\mathrm{f}}(k/k_0)$ are the functions representing interfacial fracture energy G_{f} of FRP-concrete bonded interface with regard to concrete strength f_{c}', FRP-concrete width ratio $b_{\mathrm{f}}/b_{\mathrm{c}}$ and ratio of FRP stiffness to that in the reference case k/k_0, respectively, whose details are found in Section 9.5.

9.7 Application in simulations

In this section, an alternative approach to mesoscale method is employed to simulate the debonding behaviour at FRP-concrete bonded interface using this new bond-slip model proposed in section 9.6 and the already review models in Section 9.2, thereby testing the performance of this proposed model in simulations of FRP-concrete bonded interface.

9.7.1 Methodology

In this simulation, the boundary conditions and loading approaches are as discussed in Chapter 3. In the assignments of material properties for FRP and concrete, only elastic moduli and poison's ratios are used as in Chapter 3. Compared to the geometrical modelling in the mesoscale modelling, the only variation in this approach is that FRP part is not connected to concrete part by sharing the same nodes at the interface, but connected by a series of spring elements in both 1st and 2nd directions, respectively, as shown in Figure 9.32. The spring elements in the 2nd direction are defined as elastic one with the elastic modulus of concrete. On the other hand, the spring elements in the 1st direction are defined through a force-displacement relationship, which is derived from the bond-slip model.

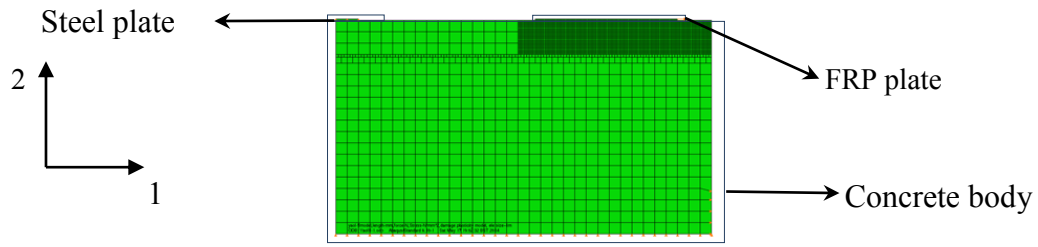

Figure 9.32 Geometrical modelling for simulations

Some special cautions are needed in the use of the spring element, especially for that in the 1st direction. Specifically, the node from FRP part should be taken as 1st node of the spring element while the node from concrete part as 2nd node. Otherwise, the springs are under compression forces although the bond-slip model is defined for tension, which means that the springs at the interface become ineffective.

9.7.2 Results and discussions

Once again, the tests employed in Chapter 8 are simulated using the already reviewed bond-slip models in Section 9.2 and the proposed model in Section 9.6 respectively to compare performances of these models in simulations. Similarly, Specimen III-1, III-2, III-3 and III-4 in Yao et al. (2005) are simulated to test the performance of these models in terms of FRP-concrete width ratio. Specimens III-7 and III-8 in Yao et al. (2005) are simulated to test the performance of these models in terms of FRP stiffness. In addition, specimens from Ali-ahmad et al. (2006) and Specimens P5A and P9B from Mazzotti et al. (2009) are simulated to further test the performance of these models in terms of concrete strength. The relevant results are shown in Table 9.1-Table 9.2.

In Table 9.2, it was found that the best performance was observed in the result from the proposed model in comparison to those with the reviewed bond-slip models in this chapter, with an error of 4.6%. Besides, it is followed by the performance of Lu et al.'s (2005a) model with an error of 8.0%, Dai et al.'s (2003) model with an error of 8.7% and Dai et al.'s (2005) model with an error of 9.1%. Besides, it is found that the above relatively good models are all obtained through Methods (a) and (c) and there is no

one obtained through FRP axial strain variation in physical tests. Thus, it has ratified again that the method to obtain bond stress through axial strain of FRP in physical tests is not reliable.

Table 9.1 Comparison of ultimate loads from test results to that from simulation results with different bond-slip models

	Test (kN)	proposed model (kN)	Lu et al.'s (2005) model (kN)	Nakaba et al.'s (2001) model (kN)	Dai et al.'s (2003) model (kN)	Dai et al.'s (2005) model (kN)	Monti et al.'s (2003) model (kN)	Savioa et al.'s (2003) model (kN)
III-1	5.94	6.01	5.66	7.34	5.21	5.76	8.57	6.82
III-2	11.66	10.47	10.12	14.71	10.45	11.39	14.95	13.67
III-3	14.63	13.79	13.59	22.09	15.76	17.04	19.74	20.53
III-4	19.07	19.67	16.24	29.50	21.12	22.81	23.27	27.42
III-7	4.78	4.95	4.61	6.24	4.49	4.85	7.00	5.80
III-8	8.02	7.94	7.79	12.51	8.81	9.52	11.83	7.91
No.5	11.5	10.83	10.04	13.89	9.71	10.91	15.46	12.90
P5A	16.5	17.35	14.82	22.76	17.45	17.09	23.62	21.22
P9B	39.50	41.63	38.286	54.36	40.30	44.11	59.32	52.45

Table 9.2 Error between test and simulation results for different bond-slip models

	Proposed model (%)	Lu et al.'s (2005) model (%)	Nakaba et al.'s (2001) model (%)	Dai et al.'s (2003) model (%)	Dai et al.'s (2005) model (%)	Monti et al.'s (2003) model (%)	Savioa et al.'s (2003) model (%)
III-1	1.2	4.7	23.6	12.3	3.0	44.3	14.8

III-2	10.2	13.2	26.2	10.4	2.3	28.2	17.2
III-3	5.7	7.1	51.0	7.7	16.5	34.9	40.3
III-4	3.1	14.8	54.7	10.7	19.6	22.0	43.8
III-7	3.6	3.6	30.5	5.0	1.5	46.4	21.3
III-8	1.0	2.9	56.0	8.6	18.7	47.5	1.4
No. 5	5.8	12.7	20.8	15.6	5.1	34.4	12.2
P5A	5.2	10.2	37.9	5.8	3.6	43.2	28.6
P9B	5.4	3.1	37.6	2.0	11.7	50.2	32.8
Average	4.6	8.0	37.6	8.7	9.1	39.0	23.6

Note: Specimens III-1 to III-6 are from Yao et al. (2005); Specimen No. 5 is from Ali-ahmad et al. (2006); Specimens P5A and P9B are from Mazzotti et al. (2009).

In addition, to further check the mechanical differences arising from these bond-slip models, global load versus displacement curves from the simulations with these models are compared to that from the test result or the mesoscale models, as shown in Figure 9.33-Figure 9.41.

Simulations of the specimens from Mazzotti et al. (2009)

The load versus displacement curves from the test of Specimens P5A (i.e. fabricated with FRP sheet) from Mazzotti et al. (2009) are compared to that from the simulations with the already reviewed and proposed bond-slip models, as shown in Figure 9.33. It is found that the ultimate load from the simulations with Proposed, Lu et al.'s (2005a), Dai and Ueda's (2003) models and Dai et al.'s (2005) model is very close to that in test, as shown in Table 9.2, although the loading stiffness of the specimen in test is not available to compare, due to the failure of obtaining an accurate and reasonable displacement in the physical tests.

In the simulation of Specimen P9B (i.e. fabricated with FRP plate), a transient zone between the perfect bonded and unbonded zones is considered with a length of 20 mm,

as discussed in Chapter 8. Eventually, similar comparison is also conducted for Specimen P9B, as shown in Figure 9.34. It is found that the load-displacement curves from the simulations with proposed, Dai and Ueda's (2003) and Dai et al.'s (2005) models are in acceptable agreement with that from the corresponding test in both loading stiffness and ultimate load. Furthermore, a good prediction is also found in the simulation with Lu et al.'s (2005a) model, in spite of severe deviation in terms of loading stiffness from its counterpart in physical test.

In addition, it is also found that Lu et al.'s (2005a) model only performs well in simulation of Specimen P9B (see Figure 9.34); by contrast, proposed, Dai and Ueda's (2003) and Dai et al.'s (2005) models perform very well in simulations of these two specimens. That is because that Lu et al.'s (2005) model did not consider the influence of FRP stiffness on the interfacial fracture energy as discussed in Section 9.5.1, while the proposed, Dai and Ueda's (2003) and Dai et al.'s (2005) models did.

Simulations of the specimens from Ali-ahmad et al. (2006)

Similarly, in the simulation of the Specimen No. 5 from Ali-ahmad et al. (2006), a transient zone between the perfect bonded and unbonded zones is also considered with a length of 7.74 mm, as discussed in Chapter 8. Once again, the load versus displacement curve from the test of Specimen No. 5 in Ali-ahmad et al. (2006) is compared to that from the simulations with these bond-slip models, as shown in Figure 9.35. It is found that the result in simulation with the proposed model is in the best agreement with that from the testing data, not only in terms of loading stiffness, but also in terms of ultimate load. Moreover, a relatively good performance is also observed in the simulation results with Dai and Ueda's (2003) and Dai et al.'s (2005) models, albeit not as good as that with the proposed model. In addition, a good prediction on the ultimate load is also found in the simulation with Lu et al.'s (2005) model, despite of its poor performance in predicting loading stiffness.

Simulations of the specimens from Yao et al. (2005)

Furthermore, the load versus displacement curves from the simulations with these bond-slip models are compared to their corresponding mesoscale models of Series III from Yao et al. (2005), as shown in Figure 9.36-Figure 9.41. That is because the load-displacement curve from test is not available from the test data, but the reliability of the mesoscale model has been proved by a large scale of tests in Chapter 8. Therefore, it is also acceptable to use the load-displacement curve from the mesoscale model to justify the reasonablity of the bond-slip models.

In general, the load-displacement curves from the simulations with the proposed bond-slip model are in good agreement with that from the mesoscale models, except that from Specimen III-4 from Yao et al. (2005). As for the reason why it failed to agree with that in mesoscale model, that is because in the process of failure of Specimen III-4 a large volume of concrete is torn off with FRP (see Figure 8.8 (d)), a phenomenon that is totally different from that assumped by the bond-slip models. Usually, the bond-slip model is derived under such a hypothesis that FRP is debonded with a thin layer of concrete (i.e. the thickness of the attached concrete layer is between 1-5 mm).

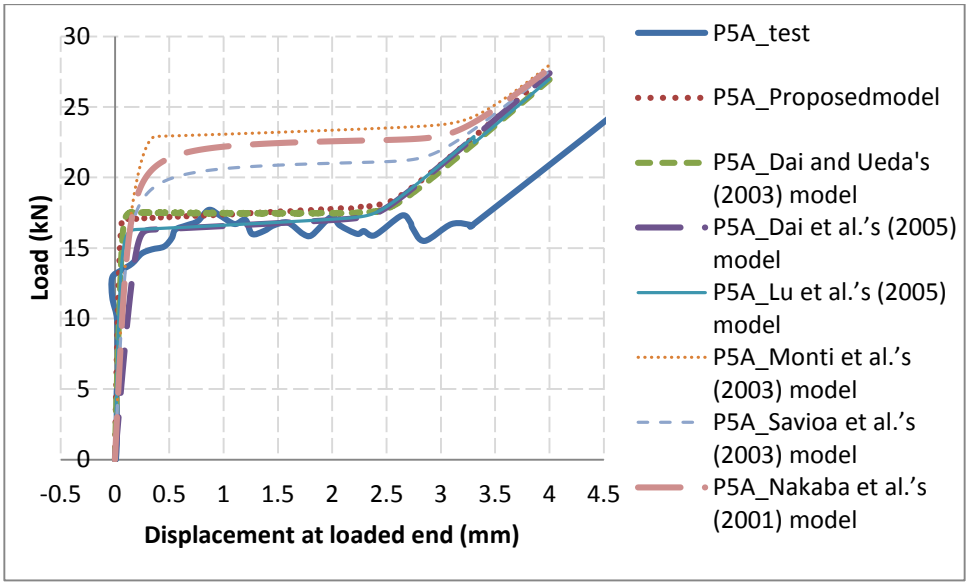

Figure 9.33 Comparison of load-displacement testing curves of Specimen P5A from Mazzotti et al. (2009) and the corresponding predicted curves from simulations with different bond-slip models

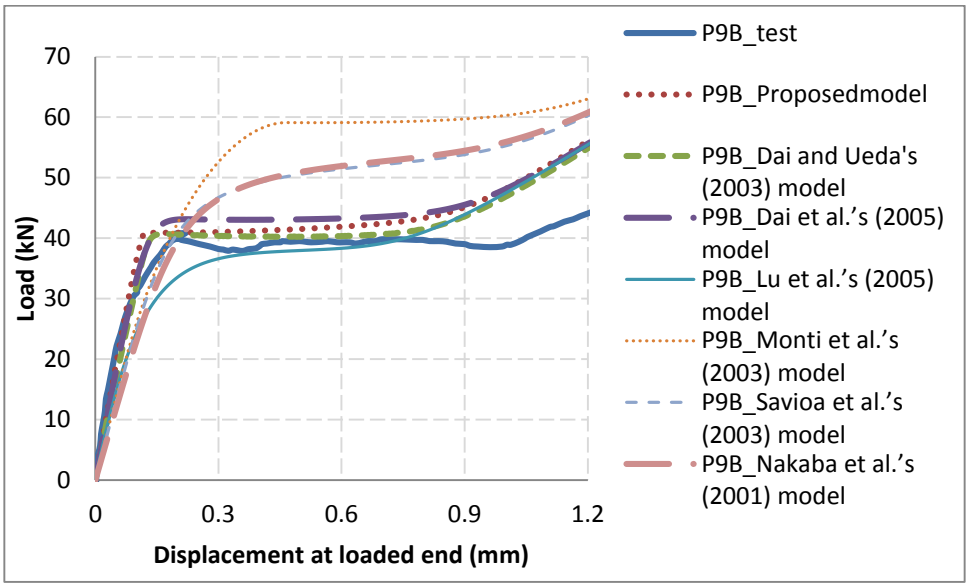

Figure 9.34 Comparison between test data from Mazzotti et al. (2009) and the corresponding simulation results with different models

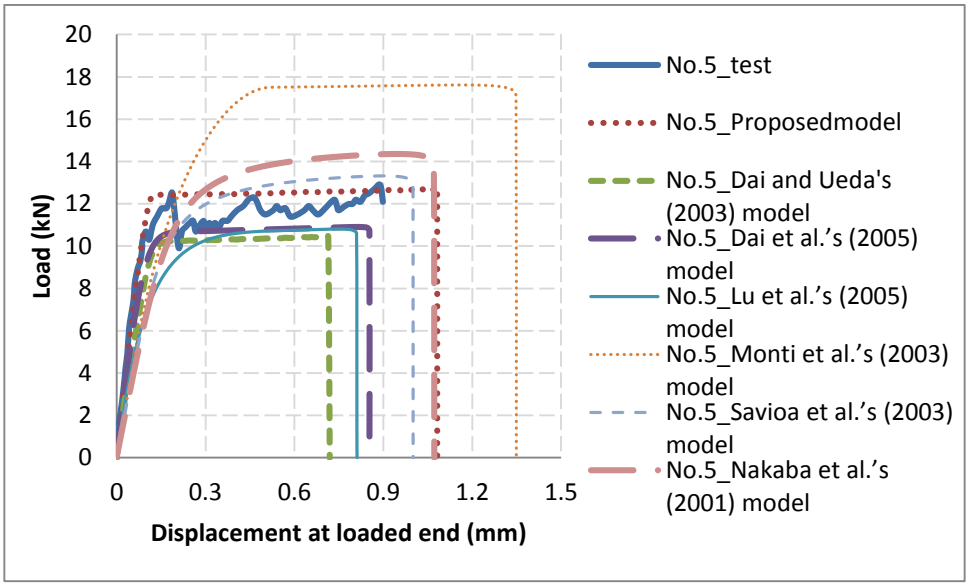

Figure 9.35 Comparison between test data from Ali-ahmad et al. (2006) and the corresponding simulation results with different models

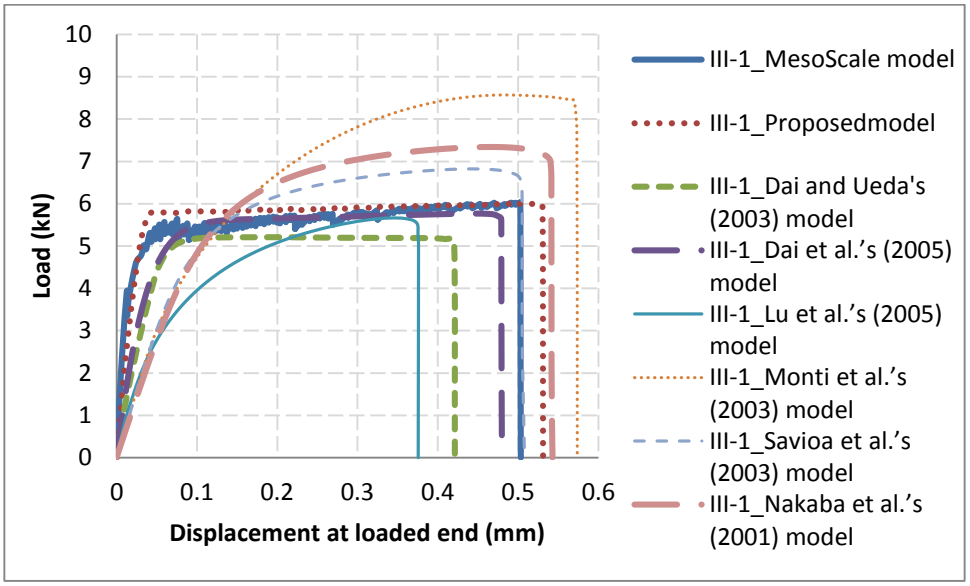

Figure 9.36 Load-displacement curves from simulations of Specimen III-1 in Yao et al. (2005) with different bond-slip models

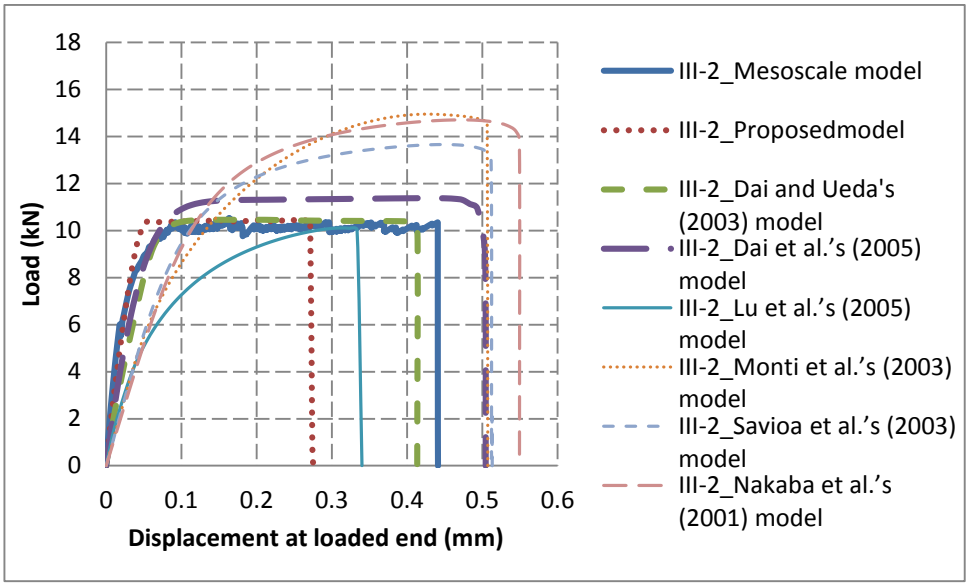

Figure 9.37 Load-Displacement curves from simulations of Specimen III-2 in Yao et al. (2005) with different bond-slip models

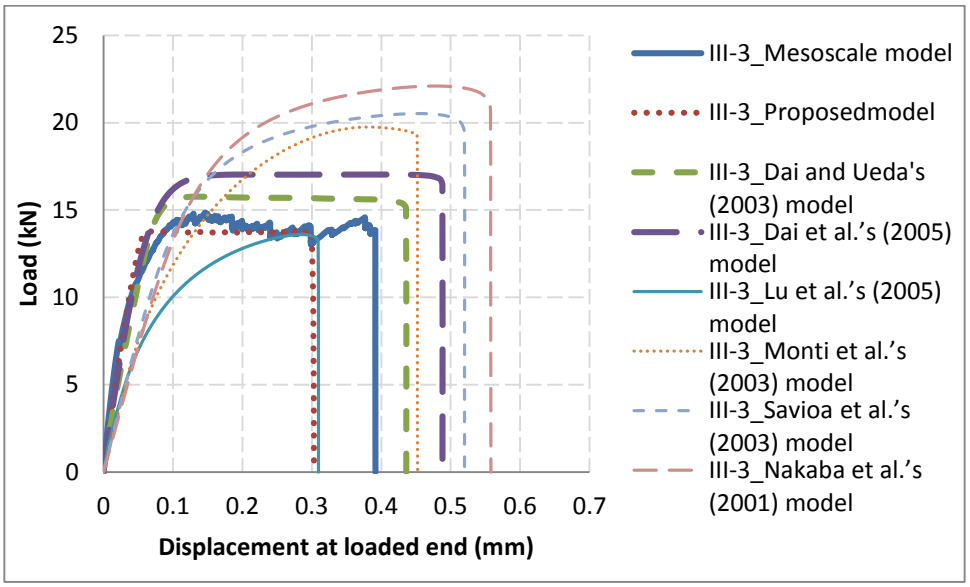

Figure 9.38 Load-displacement curves from simulations of Specimen III-3 in Yao et al. (2005) with different bond-slip models

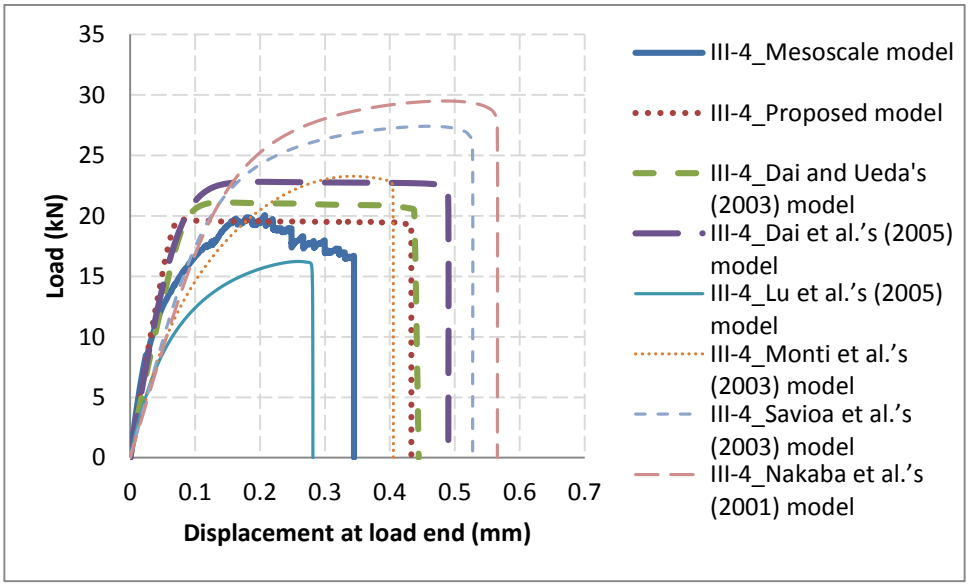

Figure 9.39 Load-displacement curves from simulations of Specimen III-4 in Yao et al. (2005) with different bond-slip models

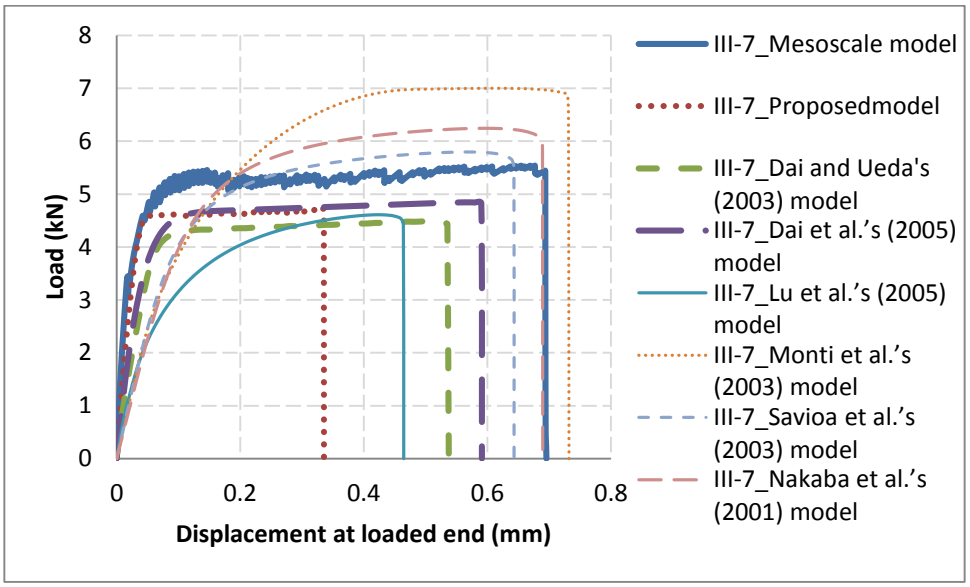

Figure 9.40 Load-displacement curves from simulations of Specimen III-7 in Yao et al. (2005) with different bond-slip models

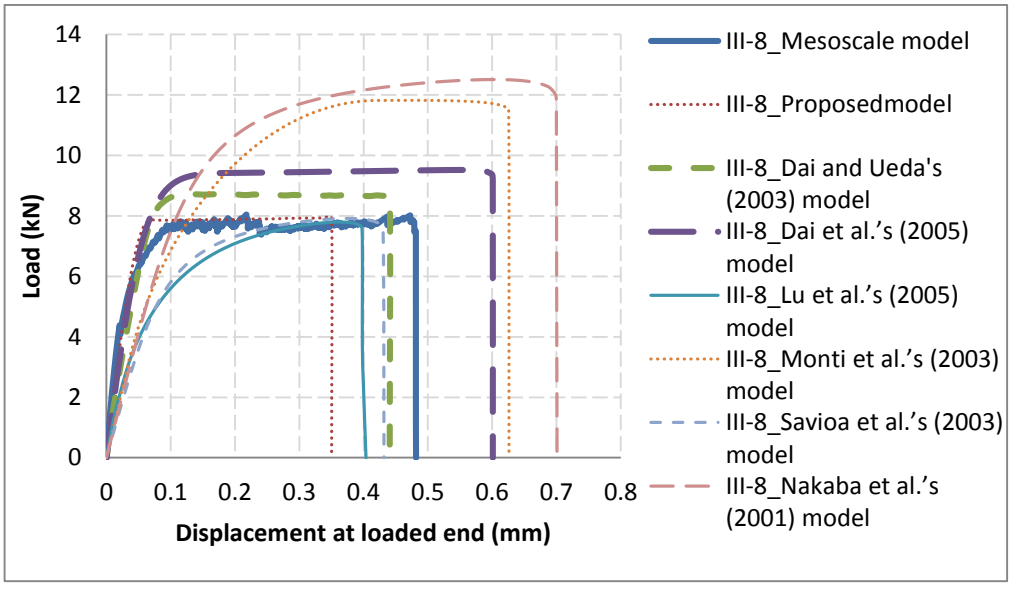

Figure 9.41 Load-displacement curves from simulations of Specimen III-8 in Yao et al. (2005) with different bond-slip models

In addition to the proposed model, the models obtained through the third method reviewed in Section 9.3.1, viz Dai and Ueda's (2003) and Dai et al.'s (2005) models, could also obtain a relatively good performance in predicting the ultimate load and

loading stiffness of the model, although the loading stiffness in simulations with these two models is still shown a little bit smaller, due to an inevitable system error in physical tests caused by the transient zone length of FRP at the FRP-concrete bonded interface before testing. As for the other bond-slip models, they are definitely inappropriate to describe the FRP-concrete interfacial debonding.

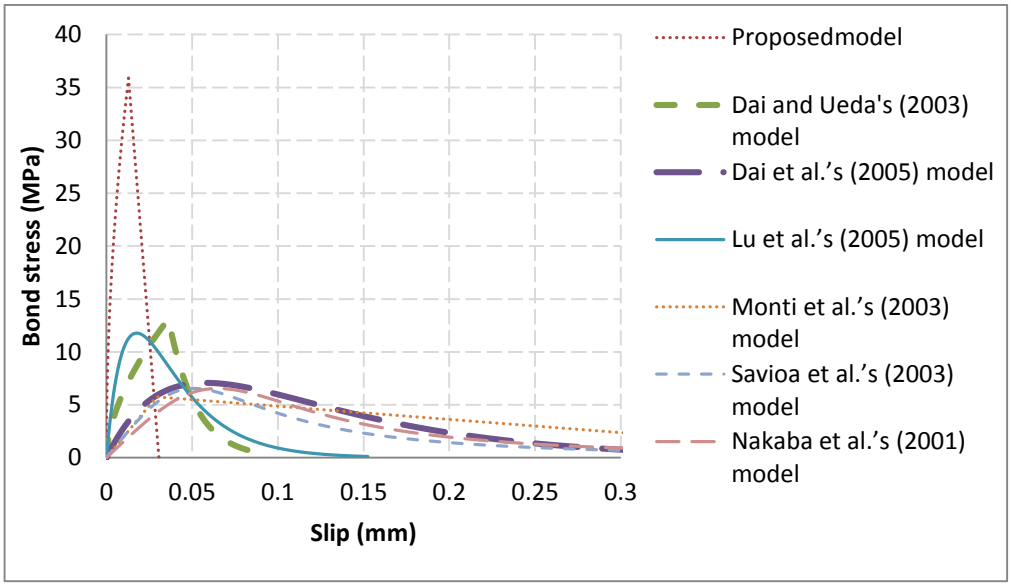

Figure 9.42 Comparisons of bond stress-slip curves from the reviewed and proposed models

Even so, for the sake of completeness of research, the bond-slip curves from the already reviewed and proposed models are demonstrated in Figure 9.42, with reference to Specimen III-1 from Yao et al. (2005). As seen in Figure 9.42, it is found that the stiffness and peak bond stress in the proposed model is much higher than that in the other models. Second to the proposed model in this aspect is Dai and Ueda's (2003) and Dai et al.'s (2005) models. Together with what have been observed in Figure 9.33-Figure 9.41, it is also found that the stiffness in the global load-displacement curve is highest in the simulation with the proposed model, which is followed by Dai and Ueda's (2003) model. Especially when comparing the simulation results with Lu et al.'s (2005a) model to that with proposed model, it is found that the stiffness is much lower than that with the proposed model, although the ultimate load is almost the same

with each other. That is because the ultimate load is only determined by the interfacial fracture energy that has been predicted with some good accuracies.

A safe conclusion is drawn that the proposed bond-slip model is the best ever model of its kind to simulate the FRP-concrete bonded interface, although the stiffness and peak bond stress is much higher than that in other existing models.

9.8 Conclusions

In this chapter, through a comprehensive review of bond-slip models and methods for determining the bond stress and slip, and further investigations using the bond-slip models obtained from these methods, the method employed in Lu et al. (2005a) is determined as the most reasonable amongst them and used to extract bond-slip relationships in the parametric studies employing the 2D mesoscale FE model presented in Chapter 8.

To achieve a better understanding of the bond-slip behaviour of FRP-concrete bonded interface, effects of the parameters in the 2D mesoscale FE model, such as the FRP stiffness, FRP-concrete width ratio and concrete strength, are considered respectively on maximum bond stress, slip at maximum bond stress and interfacial fracture energy in bond-slip models. The relevant results from the above studies are used to formulate a new bond-slip model for such bonded interfaces.

To validate the proposed bond-slip model, it is employed to simulate the specimens from Yao et al. (2005), Ali-ahmad et al. (2006) and Mazzotti et al. (2009), which are varied from concrete strength, FRP length, FRP stiffness, to FRP-to-concrete width ratio. The simulation results with these bond-slip models are compared to their corresponding test results or simulation results with mesoscale method (i.e. when test result is not available) not only on the ultimate load, as done in other literatures (e.g. Lu et al. (2005a)), but also on the load-displacement curves. Through such comparisons, it is found that the proposed model, which is specially developed for debonding case at the FRP-concrete bonded interface, is the best ever of its kind.

Chapter 10
Conclusions and suggestions for further research

10.1 Conclusions

This research presented in this thesis dealt with simulations of FRP-concrete bonded interface. This thesis contains three major parts. The first part dealt with parameter analyses of the simulations of FRP-concrete bonded interface with mesoscale model, which included the effects of Rayleigh damping ratio, damage model in CDP model, compressive stress-strain models in CDP model, tensile fracture energy and compressive strain energy in CDP model. The second part proposed a new mesoscale modelling method to simulate 3D debonding behaviour at FRP-concrete bonded interface in 2D method based on the results in the aforementioned parameter analyses. The third part proposed a new bond-slip model to simulate the debonding behaviour at FRP-concrete bonded interface based on the results of mesoscale model (i.e. obtained in the second part).

Specific conclusions on the various sub-topics have been included in the individual chapters. A summary of the major conclusions is presented in what follows.

A) Parameter analyses of the simulations of FRP-concrete bonded interface with mesoscale model
    1) The Rayleigh damping ratio, especially the stiffness proportional damping ratio, plays a very significant role on the mechanical behaviour of the structures with higher frequency response, like FRP-concrete bonded interface. A lower value may lead to a convergence issue in these simulations, whereas a higher value may lead to an accurate result. In view of this, a procedure is recommended to determine a safe interval for the stiffness proportional damping ratio in simulations.
    2) It was found that damage model plays a significant role in simulations of FRP-concrete bonded interface and different models will bring different results in

simulations. Through comparisons between the predicted unloading/reloading paths arising from different damage models and test data obtained from the experiments of cylinder specimens under cyclic loads, and further verification in simulations of FRP-concrete bonded interface, Birtel and Mark's (2006) model is found most reasonable to represent the damage behaviour of concrete in simulations.

3) The ultimate load at FRP-concrete bonded interface with debonding failure mode is highly connected to hardening compressive strain energy of concrete but not to tensile fracture energy. In contrast, the ultimate load at FRP-concrete bonded interface with CPF failure mode is highly connected to tensile fracture energy, but not to compressive strain energy of concrete. However, the ultimate loads in the cases with these two failure modes are irrelevant to the shapes of compressive stress-inelastic strain curves and tensile stress-inelastic displacement curves.
4) Due to effect of compressive strain energy, it is necessary to find out an appropriate compressive stress-strain model to simulate the debonding behaviour at FRP-concrete bonded interface. Through comparisons between different compressive stress-strain models and test data obtained from the experiments of cylinder specimens under cyclic loads, and further verification in simulations of FRP-concrete bonded interface, CEB-FIP (1990) model is regarded as the most reasonable model to represent the plasticity behaviour of concrete in simulations.

B) Proposal of a new mesoscale modelling method to simulate 3D debonding behaviour at FRP-concrete bonded interface

In this part, a new formula is derived from Chen and Teng's (2001) bond strength model to represent the 3D debonding behaviour of FRP-concrete bonded interface, a behaviour that is arising from the confining effect of FRP on concrete adjacent to FRP. Hence, a formula is proposed to quantify this effect, thereby enabling to simulate the 3D behaviour of FRP-concrete bonded interface in 2D method. It was found that the proposed model performs well in simulating the debonding behaviour of FRP-concrete

bonded interface, through comparisons of simulation results with the proposed model to their corresponding test results.

C) Proposal of a new bond-slip model to simulate the debonding behaviour at FRP-concrete bonded interface

Through a series of FE studies using mesoscale model, a new bond-slip is proposed to simulate the debonding behaviour of FRP-concrete bonded interface. It is found as the best model of this kind ever, through comparisons of physical test results of specimens from Yao et al. (2005), Ali-ahmad et al. (2006) and Mazzotti et al. (2009) to their corresponding simulation results with the proposed model and the other six already reviewed bond-slip models.

In summary, these two FE models provide powerful and economical alternatives to laboratory test, thereby providing a better understanding of the mechanical behaviour of FRP-concrete bonded interface.

10.2 Contributions

As an attempt to model the debonding behaviour at FRP-concrete interface, the following contributions have been made:

- Development of a method using 2D mesoscale model to simulate FRP-concrete 3D debonding behaviour
- Development of a method using bond-slip model to simulate FRP-concrete debonding behaviour
- Proposal of a method to obtain a safe interval of stiffness proportional Rayleigh damping ratio in simulations of FRP-concrete bonded interface through investigations of its role and effect in relevant simulations
- Evaluation of the effect of concrete damage model in simulations, and determination of an appropriate model amongst various damage models through a series of comparative analyses

- Explanation of the debonding mechanism through parameter analyses with concrete compression strain energy
- Determination of an appropriate concrete compressive stress-strain model amongst various models through a series of comparative analyses

It is also believed that this research may directly impact professional practice, as the findings have informed the debonding failure modes associated with FRP-concrete interfacial debonding behaviour and will contribute to the development of design guidelines.

10.3 Further research work

The research work conducted in this study focused on modelling of FRP-concrete interfacial bond behaviour, which serves as the foundation to understand various failure modes in FRP strengthened beams associated with debonding failure mode. In view of that, the research results could be extended into different areas listed as follows:

- The cyclic performance of FRP-concrete bonded interface may be investigated on basis of the bond-slip model;
- Strengthened RC beams with FRP could be simulated using the combination of smeared and interface models. Specifically, the concrete could be modelled through coarse elements with concrete properties used in this study and the debonding behaviour between FRP and concrete modelled with the proposed bond-slip model in this study;
- The already cracked and strengthened RC beams with FRP could be simulated using the combination of smeared and discrete crack models. Specifically, the dominant cracks in concrete are modelled with discrete crack model whereas the minor cracks in concrete are modelled with smeared crack model. Bonding behaviour between FRP and concrete is also modelled with the proposed bond-slip model in this study;
- A more general bond-slip could be proposed through considering the effect of loading offset.

References

ABAQUS. (2011). *ABAQUS 6.11 Analysis User's Manual*. Dassault Systèmes, Providence, RI, USA.

Abbasi, M. S. A., Baluch, M. H., Azad, A. K., and Abdel-Rahman, H. H. (1993). "Sensitivity study of criteria governing collapse of centrally loaded R/C slabs." *Engineering computations*, MCB UP Ltd, 10(2), 175–187.

ACI Committee 440. (2002). "Guide for the Design and Construction of Externally Bonded FRP Systems for Strengthening Concrete Structures." *Construction*, American Concrete Institute, Detroit.

Ali-Ahmad, M., Subramaniam, K., and Ghosn, M. (2006). "Experimental Investigation and Fracture Analysis of Debonding between Concrete and FRP Sheets." *Journal of Engineering Mechanics*.

Alipour, A., and Fareian, F. (2008). "Study Rayleigh Damping in structures: uncertainties and treatments." *The 14th World Conference on Earthquake Engineering*, Beijing, China.

Arduini, M., Tommaso, A. D., and Nanni, A. (1997). "Brittle failure in FRP plate and sheet bonded beam." *ACI Structural Journal*, 94(4), 363–369.

Armero, F., and Oller, S. (2000). "A general framework for continuum damage models. I. Infinitesimal plastic damage models in stress space." *International Journal of Solids and Structures*, 37(48-50), 7409–7436.

Au, C. (2005). "Moisture Degradation in FRP Bonded Concrete Systems: An Interface Fracture Approach." Ph.D Thesis. Massachusetts Institute of Technology.

Au, C., and Büyüköztürk, O. (2006). "Debonding of FRP plated concrete: A tri-layer fracture treatment." *Engineering Fracture Mechanics*, 73(3), 348–365.

Bažant, Z. P. (1976). "Instability, Ductility, and Size Effect in Strain-Softening Concrete." *Journal of EngineeringMechanics Division, ASCE*, 102(2), 331–344.

Bažant, Z. P. (1984). "Size Effect in Blunt Fracture: Concrete, Rock, Metal." *Journal of Engineering Mechanics*, American Society of Civil Engineers, 110(4), 518–535.

Bažant, Z. P. (1986). "Mechanics of Distributed Cracking." *Applied Mechanics Reviews*, 39(5), 675–705.

Bažant, Z. P., and Cedolin, L. (1979). "Blunt crack band propagation in finite element analysis." *Journal of Engineering Mechanics Division, ASCE*, 105(2), 297–315.

Bažant, Z. P., and Oh, B. H. (1983). "Crack band theory for fracture of concrete." *Matériaux et Constructions*, Bordas-Dunod, 16(3), 155–177.

Bazant, Z. P., and Planas, J. (1997). *Fracture and Size Effect in Concrete and Other Quasibrittle Materials*. New Directions in Civil Engineering, CRC Press.

Béton, C. euro-international du. (1993). *CEB-FIP model code 1990: design code*. Design Code, T. Telford.

Birtel, V., and Mark, P. (2006). "Parameterised finite element modelling of RC beam shear failure." *2006 ABAQUS User's Conference. Taiwan*.

Bizindavyi, L., and Neale, K. W. (1999). "Transfer lengths and bond strengths for composites bonded to concrete." *Journal of Composites for Construction*, 3(4), 153–160.

Blaschko, M., Niedermeier, R., and Zilch, K. (1996). "Bond failure modes of flexural members strengthened with FRP." *Fiber Compos. in Infrastruct., Proc., 2nd Int. Conf. on Compos. in Infrastruct.*, H. Saadatmanesh and and M. R. Ehsani, eds., 315–327.

de Borst, R. (1986). "Non-linear Analysis of Frictional Materials." Ph.D Thesis. Delft University of Technology.

de Borst, R. (1987). "Computation of post-bifurcation and post-failure behavior of strain-softening solids." *Computers & Structures*, 25(2), 211–224.

de Borst, R., Pamin, J., Peerlings, R., and Sluys, L. (1995). "On gradient-enhanced damage and plasticity models for failure in quasi-brittle and frictional materials." *Computational Mechanics*, 17, 130–141.

Brencich, A., and Gambarotta, L. (2001). "Isotropic damage model with different tensile–compressive response for brittle materials." *International Journal of Solids and Structures*, 38(34-35), 5865–5892.

Buyukozturk, O., Gunes, O., and Karaca, E. (2002). "Debonding Problems in FRP Strengthened Beams." *Proceedings of the Seventh U.S. National Conference on Earthquake Engineering*, Boston, MA.

Camata, G., Spacone, E., and Zarnic, R. (2007). "Experimental and nonlinear finite element studies of RC beams strengthened with FRP plates. Composites: Part B:" *Engineering*, 38(2), 277–288.

CEBFIP. (1993). *CEB-FIP model code 1990: design code*. Design Code, Thomas Telford.

Chaboche, J. L. (1993). "Development of Continuum Damage Mechanics for Elastic Solids Sustaining Anisotropic and Unilateral Damage." *International Journal of Damage Mechanics*, 2(4), 311–329.

Chaboche, J. L., Lesne, P. M., and Maire, J. F. (1995). "Continuum Damage Mechanics, Anisotropy and Damage Deactivation for Brittle Materials Like Concrete and Ceramic Composites." *International Journal of Damage Mechanics*, 4(1), 5–22.

Chajes, M. J., Finch, W. W., Januszka, T. F., and Thomson, T. A. (1996). "Bond and Force Transfer of Composite Material Plates Bonded to Concrete." *ACI Structural Journal*, 93(2), 208–217.

Chandrakanth, S., and Pandey, P. C. (1995). "An isotropic damage model for ductile material." *Engineering Fracture Mechanics*, 50(4), 457–465.

Charney, F. A. (2005). "Consequences of Using Rayleigh Damping in Inelastic Response History Analysis." *Proceedings,Congreso Chileno de Sismologia e Ingenieria Antisismica*, A10–17.

Chen, A. C. T., and Chen, F. W. (1975). "Constitutive relations for concrete." *J. Eng. Mech. Div. ASCE*, 101(4), 465–481.

Chen, G. (2010). "Behaviour and strength of Rc beams shear-strengthened with externally bonded FRP reinforcement." Ph.D Thesis. The Hong Kong Polytechnic University.

Chen, G. M., Chen, J. F., and Teng, J. G. (2012). "On the finite element modelling of RC beams shear-strengthened with FRP." *Construction and Building Materials*, Elsevier Ltd, 32, 13–26.

Chen, G. M., Teng, J. G., and Chen, J. F. (2009). "Finite element simulation of IC debonding in FRP-plated RC beams: a dynamic approach." *Proceedings, Ninth International Symposium on Fiber Reinforced Polymer Reinforcement for Concrete Structures (FRPRCS-9)*, 13–15.

Chen, G. M., Teng, J. G., Chen, J. F., and Xiao, Q. G. (2015). *Finite element modelling of debonding failures in FRP-strengthened RC beams: A dynamic approach*.

Chen, J. F., and Pan, W. K. (2006). "Three dimensional stress distribution in FRP-to-concrete bond test specimens." *Construction and Building Materials*, Elsevier, 20(1), 46–58.

Chen, J. F., and Teng, J. G. (2001). "Anchorage Strength Models for FRP and Steel Plates Bonded to Concrete." *Journal of Structural Engineering*, 127(7), 784–791.

Chen, J. F., Yang, Z. J., and Holt, G. D. (2001). "FRP or steel plate-to-concrete bonded joints: Effect of test methods on experimental bond strength." *Steel and Composite Structures*, 1(2), 231–244.

Chen, J., and Tao, Y. (2011). "Finite element modelling of FRP-to-concrete bond behaviour using the concrete damage plasticity theory combined with a plastic degradation model." *Advances in FRP Composites in Civil Engineering*, 45–50.

Chen, W. F., and Han, D. J. (1988). *Plasticity for Structural Engineers*. Springer-Verlag, New York.

Chen, Z., Huang, H., and Zhai, Y. (2010). "Stress-strain model of corroded concrete under uniaxial compressive loading." *Journal Wuhan University of Technology, Materials Science Edition*, 25(2), 303–307.

Chiao, T., Lien, P., Reifsnider, K., Morgan, R., and Hahn, H. (1980). "Simplified Formulas for Elastic Moduli of Unidirectional Continuous Fiber Composites." *Journal of Composites Technology and Research*, 2(3).

Chow, C. L., and Lu, T. J. (1989). "On evolution laws of anisotropic damage." *Engineering Fracture Mechanics*, 34(3), 679–701.

Chow, C. L., and Wang, J. (1988). "Ductile fracture characterization with an anisotropic continuum damage theory." *Engineering Fracture Mechanics*, 30(5), 547–563.

Chung, D. D. L. (1994). *Carbon Fiber Composites*. Butterworth-Heinemann.

Clarke, M. J., and Hancock, G. J. (1990). "A study of incremental interactive strategies for nonlinear analysis." *International Journal for Numerical Methods in Engineering*, 29(7), 1365–1391.

Comyn, J. (1981). (1981). *Developments in Adhesives*. (A. J. Kinloch, ed.), Applied Science Publishers, London.

Contrafatto, L., and Cuomo, M. (2006). "A framework of elastic–plastic damaging model for concrete under multiaxial stress states." *International Journal of Plasticity*, 22(12), 2272–2300.

Coulomb, C. A. (1776). "Essai sur une application des regles des maximis et minimis a quelquels problemesde statique relatifs, a la architecture." *Mem. Acad. Roy. Div. Sav*, 7, 343–387.

Crisfield, M. A. (1981). “A fast incremental/iterative solution procedure that handles ‘snap-through.’” *Computers & Structures*, 13(1-3), 55–62.

Crisfield, M. A. (1986). “Snap-through and snap-back response in concrete structures and the dangers of under-integration.” *International Journal for Numerical Methods in Engineering*, 22(3), 751–767.

Crisfield, M. A. (1991). *Non-linear Finite Element Analysis of Solids and Structures*. John Wiley & Sons Ltd, Chichester, England, UK.

Dai, J., and Ueda, T. (2003). “Local bond stress slip relations for FRP sheets concrete interfaces.” *Proc. of 6th international symposium on FRP reinforcement for concrete structures*, World Scientific Publications, Singapore, 143–152.

Dai, J., Ueda, T., and Sato, Y. (2005). “Development of the Nonlinear Bond Stress–Slip Model of Fiber Reinforced Plastics Sheet–Concrete Interfaces with a Simple Method.” *Journal of Composites for Construction*.

Darby, A., Ibell, T., and Clarke, J. (2004). *Design guidance for strengthening concrete structures using fibre composite materials*. The Concrete Society, London.

Delmon, J., and Delmon, V. R. (Eds.). (2012). *International project finance and public-private partnerships. a legal guide to key growth markets 2013*.

Desayi, P., and Krishnan, S. (1964). “Equation for the Stress-Strain Curve of Concrete.” *ACI Journal Proceedings*, 61(3), 345–350.

Drucker, D. C., and Prager, W. (1952). “Soil mechanics and plastic analysis for limit design.” *Quarterly of Applied Mathematics*, 10(2), 157–165.

Eckold, G. (1994). *Design and Manufacture of Composite Structures*. Woodhead Publishing Limited.

Elwi, A. A., and Murray, D. W. (1979). “A 3D Hypoelastic Concrete Constitutive Relationship.” *Journal of the Engineering Mechanics Division*, 105(4), 623–641.

EN 1992-1-1. (2004). “Eurocode 2: Design of concrete structures - Part 1-1: General rules and recommendations for buildings.” European Committee for Standardization, Brussels.

Evert Hoek, E. T. B. (1980). “Empirical Strength Criterion for Rock Masses.” *Journal of the Geotechnical Engineering Division*, 106(9), 1013–1035.

Fanning, P., and Kelly, O. (2000). “Smeared crack models of RC beams with externally bonded CFRP plates.” *Computational Mechanics*.

Fleming, C. J., and King, G. E. M. (1967). "The Development of Structural Adhesives for Three Original Uses in South Africa." *RILEM International Symposium, Synthetic Resins in Building Construction*, Paris, 241–251.

Garden, H. N., and Hollaway, L. C. (1998). "An Experimental Study of the Failure Modes of Reinforced Concrete Beams Strengthened with Prestressed Carbon Composite Plates." *Composites Part B*, 29(4), 411–424.

Gdoutos, E. E., Pilakoutas, K., and Rodopoulos, C. (Eds.). (2000). *Failure analysis of industrial composite materials*. McGraw-Hill.

Gopalaratnam, V. S., and Shah, S. P. (1985). "Softening Response of Plain Concrete in Direct Tension." *ACI Journal Proceedings*, 82(3), 310–323.

Grassl, P., and Jirásek, M. (2006). "Damage-plastic model for concrete failure." *International Journal of Solids and Structures*, 43(22-23), 7166–7196.

Gunes, O. (2004). "A Fracture Based Approach to Understanding Debonding in FRP Bonded Structural Members." Massachusetts Institute of Technology, Cambridge, MA.

Guo, Z. (Ed.). (1999). *Reinforced concrete structral Principle*. Tsinghua University press, Beijing.

Hearing, B. (2000). "Delamination in Reinforced Concrete Retrofitted with Fiber Reinforced Plastics." Massachusetts Institute of Technology,Cambridge, MA.

Hilber, H. M., Hughes, T. J. R., and Taylor, R. L. (1977). "Improved numerical dissipation for time integration algorithms in structural dynamics." *Earthquake Engineering & Structural Dynamics*, 5(3), 283–292.

Hiroyuki, Y., and Wu, Z. S. (1997). "Analysis of debonding fracture properties of CFS strengthened member subject to tension." *Non-metallic (FRP) reinforcement for concrete structures, Proceedings of the Third International Symposium*, Japan Concrete Institute, Sapporo, Japan, 287–294.

Hognestad, E., Hanson, N. W., and McHenry, D. (1955). "Concrete Stress Distribution in Ultimate Strength Design." *ACI Journal Proceedings*, 52(12), 455–480.

Hollaway, L., and Leeming, M. (1999). "Review of materials and techniques for plate bonding. In: , UK: Publishing; 1999." *Strengthening of reinforced concrete structures using externally bonded FRP composites in structural and civil engineering*, L. Hollaway and M. Leeming, eds., Woodhead, Cambridge, UK.

Holzenkampfer. (1994). "Ingenieurmodelle des verbundes geklebter bewehrung fu¨r betonbauteile." Ph.D Thesis. TU Braunschweig.

Hordijk, D. A. (1991). “Local approach to fatigue of concrete.” Ph.D Thesis. Delft University of Technology,Delft.

Ingraffea, A. R., and Saouma, V. (1985). “Numerical modeling of discrete crack propagation in reinforced and plain concrete.” *Fracture mechanics of concrete: Structural application and numerical calculation SE - 4*, Engineering Application of Fracture Mechanics, G. Sih and A. DiTommaso, eds., Springer Netherlands, 171–225.

Jankowiak, T., and Lodygowski, T. (2005). “Identification of parameters of concrete damage plasticity constitutive model.” *Foundations of civil and environmental engineering*, 6, 53–69.

Jason, L., Huerta, A., Pijaudier-Cabot, G., and Ghavamian, S. (2006). “An elastic plastic damage formulation for concrete: Application to elementary tests and comparison with an isotropic damage model.” *Computer Methods in Applied Mechanics and Engineering*, 195(52), 7077–7092.

Jirásek, M. (2004). “Non-local damage mechanics with application to concrete.” *Revue Française de Génie Civil*, 8(5-6), 683–707.

Jowkarmeimandi, R., and Aslani, F. (2012). “Stress–strain model for concrete under cyclic loading.” *Magazine of Concrete Research*, 64(8), 673–685.

Ju, J. W. (1989). “On energy-based coupled elastoplastic damage theories: Constitutive modeling and computational aspects.” *International Journal of Solids and Structures*, 25(7), 803–833.

Kaiser, H. P. (1989). “Strengthening of Reinforced Concrete with Epoxy-Bonded Carbon Fibre Plastics.” ETH Zurich,Switzerland.

Kalfat, R., and Al-Mahaidi, R. (2014). “A prediction model for bidirectional fiber patch anchors used to enhance the performance of FRP materials bonded to concrete.” *Composite Structures*, 117, 51–58.

Karsan, I. D., and Jirsa, J. O. (1969). “Behavior of Concrete Under Compressive Loadings.” *Journal of the Structural Division*, 95(12), 2543–2564.

Kelly, A. (Ed.). (1989). *Concise Encyclopedia of Composite Materials*. Pergamon Press.

Khalifa, A., Gold, W. J., Nanni, A., and Aziz, A. M. I. (1998). “Contribution of Externally Bonded FRP to Shear Capacity of RC Flexural Members.” *Journal of Composites for Construction*, 2(4), 195–202.

Khalifa, A., and Nanni, A. (2000). "Improving shear capacity of existing RC T-section beams using CFRP composites." *Cement and Concrete Composites*, 22(3), 165–174.

Kishi, N., Zhang, G. F., and Mikami, H. (2005a). "Numerical cracking and debonding analysis of RC beams reinforced with FRP sheet." *J. Compos. Constr.*, 9(6), 507–514.

Kishi, N., Zhang, G. F., and Mikami, H. (2005b). "Numerical cracking and debonding analysis of RC beams reinforced with FRP sheet." *J. Compos. Constr.*, 9(6), 507–514.

L'Hermite, R., and Bresson, J. (1967). "Concrete reinforced with glued plates." *RILEM International Symposium, Synthetic Resins in Building Construction*, Paris, 175–203.

Labadi, Y., and Hannachi, N. E. (2005). "Numerical Simulation of Brittle Damage in Concrete Specimens." *Strength of Materials*, 37(3), 268–281.

Lee, J., and Fenves, G. L. (1998). "Plastic-Damage Model for Cyclic Loading of Concrete Structures." *Journal of Engineering Mechanics*, American Society of Civil Engineers, 124(8), 892–900.

Leon, A. (1935). "Uberdie scherfestigkeit des Betons." *Beton und Eisen*, 34.

Lerchenthal, C. H. (1967). "Bonded sheet metal reinforcement for concrete slabs." *Proceedings of the RILEM symposium on synthetic Resins in Building Construction*, Paris, 165–174.

Li, X. (2012). "FRP-to-Concrete Bond Behaviour under High Strain Rates." Ph.D Thesis. The University of Edinburgh.

Li, X., Chen, J., and Lu, Y. (2011). "Meso-scale modelling of FRP-to-concrete bond behaviour using LSDYNA." *Advances in FRP Composites in Civil Engineering*.

Liu, B., and Xu, H. (Eds.). (2008). *Civil Engineering Material*. Ph.D Thesis. Wuhan University of Technology Press, Wuhan.

Lu, X., Teng, J., Ye, L., and Jiang, J. (2004). "Bond-slip models for FRP sheet/plate-to-concrete interfaces." *Proceedings of 2nd international Conference of advanced polymer composites for structural applications in construction (ACIC2004)*, 152–161.

Lu, X., Teng, J., Ye, L., and Jiang, J. (2005a). "Bond–slip models for FRP sheets/plates bonded to concrete." *Engineering structures*, 27(6), 920–937.

Lu, X., Teng, J., Ye, L., and Jiang, J. (2007). "Intermediate crack debonding in FRP-strengthened RC beams: FE analysis and strength model." *Journal of Composites for Construction*, 11(2), 161–174.

Lu, X., Ye, L., Teng, J., and Jiang, J. (2005b). "Meso-scale finite element model for FRP sheets/plates bonded to concrete." *Engineering Structures*, 27(4), 564–575.

Lubliner, J. (1989). "A plastic-damage model for concrete." *International Journal of Solids and Structures*, 25(3), 299–326.

Luccioni, B. M., and Rougier, V. C. (2005). "A plastic damage approach for confined concrete." *Computers & Structures*, 83(27), 2238–2256.

Luccioni, B., Oller, S., and Danesi, R. (1996). "Coupled plastic-damaged model." *Computer Methods in Applied Mechanics and Engineering*, 129(1-2), 81–89.

Maeda, T., Asano, Y., Sato, Y., Ueda, T., and Kakuta, Y. (1997). "A Study on Bond Mechanism of Carbon Fiber Sheet." *Non-Metallic (FRP) Reinforcement for Concrete Structures, Proceedings of the Third Symposium*, 279–286.

Matlab. (2014). *version 7.14.0 (R2014a)*. The MathWorks Inc., Natick, Massachusetts.

Mazzotti, C., Savoia, M., and Ferracuti, B. (2009). "A new single-shear set-up for stable debonding of FRP–concrete joints." *Construction and Building Materials*, Elsevier Ltd, 23(4), 1529–1537.

Meier, U. (1987). "Bridge Repair with High Performance Composite Matcrials." *Matierial and Technik*, 4, 125–128.

Menetrey, P., and Willam, K. J. (1995). "Triaxial Failure Criterion for Concrete and its Generalization." *ACI Structural Journal*, 92(3), 311–318.

Miller, B., and Nanni, A. (1999). "Bond between CFRP sheets and concrete." *Congress, Proceedings of the fifth ASCE materials*, Bank LC, ed., 240–247.

Von Mises, R. (1913). "Mechanik der festen Körper im plastisch deformablen Zustand." *Göttin. Nachr. Math. Phys.*, 1, 582–592.

Mohamed Ali, M. S., Oehlers, D. J., and Bradford, M. A. (2001a). "Shear peeling of steel plates bonded to the tension faces of RC beams." *Proceedings of the Institution of Civil Engineers, Structures and Buildings*, 127(12), 1453–1460.

Mohamed Ali, M. S., Oehlers, D. J., and Bradford, M. A. (2001b). "Shear Peeling of Steel Plates Adhesively Bonded to the Sides of Reinforced Concrete Beams." *Proceedings of the Institution of Civil Engineers, Structures and Buildings*, 140, 249–259.

Mohr, O. (1990). “Welche Umstände bedingen die Elastizitätsgrenze und den Bruch eines Materials.” *Zeitschrift des Vereins Deutscher Ingenieure*, 44-45(1524-1530), 1572–1577.

Monti, G., Renzelli, M., and Luciani, P. (2003). “FRP Adhesion in Uncracked and Cracked Concrete Zones.” *International Symposium on FRP Reinforcement for Concrete Structures; Fibre-reinforced polymer reinforcement for concrete structures 6th, International Symposium on FRP Reinforcement for Concrete Structures; Fibre-reinforced polymer reinforcement for conc*, 183–192.

Murakami, S. (1983). “Notion of Continuum Damage Mechanics and its Application to Anisotropic Creep Damage Theory.” *Journal of Engineering Materials and Technology*, 105(2), 99.

Murakami, S. (1988). “Mechanical Modeling of Material Damage.” *Journal of Applied Mechanics*, 55(2), 280–286.

Murakami, S., and Kamiya, K. (1997). “Constitutive and damage evolution equations of elastic-brittle materials based on irreversible thermodynamics.” *International Journal of Mechanical Sciences*, 39(4), 473–486.

Nakaba, K., Kanakubo, T., Furuta, T., and Yoshizawa, H. (2001). “Bond behavior between fiber-reinforced polymer laminates and concrete.” *ACI Structural Journal*, 98(3), 359–367.

Neale, K. W., Ebead, U. A., Baky, H. M. A., Elsayed, W. E., and Godat, A. (2006). “Analysis of the load-deformation behaviour and debonding for FRP-strengthened concrete structures.” *Advances in Structural Engineering*, 9(6), 751–763.

Nechnech, W., Meftah, F., and Reynouard, J. M. (2002). “An elasto-plastic damage model for plain concrete subjected to high temperatures.” *Engineering Structures*, 24(5), 597–611.

Neubauer, U., and Rostasy, F. (1997). “Design aspects of concrete struc-tures strengthened with externally bonded CFRP plates.” *Proc. of 7th international conference on structural faults and repair*, ECS Publications, Edinburgh (Scotland), 107–118.

Nguyen, G. D., and Houlsby, G. T. (2007). “Non-local damage modelling of concrete: a procedure for the determination of model parameters.” *International Journal for Numerical and Analytical Methods in Geomechanics*, John Wiley & Sons, Ltd., 31(7), 867–891.

Nguyen, G. D., and Korsunsky, A. M. (2006). "Damage-Plasticity Modelling of Concrete: Calibration of Parameters using Separation of Fracture Energy." *International Journal of Fracture*, 139(2), 325–332.

Nitereka, C., and Neale, K. W. (1999). "Analysis of reinforced concrete beams strengthened in flexure with composite laminates." *Canadian Journal of Civil Engineering*.

Niu, H. D., and Karbhari, V. M. (2008). "FE Investigation of Material and Preload Parameters on FRP Strengthening Performance of RC Beams, I: Model Development." *Journal of Reinforced Plastics and Composite*, 27(5), 507–522.

Niu, H., and Wu, Z. (2005). "Numerical Analysis of Debonding Mechanisms in FRP-Strengthened RC Beams." *Computer-Aided Civil and Infrastructure Engineering*, 20(5), 354–368.

Nour, A., Massicotte, B., Yildiz, E., and Koval, V. (2007a). "Finite element modelling of concrete structures reinforced with internal and external fibre-reinforced polymers." *Canadian Journal of Civil Engineering*, 34, 340–354.

Nour, A., Massicotte, B., Yildiz, E., and Koval, V. (2007b). "Finite element modeling of concrete structures reinforced with internal and external fibre-reinforced polymers." *Canadian Journal of Civil Engineering*.

Ortiz, M. (1985). "A constitutive theory for the inelastic behavior of concrete." *Mechanics of Materials*, 4(1), 67–93.

Ottosen, N. S. (1997). "A Failure Criterion for Concrete." *Journal of the Engineering Mechanics Division*, 103(4), 527–535.

Ben Ouezdou, M., Belarbi, A., and Bae, S.-W. (2009). "Effective Bond Length of FRP Sheets Externally Bonded to Concrete." *International Journal of Concrete Structures and Materials*, 3(2), 127–131.

Owen, D. R. J., and Figueiras, J. A. (1984). "Ultimate load analysis of reinforced concrete plates and shells including geometric nonlinear effects." *Finite Element Software for Plates and She*, S. E. Hinton and D. R. J. Owen, eds., Pineridge Press, Swansea, 327–388.

Pan, J., and Leung, C. K. Y. (2007). "Debonding along the FRP-concrete interface under combined pulling/peeling effects." *Engineering Fracture Mechanics*, 74(1-2), 132–150.

Peters, S. T. (1998). *Handbook of Composites*. Springer.

Pham, H., and Almahaidi, R. (2007). “Modelling of CFRP-concrete shear-lap tests.” *Construction and Building Materials*, 21(4), 727–735.

Pham, H., Almahaidi, R., and Saouma, V. (2006). “Modelling of CFRP–concrete bond using smeared and discrete cracks.” *Composite Structures*, 75(1-4), 145–150.

Pham, H. B., and Al-Mahaidi, R. (2005). “Finite element modelling of RC beams retrofitted with CFRP fabrics.” *7th International Symposium on Fiber-Reinforced (FRP) Polymer Reinforcement for Concrete Structures*, ACI Symposium Publication 230, Kansas City, Missouri, 499–513.

Popovics, S. (1970). “A Review of Stress-Strain Relationships for Concrete.” *Journal of the Americal Concrete Institute, ACI*, 67(3), 243–248.

Rabczuk, T., Akkermann, J., and Eibl, J. (2005). “A numerical model for reinforced concrete structures.” *International Journal of Solids and Structures*, 42(5–6), 1327–1354.

Rahimi, H., and Hutchinson, A. (2001). “Concrete beams strengthened by externally bonded FRP plates.” *Journal of Composites for Construction , ASCE*, 5(1), 44–56.

Rayleigh, L. (1877). *The theory of Sound*. Dover Publications, New York.

“Recommendations for an International Code of Practice for Reinforced Concrete.” (1964). Beton, Comite Europeen du, Paris.

Reinhardt, H. W., and Cornelissen, H. A. W. (1984). “Post-peak cyclic behaviour of concrete in uniaxial tensile and alternating tensile and compressive loading.” *Cement and Concrete Research*, 14(2), 263–270.

Ritchie, P. A., Thomas, D. A., Lu, L. W., and Connely, G. M. (1991). “External Reinforcement of Concrete Beams Using Fiberglass Reinforced Plastics.” *ACI Structural Journal*, 88(4), 490–500.

Rostasy, F. S. (1987). *Bonding of Steel and GFRP Plates in the Area of Coupling Joints. Talbrucke Kattenbusch*. Braunschweig, Germany.

Rots, J. (1988). “Computational modeling of concrete fracture.” Delft University of technology,Delft.

Saadatmanesh, H., and Ehsani, M. (1990). “RC Beams Strengthened With GFRP Plates.I: Experimental Study.” *Journal of Structural Engineering*, 117(11), 3417–3433.

Saenz, L. P. (1964). "Discussion of Equation for The Stress-Strain Curve of Concrete - By Desayi and Krishnan." *ACI Journal Proceedings*, 61(6), 1229–1235.

Salari, M. ., Saeb, S., Willam, K. ., Patchet, S. ., and Carrasco, R. . (2004). "A coupled elastoplastic damage model for geomaterials." *Computer Methods in Applied Mechanics and Engineering*, 193(27-29), 2625–2643.

Samani, A. K., and Attard, M. M. (2012). "A stress–strain model for uniaxial and confined concrete under compression." *Engineering Structures*, 41, 335–349.

Sargin, M. (1971). "Stress-strain Relationship for Concrete in Analysis of Structural Concrete Sections." *Solid Mechanics Division*, University of Waterloo, Ontario, Canada.

Savioa, M., Farracuti, B., and Mazzotti, D. (2003a). "Non-linear bond-slip law for FRP-concrete interface." *Proc. of 6th international symposium on FRP reinforcement for concrete structures. Singapore: World Scientific Publications*, 163–172.

Savioa, M., Farracuti, B., and Mazzotti, D. (2003b). "Non-linear bond–slip law for FRPconcrete interface." *Proc. of 6th international symposium on FRP reinforcement for concrete structures*, World Scientific Publications, Singapore, 163–172.

Serway, R., and Jewett, J. (2005). *Principles of Physics: A Calculus-Based Text*. Available 2010 Titles Enhanced Web Assign Series, Cengage Learning.

Shao, J. F., Jia, Y., Kondo, D., and Chiarelli, a. S. (2006). "A coupled elastoplastic damage model for semi-brittle materials and extension to unsaturated conditions." *Mechanics of Materials*, 38(3), 218–232.

Sharif, A., Al-Sulaimani, G. J., Basunbul, I. A., Baluch, M. H., and Ghaleb, B. N. (1994). "Strengthening of Initially Loaded Reinforced Concrete Beams Using FRP Plates." *ACI Structural Journal*, 91(2), 160–168.

Shen, X., Yang, L., and Zhu, F. (2004). "A Plasticity-based Damage Model for Concrete." *Advances in Structural Engineering*, 7(5), 461–467.

Shook, G. D. (1986). *Reinforced Plastics for Commercial Composites: Source Book*. ASM.

Simo, J. C., and Ju, J. W. (1987). "Strain- and stress-based continuum damage models—I. Formulation." *International Journal of Solids and Structures*, 23(7), 821–840.

Simo, J. C., and Ju, J. W. (1989). "Strain- and stress-based continuum damage models—II. Computational aspects." *Mathematical and Computer Modelling*, 12(3), 378.

Sinha, B. P., Gerstle, K. H., and Tulin, L. G. (1964). "Stress-Strain Relations for Concrete Under Cyclic Loading." *ACI Journal Proceedings*, 61(2), 195–212.

Smith, G. M., and Young, L. E. (1955). "Ultimate Theory in Flexure by Exponential Function." *ACI Journal. Proceedings*, 52(3), 349–360.

Smith, S. T., and Teng, J. G. (2001). "Interfacial Stresses in Plated Beams." *Engineering Structures*, 23(7), 857–871.

Swamy, R. N., and Mukhopadhyaya, P. (1995). "Role and effectiveness of non-metallic plates in strengthening and upgrading concrete structures." Non-Metallic (FRP) Reinforcement for Concrete Structures, 2nd International RILEM Symposium FRPRCS-2.

Taljsten, B. (1994). "Plate bonding: strengthening of existing concrete structures with epoxy bonded plates of steel or fiber reinforced plastics." Ph.D Thesis. Lulea University of Technology.

Taljsten, B. (1997). "Strengthening of Beams by Plate Bonding." *Journal of Materials in Civil Engineering,* 9(4), 206–211.

Tao, X., and Phillips, D. V. (2005). "A simplified isotropic damage model for concrete under bi-axial stress states." *Cement and Concrete Composites*, 27(6), 716–726.

Tao, Y., and Chen, J. F. (2015). "Concrete Damage Plasticity Model for Modeling FRP-to-Concrete Bond Behavior." *Journal of Composites for Construction*, 19(1), 0401–4026.

Taqieddin, Z. N. (2008). "Elasto-plastic and damage modeling of reinforced concrete." Ph.D Thesis. Louisiana State University.

Teng, J. G., Chen, J. F., Smith, S. T., and Lam, L. (2002). *FRP: Strengthened RC Structures*. UK: John Wiley&Sons.

Teng, J. G., Smith, S. T., Yao, J., and Chen, J. F. (2003). "Intermediate crack-induced debonding in RC beams and slabs." *Construction and Building Materials*, 447–462.

Tikhomirov, D., and Stein, E. (2001). "Finite element computations of anisotropic continuum damage in reinforced concrete." *Computers & Structures*, 79(22–25), 2249–2260.

Tulin, L. G., and Gerstle, K. D. (1964). "Discussion of Equation for the Stress-Strain Curve of Concrete - By Desayi and Krishnan." *ACI Journal Proceedings*, 61(6), 1236–1238.

Ueda, T., Dai, J., and Sato, Y. (2003). "A nonlinear bond stress–slip relationship for FRP sheet–concrete interface." *Proc. of international symposium on latest achievement of technology and research on retrofitting concrete structures*, 113–120.

UK Department of Transport Advice Note. (1994). "BA 30/94, Strengthening of Concrete Highway Structures Using Externally Bonded Plates." UK Department of Transport Advice Note.

Umemura, H., and Aoyama, H. M. T. (1970). *Experimental Studies on Reinforced Concrete Members and Composite Steel and Reinforced Concrete Members*. University of Tokyo Publication, Tokyo,Japan.

Vinson, J. R. (1999). *The Behavior of Sandwich Structures of Isotropic and Composite Materials*. Taylor & Francis.

Voyiadjis, G., and Abu-Lebdeh, T. (1993). "Damage Model for Concrete Using Bounding Surface Concept." *Journal of Engineering Mechanics*, American Society of Civil Engineers, 119(9), 1865–1885.

Voyiadjis, G. Z., and Kattan, P. I. (1992). "A plasticity-damage theory for large deformation of solids—I. Theoretical formulation." *International Journal of Engineering Science*, 30(9), 1089–1108.

Wang, P. T., Shah, S. P., and Naaman, A. E. (1978). "STRESS-STRAIN CURVES OF NORMAL AND LIGHTWEIGHT CONCRETE IN COMPRESSION." *ACI Journal Proceedings*, 75(11), 603–611.

Wang, Z. (1996). "Crack growth, computer strength and deformation of non-homogeneous materials (concrete)." Ph.D Thesis. Tsinghua University.

Weeton, J. W., Peter, D. M., and Thomas, K. L. (1987). *Engineers' Guide to Composite Materials*. American Society for Metals.

Wikipedia. (2015). "Carbon (fiber)." *the free encyclopedia*, <http://en.wikipedia.org/wiki/Carbon_%28fiber%29>.

Wolf, R., and Miessler, H. J. (1989). "HLV-Spannglieder in der praxis." *erfahrungen mit glasfaserverbundstaben*, 2, 47–51.

Wong, R., and Vecchio, F. (2003). "Towards modeling of reinforced concrete members with externally bonded fiber-reinforced polymer composite." *ACI Structural Journal*, 100(1), 47–55.

Wu, J. Y., Li, J., and Faria, R. (2006). "An energy release rate-based plastic-damage model for concrete." *International Journal of Solids and Structures*, 43(3–4), 583–612.

Wu, Z., Yuan, H., and Niu, H. (2002). "Stress Transfer and Fracture Propagation in Different Kinds of Adhesive Joints." *Journal of Engineering Mechanics*, 128(5), 562–573.

Wu, Z., Yuan, H., Yoshizawa, H., and Kanakubo, T. (2001). "Exprimental/Analytical Study on Interfacial Fracture Energy and Fracture Propagation Along FRP-Concrete Interface." *Fracture mechanics for concrete materials*, 201, 133–152.

Yang, Z. J., Chen, J. F., and Proverbs, D. (2003). "Finite element modelling of concrete cover separation failure in FRP plated RC beams." *Construction and Building Materials*, 17(1), 3–13.

Yao, J. (2004). "Debonding failures in RC beams and slabs strengthened with FRP plates." Ph.D Thesis. The Hong Kong Polytechnic University.

Yao, J., Teng, J., and Chen, J. (2005). "Experimental study on FRP-to-concrete bonded joints." *Composites Part B: Engineering*, 36(2), 99–113.

Yazdani, S., and Schreyer, H. (1990). "Combined Plasticity and Damage Mechanics Model for Plain Concrete." *Journal of Engineering Mechanics*, American Society of Civil Engineers, 116(7), 1435–1450.

Young, L. E. (1960). "Simplifying Ultimate Flexural Theory by Maximizing the Moment of the Stress Block." *ACI Journal Proceedings*, 57(11).

Yu, R. C., Ruiz, G., and Chaves, E. W. V. (2008). "A comparative study between discrete and continuum models to simulate concrete fracture." *Engineering Fracture Mechanics*, 75(1), 117–127.

Yu, T., Teng, J. G., Wong, Y. L., and Dong, S. L. (2010). "Finite element modeling of confined concrete-II: Plastic-damage model." *Engineering Structures*, Elsevier Ltd, 32(3), 680–691.

Yuan, H., and Wu, Z. (1999). "Interfacial fracture theory in structures strengthened with composite of continuous fiber." *Proc., Symp. of China and Japan: Sci. and Technol. of 21st Century*, Tokyo, 142–155.